Design and synthesis of high-performance nanomaterials for electrochemical water splitting

Yuanyuan Miao

Design and Synthesis of High-Performance Nanomaterials for Electrochemical Water Splitting

Prepared at IRI-IEMN by

Yuanyuan MIAO

A thesis submitted in fulfillment of the requirements for the degree of

Doctor of Philosophy in **Micro-Nanosystems and Sensors**

Defended on September 30, 2022 before the committee members:

Mathieu Etienne	**Research Director, University of Lorraine**	**Reviewer**
Sorin Melinte	**Professor, Catholic University of Louvain**	**Reviewer**
Corinne Lagrost	**Research Director, UMR CNRS6226**	**Examiner**
Henri Happy	**Professor, IEMN, University of Lille**	**President/Examiner**
Sabine Szunerits	**Professor, IEMN, University of Lille**	**Examiner**
Rabah Boukherroub	**Research Director, HDR, IEMN**	**Supervisor**
Yannick Coffinier	**Researcher, HDR, IEMN**	**Co-supervisor**

THÈSE

Présentée

pour obtenir le grade de

DOCTEUR

En

La spécialité: Micro-nanosystèmes et capteurs

Par

Yuanyuan MIAO

DOCTORAT DELIVRE PAR UNIVERSITE DE LILLE

Titre de la these :

Conception et Synthèse de Nanomatériaux Performants pour la Séparation Electrochimique de L'eau

Soutenue le 30 Septembre 2022 devant le jury d'examen :

Mathieu Etienne	**DR, Université de Lorraine**	**Rapporteur**
Sorin Melinte	**Pr, Université catholique de Louvain**	**Rapporteur**
Corinne Lagrost	**DR, ISCR – UMR CNRS6226**	**Examinateur**
Henri Happy	**Pr, IEMN, Université de Lille**	**Président/Examinateur**
Sabine Szunerits	**Pr, IEMN, Université de Lille**	**Examinateur**
Rabah Boukherroub	**DR&HDR, IEMN**	**Directeur de thèse**
Yannick Coffinier	**CR&HDR, IEMN**	**Co-directeur de thèse**

Acknowledgment

Graduate school is a challenging experience in many ways. I would not have been able to complete this dissertation without help and support from many wonderful mentors, colleagues, friends, and family members.

Firstly, I would like to thank my supervisor, Dr. Rabah Boukherroub and Dr. Yannick Coffinier, for their patience and guidance from the begging of the projects to finish all of the dissertation. From them, I have learned a lot about how to make research in a scientific way, and obtained a lot of research ability including experiments technologies and theoretically analysis knowledges. It is really a great pressure to study under their mentorships.

I would like to express my thanks to for accepting to be in my thesis defense committee. I truly appreciate your time and your helpful comments.

I sincerely thank Dr. Ahmed Addad for TEM and SEM tests, Dr Pascal Roussel for XRD tests, Dr. Alexandre Barras for Raman test, Prof. Sabine Szunerits for XPS tests in the past four years.

I wish to thank the China Scholarship Council (CSC), Which offer me the opportunity to pursue my PhD study in Lille, France.

My heartfelt thanks go to all my colleagues Dr. Min Li, Dr. Liuqing Pang, Dr.Yuan Zhang, Dr. Jin Zhang, Dr. Tianlong Yu, Dr. Léa Rosselle, Quentin Pagneux, Dr. Anna Voronova, Dr. Vladyslav Mishyn, Dr. Tamazouzt Nait Saada, Dr. Chengnan Li, Elizaveta Sviridova, ZhaoHui Zhang, Yi Zhang, Zhiran Yu, Sravan Kumar Kilaparthi, Ines De hoon, Teresa Rodrigues and Michele Lodato for all those generous help and valuable advice in both research and life. It is truly my honor to know all of you.

Least but not last, I want to say thank you to my family members and my friends

who are not in France, all of your supports and advices made me become stronger and stronger.

Miao Yuanyuan

Villeneuve D'ASCQ, France

10 July, 2022

Abstract

In thesis, we have designed and developed high-efficiency, high-stability, and cost-effective electrocatalysts using a facile and environmentally friendly process. Firstly, we developed an ultrathin hierarchical P-doped MoS_2/Ni_3S_2 heterostructure on nickel foam (NF) by one-pot synthesis. Owing to its optimized electronic structure configuration and hierarchical structure with plenty of active sites, the selected catalyst $P_{1.0}$-doped MoS_2/Ni_3S_2/NF showed promising activity for both hydrogen evolution reaction (HER) and oxygen evolution (OER) in an alkaline medium requiring an overpotential of respectively 0.449 and 0.239 V at 100 mA/cm^2. Furthermore, the $P_{1.0}$-MoS_2/Ni_3S_2/NF electrode was applied for overall water splitting using a two-electrode system. The electrolyzer achieved low cell voltages of 1.50 and 1.65 V at current densities of respectively 20 and 40 mA cm^{-2} with excellent stability over 60 h when compared with previously reported Ni_3S_2-based materials.

Secondly, we have prepared a unique nitrogen-doped MoS_2/N-doped reduced graphene oxide (N-MoS_2/N-rGO) heterostructure by a one-step hydrothermal method possesses, which catalyze HER in both acid and alkaline solution and 0.114 V and 0.2980V to arrive the current density of 100 mA cm^{-2}, and OER in alkaline solution at a overpotential of 0.38mV to arrive the current density of 50 mA cm^{-2}.

Thirdly, we have synthesized the flake-shaped $Ti_xC_yT_x$ MXenes using 0,2M NaBF4 and 8M HCl at 160 ℃ for 12h, which shows promising HER performance with an overpotential of 157.2 mV (vs RHE) to arrive at 10mA cm^{-2} and Tafel slope of 43.87 mv dec^{-1}, and could also maintain a stable current density of 20, 40, 60, 80, and 100 mA cm^{-2} at an overpotential of respectively 160, 217, 251, 269, and 315 V for 28 h.

Our strategy provides a promising pathway for the facile and sustainable production of highly stable MXenes materials.

All of these materials were characterized by a variety of different techniques, such as SEM, TEM, XRD, XPS, and Raman, and the catalytic performance were tested by electrochemical technique including LSV, CV, EIS, and chronopotentiometry.

Key words: Hydrogen Generation, Electrolysis of Water, Electrocatalysis, Molybdenum Disulphide, Graphene Oxide, Nanocatalysts

Résumé

Dans cette thèse, nous avons conçu et développé des électrocatalyseurs à hauts rendement et stabilité et à faible cout en utilisant des méthodes simples et non polluantes. Dans un premier temps, nous avons développé une hétérostructure MoS2/Ni3S2 hiérarchisée ultrafine dopée P sur le mousse de nickel (NF) par synthèse en un seul pot. En raison de sa configuration électronique bien optimisée et de sa structure hiérarchique qui présente de nombreux sites actifs, le catalyseur sélectionné MoS_2/Ni_3S_2/NF dopé $P_{1.0}$ a montré une activité prometteuse pour la réaction de dégagement d'hydrogène (HER) et le dégagement d'oxygène (OER) en milieu alcalin qui nécessitent une surtension de 0,449 et 0,239 V à 100 mA/cm^2 respectivement. En outre, l'électrode $P_{1.0}$-MoS_2/Ni_3S_2/NF a été appliquée pour l'électrolyse de l'eau à l'aide d'un système à deux électrodes. L'électrolyseur a atteint des surtensions de 1,50 et 1,65 V à des densités de courant de respectivement 20 et 40 mA/cm^2, ce système présente une excellente stabilité pendant 60 h par rapport aux systèmes à base de Ni_3S_2 seul rapportés précédemment.

Deuxièmement, nous avons préparé une hétérostructure a base d'oxyde de graphène réduit dopé à l'azote MoS_2/N dopé (N-MoS_2/N-rGO) par la synthèse hydrothermale en une seul étape, la réaction de dégagement d'hydrogène HER dans une milieu acide et alcaline présente une surtension de 0,114 V et 0,2980V respectivement pour atteindre une densité de courant de 100 mA cm^{-2}, et la réaction de dégagement d'oxygène OER dans un milieu alcaline présente une surtension de 0,38mV pour atteindre la densité de courant de 50 mA cm^{-2}.

Troisièmement, nous avons synthétisé les MXènes $Ti_xC_yT_x$ en forme de flocons en utilisant 0.2M $NaBF_4$ et 8M HCl à 160 ℃ pendant 12h, ce qui montre des

performances HER prometteuses avec une surtension de 157.2 mV (vs RHE) pour arriver à 10mA cm^{-2} et Tafel pente de 43.87 mv dec^{-1}, et pourrait également maintenir une densité de courant stable de 20, 40, 60, 80 et 100 mA cm-2 à une surtension de respectivement 160, 217, 251, 269 et 315 V pendant 28 h. Notre stratégie offre une voie prometteuse pour la production facile et durable de matériaux MXenes hautement stables.

Tous ces matériaux ont été caractérisés par une variété de techniques différentes, telles que SEM, TEM, XRD, XPS et Raman, et les performances catalytiques ont été testées par une technique électrochimique comprenant LSV, CV, EIS et chronopotentiométrie.

Mots clé: Génération d'hydrogène, Eau – Électrolyse, Électrocatalyse, Bisulfure de molybdène, Oxyde de graphène, Nanocatalyseurs

List of Acronyms and Symbols

$(NH_4)_6Mo_7O_{24}\cdot 4H_2O$	**Ammonium molybdate tetrahydrate**
$(NH_4)_2HPO_4$	**Ammonium phosphate dibasic**
CH_3CSNH_2	**Thioacetamide**
$NH_2C(=NH)NHCN$	**Dicyandiamide**
C_2H_5OH	**Ethanol**
KOH	**Potassium hydroxide**
DMF	***N, N*-dimethylformamide**
HCl	**Hydrochloric acid**
HF	**Hydrofluoric acid**
H_2SO_4	**Sulfuric acid**
HNO_3	**Nitric acid**
$NaBF_4$	**Sodium tetrafluoroborate**
Ti_3AlC_2	**Titanium Aluminum Carbide**
GO	**Graphene oxide**
NF	**Nickle foam**
CV	**Cyclic voltammetry**
LSV	**Linear sweep voltammetry**
EIS	**Electrochemical Impedance Spectroscopy**
GC	**Glass carbon**

SEM	**Scanning electron microscopy**
TEM	**Transmission electron microscopy**
XRD	**X-ray diffraction spectra**
XPS	**X-ray Photoelectron Spectroscopy**

General introduction

With the increase of energy demand and impending climate change, major efforts have been made to develop sustainable and fossil-free energy all over the world. Hydrogen have caught major attention and interest due to the high-density energy carrier and carbon-free after oxidation. A lot of efforts have been made to produce hydrogen by green, cost-effective methods over the last decades. One prospective way is to develop electrochemical water splitting coupling with renewable energy. This requires an effective catalysis for both hydrogen evolution and oxygen evolution reactions perfectly based on catalyst with low prize and large abundant.

Pt-based, Ru/Ir-based materials have the best performance for HER and OER, respectively. However high price and scarcity limited the large-scale application of electrochemical water splitting. Thus, major concerns have been raised to find alternatives to noble metal-based materials. And enormous efforts have been made to develop noble-metal free nanostructure materials with high activity and excellent stability for electrochemical water splitting.

Table of content

Acknowledgment iii

Abstract v

List of Acronyms and Symbols ix

General introduction xi

Table of content xii

Chapter 1 1

1.1 Background of world energy 1

1.1.1 Energy crisis all over the world 1

1.1.2 The progress of hydrogen 2

1.1.3 Electrochemistry of water splitting 4

1.1.4 Mechanisms of the Water-Splitting Reactions 10

1.1.5 HER catalysts 14

1.1.6 OER catalysts 23

1.2 Summary 26

1.3 Objectives 27

1.4 References 28

Chapter 2 47

Interface Engineering of Ultrathin Hierarchical P-doped MoS_2/Ni_3S_2 Heterostructure on Nickel Foam for Efficient Water Splitting 47

2.1 Introduction 47

2.2 Experiment section 49

2.2.1 Preparation of P-MoS_2/Ni_3S_2/NF 49

2.2.2. Electrochemical measurements....50
2.2.3 DFT calculation....53
2.3 Results and discussion....54
2.3.1 Materials characterization....54
2.3.2 OER Performance of P-doped MoS_2/Ni_3S_2/NF....62
2.3.5 HER Performance of P- MoS_2/Ni_3S_2/NF....72
2.3.4 Turnover Frequency (TOF) calculation....75
2.3.5 Faradaic efficiency calculations....76
2.3.6 Water splitting performance....77
2.3.7 Theoretical calculation analysis....79
2.3 Conclusion....83
References....85
Chapter 3....93
Dual-Functional N Dopants in MoS_2/rGO Heterostructure - toward Efficient and Durable Water Splitting....93
3.1 Introduction....93
3.2. Experimental section....95
3.2.1. Synthesis of N-doped MoS_2/N-doped rGO catalysts....95
3.2.2. Electrochemical measurements....96
3.3. Results and discussion....98
3.3.1. Materials characterization....98
3.3.2 OER performance of N-MoS_2/N-rGO....108
3.3.3 HER performance of N-MoS_2/N-rGO....114
3.3.4 Turnover Frequency (TOF) Calculation....122
3.3.5 Faradaic efficiency measurements....123

3.3.6 Water splitting performance 126
3.4. Conclusion 128
3.5 References 129
Chapter 4 136
Exfoliation of Ti_3AlC_2 in $NaBF_4$/HCl Aqueous Solution for Effective Hydrogen Evolution Reaction in Acidic Medium 136
4.1 Introduction 136
4.2 Experimental section 138
4.2.1 Synthesis of MXenes 138
4.2.2 Electrochemical experiments 139
4.3 Results and discussion 140
4.3.3 HER performance of MXenes 154
4.4 Conclusion 168
4.5 References 170
Chapter 5 175
Conclusion and Perspective 175
Appendix 178
Experiment part 178
6.1 Characterization technologies 178
Publications 180

Chapter 1

1.1 Background of world energy

1.1.1 Energy crisis all over the world

The global energy consumption increases rapidly around the world at the time of fossil fuels depleting. According to the newest data from Global Energy Statistical Yearbook 2021, global energy consumption increased with an average 2% per year over the period of 2000-2018. Additionally, the fossil fuels could release greenhouse gases into the atmosphere, which is leading to global warming.

In 2015, a universal legally binding global climate agreement was signed by 195 nation states on Paris Climate Conference with the aim of limiting the average temperature rise to below 2 °C above pre-industrial levels. To achieve this goal, a significant decrease in greenhouse gas emissions must be undertaken globally — estimated to 25% by 2030, with the threshold reaching 50% if the more ambitious 1.5°C target is to be achieved. Therefore, numerous countries, cities and companies have adopted net-zero targets for energy-related carbon dioxide (CO_2) emissions, bringing the energy transformation from fossil fuel to renewable resource to the forefront.[1]

In order to tackle the energy problem, we need to implement energy transformation, especially the power generated from renewable sources like solar and wind, which provide greater energy efficiency and wider use of electricity in various areas ranging from auto vehicles to heating and cooling systems in buildings.[1,2] Still, not all sectors or industries, including steel, cement, chemicals, long-haul road transport, maritime shipping and aviation (IRENA, 2020b) can easily make the switch from fossil fuels to electricity.

Green and clean hydrogen gas can bridge the gap between growing and sustainable

renewable electricity generation and the hard-to-electrify sectors (IRENA, 2018). In general, hydrogen is a suitable and clean-energy carrier with a high energy density, and it can be easily stored and transported similar to natural gas. There are various advantages with hydrogen energy: (1) Hydrogen can help to tackle various critical energy challenges. It can become an alternative solution for hard to electrify sectors. It can also help in improving air quality and strengthen energy security. (2) Hydrogen is one of the leading options for storing energy from renewables due to the potential of additional system flexibility and storage.[3,4] It has the potential to help with variable output from solar photovoltaics (PV) and wind, whose availability is not always well-matched with demand. Hydrogen and hydrogen-based fuels can transport energy from renewables over long distances.

Nevertheless, green hydrogen will have to overcome several barriers to get completely commercialized. Overcoming the barriers and transitioning green hydrogen from a niche player to a widespread energy carrier will require a cost-effective technology to produce hydrogen.

1.1.2 The progress of hydrogen

Hydrogen can be generated from fossil fuels and biomass, from water, or from a mix of both.[2,3] Currently, fossil fuels is currently the primary source (around 96%) of hydrogen production, including 49% from natural gas, 29% from liquid hydrocarbons, and 18% from coal. [5] Only about 4% of hydrogen is generated from water electrolysis and other byproduct sources of hydrogen. The industry routes of hydrogen generated from fossil fuels include hydrocarbon reforming, coal gasification, hydrocarbon pyrolysis and plasma reforming, all of which are thermochemical processes. Here takes nature gas as a source of hydrogen, the production cost of hydrogen from natural gas is mainly influenced by the gas price, accounting for 45% - 75% of the production costs.

Particularly, for gas importers like Japan, Korea, China and India, they have to contend with higher gas import prices, which in turn makes hydrogen production impractical in terms of costs. Moreover, carbon monoxide (CO) is inevitably produced in the reforming process, which is poisonous to the catalysts, especially the noble-metal involved electrocatalysts. In addition, large amounts of carbon dioxide and other greenhouse gases were released during the gasification of coal steam or reforming of methane. [6]

Biomass have high promising to be the alternative fuel source that can help to meet future energy demands. Biomass can be extracted from a wide range of sources such as crops and crop residue, wood and wood residue, industrial residue, animal waste, municipal solid waste, sawdust, aquatic plants and algae, and ect.[7] It has been forecasted that more than 25% energy will be generated from biomass by the year 2050.[8] Unlike fossil fuels, the mainly gas emissions from biomass is CO_2, which could be recycled from the air through plant photosynthesis. However, the hydrogen products from biomass is not a pure hydrogen product. Besides, the cost of biomass logistics (collection and transportation) for the gasification plant is costly.

Thus, more attention is focused on hydrogen production by water electrolysis. One reason is that hydrogen products from water electrolysis is pure hydrogen.[5,9] Besides, the declining costs for renewable electricity, in particular from solar PV and wind, also promote the development of hydrogen generation from water electrolysis. Moreover, no greenhouse gas emitted from water electrolysis. However, the wide production of hydrogen from water electrolysis is limited by the electrolyser design and construction, electrocatalysis materials, the cost of electricity and policy supporting.

1.1.3 Electrochemistry of water splitting

1.1.3.1 Current state of electrochemistry of water splitting

Water electrolysis is the process of using electricity to decompose water molecules into oxygen and hydrogen gas. Thus, the basic principle of a water electrolysis cell consists of two electrodes, anode and cathode separated by an electrolyte. The two primary reactions are performed on two electrodes, while the electrolyte is the medium responsible for transporting the anions (-) or cations (+) from one electrode to the other. This allows the construction of four main technologies based on the electrolyte and temperature of operation, including alkaline, polymer electrolyte membrane (PEM), anion exchange membrane (AEM), and solid oxide electrolyzers (SOEC); the structure of commercially available electrolysis technologies is shown in **Figure 1**. In PEM, AEM, and SOEC, there is no use of liquid electrolyte solution, and the ion transport happens within the PEM, AEM, or SOEC.

Alkaline electrolyzers shown in Figure 1a are relatively easy to manufacture due to a simple stack and system design, which are known to be reliable over 30 years. However, these electrolyzers allow the intermixing of the produced hydrogen and oxygen dissolved in the electrolyte, limiting the power-operating range and the ability to operate at harsher pressure levels.

PEM electrolyzers displayed in Figure 1b, on the other hand, offer higher efficiencies (*i.e.* less resistance) due to the thin (0.2 mm) perfluorosulfonic acid (PFSA) PFSA membrane and electrodes with advanced architecture. However, the harsh oxidative environment in the anode caused by the PFSA membrane requires anti-corrosion materials that can guarantee both optimal electron conductivity and cell efficiency. Up to now, titanium-based materials, and noble metal catalysts with protective coatings are commonly used. However, these requirements have caused

PEM stacks to be more expensive than alkaline electrolyzers. PEMs have one of the most compact and simplest system designs, yet they are sensitive to water impurities such as iron, copper, chromium and sodium and can suffer from calcination.

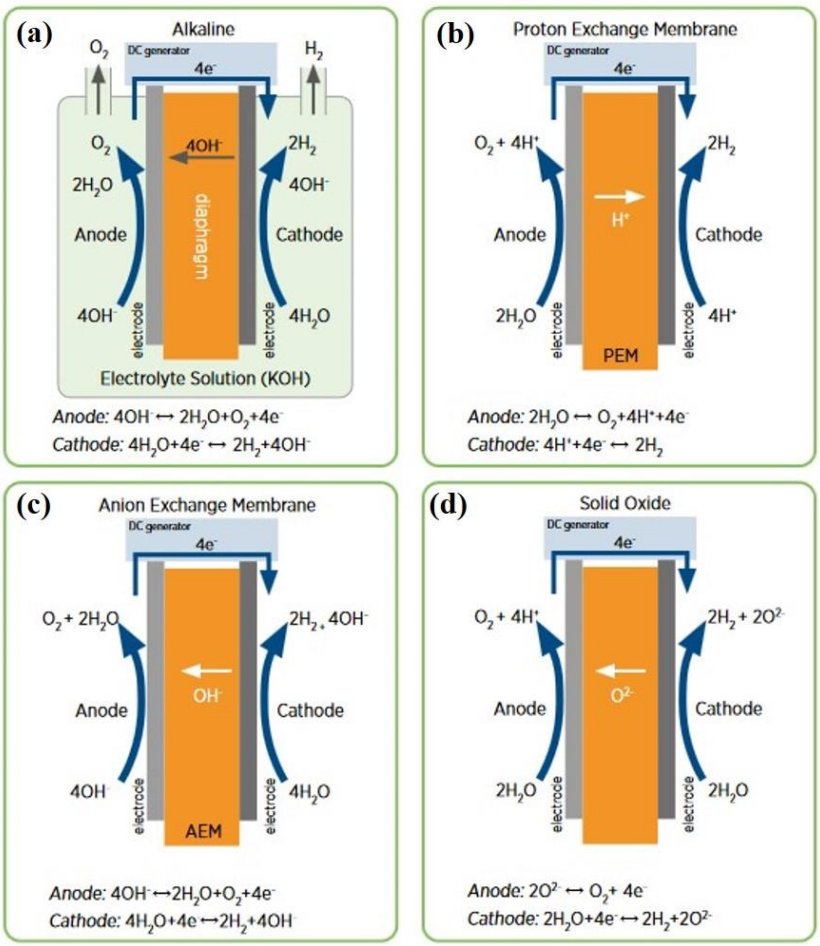

Figure 1. Different types of commercially available electrolysis technologies. [1]

Solid oxide electrolyzers (SOEC) in Figure 1c operate at high (700-850°C) temperatures, extending the capability to use of relatively cheap nickel electrodes, decreasing the electricity demand due to a part of the energy from heat, the potential for reversing into fuel cells, and co-electrolysis of CO_2 and water to produce syngas which is the fundamental block for the chemical industry. On the downside, faster degradation under high temperature and pressure and electrode contamination by silica

used as sealants, also limit the development of SOECs.

Lastly, **Anion Exchange Membranes (AEM)** is the latest technology with limited deployment **(Figure 1d**). AEM's potential lies in the combination of alkaline and PEM electrolyzers. It uses cheap non-noble metal catalysts and titanium-free components, which causes chemical and mechanical stability problems, leading to poor lifetime profiles. Moreover, the performance is not yet as good as expected, mostly due to low AEM conductivity, poor electrode architectures, and slow catalyst kinetics.

For AEM and solid oxide electrolyzers, this cost considerations are much more challenging, as there are only a few companies responsible for their commercialization. Moreover, many of their components are still laboratory scale based, with no original equipment manufacturers (OEM) responsible for their manufacturing and commercialization. These are small stacks, and system sizes are only up to a few kilowatts. While these two technologies can still contribute to a low production cost of green hydrogen, much more research indeed is required as compared to alkaline or PEM electrolyzers.

Despite their market availability and reliability, PEM and alkaline water electrolyzers are still considered highly expensive, compared to fossil fuel-based hydrogen production. Critical materials are mostly a limitation for PEM. The anode side is subject to a high potential for oxidizing (> 1.4 V) and not many materials can provide long-term operation under these conditions. Because of this, iridium – a scarce material – is used and the porous transport layer (PTL) requires significant amounts of titanium-based (*i.e.* expensive) materials, coated with platinum. Alkaline electrolyzers mostly use nickel to resist the highly caustic environment. Some designs derived from the chlor-alkali industry include platinum and cobalt. For alkaline water electrolysis designs optimized for green hydrogen production, however, we have commercial

examples available today that do not use these materials.

However, platinum is used currently at about 1 g/kW.[10] At the same time, primary platinum production is in the order of 200 tons per year (t/year), which would support the deployment of 200 GW/year or 2000 GW of electrolyser capacity in the next decade. To avoid becoming a barrier to large-scale deployment, all the alkaline designs need to transition a platinum and cobalt-free designs and the amounts of platinum and iridium in PEM need to be significantly reduced.

Currently, iridium is being used roughly at 1-2.5 g/kW. Global iridium production is about 7-7.5 t/year,[11] which would support the deployment of 3-7.5 GW/year or 30-75 GW of electrolyser capacity in the next decade, reflecting the criticality of reducing iridium content rapidly and significantly.

Additionally, platinum and iridium are two of the most carbon and energy intensive materials in the electrolyzers (see **Figure 2**). Platinum production emits about 12.5 tons of carbon dioxide (tCO_2-eq) per kilo of metal. This translates into about 0.01 kg CO_2 -eq/kg H_2,[11] which is relatively small compared to the electricity input (only 10 grams of CO_2 -eq/kWh would be equivalent to 0.5 kg CO_2-eq/kg H_2). Similarly, platinum production is the most energy intensive among the critical materials in electrolyzers with 243 gigajoules per kilo (GJ/kg). The supply of critical materials in electrolyzers is mostly dominated by a few countries (see **Figure 3)**. South Africa supplies over 70% of global platinum and over 85% of global iridium. This would strongly link PEM electrolyser deployment to supply from a few (mainly one) countries, with limited short-term alternatives in sight for replacing these materials for PEM.

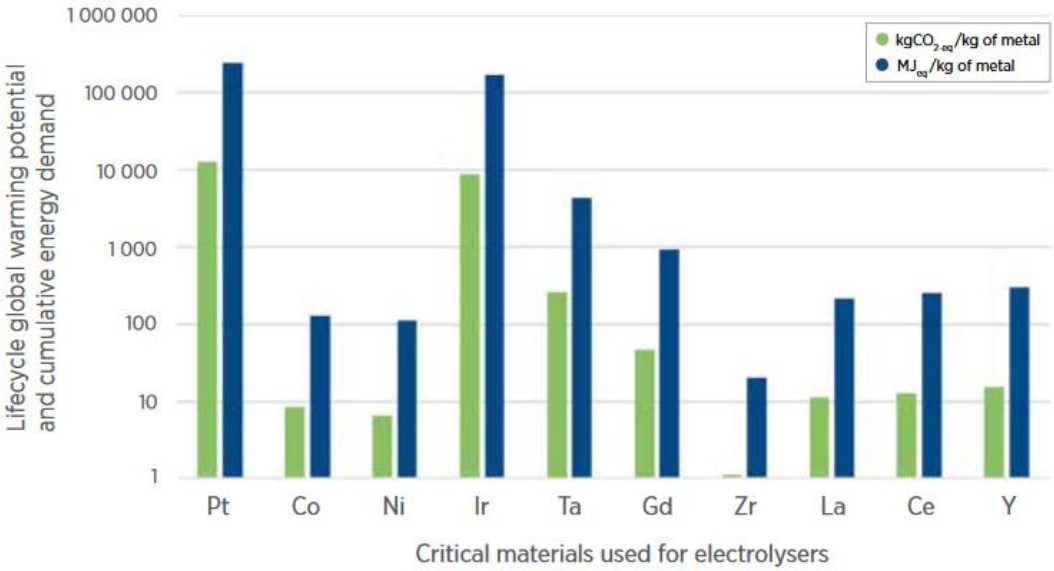

Figure 2 Global warming potential and cumulative energy demand for critical materials used in electrolysers[11]

Solid oxide electrolyzers, which have the potential for much higher efficiencies, would also suffer from a similar risk, since almost 95% of the supply for all their critical materials (see **Figure 3)** currently comes almost exclusively from China.

Alkaline electrolyzers do use some platinum and cobalt, but there are already commercial designs that do not include these materials and the supply of nickel is more diversified when compared to the other metals. The same applies to AEM, which does not use scarce materials and mostly requires steel and nickel.

One of the strategies to reduce dependence on critical materials [5] is **prevention or reduction of use.** This covers substitution of the materials, reducing their amount per unit of installed capacity, or varying the technology mix to achieve a lower use overall (*e.g.* more alkaline instead of PEM that uses iridium). Here, we will focus on discussing the substitution of Pt/Ir materials. There are various options being investigated:

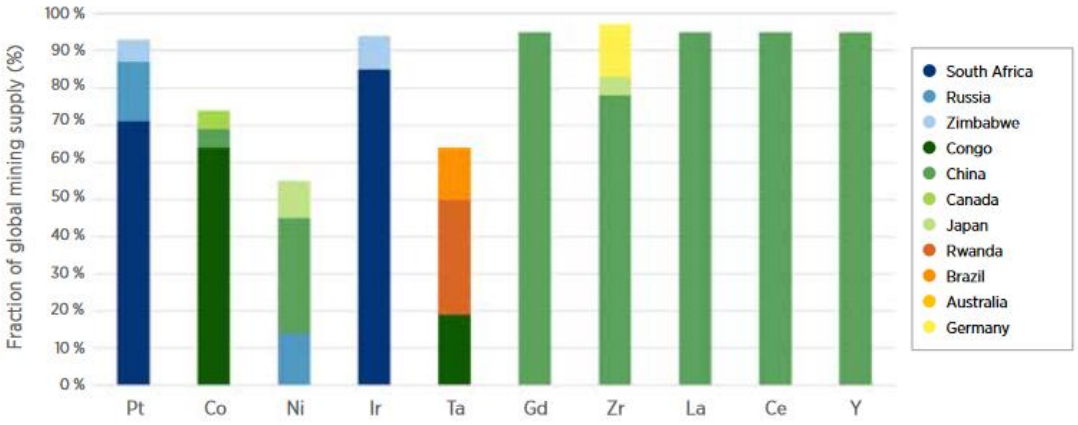

Figure 3 Top producers of critical materials in electrolyzers

Research and development (R&D) lower content noble metal catalysts, for example Pt species supported on earth-abundant materials. Support species of iridium or platinum on high conductive semi-conductor oxides, alloy iridium or platinum to other transition metals, change the morphology of the electrode and shape the species of iridium or platinum. Additionally, using a thin layer of coating material, such as atomic layer deposition.

R&D earth-abundant metal catalysts with high efficiency and excellent stability, transition metal sulfides, oxides, hydroxides, nitrides and carbides, which exhibit promising alternative to noble metal catalysts.

1.1.3.2 Basic set-up of water splitting system

In a conventional water electrolyte, the oxygen evolution reaction (OER) and hydrogen evolution reaction (HER) occur simultaneously at the anode and cathode, respectively. The overall water-splitting reaction and two half-reactions depend on the electrolyte, including alkaline, acidic, and neutral (including seawater) solutions, and they could be expressed as following reactions:[12–18]

Total reaction:

$$2H_2O \rightarrow O_2 (\uparrow) + 2H_2 (\uparrow) \quad (1)$$

In acidic media

$$\text{OER} \quad \text{(Anode): } 2H_2O - 4e^- \rightarrow O_2 (\uparrow) + 4H^+ \quad E_{0\text{anode}} = 1.23\ \text{V} \quad (2)$$

$$\text{HER} \quad \text{(Cathode): } 2H^+ + 2e^- \rightarrow H_2 (\uparrow) \quad E_{0\text{cathode}} = 0.00\ \text{V} \quad (3)$$

In alkaline or neutral media

$$\text{OER (Anode):} \quad 4OH^- - 4e^- \rightarrow O_2 (\uparrow) + 2H_2O \quad E_{0\text{anode}} = 1.23\text{V} \quad (4)$$

$$\text{HER (Cathode):} \quad 2H_2O + 2e^- \rightarrow H_2 (\uparrow) + 2OH^- \quad E_{0\text{cathode}} = 0.00\ \text{V} \quad (5)$$

According to equations (1) – (5), water splitting is an up-hell process, and the thermodynamic voltage of total electrochemical reaction is 1.23 V (*versus* reversible hydrogen electrode (RHE) at room temperature), and this value is independent of the reaction medium and system, because extra voltage must be added to the cell, and the overall cell voltage (V_{oc}) can be expressed as below:

$$V_{oc} = 1.23\text{V} + \eta_a + ||\eta_c|| + i_R \quad (6)$$

Where η_a and η_c are the overpotentials, which is the gap between the actually applied electrode potential on anodic and cathodic reactions and the equilibrium potential, respectively, and i_R represents the ohmic drop. With the aim of high scale production of hydrogen *via* the water electrolysis, great efforts should be devoted to understand the interface science and nature of catalysts for chemical transformation, which is one of the core missions to develop hydrogen economy.

1.1.4 Mechanisms of the Water-Splitting Reactions

1.1.4.1 Hydrogen Evolution Reaction (HER)

Based on plethora of experimental results and analysis, a widely-accepted mechanism for hydrogen evolution in acid and alkaline solution involves Volmer reaction in equations (7) and (10), respectively, followed either by the Heyrovsky or

the Tafel reaction, as seen in equations (8), (11) and (9), and (12), respectively,[19–27] and illustrated in **Figures 4** and **5**. For the Volmer reaction, protons in acid solutions gain an electron to form adsorbed hydrogen atoms ($H_{ads.}$). While, in alkaline solutions, water molecules are reduced to produce adsorbed hydrogen atoms ($H_{ads.}$) on active metal sites (M) and hydroxide ions. Thus, HER reaction in alkaline electrolytes is notably sluggish than that in acid ones due to the water dissociation.

The typical HER mechanism in acidic medium is shown in **Figure 4**:

Volmer step:

$$e^- + H^+ + * \rightarrow H^* \text{ (Tafel slope, 120 mV dec}^{-1}\text{)} \quad (7)$$

Heyrovsky step:

$$H^+ + H^* + e^- \rightarrow H_2 \text{ (Tafel slope, 40 mV dec}^{-1}\text{)} \quad (8)$$

Tafel step:

$$H^* + H^* \rightarrow H_2 + 2^* \text{ (Tafel slope, 30 mV dec}^{-1}\text{)} \quad (9)$$

The typical HER mechanism in alkaline or neutral media is depicted in **Figure 5**:

Volmer step:

$$H_2O + e^- + * \rightarrow OH^- + H^* \text{ (Tafel slope, 120 mV dec}^{-1}\text{)} \quad (10)$$

Heyrovsky step:

$$H_2O + H^* + e^- \rightarrow H_2 + OH^- \text{ (Tafel slope, 40 mV dec}^{-1}\text{)} \quad (11)$$

Tafel step:

$$H^* + H^* \rightarrow H_2 + 2^* \text{ (Tafel slope, 30 mV dec}^{-1}\text{)} \quad (12)$$

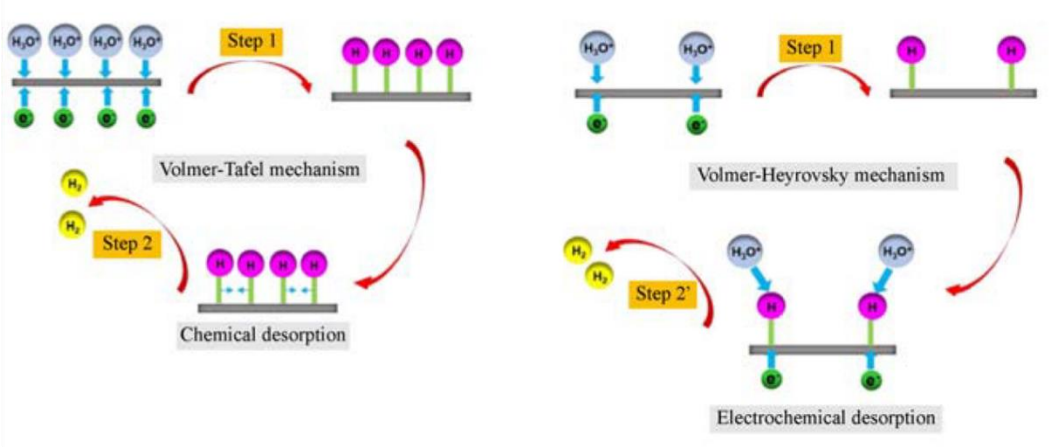

Figure 4. Two mechanisms of hydrogen evolution reaction (HER) on the surface of catalysts in acidic solution: (**a**) Volmer-Tafel mechanism and (**b**) Volmer-Heyrovsky mechanism.[28]

The * represents the active site on the electrocatalyst surface. For the Volmer step, hydrogen intermediate H* is adsorbed on the surface of the electrocatalyst. Then, H2 is produced by combining with H+ or H2O (the Heyrovsky step) or with another formed H* (the Tafel step) in acidic and alkaline media, respectively. The adsorption energy of the hydrogen atom on electrocatalyst surface is mainly responsible for the total HER process.

1.1.4.2 Oxygen Evolution Reaction (OER)

The OER is a four-electron/proton coupled heterogeneous reaction with three different oxygen-related intermediates, including *OH, *O, and *OOH, in all pH solutions.[30–32] Due to the four-electron transfer process, the OER is regarded as the bottleneck of a whole water-splitting system. The widely accepted OER mechanism in acidic and alkaline media are given below.[14,33–35]

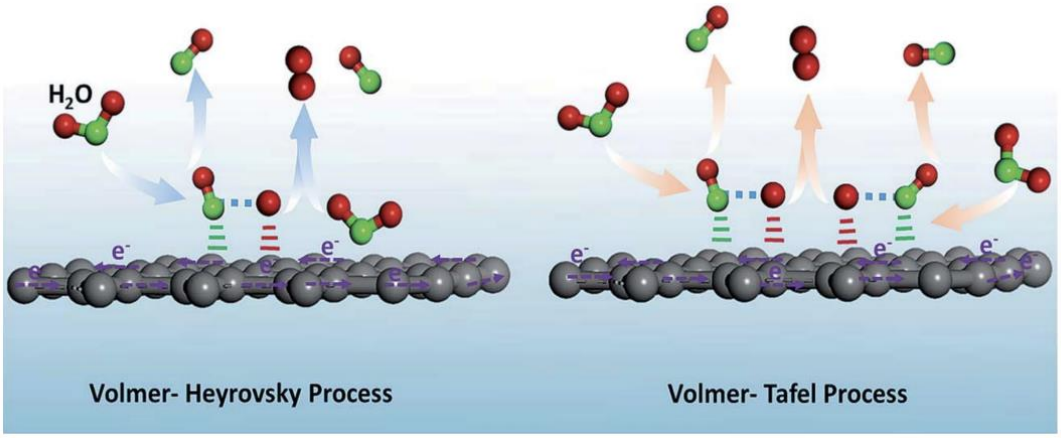

Figure 5. Schematic representation of the two pathways of the hydrogen evolution reaction in alkaline solution. [29]

In acid media:

$$H_2O + * \rightarrow {}^*OH + e^- + H^+ \quad (13)$$

$${}^*OH \rightarrow {}^*O + e^- + H^+ \quad (14)$$

$${}^*O + H_2O \rightarrow {}^*OOH + e^- + H^+ \quad (15)$$

$${}^*OOH \rightarrow O_2 + e^- + H^+ + * \quad (16)$$

In alkaline or neutral media:

$$* + OH^- \rightarrow {}^*OH + e^- \quad (17)$$

$${}^*OH + OH^- \rightarrow {}^*O + H_2O + e^- \quad (18)$$

$${}^*O + OH^- \rightarrow {}^*OOH + e^- \quad (19)$$

$${}^*OOH + OH^- \rightarrow O_2 + H_2O + e^- + * \quad (20)$$

The * represents the active sites on the electrocatalyst surface. The OER process starts with the adsorption of a hydroxyl radical or molecular water at an active site on the electrocatalyst surface to provide *OH (eq (13) and (17). Then, a coupled proton and electron removal from *OH produces *O (eq (14) and (18). However, it is extremely difficult to release O_2 directly by two adjacent immediate *O due to the high thermodynamic barrier. [34] Thus, the nucleophilic attack of OH^- and H_2O on *O yields

another intermediate *OOH (eq (15) and (19). Finally, *OOH deprotonates an electron to generate one oxygen molecule and release a free active site (eq (16) and (20).

1.1.5 HER catalysts

1.1.5.1 Platinum (Pt)-Metal-Based Catalysts

Platinum (Pt) exhibits the yet best HER activity and stability in all pH solutions. [36,37] However, high cost and low availability, its potential for large-scale commercialization will not be feasible. The most potentially feasible strategy is to develop low Pt content electrocatalysts (LPCE), which load a lower amount of Pt, even single atoms, without sacrificing the high catalytic efficiency. [37]

Generally, one strategy is to reduce the size and increase the dispersion of Pt nanoparticles on conductive supporting materials to enhance the efficiency of single Pt species. Recently, Pt nanoparticles or nanoclusters dispersed on different cost-effective supports including carbon materials [38–41], transition metal sulfides [42,43], transition metal hydroxides [44], and MXenes [45–47] are developed as a promising way to enhance their catalytic activity toward HER. All these supporting materials have a good conductivity, which helps in enhancing the kinetic and fast electron transfer. Moreover, most of them display a high HER performance in noble metal-free catalysts. When coupled with Pt nanoparticles, a super catalyst performance can be induced by the synergistic effects of the quantum size effects of the Pt nanoparticles and strong interface interaction between Pt and supporting materials ,which could also prevents agglomeration of the Pt nanoparticles during the preparation and electrocatalytic processes. [37]

If the Pt nanocluster is further reduced to atomic size, a new type of single-atom catalyst can be obtained. In theory, the intrinsic activity of Pt species supported catalyst will be deeply enhanced, because more unsaturated coordination environment of the Pt center appears. However, for Pt supported catalysts, there are still some challenges to

overcome. The preparation of homogeneous dispersion of Pt species on conductive supporting materials require a pre-functionalization step to provide more sites and strong adhesion to stabilize Pt species toward stable HER performance.[48] And it is still a big challenge to further increase the amount of Pt active sites, because of the aggregation of Pt under a higher loading due to the extremely high surface energy.[49,50]

Metal alloying process has emerged as another promising strategy for advancing Pt-based HER catalysts.[51,52] The HER performance of Pt alloyed catalysts is improved by tuning the electron structure, cumulative strain, and bond length during the alloy process. Pt-based bimetallic systems, formed by decoration of other transition metal species on Pt-based materials, have also been reported.[52,53] Bimetallic alloy catalysts exhibit unprecedented electronic and chemical properties, which are distinctively different from their parent metals. Fundamental surface science research conducted on bimetallic catalysts has proven that the modification is crucial to the unexpected property, which originates from a change in heteroatom bonds and the novel nanostructure within the bimetallic system. These factors endow Pt-based metallic catalysts with excellent activity. However, chemical synthesis of Pt alloys is truly challenging, because the low reduction potentials of rare earth metals are far beyond the stability range of water. Deep understanding of basic mechanism between the alloying parameters, including composition, surface state, morphology, charge-carrier (electrons and holes) mobility, and the unprecedented catalytic properties seems more important for Pt alloyed catalysts before commercial-scale utilization.

1.1.5.2 Transition metal dichalcogenide (TMD) materials

Transition metal dichalcogenides (TMDs) have attracted considerable attention for enhanced electrocatalytic HER, owing to their layered morphology and special electronic structure. TMDs have a general chemical composition MX_2 (M and X

represent the transition metal and the chalcogen, respectively). Molybdenum disulfide (MoS_2), as a typical 2D transition metal dichalcogenide (TMD), being earth abundant and cost effective, was confirmed to be active for HER inspired by the hydrogenases and nitrogenases in nature. [54] The active sites on MoS_2 for HER are confirmed theoretically and experimentally on the Mo (1010) edge sites with a ΔG_{H*} of 0.08 eV close to optimal value of 0 eV, far smaller than that of basal plane (1.92 eV) which could explain the inert activity of bulk MoS_2. [54,55] The combination of theoretical and experimental studies provides the key insights to improve the HER performance of MoS_2 by increasing the amount of exposed edge sites.

In order to achieve this exposure, one promising strategy is through nanostructuring the MoS_2 catalysts. Double-gyroid, [56] nanowires, [57] vertically aligned, [58,59] and cracks-rich MoS_2 nanostructures [60] were prepared to expose much more edge sites and minimize the formation of extended basal planes. Another attractive approach is to disperse MoS_2 nanoparticles on supports with high surface area and conductivity, like reduced graphene oxides sheets.[61]

Apart from increasing of the amount of edges sites, activating the basal planes and improving the intrinsic activity of MoS_2 are other significant and meaningful methods for the development of efficient electrocatalysts.[62] Thus, phase engineering and activation of inert basal planes have caught attention in past decades. [63–65] For MoS_2, the basal plane of 1T -MoS_2 possesses a better activity than those of 2H and 3R-MoS_2 phases due to enhanced edge sites, and decrease in charge transfer resistance.[66] Inspired by this mechanism, phase transition from 2H into 1T MoS_2 is developed by alkali metals intercalation[59,67,68], Re-doping[69], laser-induced[70], mechanical strain[71], weak Ar-plasma treatment[72], electron/ion irradiation[73] and hot electron doping [72].

The incorporation of heteroatoms is one of the effective approaches to tune the

electronic/surface structure and enhance the activity of MoS_2 for HER. Up to now, metal atoms including Ni, Co, Mn, and Fe have been introduced into MoS_2 matrix to tuning the intrinsic activity of in-plane atoms of MoS_2 and improve the HER performance in both acid and alkaline solutions.[63,74–76] Bao's group has systematically-studied the effects of metal dopants on the HER performance of in-plane atoms of MoS_2, and provided a volcano-plot between the HER activity and adsorption free energy.[77] Another possible strategy is the incorporation of nonmetal atoms (N, P, C and O) into MoS_2 matrix because of the smaller size, especially N atoms, which could increase exposure of more active sites and improve the conductivity. Qing et al. found that the 2H-MoS_2/N-doped mesoporous graphene with the interfacial Mo−pyridinic N coordination could improve the HER activity of S edges on MoS_2 in all pH range by tuning the charge transfer to enhance the H_2O dissociation in alkaline and neutral solutions. [78]

Furthermore, heterostructure materials own great potential for constructing high active catalysts *via* a synergistic effect.[79–81] These heterostructure catalysts usually exhibit remarkable advantages for the HER by combination at least double types of active sites on the surface. The heterostructure materials could realize a better activity by tuning the electron distribution and boost charge transfer at the interface of two compounds, which provides a way to improve the HER performance in alkaline solution. Coupling water dissociation "promoters" to TMDs *via* a synergistic catalytic pathway is a promising strategy to lower water dissociation energy in alkaline and neutral solutions. Metal oxides/hydroxides are highly favorable for H_2O dissociation, thus constructing a heterostructure with MoS_2 could enhance the alkaline HER due to synergetic effects. In this line, Zhang et al. prepared $Ni(OH)_2$/MoS_2 heterostructure and confirmed the excellent HER property of this heterostructure in alkaline solution.[82] The

$Ni(OH)_2$ could not only promote water dissociation, but also boost the charge transfer from $Ni(OH)_2$ to the MoS_2 which could optimize ΔG_{H^*} of MoS_2 catalyst. This hybrid catalyst only required an overpotential of 80 mV to achieve 10 $mA \cdot cm^{-2}$. Zhu et al. found that $Ni(OH)_2$ and $Co(OH)_2$ hybridized with ultrathin MoS_2 and WS_2 nanosheet catalysts exhibited significantly enhanced alkaline HER activity and stability compared to their pure counterparts due to the decrease of the kinetic energy barrier of the water dissociation step.[83] In addition, Ni_3S_2, as one of Ni chalcogenides (NiS, NiS_2 and Ni_3S_2) which have attracted substantial interest for electrochemical water splitting,[84–89] has been recognized as an efficient electrocatalyst for water splitting due to its high conductivity, unique structure configuration and earth-abundance. Despite these beneficial features, the low density of surface-active sites and poor stability in aqueous media hindered its wide utilization as a bi-functional catalyst for water splitting. [90] Therefore, many efforts have been devoted to enhance the activity and stability of Ni_3S_2-based catalysts for efficient water splitting. For instance, heterostructure Ni_3S_2-based nanomaterials such as MoS_2–Ni_3S_2 hetero-nanorods, [91,92] and MoS_2/Ni_3S_2 hetero-porous structure [93] could improve the activity and enhance the stability by controlling the morphology and providing more active surface sites. Zhang et al. prepared Mo-doped Ni_3S_2/Ni_xP_y hollow heterostructure on nickel foam (NF) through a solvothermal process and phosphorization treatment; the developed catalyst displayed hierarchical porous morphology and improved overall water splitting performance.[94] Despite the advantages brought up by element doping, there are only a few reports on element-doped heterostructure MoS_2-based materials. [94–97]

1.1.5.3 MXenes

MXenes, an emerging class of two-dimensional (2D) transition metals carbides, nitrides, and carbonitrides, have caught great attention as electrocatalysts for HER due

to their special layered structure, high carrier mobility (comparable to metals), and excellent long-term stability.[98] The general chemical formula of MXenes is $M_{n+1}X_nT_x$, where M is early transition metal atom (Ti, Mo, Zr, W, Nb, V, etc...); X is carbon and/or nitrogen; n = 1-4; T_x is the surface termination group, including O, F, OH, or Cl. Until now, more than 30 MXenes compositions, including mono transition metal MXenes ($Ti_3C_2T_x$[99], TiC_2T_x[100]), double transition metal MXenes ($Mo_2TiC_2T_x$, $Mo_2Ti_2C_3T_x$, and $Cr_2TiC_2T_x$)[101] and even four transition metal high-entropy 2D carbide MXenes ($TiVNbMoC_3$, $TiVCrMoC_3$)[98] have been synthesized since $Ti_3C_2T_x$ was firstly described by Gogotsi's group in 2011.[98,99] Double metal MXenes usually take two forms: (1) solid solutions MXenes, a random arrangement of two different transition metals in the M layers; (2) ordered MXenes, share the general formulas: $M'_2M''C_2$ or $M'_2M''_2C_3$ where M' and M'' are different transition metals. MXenes are generally prepared by selectively etching A elements layer from ternary metal carbides or nitride precursors MAX phase with a general formula $M_{n+1}AX_n$ (M: early transition metal, A: element from group 13 or 14 of the periodic table, X: C and/or N, and n = 1–4).[102]

Etching with hydrofluoric acid (HF)[19] or reaction-generated HF[103] at room temperature has been recognized as a standard preparation method of MXenes. However, this method could limit the synthesis of various MXenes due to the instability of Al-containing MAX-phase precursors in fluoride-based aqueous solutions, reduce material performance with inert F-termination, and cause environment problem by F-containing solution. Therefore, the development of F-containing salt or even no-F-containing etching solution is intensively important for the further applications of MXenes.

Alkali could avoid the problems mentioned above and is theoretically a solution to etching MAX.[104] However, the alkali etching is hindered by the reaction kinetics due

to the formation of oxides and hydroxides on the surface of MXenes during the treatment of alkali. [105–107] In order to overcome this problem, alkali etching of MAX phase assisted by hydrothermal in an argon atmosphere condition could provide pure MXenes with O/OH-terminated group. [108] Electrochemical method was also proposed to prepare MXenes by etching MAX phases. However, the etching condition requires well-controlled conditions to avoid over-etching and produce carbines-derived carbon.[109] At present, Lewis acid etching and iodine-assisted etching routes are employed to produce corresponding MXenes with Cl^- or oxygen-rich terminal groups on the surface.[98] Although the preparation methods still need to be optimized, MXenes materials have been recognized as promising materials in catalysis [98,110–112], electrodes materials for batteries [113,114], supercapacitors [115], sensor [116], and electromagnetic interference shielding [117]. Here, we will focus on the MXenes as a potential electrode material for HER electrocatalysis.

Compared with other noble metal-based HER electrocatalysts, MXenes have a lot of potential properties, including tunable surface termination, superior electrical conductivity, enhanced efficient charge-carrier transfer, improved exposed metal sites, excellent hydrophilicity, and good structural and chemical stability in aqueous solutions. [104] In recent years, the HER performance of MXenes and MXenes-based materials has been optimized by surface modification, metal-atom doping, nanostructure fabrication, and hybridization. [118]

Surface modification could enhance the MXenes-based catalysts by improving the conductivity and electron structure on the surface of MXenes.[119] In MXenes-O/OH, it has been confirmed that O/OH terminal group could improve the exchange current and promote hydrogen evolution due to the enhanced conductivity and excellent charge transfer property, especially O-terminated group. O atoms on the surface of MXenes-

based materials have been theoretically and experimentally proved as the active sites for HER by enhancing the interaction between H* and MXenes matrix.[116,120,121] In contrast, F-terminal groups are inert and could not improve the activity of MXenes.[122] For example, Jiang et al. prepared an ultrathin O-functionalized Ti_3C_2 by reducing the F-termination into OH in KOH aqueous solution before transformation OH groups into O-terminal group *via* dehydration reaction. The resulted $Ti_3C_2O_x$ nanosheets featured a lower overpotential of 190 mV at a current density of 10 mA cm^{-2}, far excellent than that of $Ti_3C_2(OH)_x$ (217 mV) and $Ti_3C_2T_x$-450 (266 mV).[121] Although other terminations, including Br, Cl and S, have been prepared successfully, the HER properties are rarely reported and discussed.[123,124]

Metal doping is also a promising way to improve the HER performance of MXenes.[125–128] Huang et al. studied the HER performance of transition metal (TM) atoms (Ir, Os, Re, Rh, Fe and Zn)-doped Ti_3CNO_2 by DFT.[125] The calculation results indicated that O/OH terminal groups and TM modification could significantly improve the HER activity, and O atoms on the C-side of Ir, Rh, Zn dopants could enhance the HER activity. [125] Apart from above methods, hybridization with other chalcogenides[129,130], layered hydroxides, phosphides[130], carbides [131] and even metal-free black phosphorus[132], could improve the HER activity of MXenes materials. As a new type of 2D materials, the big challenge is to develop safe and environmentally friendly synthesis methods and expend the range of MXenes to five or even more metals containing types.

1.1.5.4 Metal-free catalysts

Carbon-based metal-free materials have been developed as cost-effective alternative electrocatalysts for noble metal-based materials for overall water splitting due to their low cost, excellent thermal and electrical conductivities,

mechanical/chemical stability, and structural flexibility throughout a wide potential window and pH range.[133,134] In addition, the various morphologies and highly tunable electronic structures of carbon materials make them a potential platform to design catalysts on the atomic level. Tuning the electron structure and then optimizing the morphology is the main way to maximize the HER performance of carbon materials.[135] Tuning the electronic structure of carbon materials is realized by introducing dopant atoms like N, P, O, F, B or S or defects into the carbon matrix by either inducing electron- or spin-redistribution in the sp^2 conjugated carbon matrix.[135] The carbon materials with high performance for HER could be produced in large-scale through the nanostructure engineering techniques. [136] Recently, most researches focused on electronic structure optimization by introducing dopant, edges, topological defects and hybridization with metal-based materials and other carbon materials. [135,137]

Doping heteroatoms like N, O, S, F or B into carbon matrix is one of a common and efficient way to enhance the HER performance of carbon materials by tuning the electron structure of carbon matrix.[137] According to the literature data, the active sites may be located in the C atoms adjacent dopant atoms.[135]

HER process depends on the adsorption and desorption ability towards the main reaction intermediates (H*). However, the effects of specific electronic states toward reaction intermediate energetics on carbon materials is still non-conclusive unlike the metal-based materials. [136,138]

Then co-doping with other elements such as N, S, and P *via* bottom-up annealing or post treatment methods have been reported. For instance, Dai et al. prepared two-dimensional N, S-co-doped graphitic sheets (SHG) with a unique hierarchical structure. [134] The two-electrode water splitting polarization of the SHG-based cell required a potential of 1.70 V to deliver 10 mA cm^{-2} at the initial stage, followed by a stable ≈

1.68 V for continuous operation. After the long-term operation over 19 h, the catalytic behaviors of SHG-based cell outperformed the Pt/RuO_2 system. The outstanding catalytic performance of SHG was rationalized by its unique architecture with a large surface area, rich active sites, and good electron/electrolyte transport properties.[134]

1.1.6 OER catalysts

As an electrochemical half-reaction of overall water splitting reaction, OER has much higher overpotential than that of HER due to the complex four electron oxidation process. Until now, Ir and Ru-based materials have the best performance for OER, but their scarcity and high cost limit their wide application. [139,140]

A large amount of efforts has been invested in the development of earth abundant OER electrochemical catalysts with high activity and stability to replace Ir and Ru-based materials. Until now, transition metal compounds (such as oxides, hydroxides, oxyhydroxides, phosphides etc.) have shown higher promises to replace the noble metal-based catalysts.[141–143]

1.1.6.1 Nobel metals-based catalysts for OER

Currently, noble metals (ruthenium (Ru), iridium (Ir), palladium (Pd), rhodium (Rh), and platinum (Pt)), their oxides, alloys and composites are extensively applied catalysts for OER due to their tremendous activity.[144] For noble metals, Rh and Ir possess the best performance for OER in both alkaline and acid solution. However, their poor stability, scarcity and high cost restrict their wide application in industry. [145]

Noble metal oxides like RuO_2 and IrO_2 exhibit high activity in both acid and alkaline solution. But for RuO_2, it is easy to oxide to Ru (OH) O_2 and then transfer into RuO_3 (8^+) in high anodic potential region.[146] IrO_2 performance for OER is worse than RuO_2, but its stability is comparatively greater than ruthenium oxide.[147] Thus, one

effective strategy to improve the performance is through hybridization of IrO_2 and RuO_2. [148–150] So, some research works are developed to prepare RuO_2-IrO_2 core-shell structure in order to improve the stability of RuO_2. [151–153]

1.1.6.2 Nickel-based catalysts for OER

Ni-based materials have a high potential to substitute the noble-metal catalysts due to facile preparation, environmental friendliness, cost-effective, earth abundant and special electron structure.[144]

To date, numerous efforts have been made to exploit high performance Ni-based catalysts for OER, such as Ni oxides, (oxy) hydroxides, sulfides and phosphates. Coupling Ni-based catalysts with OER catalysts could further enhance the catalytic performance. [84,93,94,154–158]

Recently, Ni chalcogenides (NiS, NiS_2 and Ni_3S_2) have attracted substantial interest for electrochemical oxygen evolution. [84–89] Among them, Ni_3S_2, due to its high conductivity, unique structure configuration and earth-abundance, has been recognized as an efficient electrocatalyst for water splitting. Despite these beneficial features, the low density of surface-active sites and poor stability in aqueous media hinder its wide utilization as a bi-functional catalyst for water splitting. [90] Therefore, many efforts have been devoted to enhance the activity and stability of Ni_3S_2-based catalysts for efficient water splitting. For instance, heterostructure Ni_3S_2-based nanomaterials such as CoS_x-Ni_3S_2/NF nanoarray,[159] MoS_2−Ni_3S_2 hetero-nanorods,[158,160] MoS_2/Ni_3S_2 hetero-porous structure,[155] Ni_3S_2/MnS ultrathin nanosheets with abundant vacancies[161] could improve the activity and enhance the stability by controlling the morphology and providing more active surface sites. All these materials were prepared on Ni foam (NF) by hydrothermal or electrochemical methods.

Besides, doping represents an efficient way to change the electron energy density

and increase the density of active sites. For example, Zhang et al. prepared Mo-doped Ni_3S_2/Ni_xP_y hollow heterostructure on NF through a solvothermal process and phosphorization treatment; the developed catalyst displayed hierarchical porous morphology and improved overall water splitting performance.[94] Despite the advantages brought up by element doping, there are only a few reports on element-doped heterostructure Ni_3S_2-based materials.[94,95,97,162]

1.1.6.3 Carbon-based metal-free catalyst for OER

Carbon-based materials, including graphene, carbon nanotubes (CNTs), graphene oxide (GO), reduced graphene oxide (RGO) have been studied for OER, owing to their large surface area, excellent conductivity and easy-tuning electron and geometric structure by doping foreign atoms[163] or hybridizing with other OER catalysts by interface engineering.[164–166] The activity of carbon-based materials is mainly driven by their electronic structure.[163] Thus, substantial efforts have been made to introduce foreign atoms, like B, N, O, P and S, to optimize the electron structure and enhance the catalytic performance of carbon-based materials.[163]

N, O and S could introduce a positive charge into carbon-based materials, which could facilitate intermediate (OH*) adsorption on the catalyst surface along with reaction intermediates recombination to release O_2 gas by tuning the electron structure and introducing strain.[163,167] Take N as an example, N doping could enhance the performance of carbon-based materials by forming quaternary and pyridinic nitrogen structure, which possess high OER performance. [168,169]

Besides, doping two or more types of atoms has also been studied to improve the OER performance of carbon-based materials. For example, P, N-co-doped carbon foam, N and P dual-doped graphene/carbon nanosheets,[170] N and O dual-doped graphene carbon nanotubes[171], dual doping of S and N into graphite foam[172], nitrogen,

phosphorous and fluoride doped graphene,[173] quaternary heteroatom (N, S, P, O)-doped multi-shelled carbon (NSPO-C) nanospheres[174] have been synthesized. Introducing foreign atoms could enhance the OER performance of carbon-based materials by: (1) the large active surface area and the hierarchical porous structure could load a large amount of active sites and ensure rapid mass transportation, (2) more active sites due to more defects, dangling bonds positioned at edges, and surface functional groups, (3) multiple-element doped carbon materials possess bi/multi-functional catalytic activity than single-doped ones due to the synergetic effects, (4) the integrated crystalline could promote charge transfer during redox process.[144]

1.2 Summary

As the energy crisis and global climate change, the energy transformation from fossil fuel to clean and renewable energy becomes a hot topic. Hydrogen is one of the leading options due to its high combustion value, clean and pollution-free products, and reproducible use. Hydrogen production by water electrolysis shows great potential to replace the common ways to produce hydrogen from fossil dues and biomass due to carbon-zero release and decreasing cost.

For the electrochemical water splitting, one of the big challenges is to develop cost-effective catalysts with high activity and excellent stability for both HER and OER processes. Although noble metal-based catalysts display the best performance for water splitting, their scarcity and high-cost limit the wide and long-term development of green hydrogen industry. Thus, a large amount of efforts has been devoted to studying other earth-abundant materials for these noble metal-based catalysts.

In recent years, transition metal dichalcogenides (TMDs) have been brought to forefront due to their special morphology and tunable electronic structure. However, their poor conductivity, limited active sites and poor stability were not favorable to

achieve good HER and OER performances as compared to those of noble metal-based catalysts. Thus, more attention has been devoted to the design and preparation of nanostructured catalysts by doping foreign atoms, interface engineering, and alloying to increase the intrinsic activity, the number of active sites, electronic conductivity, and stability.

In addition, most lab research works focus on the half reaction of water splitting, i.e. only on HER or OER. The condition of lab works are far from the industry application. In addition, it is necessary to develop bifunctional catalysts for both HER and OER in one system.

1.3 Objectives

Through literature reports and results, the current research on the electrochemical catalysts for HER and OER processes is is mainly focused on the design and development of low cost, efficient and highly stable nanostructured catalysts. In this PhD thesis, we have studied and improved the following aspects: (1) Interface engineering of ultrathin hierarchical P-doped MoS_2/Ni_3S_2 heterostructure on nickel foam for efficient water splitting; (2) dual-functional N dopants in MoS_2/rGO heterostructure toward efficient and durable water splitting; (3) $Ti_xC_yT_x$ MXenes etched with $NaBF_4$ and HCl for efficient hydrogen evolution.

The results obtained in this work could provide some data and ways to design of advanced materials in electrocatalysis.

1.4 References

1.IRENA, Green hydrogen cost reduction. https://www.irena.org/DigitalArticles/2021/Jan/Hydrogen (2020).

2.IRENA. Global Energy Transformation: A Roadmap to 2050. *Global Energy Transformation. A Roadmap to 2050* 52 (10–23) www.irena.org (2019).

3.IEA. The Future of hydrogen. https://www.iea.org/reports/the-future-of-hydrogen.

4.IRENA, How to scale-up green hydrogen. Https://www.irena.org/DigitalArticles/2021/Jan/Hydrogen.

5. Kiemel, S. *et al.* Critical materials for water electrolysers at the example of the energy transition in Germany. *Int. J. Energy Res.* **45**, 9914–9935 (2021).

6. Tsunoyama, H., Yamano, Y., Zhang, C., Komori, M. & Eguchi, T. Size-effect on electrochemical hydrogen evolution reaction by single-size platinum nanocluster catalysts immobilized on strontium titanate. *Top. Catal.* **61**, 126–135 (2018).

7. Demirbaş, A. Biomass resource facilities and biomass conversion processing for fuels and chemicals. *Energy Convers. Manag.* **42**, 1357–1378 (2001).

8. Hosseini, S. E. & Wahid, M. A. Hydrogen production from renewable and sustainable energy resources: promising green energy carrier for clean development. *Renew. Sustain. Energy Rev.* **57**, 850–866 (2016).

9. Li, Z., Luo, W., Zhang, M., Feng, J. & Zou, Z. Photoelectrochemical cells for solar hydrogen production: current state of promising photoelectrodes, methods to improve their properties, and outlook. *Energy Environ. Sci.* **6**, 347–370 (2013).

10. Fuel Cells and Hydrogen 2 Joint Undertaking (FCH JU). *Addendum to the multi-annual work plan 2014-2020*. (2018).

11.IRENA. Green hydrogen a guide to policy making. 105

https://www.irena.org/publications/2020/Dec/Green-hydrogen-cost-reduction (2020).

12. Wang, J. *et al.* Earth-abundant transition-metal-based bifunctional catalysts for overall electrochemical water splitting: A review. *J. Alloys Compd.* **819**, 153346 (2020).

13. Anantharaj, S. *et al.* Recent trends and perspectives in electrochemical water splitting with an emphasis on sulfide, selenide, and phosphide catalysts of Fe, Co, and Ni: a review. *ACS Catal.* **6**, 8069–8097 (2016).

14. Yan, Y., Xia, B. Y., Zhao, B. & Wang, X. A review on noble-metal-free bifunctional heterogeneous catalysts for overall electrochemical water splitting. *J. Mater. Chem. A* **4**, 17587–17603 (2016).

15. Ifkovits, Z. P., Evans, J. M., Meier, M. C., Papadantonakis, K. M. & Lewis, N. S. Decoupled electrochemical water-splitting systems: a review and perspective. *Energy Environ. Sci.* **14**, 4740–4759 (2021).

16. McHugh, P. J., Stergiou, A. D. & Symes, M. D. Decoupled electrochemical water splitting: from fundamentals to applications. *Adv. Energy Mater.* **10**, 2002453 (2020).

17. Li, S. *et al.* Transition metal-based catalysts for electrochemical water splitting at high current density: current status and perspectives. *Nanoscale* **13**, 12788–12817 (2021).

18. Lee, J. E. *et al.* Mini review on H_2 production from electrochemical water splitting according to special nanostructured morphology of electrocatalysts. *Fuel* **308**, 122048 (2022).

19. Naguib, M., Mochalin, V. N., Barsoum, M. W. & Gogotsi, Y. 25th anniversary article: MXenes: a new family of two-dimensional materials. *Adv. Mater.* **26**, 992–1005 (2014).

20. M.R.Gennero & Chialvo, A. C. Hydrogen evolution reaction: analysis of the Volmer-Heyrovsky-Tafel mechanism with a generalized adsorption model. *J.*

Electroanal. Chem. **372**, 209–223 (1994).

21. Franceschini, E. A., Lacconi, G. I. & Corti, H. R. Kinetics of the hydrogen evolution on nickel in alkaline solution: new insight from rotating disk electrode and impedance spectroscopy analysis. *Electrochim. Acta* **159**, 210–218 (2015).

22. Lasia, A. Mechanism and kinetics of the hydrogen evolution reaction. *Int. J. Hydrogen Energy* **44**, 19484–19518 (2019).

23. Choudhury, D., Das, R., Tripathi, A. K., Priyadarshani, D. & Neergat, M. Kinetics of hydrogen evolution reactions in acidic media on Pt, Pd, and MoS_2. *Langmuir* **38**, 4341–4350 (2022).

24. McCrum, I. T. & Koper, M. T. M. The role of adsorbed hydroxide in hydrogen evolution reaction kinetics on modified platinum. *Nat. Energy 2020 511* **5**, 891–899 (2020).

25. Rheinländer, P. J., Herranz, J., Durst, J. & Gasteiger, H. A. Kinetics of the hydrogen oxidation/evolution reaction on polycrystalline platinum in alkaline electrolyte reaction order with respect to hydrogen pressure. *J. Electrochem. Soc.* **161**, F1448–F1457 (2014).

26. Bao, F. *et al.* Understanding the hydrogen evolution reaction kinetics of electrodeposited nickel-molybdenum in acidic, near-neutral, and alkaline conditions. *ChemElectroChem* **8**, 195–208 (2021).

27. Bhardwaj, M. & Balasubramaniam, R. Uncoupled non-linear equations method for determining kinetic parameters in case of hydrogen evolution reaction following Volmer–Heyrovsky–Tafel mechanism and Volmer–Heyrovsky mechanism. *Int. J. Hydrogen Energy* **33**, 2178–2188 (2008).

28. Zhang, Y., Xiao, J., Lv, Q. & Wang, S. Self-supported transition metal phosphide based electrodes as high-efficient water splitting cathodes. *Front. Chem. Sci. Eng. 2018*

123 **12**, 494–508 (2018).

29. Chen, Z., Duan, X., Wei, W., Wang, S. & Ni, B. J. Recent advances in transition metal-based electrocatalysts for alkaline hydrogen evolution. *J. Mater. Chem. A* **7**, 14971–15005 (2019).

30. Liang, Q., Brocks, G. & Bieberle-Hütter, A. Oxygen evolution reaction (OER) mechanism under alkaline and acidic conditions. *J. Phys. Energy* **3**, 026001 (2021).

31. Shi, Z., Wang, X., Ge, J., Liu, C. & Xing, W. Fundamental understanding of the acidic oxygen evolution reaction: mechanism study and state-of-the-art catalysts. *Nanoscale* **12**, 13249–13275 (2020).

32. Yan, Z. *et al.* Electrodeposition of (hydro)oxides for an oxygen evolution electrode. *Chem. Sci.* **11**, 10614–10625 (2020).

33. Yu, M., Budiyanto, E. & Tüysüz, H. Principles of water electrolysis and recent progress in cobalt-, nickel-, and iron-based oxides for the oxygen evolution reaction. *Angew. Chemie - Int. Ed.* **61**, (2022).

34. Song, J. *et al.* A review on fundamentals for designing oxygen evolution electrocatalysts. *Chem. Soc. Rev.* **49**, 2196–2214 (2020).

35. Bai, L., Lee, S. & Hu, X. Spectroscopic and electrokinetic evidence for a bifunctional mechanism of the oxygen evolution reaction. *Angew. Chemie - Int. Ed.* **60**, 3095–3103 (2021).

36. Chhetri, M. *et al.* Mechanochemical synthesis of free-standing platinum nanosheets and their electrocatalytic properties. *Adv. Mater.* **27**, 4430–4437 (2015).

37. Li, Z., Ge, R., Su, J. & Chen, L. Recent progress in low Pt content electrocatalysts for hydrogen evolution reaction. *Adv. Mater. Interfaces* **7**, 1–13 (2020).

38. Zhang, H. *et al.* Dynamic traction of lattice-confined platinum atoms into mesoporous carbon matrix for hydrogen evolution reaction. *Sci. Adv.* **4**, (2018).

39. Yan, X. *et al.* Pt nanoparticles decorated high-defective graphene nanospheres as highly efficient catalysts for the hydrogen evolution reaction. *Carbon N. Y.* **137**, 405–410 (2018).

40. Shang, X. *et al.* Pt-C interfaces based on electronegativity-functionalized hollow carbon spheres for highly efficient hydrogen evolution. *ACS Appl. Mater. Interfaces* **10**, 43561–43569 (2018).

41. Nayak, P. *et al.* Monolithic laser scribed graphene scaffolds with atomic layer deposited platinum for the hydrogen evolution reaction. *J. Mater. Chem. A* **5**, 20422–20427 (2017).

42. Liu, G. *et al.* Efficiently synergistic hydrogen evolution realized by trace amount of Pt-decorated defect-rich SnS_2 nanosheets. *ACS Appl. Mater. Interfaces* **9**, 37750–37759 (2017).

43. Jiang, K. *et al.* Single platinum atoms embedded in nanoporous cobalt selenide as electrocatalyst for accelerating hydrogen evolution reaction. *Nat. Commun. 2019 101* **10**, 1–9 (2019).

44. Yan, Q. *et al.* A highly efficient and durable water splitting system: platinum sub-nanocluster functionalized nickel–iron layered double hydroxide as the cathode and hierarchical nickel–iron selenide as the anode. *J. Mater. Chem. A* **7**, 2831–2837 (2019).

45. Cui, B. *et al.* Solution-plasma-assisted bimetallic oxide alloy nanoparticles of Pt and Pd embedded within two-dimensional $Ti_3C_2T_x$ nanosheets as highly active electrocatalysts for overall water splitting. *ACS Appl. Mater. Interfaces* **10**, 23858–23873 (2018).

46. Wang, Y., Chen, L., Yu, X., Wang, Y. & Zheng, G. Superb alkaline hydrogen evolution and simultaneous electricity generation by Pt-decorated Ni_3N nanosheets. *Adv. Energy Mater.* **7**, 1601390 (2017).

47. Zhang, J. *et al.* Single platinum atoms immobilized on an MXenes as an efficient catalyst for the hydrogen evolution reaction. *Nat. Catal. 2018 112* **1**, 985–992 (2018).

48. Tan, T., *et al.* Platinum nanoparticle during electrochemical hydrogen evolution : adsorbate distribution , active reaction species and size effect. *ACS Catalysis* **5**. 2376-2383 (2015).

49. Zhang, L., Doyle-Davis, K. & Sun, X. Pt-based electrocatalysts with high atom utilization efficiency: from nanostructures to single atoms. *Energy Environ. Sci.* **12**, 492–517 (2019).

50. Cai, J., Javed, R., Ye, D., Zhao, H. & Zhang, J. Recent progress in noble metal nanocluster and single atom electrocatalysts for the hydrogen evolution reaction. *J. Mater. Chem. A* **8**, 22467–22487 (2020).

51. Yang, Y. *et al.* Non-precious alloy encapsulated in nitrogen-doped graphene layers derived from MOFs as an active and durable hydrogen evolution reaction catalyst. *Energy Environ. Sci.* **8**, 3563–3571 (2015).

52. Kim, J. *et al.* Highly durable platinum single-atom alloy catalyst for electrochemical reactions. *Adv. Energy Mater.* **8**, 1701476 (2018).

53.Du, N. *et al.* Trimetallic triStar nanostructures: tuning electronic and surface structures for enhanced electrocatalytic hydrogen evolution. *Adv. Mater.* **28**, 2077–2084 (2016).

54. Hinnemann, B. *et al.* Biomimetic hydrogen evolution: MoS_2 nanoparticles as catalyst for hydrogen evolution. *J. Am. Chem. Soc.* **127**, 5308–5309 (2005).

55. Jaramillo, T. F. *et al.* Identification of active edge sites for electrochemical H_2 evolution from MoS_2 nanocatalysts. *Science (80-.).* **317**, 100–102 (2007).

56. Kibsgaard, J., Chen, Z., Reinecke, B. N. & Jaramillo, T. F. Engineering the surface structure of MoS_2 to a preferentially expose active edge sites for a electrocatalysis. *Nat.*

Mater. **11**, 963–969 (2012).

57. Chen, Z. *et al.* Core-shell MoO_3-MoS_2 nanowires for hydrogen evolution: A functional design for electrocatalytic materials. *Nano Lett.* **11**, 4168–4175 (2011).

58. Kong, D. *et al.* Synthesis of MoS_2 and $MoSe_2$ films with vertically aligned layers. *Nano Lett.* **13**, 1341–1347 (2013).

59. Wang, H. *et al.* Electrochemical tuning of vertically aligned MoS_2 nanofilms and its application in improving hydrogen evolution reaction. *Proc. Natl. Acad. Sci. U. S. A.* **110**, 19701–19706 (2013).

60. Ye, G. *et al.* Defects engineered monolayer MoS_2 for improved hydrogen evolution reaction. *Nano Lett.* **16**, 1097–1103 (2016).

61. Li, Y. *et al.* MoS_2 nanoparticles grown on graphene: An advanced catalyst for the hydrogen evolution reaction. *J. Am. Chem. Soc.* **133**, 7296–7299 (2011).

62. Wang, Y. *et al.* Fluorine- and nitrogen-codoped MoS_2 with a catalytically active basal plane. *ACS Appl. Mater. Interfaces* **9**, 27715–27719 (2017).

63. Ma, F. *et al.* One-step synthesis of Co-doped 1T-MoS_2 nanosheets with efficient and stable HER activity in alkaline solutions. *Mater. Chem. Phys.* **244**, 122642 (2020).

64. Yu, Y. *et al.* High phase-purity 1T′-MoS_2- and 1T′-$MoSe_2$-layered crystals. *Nat. Chem.* **10**, 638–643 (2018).

65. Attanayake, N. H. *et al.* Effect of intercalated metals on the electrocatalytic activity of 1T-MoS_2 for the hydrogen evolution reaction. *ACS Energy Lett.* **3**, 7–13 (2018).

66. Lukowski, M. A. *et al.* Enhanced hydrogen evolution catalysis from chemically exfoliated metallic MoS_2 nanosheets. *J. Am. Chem. Soc.* **135**, 10274–10277 (2013).

67. Wu, L. *et al.* Unraveling the role of lithium in enhancing the hydrogen evolution activity of MoS_2: intercalation versus adsorption. *ACS Energy Lett.* **4**, 1733–1740 (2019).

68. Sun, X., Wang, Z., Li, Z. & Fu, Y. Q. Origin of structural transformation in mono- and bi-layered molybdenum disulfide. *Sci. Rep.* **6**, 2–10 (2016).

69. Yang, S. Z. *et al.* Rhenium-doped and stabilized MoS_2 atomic layers with basal-plane catalytic activity. *Adv. Mater.* **30**, 1–7 (2018).

70. Gao, Z. W., Liu, M., Zheng, W., Zhang, X. & Lee, L. Y. S. Surface engineering of MoS_2 via laser-induced exfoliation in protic solvents. *Small* **15**, 1–7 (2019).

71. Lee, J. H., Jang, W. S., Han, S. W. & Baik, H. K. Efficient hydrogen evolution by mechanically strained MoS_2 nanosheets. *Langmuir* **30**, 9866–9873 (2014).

72. Tao, L., Duan, X., Wang, C., Duan, X. & Wang, S. Plasma-engineered MoS_2 thin-film as an efficient electrocatalyst for hydrogen evolution reaction. *Chem. Commun.* **51**, 7470–7473 (2015).

73. Sun, C. *et al.* Defect engineering of molybdenum disulfide through ion irradiation to boost hydrogen evolution reaction performance. *Nano Res.* **12**, 1613–1618 (2019).

74. Zhang, J. *et al.* Engineering water dissociation sites in MoS_2 nanosheets for accelerated electrocatalytic hydrogen production. *Energy Environ. Sci.* **9**, 2789–2793 (2016).

75. Ma, X. *et al.* Ultrathin Co(Ni)-doped MoS_2 nanosheets as catalytic promoters enabling efficient solar hydrogen production. *Nano Res.* **9**, 2284–2293 (2016).

76. Shi, Y. *et al.* Energy level engineering of MoS_2 by transition-metal doping for accelerating hydrogen evolution reaction. *J. Am. Chem. Soc.* **139**, 15479–15485 (2017).

77. Deng, J. *et al.* Triggering the electrocatalytic hydrogen evolution activity of the inert two-dimensional MoS_2 surface via single-atom metal doping. *Energy Environ. Sci.* **8**, 1594–1601 (2015).

78. Qin, J. *et al.* Activating edge-Mo of 2H-MoS_2 via coordination with pyridinic N-C for pH-universal hydrogen evolution electrocatalysis. *ACS Catal.* **11**, 4486–4497

(2021).

79. Hu, J. *et al.* Interface modulation of MoS_2/metal oxide heterostructures for efficient hydrogen evolution electrocatalysis. *Small* **16**, 1–9 (2020).

80. Liu, D. *et al.* Nitrogen-doped $MoS_2/Ti_3C_2T_X$ heterostructures as ultra-efficient alkaline HER electrocatalysts. *Inorg. Chem.* **60**, 9932–9940 (2021).

81. Bawari, S. *et al.* On the hydrogen evolution reaction activity of graphene-hBN van der Waals heterostructures. *Phys. Chem. Chem. Phys.* **20**, 15007–15014 (2018).

82. Zhang, B. *et al.* Interface engineering: The $Ni(OH)_2/MoS_2$ heterostructure for highly efficient alkaline hydrogen evolution. *Nano Energy* **37**, 74–80 (2017).

83. Zhu, Z. *et al.* Ultrathin transition metal dichalcogenide/3d metal hydroxide hybridized nanosheets to enhance hydrogen evolution activity. *Adv. Mater.* **30**, 1801171 (2018).

84. Zhang, D., Mou, H., Lu, F., Song, C. & Wang, D. A novel strategy for 2D/2D NiS/graphene heterostructures as efficient bifunctional electrocatalysts for overall water splitting. *Appl. Catal. B Environ.* **254**, 471–478 (2019).

85. Wan, K. *et al.* Hierarchical porous Ni3S4 with enriched high-valence Ni sites as a robust electrocatalyst for efficient oxygen evolution reaction. *Adv. Funct. Mater.* **29**, 1900315 (2019).

86. Kang, Z. *et al.* Engineering an earth-abundant element-based bifunctional electrocatalyst for highly efficient and durable overall water splitting. *Adv. Funct. Mater.* **29**, 1807031 (2019).

87. Wang, J. *et al.* Water dissociation kinetic-oriented design of nickel sulfides via tailored dual sites for efficient alkaline hydrogen evolution. *Adv. Funct. Mater.* **31**, 2008578 (2021).

88. Li, Y. *et al.* Facile dynamic synthesis of homodispersed Ni_3S_2 nanosheets as a high-

efficient bifunctional electrocatalyst for water splitting. *ChemCatChem* **11**, 1320–1327 (2019).

89. Fei, B. *et al.* Ultrathinning nickel sulfide with modulated electron density for efficient water splitting. *Adv. Energy Mater.* **10**, 2001963 (2020).

90. Zhang, J. *et al.* Interface engineering of MoS_2/Ni_3S_2 heterostructures for highly enhanced electrochemical overall-water-splitting activity. *Angew. Chemie Int. Ed.* **55**, 6702–6707 (2016).

91. Zhao, Y. *et al.* Hatted 1T/2H-Phase MoS_2 on Ni_3S_2 nanorods for efficient overall water splitting in alkaline media. *Chem. - A Eur. J.* **26**, 2034–2040 (2020).

92. Cao, J., Zhou, J., Zhang, Y., Wang, Y. & Liu, X. Dominating role of aligned MoS_2/Ni_3S_2 nanoarrays supported on three-dimensional Ni foam with hydrophilic interface for highly enhanced hydrogen evolution reaction. *ACS Appl. Mater. Interfaces* **10**, 1752–1760 (2018).

93. Li, F., Zhang, D., Xu, R.-C., Fu, W.-F. & Lv, X.-J. Superhydrophilic heteroporous MoS_2/Ni_3S_2 for highly efficient electrocatalytic overall water splitting. *ACS Appl. Energy Mater.* **1**, 3929–3936 (2018).

94. Luo, X. *et al.* Interface engineering of hierarchical branched Mo-doped Ni_3S_2/Ni_xP_y hollow heterostructure nanorods for efficient overall water splitting. *Adv. Energy Mater.* **10**, 1903891 (2020).

95. Qin, Y. *et al.* Nitrogen-doped $Ni_2P/Ni_{12}P_5/Ni_3S_2$ three-phase heterostructure arrays with ultrahigh areal capacitance for high-performance asymmetric supercapacitor. *Electrochim. Acta* **393**, 139059 (2021).

96. Lv, X.; Liu, G.; Liu, S.; Chen, W.; Cao, D.; Song, T.; Wang, N.; Zhu, Y. Three-dimensional flower-like Fe, C-doped-MoS_2/Ni_3S_2 heterostructures spheres for accelerating electrocatalytic oxygen and hydrogen evolution. *Crystals* **11**, 340 (2021).

97.Kong, Q. *et al.* Interface engineering of N-doped Ni_3S_2/CoS_2 heterostructures as efficient bifunctional catalysts for overall water splitting. *J. Electroanal. Chem.* **895**, 115516 (2021).

98. Bai, S. *et al.* Recent advances of MXenes as electrocatalysts for hydrogen evolution reaction. *npj 2D Mater. Appl.* **5**, (2021).

99. Anasori, B., Lukatskaya, M. R. & Gogotsi, Y. 2D metal carbides and nitrides (MXenes) for energy storage. *Nat. Rev. Mater.* **2**, (2017).

100. Naguib, M. *et al.* Two-dimensional nanocrystals produced by exfoliation of Ti_3AlC_2. *Adv. Mater.* **23**, 4248–4253 (2011).

101. Anasori, B. *et al.* Two-dimensional, ordered, double transition metals carbides (MXenes). *ACS Nano* **9**, 9507–9516 (2015).

102. Deysher, G. *et al.* Synthesis of Mo_4VAlC_4 MAX phase and two-dimensional $Mo4VC_4$ MXenes with five atomic layers of transition metals. *ACS Nano* **14**, 204–217 (2020).

103. Ghidiu, M., Lukatskaya, M. R., Zhao, M. Q., Gogotsi, Y. & Barsoum, M. W. Conductive two-dimensional titanium carbide 'clay' with high volumetric capacitance. *Nature* **516**, 78–81 (2015).

104. Wei, Y., Zhang, P., Soomro, R. A., Zhu, Q. & Xu, B. Advances in the synthesis of 2D MXenes. *Adv. Mater.* **33**, 1–30 (2021).

105. Xuan, J. *et al.* Organic-base-driven intercalation and delamination for the production of functionalized titanium aarbide nanosheets with superior photothermal therapeutic performance. *Angew. Chemie* **128**, 14789–14794 (2016).

106. Zou, G. *et al.* Hydrogenated core–shell $MAX@K_2Ti_8O_{17}$ pseudocapacitance with ultrafast sodium storage and long-term cycling. *Adv. Energy Mater.* **7**, 1700700 (2017).

107. Li, L., Li, G., Tan, L., Zhang, Y. & Wu, B. Highly efficiently delaminated single-

layered MXenes nanosheets with large lateral size. *Langmuir* **33**, 9000–9006 (2017).

108. Li, T. *et al.* Fluorine-free synthesis of high-purity $Ti_3C_2T_x$ (T=OH, O) via alkali treatment. *Angew. Chemie - Int. Ed.* **57**, 6115–6119 (2018).

109. Sun, W. *et al.* Electrochemical etching of Ti_2AlC to Ti_2CT:X (MXenes) in low-concentration hydrochloric acid solution. *J. Mater. Chem. A* **5**, 21663–21668 (2017).

110. Morales-garc, A., Calle-vallejo, F. & Illas, F. MXenes : new horizons in catalysis. *ACS Catal.* **10**, 13487–13503 (2020).

111. Yao, F. *et al.* Ensemble-exciting effect in Pd/alk-Ti3C2 on the activity for efficient hydrogen production. *ACS Sustain. Chem. Energy* **36**, 12332–12340 (2021).

112. Tang, Y. *et al.* MXenes nanoarchitectonics : defect-engineered 2D MXenes towards enhanced electrochemical water splitting. **12**, 2103867 (2022).

113. Ming, F., Liang, H., Huang, G., Bayhan, Z. & Alshareef, H. N. MXenes for rechargeable batteries beyond the lithium-ion. **33**, 2004039 (2020).

114. Syamsai, R., Rodriguez, J. R., Pol, V. G. & Le, Q. Van. Double transition metal MXenes as anodes for Li ‑ ion batteries. *Sci. Rep.* **11**, 688 (2021).

115. Das, P. & Wu, Z. MXenes for energy storage : present status and future perspectives. *J. Phys. Energy* **2**, 032004 (2020).

116. Rhouati, A., Berkani, M., Vasseghian, Y. & Golzadeh, N. Chemosphere MXenes-based electrochemical sensors for detection of environmental pollutants : A comprehensive review. *Chemosphere* **291**, 132921 (2022).

117. Shahzad, F., Alhabeb, M., Hatter, C. B. & Anasori, B. Electromagnetic interference shielding with 2D transition metal carbides (MXenes). *Science (80-.).* **353**, 1137–1140 (2016).

118. Kang, Z. *et al.* Recent progress of MXenes and MXenes-based nanomaterials for the electrocatalytic hydrogen evolution reaction. *J. Mater. Chem. A* **9**, 6089–6108

(2021).

119. Li, S. *et al.* Ultrathin MXenes nanosheets with rich fluorine termination groups realizing efficient electrocatalytic hydrogen evolution. *Nano Energy* **47**, 512–518 (2018).

120. Ling, C., Shi, L., Ouyang, Y. & Wang, J. Searching for highly active catalysts for hydrogen evolution reaction based on O-terminated MXenes through a Simple descriptor. *Chem. Mater.* **28**, 9026–9032 (2016).

121. Xie, Y. *et al.* Role of surface structure on Li-ion energy storage capacity of two-dimensional transition-metal carbides. *J. Am. Chem. Soc.* **136**, 6385–6394 (2014).

122. Handoko, A. D. *et al.* Tuning the basal plane functionalization of two- dimensional metal carbides (MXenes) to control hydrogen evolution activity. *ACS Appl. Energy Mater.* **1**, 173–180 (2017).

123. Bao, Z. *et al.* Role of MXenes surface terminations in electrochemical energy storage: A review. *Chinese Chem. Lett.* **32**, 2648–2658 (2021).

124. Bai, S. *et al.* Recent advances of MXenes as electrocatalysts for hydrogen evolution reaction. *npj 2D Mater. Appl.* **5**, (2021).

125. Huang, B., Zhou, N., Chen, X., Ong, W. & Li, N. Insights into the electrocatalytic hydrogen evolution reaction mechanism on two-dimensional transition-metal carbonitrides (MXenes). *Chem. Eur. J.* **24**, 18479–18486 (2018).

126. Anand, R. *et al.* Late transition metal doped MXenes showing superb bifunctional electrocatalytic activities for water splitting via distinctive mechanistic pathways. *Adv. Energy Mater.* **11**, 2102388 (2021).

127. Li, P., Zhu, J. & Handoko, A. D. High-throughput theoretical optimization of the hydrogen evolution reaction on MXenes by transition metal modification. *J. Mater. Chem. A* **6**, 4271–4278 (2018).

128. Kuznetsov, D. A. *et al.* Single-atom-substituted Mo_2C Tx: Fe-layered carbide for selective oxygen reduction to hydrogen peroxide: tracking the evolution of the MXenes phase. *J. Am. Chem. Soc.* **143**, 5771–5778 (2021).

129. Liu, J. *et al.* Hierarchical "nanoroll" like $MoS_2/Ti_3C_2T_x$ hybrid with high electrocatalytic hydrogen evolution activity. *"Applied Catal. B, Environ.* **241**, 89–94 (2018).

130. Xiu, L., Wang, Z., Yu, M. & Qiu, J. Aggregation-resistant 3D MXenes based architecture as efficient bifunctional electrocatalyst for overall water splitting. *ACS Nano* **12**, 8017–8028 (2018).

131. Wu, X. *et al.* Engineering multifunctional collaborative catalytic interface enabling efficient hydrogen evolution in all pH range and seawater. *Adv. Energy Mater.* **9**, 1901333 (2019).

132. Zhu, X. D., Xie, Y. & Liu, Y. T. Exploring the synergy of 2D MXenes-supported black phosphorus quantum dots in hydrogen and oxygen evolution reactions. *J. Mater. Chem. A* **6**, 21255–21260 (2018).

133. Zhou, W. *et al.* Recent developments of carbon-based electrocatalysts for hydrogen evolution reaction. *Nano Energy* **28**, 29–43 (2016).

134. Hu, C. & Dai, L. Multifunctional carbon-based metal-free electrocatalysts for simultaneous oxygen reduction, oxygen evolution, and hydrogen evolution. *Adv. Mater.* **29**, 1604942 (2017).

135. Jiao, Y., Zheng, Y., Davey, K. & Qiao, S. Z. Activity origin and catalyst design principles for electrocatalytic hydrogen evolution on heteroatom-doped graphene. *Nat. Energy* **1**, 16130 (2016).

136. Wang, X., Vasileff, A., Jiao, Y., Zheng, Y. & Qiao, S. Z. Electronic and structural engineering of carbon-based metal-free electrocatalysts for water splitting. *Adv. Mater.*

31, 1803625 (2019).

137. Zheng, Y. *et al.* Toward design of synergistically active carbon-based catalysts for electrocatalytic hydrogen evolution. *ACS Nano* **8**, 5290–5296 (2014).

138. Bhatt, M. D. & Lee, J. Y. Advancement of platinum (Pt)-free (Non-Pt precious metals) and/or metal-free (non-precious-metals) electrocatalysts in energy applications: a review and perspectives. *Energy and Fuels* **34**, 6634–6695 (2020).

139. Li, L., Wang, P., Shao, Q. & Huang, X. Recent progress in advanced electrocatalyst design for acidic oxygen evolution reaction. *Adv. Mater.* **33**, 2004243 (2021).

140. Zhao, Y., You, J., Wang, L., Bao, W. & Yao, R. Recent advances in Ni_3S_2-based electrocatalysts for oxygen evolution reaction. *Int. J. Hydrogen Energy* **46**, 39146–39182 (2021).

141. Lu, F., Zhou, M., Zhou, Y. & Zeng, X. First-row transition metal based catalysts for the oxygen evolution reaction under alkaline conditions: basic principles and recent advances. *Small* **13**, 1701931 (2017).

142. Li, W., Xiong, D., Gao, X. & Liu, L. The oxygen evolution reaction enabled by transition metal phosphide and chalcogenide pre-catalysts with dynamic changes. *Chem. Commun.* **55**, 8744–8763 (2019).

143. Sun, H. *et al.* Self-supported transition-metal-based electrocatalysts for hydrogen and oxygen evolution. *Adv. Mater.* **32**, 1806326 (2020).

144. Noor, T., Yaqoob, L. & Iqbal, N. Recent advances in electrocatalysis of oxygen evolution reaction using noble-metal, transition-metal, and carbon-based materials. *ChemElectroChem* **8**, 447–483 (2021).

145. Spöri, C. *et al.* Experimental activity descriptors for iridium-based catalysts for the electrochemical oxygen evolution reaction (OER). *ACS Catal.* **9**, 6653–6663 (2019).

146. Piaget, J. Electrocatalytic properties of transition metal oxides for oxygen evolution reaction. *Chem. Br.* **0182**, 7 (1986).

147.Over, H. Atomic scale insights into electrochemical versus gas phase oxidation of HCl over RuO_2-based catalysts: A comparative review. *Electrochim. Acta* **93**, 314–333 (2013).

148. Marshall, A. T. & Haverkamp, R. G. Electrocatalytic activity of IrO_2–RuO_2 supported on Sb-doped SnO2 nanoparticles. *Electrochim. Acta* **55**, 1978–1984 (2010).

149. Audichon, T. *et al.* Electroactivity of RuO_2–IrO_2 mixed nanocatalysts toward the oxygen evolution reaction in a water electrolyzer supplied by a solar profile. *Int. J. Hydrogen Energy* **39**, 16785–16796 (2014).

150. Corona-Guinto, J. L. *et al.* Performance of a PEM electrolyzer using $RuIrCoO_x$ electrocatalysts for the oxygen evolution electrode. *Int. J. Hydrogen Energy* **38**, 12667–12673 (2013).

151. Audichon, T. *et al.* IrO_2 Coated on RuO_2 as Efficient and Stable Electroactive Nanocatalysts for Electrochemical Water Splitting. *J. Phys. Chem. C* **120**, 2562–2573 (2016).

152. Cook, T. R. *et al.* Solar energy supply and storage for the legacy and nonlegacy worlds. *Chem. Rev.* **110**, 6474–6502 (2010).

153. Ma, Z. *et al.* Reaction mechanism for oxygen evolution on RuO_2, IrO_2, and RuO_2@IrO_2 core-shell nanocatalysts. *J. Electroanal. Chem.* **819**, 296–305 (2018).

154. Liu, Y. *et al.* Interface engineering of (Ni, Fe)S_2@MoS_2 heterostructures for synergetic electrochemical water splitting. *Appl. Catal. B Environ.* **247**, 107–114 (2019).

155. Li, F., Zhang, D., Xu, R. C., Fu, W. F. & Lv, X. J. Superhydrophilic Heteroporous MoS_2/Ni_3S_2 for Highly Efficient Electrocatalytic Overall Water Splitting. *ACS Appl.*

Energy Mater. **1**, 3929–3936 (2018).

156. Zhang, Y. *et al.* Tremella-like Ni_3S_2/MnS with ultrathin nanosheets and abundant oxygen vacancies directly used for high speed overall water splitting. *Appl. Catal. B Environ.* **257**, 117899 (2019).

157. Xu, Y. *et al.* Synergism of interface and electronic effects: bifunctional N-doped Ni_3S_2/N-doped MoS_2 hetero-nanowires for efficient electrocatalytic overall water splitting. *Chem. – A Eur. J.* **25**, 16074–16080 (2019).

158. Cao, J., Zhou, J., Zhang, Y., Wang, Y. & Liu, X. Dominating role of aligned MoS_2/Ni_3S_2 nanoarrays supported on three-dimensional Ni foam with hydrophilic interface for highly enhanced hydrogen evolution reaction. *ACS Appl. Mater. Interfaces* **10**, 1752–1760 (2018).

159. Shit, S. *et al.* Cobalt sulfide/nickel sulfide heterostructure directly grown on nickel foam: an efficient and durable electrocatalyst for overall water splitting application. *ACS Appl. Mater. Interfaces* **10**, 27712–27722 (2018).

160. Zhao, Y. *et al.* Hatted 1T/2H-Phase MoS_2 on Ni_3S_2 nanorods for efficient overall water splitting in alkaline media. *Chem. – A Eur. J.* **26**, 2034–2040 (2020).

161. Zhang, Y. *et al.* Tremella-like Ni_3S_2/MnS with ultrathin nanosheets and abundant oxygen vacancies directly used for high speed overall water splitting. *Appl. Catal. B Environ.* **257**, 117899 (2019).

162. Lv, X. *et al.* Three-dimensional flower-like Fe, C-doped-MoS_2/Ni_3S_2 heterostructures spheres for accelerating electrocatalytic oxygen and hydrogen evolution. *Cryst. 2021, Vol. 11, Page 340* **11**, 340 (2021).

163. Priyadarsini, A. & Mallik, B. S. Effects of doped N, B, P, and S atoms on graphene toward oxygen evolution reactions. *ACS Omega* **6**, 5368–5378 (2021).

164. Zhou, S., Liu, N., Wang, Z. & Zhao, J. Nitrogen-doped graphene on transition

metal substrates as efficient bifunctional catalysts for oxygen reduction and oxygen evolution reactions. *ACS Appl. Mater. Interfaces* **9**, 22578–22587 (2017).

165. Li, M., Zhang, L., Xu, Q., Niu, J. & Xia, Z. N-doped graphene as catalysts for oxygen reduction and oxygen evolution reactions: Theoretical considerations. *J. Catal.* **314**, 66–72 (2014).

166. Zhao, J. *et al.* Nitrogen and sulfur co-doped graphene/carbon nanotube as metal-free electrocatalyst for oxygen evolution reaction: The enhanced performance by sulfur doping. *Electrochim. Acta* **204**, 169–175 (2016).

167. Zhai, Q., Pan, Y. & Dai, L. Carbon-based metal-free electrocatalysts: past, present, and future. *Accounts Mater. Res.* **2**, 1239–1250 (2021).

168. Zhao, Y., Nakamura, R., Kamiya, K., Nakanishi, S. & Hashimoto, K. Nitrogen-doped carbon nanomaterials as non-metal electrocatalysts for water oxidation. *Nat. Commun. 2013 41* **4**, 1–7 (2013).

169. Li, X. *et al.* Nitrogen-doped mesoporous carbon nanosheet/carbon nanotube hybrids as metal-free bi-functional electrocatalysts for water oxidation and oxygen reduction. *J. Mater. Chem. A* **4**, 13133–13141 (2016).

170. Li, R., Wei, Z. & Gou, X. Nitrogen and phosphorus dual-doped graphene/carbon nanosheets as bifunctional electrocatalysts for oxygen reduction and evolution. *ACS Catal.* **5**, 4133–4142 (2015).

171.Chen, S. *et al.* Nitrogen and oxygen dual-doped carbon hydrogel film as a substrate-free electrode for highly efficient oxygen evolution reaction. *Adv. Mater.* **26**, 2925–2930 (2014).

172. Chen, S. *et al.* Ionic liquid-assisted synthesis of N/S-double doped graphene microwires for oxygen evolution and Zn–air batteries. *Energy Storage Mater.* **1**, 17–24 (2015).

173. Zhang, J. & Dai, L. Nitrogen, phosphorus, and fluorine tri-doped graphene as a multifunctional catalyst for self-powered electrochemical water splitting. *Angew. Chemie Int. Ed.* **55**, 13296–13300 (2016).

174. Abbas, Y. *et al.* Substantial role of nitrogen and sulfur in quaternary-atom-doped multishelled carbon nanospheres for the oxygen evolution reaction. *ACS Sustain. Chem. Eng.* **8**, 4284–4291 (2020).

Chapter 2

Interface Engineering of Ultrathin Hierarchical P-doped MoS_2/Ni_3S_2 Heterostructure on Nickel Foam for Efficient Water Splitting

2.1 Introduction

Increasing global warming has led to the development of new energy fuels, which can potentially compete with existing carbon-based fuels. Hydrogen (H_2) has attracted immense attention in the last few decades, owing to its sustainability and environmentally-friendly features. [1,2] Electrochemical water splitting represents an effective and valuable strategy to produce high-quality H_2 without releasing any potential greenhouse gases.[3] One main hurdle to overcome for H_2 and O_2 effective production by water splitting using electrochemical means is the high Gibbs free energy barrier of 1.23V. To lower this barrier, researchers have utilized Pt- and Ru/In oxide-based electrocatalysts endowed with effective activity for hydrogen evolution reaction (HER), and oxygen evolution reaction (OER). However, the scarcity and high price of these materials are the major limitations for their commercial widespread applications. [4]In addition, most electrocatalysts are not effective for both OER and HER under the same conditions.[5] Thus, it becomes necessary to design noble metal-free, bi-functional electrocatalysts featuring high activity, excellent stability and operating under the same conditions for water splitting.

Recently Ni chalcogenides (NiS, NiS_2 and Ni_3S_2) have attracted substantial interest for electrochemical water splitting.[6–11] Among them, Ni_3S_2, due to its high conductivity, unique structure configuration and earth-abundance, has been recognized as an efficient electrocatalyst for water splitting. Despite these beneficial features, the low density of surface-active sites and poor stability in aqueous media hinder its wide utilization as a bi-functional catalyst for water splitting.[12] Therefore, many efforts have been devoted to enhance the activity and stability of Ni_3S_2-based catalysts for efficient water splitting. For instance, heterostructure Ni_3S_2-based nanomaterials such as CoS_x-Ni_3S_2/NF nanoarray,[13] MoS_2−Ni_3S_2 hetero-nanorods,[14, 15] MoS_2/Ni_3S_2 hetero-porous structure,[16] Ni_3S_2/MnS ultrathin nanosheets with abundant vacancies [17] could improve the activity and enhance the stability by controlling the morphology and providing more active surface sites. All these materials were prepared on Ni foam (NF) by hydrothermal or electrochemical methods. Besides, doping represents an efficient way to change the electron energy density and increase the density of active sites. Zhang et al. prepared Mo-doped Ni_3S_2/Ni_xP_y hollow heterostructure on NF through a solvothermal process and phosphorization treatment; the developed catalyst displayed hierarchical porous morphology and improved overall water splitting performance.[18] Despite the advantages brought up by element doping, there are only a few reports on element-doped heterostructure Ni_3S_2-based materials.[18–21]

In this investigation, we applied a one-step hydrothermal reaction to prepare P-doped MoS_2/Ni_3S_2 heterostructure on NF. The P-MoS_2/Ni_3S_2/NF flower-like clusters were produced through precise control of P-doping to optimize the electronic structure and enhance the interaction between MoS_2 and Ni_3S_2. As expected, the optimized $P_{1.0}$-MoS_2/Ni_3S_2/NF material exhibited an excellent performance toward both HER and OER with an overpotential of respectively 1.67 and 0.255 V at 100 mA/cm^2 in 1M

KOH solution. In addition, when $P_{1.0}MoS_2/Ni_3S_2/NF$ was applied as anode and cathode in an alkaline electrolyzer, it was possible to achieve overall water splitting at 20 and 40 mA/cm^2 under an ultralow cell voltage of 1.50 and 1.65 V, respectively, with excellent stability over 60 h.

2.2 Experiment section

2.2.1 Preparation of P-$MoS_2/Ni_3S_2/NF$

$(NH_4)_6Mo_7O_{24}•4H_2O$ (54.3 mg), CH_3CSNH_2 (92.2 mg) and $(NH_4)_2HPO_4$ (0.2, 0.4, 0.8, 1 or 2 mM) as respectively Mo, S and P precursors were dissolved sequentially into 30 mL of *N*, *N*-dimethylformamide (DMF). Then, the solution and 1×1.5 cm^2 nickel foam (NF) substrate were transferred into a 50 mL Teflon-lined stainless-steel autoclave and heated at 200 °C for 12 h. Finally, the resulting samples were washed sequentially with pure water and ethanol for at least three times and dried at 60°C overnight.

Similarly, $MoS_2/Ni_3S_2/NF$ was prepared using the same method without ammonium phosphate dibasic.

Ni_3S_2/NF was prepared by placing a 1×1.5 cm^2 piece of NF, CH_3CSNH_2 (92.2 mg) and DMF (30 mL) into a Teflon-lined stainless-steel autoclave and heated at 200 °C for 12 h. The resulting sample was washed sequentially with ethanol and pure water for at least three times and dried at 60 °C overnight.

Similarly, MoS_2 powder was prepared by heating a mixture of 54.3 mg of $(NH_4)_6Mo_7O_{24}•4H_2O$, 92.2 mg of CH_3CSNH_2 and 30 mL of DMF in a Teflon-lined stainless-steel autoclave at 200 °C for 12 h. The resulting MoS_2 powder was washed sequentially with ethanol and pure water for at least three times and dried at 60 °C overnight.

2.2.2. Electrochemical measurements

All electrochemical measurements were performed on a ModuLab-MTS electrochemical test station (Solartron, France) within a standard three electrodes system using the prepared catalyst as the working electrode, SCE (0.241 V *vs.* RHE) as the reference electrode, and carbon rod as the counter electrode. All samples were cut into 1×1.5 cm and used as working electrodes directly. For MoS_2 and RuO_2 electrodes, 20 mg of powder was dispersed in a Nafion (15 μL) and ethanol-water solution (V_{H2O}: $V_{ethanol}$=2:1), then sonicated until formation of uniform ink. 100 μL of the ink were dropped on a 1×1.5 cm piece of nickel foam and dried at 60 °C overnight.

Linear sweep voltammetry (LSV) and long-term cyclic voltammetry (*CV*) measurements were performed in 1.0 M KOH at the scan rates of 2 and 100 mV s^{-1}, respectively.

The two-electrode alkaline water electrolyzer was constructed using $P_{1.0}$-MoS_2/Ni_3S_2/NF as both cathode and anode for full water splitting in 1.0 M KOH.

Electrochemical Impedance Spectroscopy (EIS) measurements were performed in the frequency range of 0.01 Hz to 100 KHz using an AC potential of 10 mV. Then, the data were simulated with the Zview 2.0 software. A simple equivalent circuit model (**Figure 1**), comprising the solution resistance (R_s) in series with a charge-transfer resistance (R_{ct}) parallel with the corresponding double-layer capacitance (C_{dl}) at the catalyst/electrolyte interface, was used.

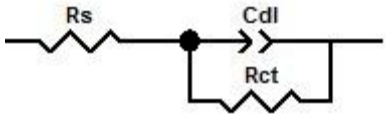

Figure 1. The equivalent circuit model for EIS.

The electrochemical active surface area (ECSA) was indirectly obtained by using

double layer capacitance (C_{dl}) measurements in a non-faradic potential range from -0.27 to -0.32 V at various scan rates (20 to 70 mV s^1). ECSA was obtained from the **Eq 2.1**:

$$\mathrm{ECSA} = \frac{\mathrm{C_{catalyst}\ mF.cm^{-2}}}{\mathrm{C_{dl}(NF)mFcm^{-2}per\ ECSA\ cm^{-2}}} \quad (2.1)$$

Where the C_{dl} value of the bare NF was used as a standard instead of the general specific capacitance to exclude the effect of the larger capacitance value of bare NF.

Cyclic voltammetry measurements were used to calculate the number of active sites *n* for the investigated electrocatalysts using the **Eq 2.2**. [2223]

$$\mathrm{n} = \frac{\mathrm{Q}}{2\mathrm{nF}} \quad (2.2)$$

Where the number 2 is the stoichiometric number of electrons consumed by the HER reaction of the electrode, and *F* is the Faraday constant (96485 C mol^{-1}). The catalyst's net voltammetry charge (*Q*) was calculated *via* subtracting charges resulting from the P_x-MoS_2/Ni_3S_2/NF and counterparts, including MoS_2/NF, Ni_3S_2/NF, RuO_2/NF and NF electrodes.

The formula presented in **Eq 2.3** [24] was employed to calculate the per-site turnover frequencies (TOFs, s^{-1}), where *I* (measured in A cm^{-2}) is the value of the current at a specific overpotential.

$$\mathrm{TOF} = \frac{|\mathrm{I}|}{2\mathrm{Fn}} \quad (2.3)$$

Combining ***Eq 2.2*** and **2.3** yields **Eq 2.4**:

$$\mathrm{TOF} = \frac{|\mathrm{I}|}{\mathrm{Q}} \quad (2.4)$$

The Faradaic efficiency (ε %) of the best performing electrocatalyst, namely $P_{1.0}MoS_2$/Ni_3S_2/NF the HER and OER was also estimated to further assess and confirm its electrocatalytic performance. The amount of the gas evolved (expressed in µmol per

hour) during a controlled galvanostatic electrolysis (CGE), symbolized here as V_m, was first measured by gas chromatography (GC), as described below, see **Eq.2.5**:

$$V_m = \text{mol gas(GC)} \tag{2.5}$$

The value of V_c, the expected quantity of the liberated gas theoretically calculated based on the charge passed (presuming 100% Faradaic efficiency) during that CGE, was then calculated using **Eq.2.6**:

$$V_c = \frac{Q(CGE)}{nF} \tag{2.6}$$

Where F is the Faraday's constant (F = 96485 C mol^{-1}) and Q (CGE) is the charge passed through the *WE* during the controlled process of galvanostatic electrolysis (CPE). The factor n represents the number of electrons transferred during the HER ($2H^+ + 2e^- = H_2$, n = 2) and OER ($4OH^- = 2H_2O + 4e^- + O_2$, n = 4). The value of ε was determined by dividing V_m by V_c, the expected quantity of the liberated gas theoretically calculated based on the charge passed (assuming 100% Faradaic efficiency) during that CGE. Finally, the tested electrocatalyst's Faradaic efficiency (ε%) was determined by multiplying the quotient of the ratio (V_m/V_c) by 100, **Eq 2.7**:[25,26]

$$\text{Faradaic efficiency (\%)} = \frac{[F \times n \times V_m]}{Q(CGE)} \times 100\% \tag{2.7}$$

Faradaic efficiency measurements were carried out in a custom-made airtight electrolysis cell. Gas chromatography was conducted on an Agilent 7890A gas chromatograph with a pneumatically operated automatic gas sampling valve to monitor the evolved H_2 and O_2 gases. The electrolysis cell was connected to the gas chromatography system *via* bespoke airtight glass-to-metal adapters and copper tubing with an internal diameter of 1/8 in. The oven temperature was set to 45 °C, and the carrier gas was Ar with a flow rate of approximately 3 mL min^{-1}.

2.2.3 DFT calculation

All spin-polarized calculations were performed by using density functional theory (DFT) based on the Vienna Ab initio Simulation Package (VASP). [27–29] The projector-augmented wave (PAW) method and the Perdew-Burke-Ernzerhof (PBE) exchange-correlation functional were used. The V_{dW} interaction was considered in the DFT-D3 correction method.[30] The pseudo-wavefunctions were expanded in a plane wave basis set with a cut off energy of 400 eV. A gamma centered k-sampling was adopted to sample the first Brillouin zone. All the structures were fully relaxed until the convergence criterion for the electronic structure iteration was set to be 1×10^{-6} eV and the forces on each atom were less than $0.02\ \mathrm{eV/Å}$. The theoretical models of P_n-MoS_2/Ni_3S_2 (n represents the number of S atoms replaced by P atoms) were constructed to represent P-doped MoS_2/Ni_3S_2 for exploring electrocatalytic activity in HER and OER. The Poisson-Boltzmann implicit solvent was used to consider the solvent effects with a relative permittivity ε of water as 78.3. The crystal planes of Ni_3S_2 and MoS_2 utilized in DFT calculation are MoS_2 (001)/Ni_3S_2 (001) and MoS_2 (001)/Ni_3S_2(110).

As for HER, the Gibbs free energy of the intermediate was calculated based on the **Eq. 2.8**,

$$\Delta G_{H^*} = \Delta E_{H^*} + \Delta E_{ZPE} - T\Delta S \tag{2.8}$$

Where ΔE_{H^*}, $\Delta EZPE$, ΔS are the binding energy of H, the change of zero-point energy and entropy, respectively. And ΔE_{H^*} can be obtained using **Eq.2.9**,

$$\Delta E_{H^*} = E_{H^*} - E_* - \frac{1}{2} E_{H_2} \tag{2.9}$$

Where E_{H^*}, and E_{H_2} represent the adsorption energy of H, the energy of bare surface and H_2 gas molecule, respectively. According to a previous study, $\Delta E_{ZPE} - T\Delta S$ is equal to 0.24 eV. [31] And the adsorption energy of H_2O is calculated by **Eq. 2.10**.

$$\Delta E_{H_2O} = E_{H_2O^*} - E_* - E_{H_2O} \quad (2.10)$$

The elementary reactions during OER in alkaline medium involves four proton-transfer steps:

$$* + OH^- \rightarrow OH^* + e^- \quad (1)$$

$$OH^* + OH^- \rightarrow O^* + H_2O + e^- \quad (2)$$

$$O^* + OH^- \rightarrow OOH^* + e^- \quad (3)$$

$$OOH^* + OH^- \rightarrow O_2 + H_2O + e^- \quad (4)$$

Where * represents the active site, and M* corresponds to an intermediate adsorbing on the active site. The Gibbs free energy changes of these elementary reactions can be calculated by the following **Eq. 2.15**,

$$\Delta G = \Delta E + \Delta E_{ZPE} - T\Delta S \quad (2.15)$$

Where ΔE represents the total energy difference between reactants and products, $\Delta EZPE$ is the change of zero-point energy, and $T\Delta S$ is the vibrational entropy change at finite temperature T. The over potential η was evaluated using **Eq. 2.16**,

$$\eta = \frac{\max[\Delta G_1, \Delta G_2, \Delta G_3, \Delta G_4]}{e} - 1.23 \quad (2.16)$$

Where ΔG_1, ΔG_2, ΔG_3, ΔG_4 represent the free energy change of elementary reactions (2.11) to (2.14).

2.3 Results and discussion

2.3.1 Materials characterization

The P-doped MoS_2/Ni_3S_2/NF materials were obtained by a facile hydrothermal process by controlling the phosphorus precursor concentration, as depicted in **Figure 2**. Briefly, ammonium molybdate tetrahydrate, thioacetamide, and ammonium phosphate dibasic were dispersed in 30 mL of N, N-dimethylformamide containing nickel foam (NF) support. Owing to its open porous structure and good conductivity, NF was

selected as the Ni source. After heating at 200°C for 12 h and rinsing with deionized water and ethanol several times, the obtained samples were directly investigated as electrodes for electrochemical HER and OER. Here, the microstructure and activity were altered by varying the initial P precursor concentration. Electrochemical measurements revealed that $P_{1.0}$-MoS_2/Ni_3S_2/NF was the most active material. Therefore, it was characterized in detail in the following, and its performance for HER, OER, and overall water splitting was assessed.

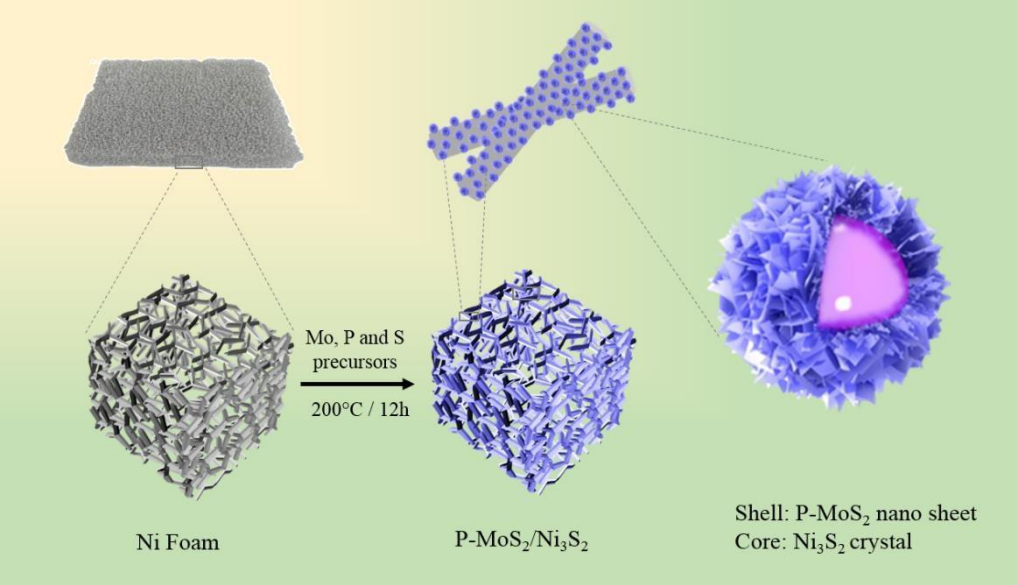

Figure 2. Schematic illustration of the fabrication process of P-MoS_2/Ni_3S_2/NF.

Figure 3 display the scanning electron microscopy (SEM) micrographs of MoS_2/Ni_3S_2/NF and P_x-MoS_2/Ni_3S_2/NF (x represents the concentration of the P precursor: 0.4, 0.8, 1.0 and 2.0 mM). The SEM image of pristine MoS_2/Ni_3S_2/NF revealed uniform nanosheets coated on the NF structure, while the nanosheets grew up (**Figure 3a**) when the P precursor concentration was increased to 0.4 mM (**Figure 3b**) and started to form nano-flowers (**Figure 3c**) at a concentration of 0.8 mM. The nano-flowers (500-700 nm average diameter) became more evident when the concentration

of the P precursor reached 1.0 mM (**Figure 3d-e**). This contrasts with the decrease of the nanoflowers' size (**Figure 3f**) observed when the P precursor concentration was 2.0 mM.

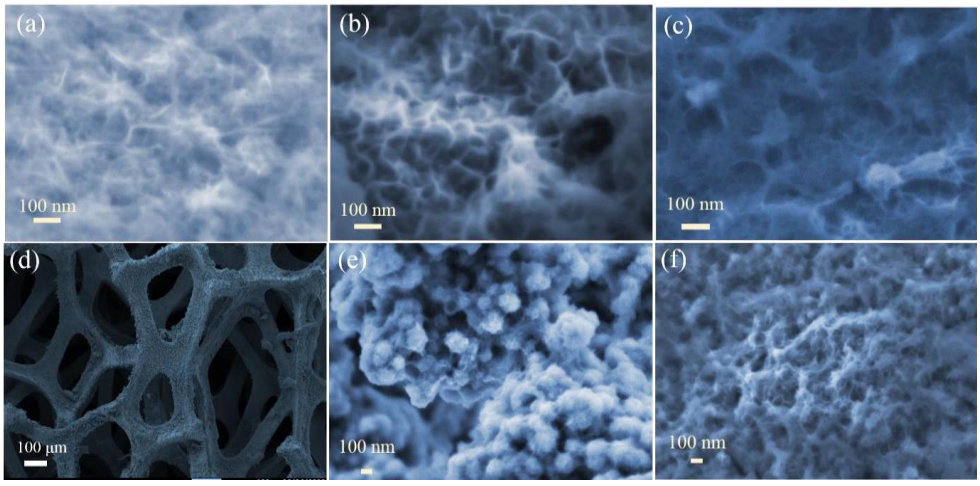

Figure 3. SEM images of (**a**) MoS_2/Ni_3S_2/NF and P_x-MoS_2/Ni_3S_2/NF (x represents the concentration of $(NH_4)_2HPO_4$): (**b**) 0.4, (**c**) 0.8, (**d-e**) 1.0mM, and (f) 2.0 mM.

Figure 4a-f depict the transmission electron microscopy (TEM) images of the selected $P_{1.0}$-MoS_2/Ni_3S_2/NF sample, which revealed that the surface was covered by MoS_2 nanosheets. The individual MoS_2 nanosheets showed an electron-beam transparent ultrathin texture and layered edge (noted by white arrows). In addition, the edge lattice fringes with a d-spacing of 0.617, 0.62, and 0.63 nm, discerned in the high-resolution TEM (HRTEM, **Figure 4a-f,** and **g, h**) images, can be typically indexed to MoS_2 (002) facets, [32] while d-spacing values of 0.29 and 0.23 nm ascribed respectively to Ni_3S_2 (110) and (001) planes were also evidenced in **Figure 4g, h** and **Figure 4d-f**. Moreover, energy-dispersive X-ray spectroscopy (EDX) elemental mapping in **Figure 4i-n** confirmed the existence of Ni, Mo, P, S, and some O in the $P_{1.0}$-MoS_2/Ni_3S_2/NF sample, in good agreement with its composition. The presence of the O element could originate from partial oxidation during the hydrothermal process. The EDX spectra of

areas 1 and 2 in **Figure 4j** are depicted in **Figure 4o** and evidenced the central body distribution of Ni and the edge distribution of Mo, inferring the heterostructure of $P_{1.0}$-MoS_2/Ni_3S_2/NF. This vertical growth of P_x-MoS_2 on Ni_3S_2 structure could provide a larger surface area to generate enough active sites for electrocatalytic HER and OER.

In the X-ray photoelectron spectroscopy (XPS) wide scan, elemental peaks of Ni, Mo, S, P, and O were visible, testifying the formation of the hybrid material (**Figure 5a**). The existence of low amounts of O and C elements was attributed to the inevitable material oxidation and contamination upon sample exposure to ambient. The Ni 2p high-resolution XPS profile of Ni_3S_2/NF (**Figure 5b**) can be fitted with two components at around 852.9 and 870.5 eV ascribed respectively to Ni $2p_{3/2}$ and Ni $2p_{1/2}$. In addition, the Ni $2p_{3\backslash2}$ could be decomposed into Ni^{3+} at around 856.5 eV, Ni^{2+} at around 854.3 eV, and $Ni^{\delta+}$ (δ is close to 0) at around 852.6 eV, which is in agreement with the characteristic peaks of Ni_3S_2.[18,33,34] The two peaks at around 859.2 and 877.1 eV represent satellite peaks. However, the binding energy of Ni $2p_{3/2}$ (Ni $2p_{1/2}$) in MoS_2/Ni_3S_2/NF experienced a positive shift to 853.5 eV (871.3 eV), which is related to the charge transfer and electron distribution on the interface of MoS_2/Ni_3S_2 structure through MoS-Ni bond. After P doping, these peaks exhibited a slight negative shift of 0.1 eV (0.2 eV) to 853.4 eV (871.1 eV), respectively, compared to MoS_2/Ni_3S_2/NF (**Figure 5b**).

At the same time, Mo 3d in MoS_2 (**Figure 5c**) could be decomposed into Mo^{4+}, Mo^{6+}, and S 2s. The peaks at ~228.7, 231.6 and 226.0 eV correspond to the Mo^{4+} $3d_{5/2,}$ Mo^{4+} $3d_{3/2}$ and S 2s which are the characteristic peaks of MoS_2. These peaks for MoS_2/Ni_3S_2/NF shifted respectively to 229.0, 231.8 and 226.4 eV compared with pure MoS_2 powder. The shift of these characteristic peak positions of Mo 3d and Ni 2p suggests strong electronic interaction of Mo-S-Ni bonds at the interface of

MoS_2/Ni_3S_2.[32,36] After doping, these peaks in $P_{1.0}$-MoS_2/Ni_3S_2/NF featured a negative shift of 0.4, 0.1, and 0.5 eV, respectively. In the meantime, a doublet at around 227.2 and 230.3 eV ascribed to Mo^{3+} was evident and might be related to P-Mo bonding due to the reduction of the Mo valence by P-doping.[35,37] The doublet peaks of Mo^{6+} at around 232.6~232.8 eV and 235.4~236.0 eV in MoS_2, MoS_2/Ni_3S_2/NF, and $P_{1.0}$-MoS_2/Ni_3S_2/NF is related to oxidation during the preparation or test process.

For the S 2p spectrum of Ni_3S_2/NF (**Figure 5d**), the two characteristic components at 162.7 eV (S $2p_{3/2}$) and 164.0 eV (S $2p_{1/2}$) are ascribed to the S^{2-} states.[38–40] And two-character peaks of S 2p around at 161.5eV and 162.9eV are assigned to MoS_2. The S 2p3/2 (S 2p1/2) features of MoS_2 and Ni_3S_2 are visible at respectively 161.8eV (163.6eV) and 162.8eV (164.5eV) in MoS_2/Ni_3S_2. The S 2p3/2 and S 2p1/2 have a small positive shift of 0.5eV (0.7eV) and 0.1eV (0.5eV) compared with those of MoS_2 and Ni_3S_2 originates most likely from the charge transfer and redistribution between MoS_2 and Ni_3S_2. After P-doping, S 2p3/2 have a positive shift of 0.6 eV and 0.7 eV to 162.4 and 163.5eV, and S 2p1/2 also have a positive shift of 0.6eV and0.7eV to 164.4eV and 165.2eV, confirming that P could tune the charge distribution at the MoS_2/Ni_3S_2 interface [41] and further optimizing the adsorption energy of intermediate product and enhance OER and HER. Further, S 2p1/2 of S-O band merged at a high binding energy of 168.4eV, 168.9 and 169.1 eV in MoS_2, MoS_2/Ni_3S_2/NF and $P_{1.0}$-MoS_2/Ni_3S_2/NF, respectively, caused by partial oxidation during the preparation.

The P 2p characteristic peaks (Figure 3d) at 129.8 eV (2p3/2) and 130.6 eV (2p1/2) could be assigned to P-Mo/P-Ni species, further confirming the successful P-doping in MoS_2/Ni_3S_2/NF [42–45] The peak at 132.6 eV and 131.3 eV corresponds to P-O, which was introduced by the oxidation during the preparation. Meanwhile, the above results could explain that P could optimize the interaction of Ni_3S_2 and MoS_2, thereby

improving the charge transfer and reaction dynamics during the electrocatalytic process.

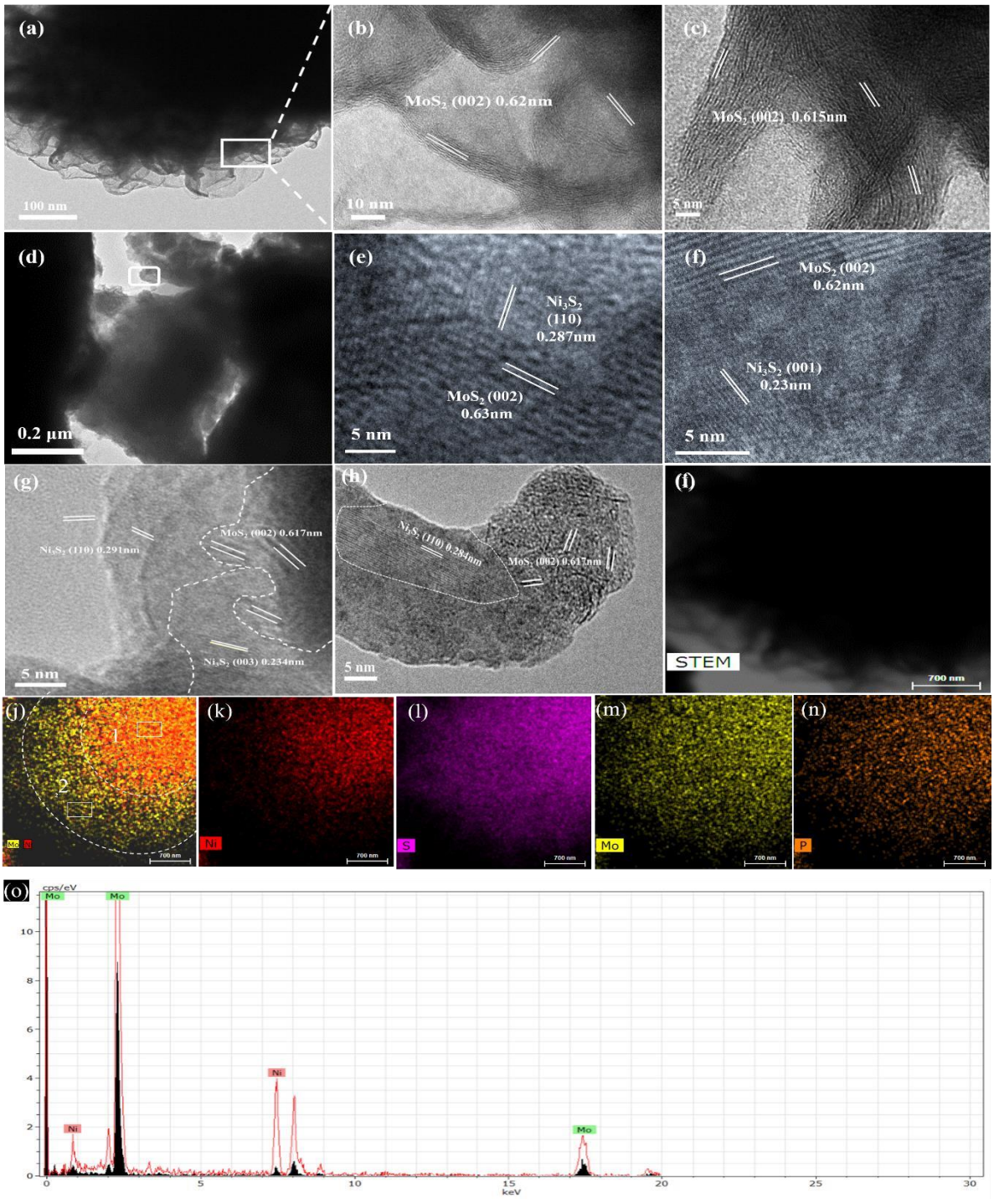

Figure 4. TEM images(a-i); STEM image and the corresponding element mapping of (j) overlap mapping of Ni and Mo, (**k**) Ni, (**l**) S, (**m**) Mo, and (**n**) P of $P_{1.0}$-MoS_2/Ni_3S_2/NF. EDX spectra from areas 1 and 2 in **Figure 4j** are displayed in **Figure 4o**.

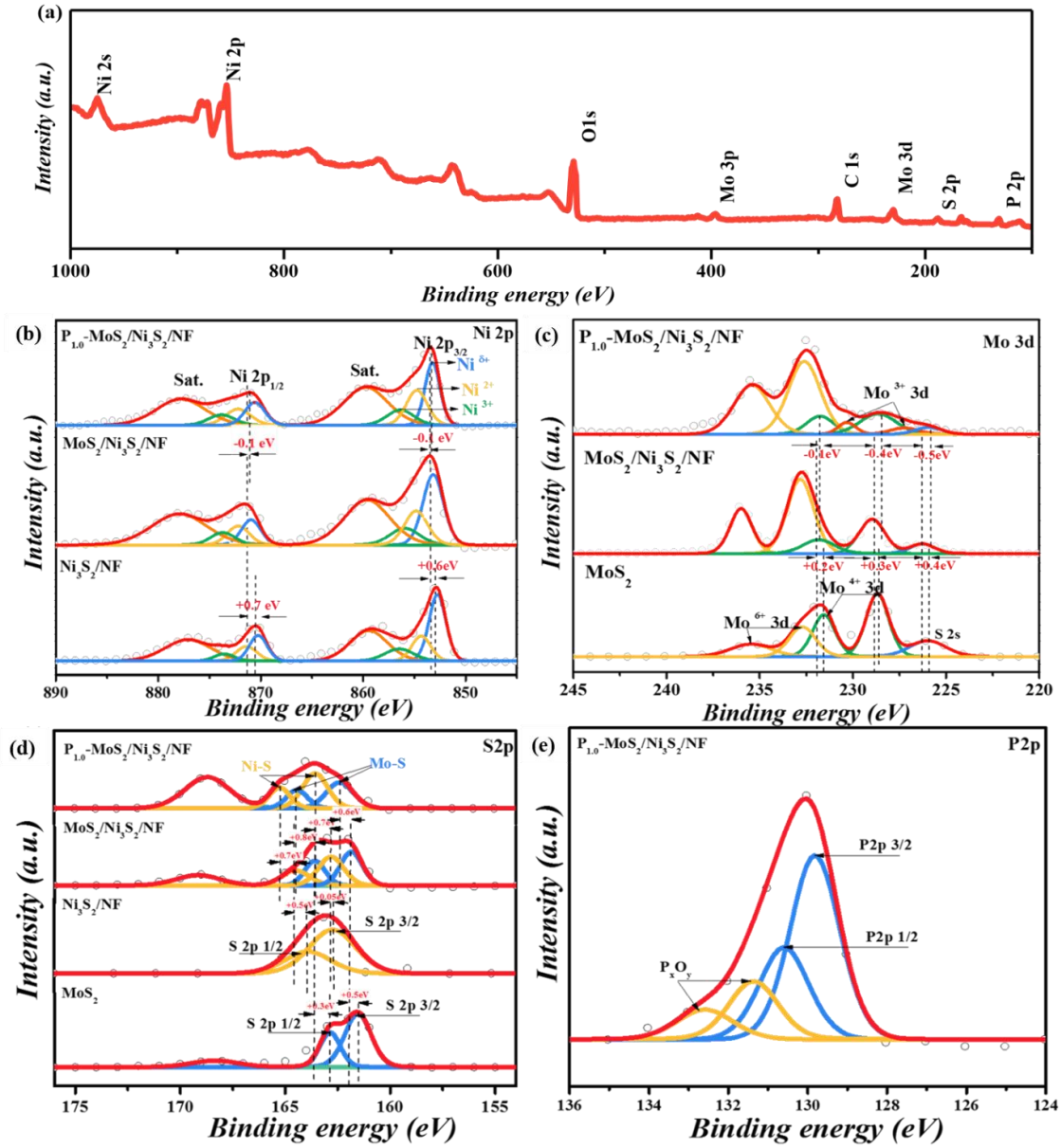

Figure 5. XPS survey spectrum of $P_{1.0}$-MoS_2/Ni_3S_2/NF (a), high-resolution XPS plots of Ni 2p (b); Mo 3d (c); S 2p (d) of Ni_3S_2/NF or MoS_2, MoS_2/Ni_3S_2/NF, and $P_{1.0}$-MoS_2/Ni_3S_2/NF; (e) P 2p high resolution of $P_{1.0}$-MoS_2/Ni_3S_2/NF.

The X-ray diffraction of $P_{1.0}$-MoS_2/Ni_3S_2 powder is shown in **Figure 6a**. It comprises two diffraction peaks at 2θ of 44.5° and 51.8° ascribed to Ni (JCPDS 65-2865) from supporting Ni foam. The peaks at around 21.8°, 31.2°, 37.9°, 38.4°, 49.9°, 50.25°, 54.7°, and 55.3° (2θ) are ascribed to the (101), (110), (003), (021), (113), (211), (104), and (300) planes of Ni_3S_2 (JCPDS 44-1418), which is formed by sulfurization of

NF during the hydrothermal process. But MoS_2 diffraction peaks were not observed due to low crystallization, consistent with HRTEM data.

Raman spectra of $P_{1.0}$-MoS_2/Ni_3S_2/NF, MoS_2/Ni_3S_2/NF, Ni_3S_2/NF and MoS_2 are displayed in **Figure 6b**. The Raman shifts at 285.5, 375.6, and 401.9 cm^{-1} are due to $E_g{}^1$, $E2^1g$, and $A_g{}^1$ Raman vibrations of MoS_2, and the peaks at around 196.0, 220.1, 242.5, 298.9 and 346.1 cm^{-1} are ascribed to Raman modes of Ni_3S_2/NF. In contrast, for MoS_2/Ni_3S_2/NF heterostructures, the Raman bands of Ni_3S_2 shifted to 194.9, 225.4, 251.7, 302.6 and 343.4 cm^{-1}, and the peaks of MoS_2 to 371.8, 401.8 and 445.2 cm^{-1}. The Raman shift could be probably caused by the formation of the MoS_2/Ni_3S_2 interface. The peak at around 358.9 cm^{-1} could also confirm the existence of MoS_2/Ni_3S_2. [46] After P doping, the Raman spectra appeared broadened, which revealed the poor crystallinity and the presence of defects in $P_{1.0}$-MoS_2/Ni_3S_2/NF in **Figure 6b**. Besides, the absence of MoP and NiP peaks in the Raman spectra of $P_{1.0}$-MoS_2/Ni_3S_2/NF proves the P-doping into MoS_2/Ni_3S_2, inferring the replacement of S by P in MoS_2/Ni_3S_2 in agreement with the XPS results. [47]

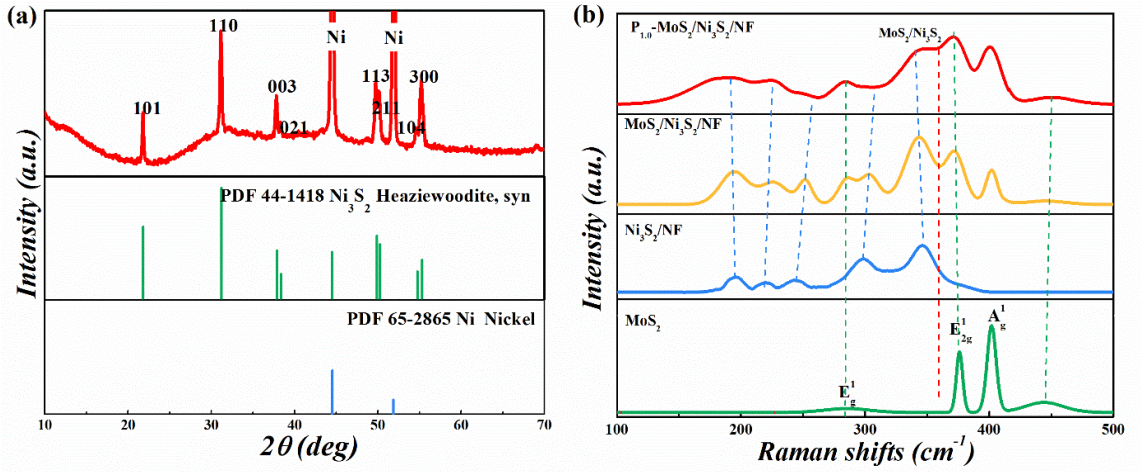

Figure 6. (**a**) XRD pattern of $P_{1.0}$-MoS_2/Ni_3S_2/NF and (**b**) Raman spectra of MoS_2 powder Ni_3S_2/NF, MoS_2/Ni_3S_2/NF, and $P_{1.0}$-MoS_2/Ni_3S_2/NF.

2.3.2 OER Performance of P-doped $MoS_2/Ni_3S_2/NF$

The electrocatalytic OER performance of pure $MoS_2/Ni_3S_2/NF$ and P_x-$MoS_2/Ni_3S_2/NF$ samples (with different P initial concentrations: $P_{0.2}$-$MoS_2/Ni_3S_2/NF$, $P_{0.4}$-$MoS_2/Ni_3S_2/NF$, $P_{0.8}$-$MoS_2/Ni_3S_2/NF$, $P_{1.0}$-$MoS_2/Ni_3S_2/NF$ and $P_{2.0}$-$MoS_2/Ni_3S_2/NF$) were first evaluated in alkaline conditions at 2 mV s^{-1}. Initially, we have acquired linear sweep voltammetry (LSV) and Tafel plots in a standard 3-electrode cell with as-prepared materials acting as working electrode; carbon rod and saturated calomel electrodes served respectively as auxiliary and reference electrodes (**Figure 7 a, b**). **Figure 7c** and **Table 1** summarize the evolution of the overpotential at 100 mA cm^{-2} and Tafel slope values versus the initial P precursor concentration. The OER activity of $P_{1.0}$-$MoS_2/Ni_3S_2/NF$ was improved after P doping, although there was a slight decrease in OER performance at a lower P concentration. Further, $P_{1.0}$-$MoS_2/Ni_3S_2/NF$ owns the lowest energy barrier and the fastest kinetics due to the lowest overpotential (0.449 V) and Tafel slope (34.67 mV dec^{-1}).

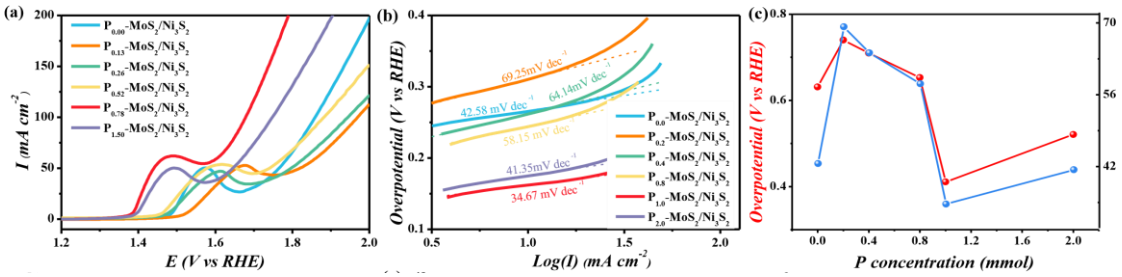

Figure 7. (**a**) LSV curves, (b) Tafel plots, and (c) Overpotential at 100 mA cm^{-2} and Tafel slope values of P_x-$MoS_2/Ni_3S_2/NF$ (x=0, 0.2, 0.4, 0.8, 1.0, and 2.0).

To further understand the influence of phosphorus doping on the catalytic activity, the electrochemical active surface areas (ECSA) of P_x-$MoS_2/Ni_3S_2/NF$ (x=0, 0.4, 0.8, 1, and 2 mM) were calculated using the double-layer capacitance (C_{dl}) values in **Figure 8f** which are obtained from the CV curve in **Figure 8a-e.** The effective ECSA values

of P_x-MoS_2/Ni_3S_2/NF in **Figure 8g** decreased at low P dopant concentration compared with pristine MoS_2/Ni_3S_2, then increased with the formation of nanoflowers and reached the highest peak value of 30.5 cm^2 at a concentration of 1 mM, for which the surface was covered by nanoflowers. Beyond this concentration, the ECSA decreases drastically.

In addition, the electrochemical impedance analysis revealed that $P_{1.0}$-MoS_2/Ni_3S_2/NF provides the smallest impedance resistance of 1.821 Ohm (**Figure 8h** and **Table 2**) compared to other P concentrations, suggesting a high charge transfer rate. Hence, $P_{1.0}$-MoS_2/Ni_3S_2/NF features the highest OER electrochemical activity among the prepared samples using different amounts of P precursor, suggesting that 1.0 mM is the most suitable amount.

To further understand the interface engineering, the OER performance of $P_{1.0}MoS_2$/Ni_3S_2/NF, MoS_2/Ni_3S_2/NF, Ni_3S_2/NF, and MoS_2/NF was also assessed under the same operating conditions. For comparison, the performance of RuO_2/NF and bare NF were also examined. The $P_{1.0}$-MoS_2/Ni_3S_2/NF could reach a current density of 100 mA/cm^2 at a lower potential of 1.679 V in 1M KOH solution, compared with MoS_2/NF (1.775 V), Ni_3S_2/NF (1.809 V), and NF (1.81 V), **Figure 9a**. Although this value is slightly higher than that of RuO_2/NF (1.607 V at 100 mV/cm^2), $P_{1.0}$-MoS_2/Ni_3S_2/NF recorded the smallest Tafel slope (34.67 mV dec^{-1}) compared with RuO_2/NF (54.24 mV dec^{-1}), MoS_2/Ni_3S_2/NF (42.58 mV dec^{-1}), Ni_3S_2/NF (80.11 mV dec^{-1}), MoS_2/NF (132 mV dec^{-1}), and NF (140 mV dec^{-1}), **Figure 9b.** The overpotential (160 mV at 10 mA cm^{-2}) and Tafel slope of $P_{1.0}$-MoS_2/Ni_3S_2/NF are much lower compared to other MoS_2 heterostructure materials and metal oxides or sulfides (**Figure 9c** and **Table 3**). This testifies that P_x-MoS_2 nanosheets covered Ni_3S_2 heterostructure could enhance the kinetics of water oxidation due to the strong interface interaction.

Table 1. Overpotential at 100 mA cm^{-2} and Tafel slope of P_x-MoS_2/Ni_3S_2/NF (x=0, 0.2, 0.4, 0.8, 1.0, and 2.0 mM).

Sample	Overpotential (V) at 100 mA cm^{-2}	Tafel slope ($mV\ dec^{-1}$)
$P_{0.0}$-MoS_2/Ni_3S_2/NF	0.631	42.58
$P_{0.2}$-MoS_2/Ni_3S_2/NF	0.74	69.25
$P_{0.4}$-MoS_2/Ni_3S_2/NF	0.71	64.14
$P_{0.8}$-MoS_2/Ni_3S_2/NF	0.653	58.15
$P_{1.0}$-MoS_2/Ni_3S_2/NF	0.411	34.67
$P_{2.0}$-MoS_2/Ni_3S_2/NF	0.521	41.35

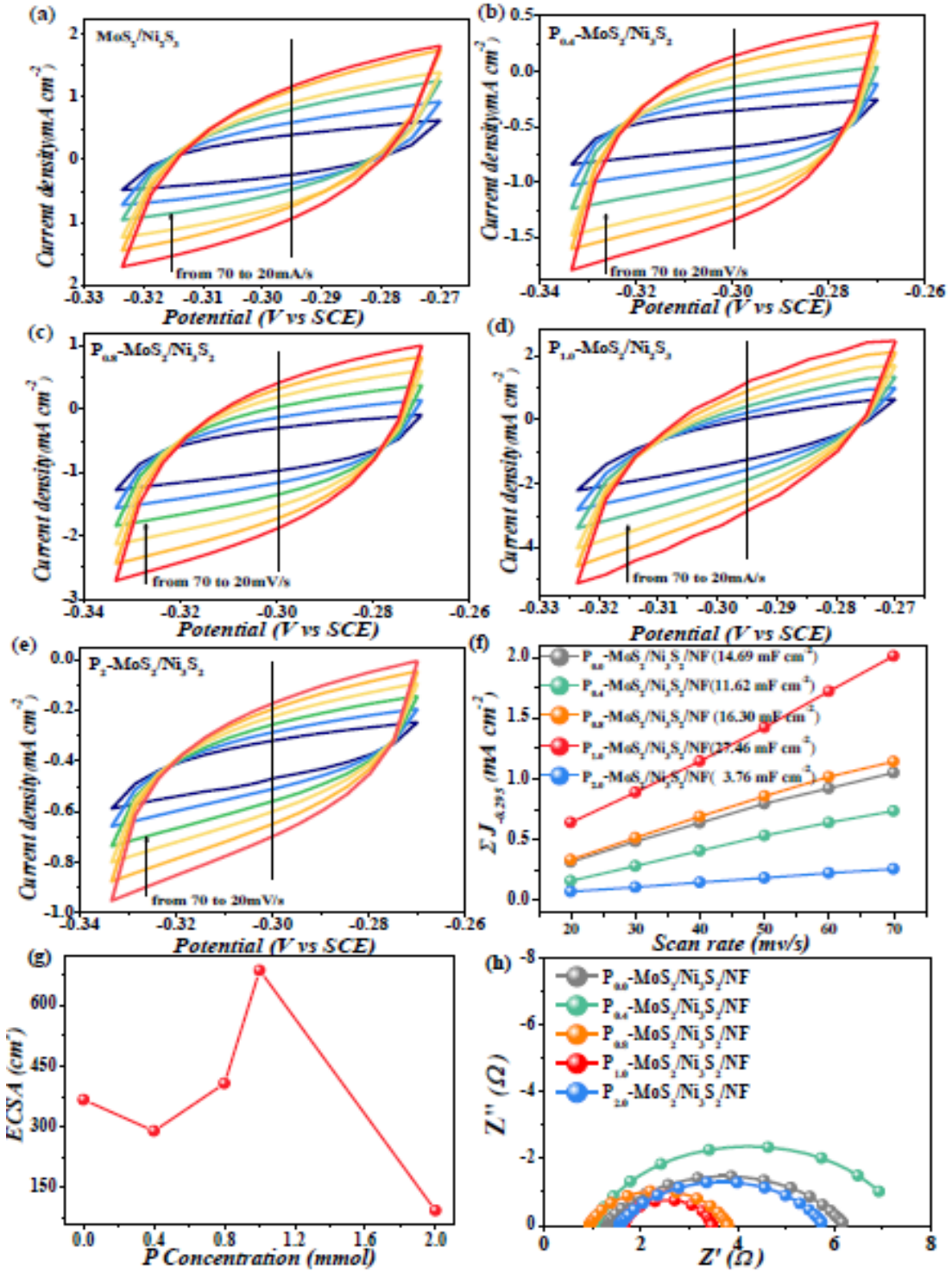

Figure 8. (a-f) CV of P_x-MoS_2/Ni_3S_2/NF (x=0, 0.4, 0.8, 1.0, and 2.0) at different scan rates (20 to 70 mV s^{-1}), (**f**) estimation of C_{dl} by plotting the current density variation versus the scan rate, (**g**) variation of ECSA *versus* the concentration of P precursor, (**h**) electrochemical impedance resistance for P_x-MoS_2/Ni_3S_2/NF (x = 0, 0.4, 0.8, 1.0 and 2.0 mM).

Table 2. The fitting parameters of EIS of NF, MoS_2/NF, Ni_3S_2/MoS_2/NF, and P_x-Ni_3S_2/MoS_2/NF (x= 0.4, 0.8, 1.0 and 2.0 mM).

Name	R_s /Ohm	C_{ct} /mF cm^{-2}	R_{ct} /Ohm
NF	1.092	0.032	80.28
MoS_2/NF	1.188	0.0019	6.493
Ni_3S_2/NF	1.237	0.0042	6.67
NF/RuO_2	1.786	0.2856	1.712
$P_{0.0}$-MoS_2/Ni_3S_2/NF	1.27	0.1131	4.946
$P_{0.4}$-MoS_2/Ni_3S_2/NF	1.026	0.0080	6.416
$P_{0.8}$-MoS_2/Ni_3S_2/NF	1.561	0.1105	4.229
$P_{1.0}$-MoS_2/Ni_3S_2/NF	**1.65**	**0.2401**	**1.821**
$P_{2.0}$-MoS_2/Ni_3S_2/NF	0.95	0.01178	2.853

The ECSA was calculated using C_{dl} values deduced from the CV measurements performed in a non-faradaic region from -0.32 to -0.27V (*vs.* SCE) at different scan rates. From the results in **Figure 10 a-d** and **8d**, the C_{dl} of $P_{1.0}$-MoS_2/Ni_3S_2/NF was estimated as 27.46 mF cm^{-2}, which is close to that of RuO_2/NF (32.69 mF cm^{-2}), and larger than that of MoS_2/Ni_3S_2/NF (14.69 mF cm^{-2}), MoS_2/NF (6.7 mF cm^{-2}), Ni_3S_2/NF (1.2 mF cm^{-2}) and NF (0.9 mF cm^{-2}). The larger C_{dl} value illustrates that $P_{1.0}$-MoS_2/Ni_3S_2/NF possesses more accessible active sites favorable for OER activity. Meanwhile, from the above results, the $P_{1.0}$-MoS_2/Ni_3S_2/NF features more electrochemical active sites, lower charger transfer resistance for OER than other counterparts.

The electrochemical impedance spectroscopy (EIS) was applied to value the surface kinetics of the different heterostructure interfaces. From **Figure 10f** and corresponding fitted parameters solution resistance (R_s), charge transfer resistance (R_{ct}), and double layer capacitance (C_{dl}) listed in **Table 2**, the R_{ct} follows the trend: RuO_2/NF (1.712 Ω) < $P_{1.0}$-MoS_2/Ni_3S_2/NF (1.82 Ω) < MoS_2/Ni_3S_2/NF (4.95 Ω) < MoS_2/NF (6.49

Ω) < Ni_3S_2/NF (6.67 Ω) < NF (80.28 Ω). The smaller R_{ct} value of $P_{1.0}$-MoS_2/Ni_3S_2/NF confirms the fast charge transfer. Meanwhile, the surface interaction between P_x-MoS_2 and P_x-Ni_3S_2 plays a central role in the enhancement of OER performance.

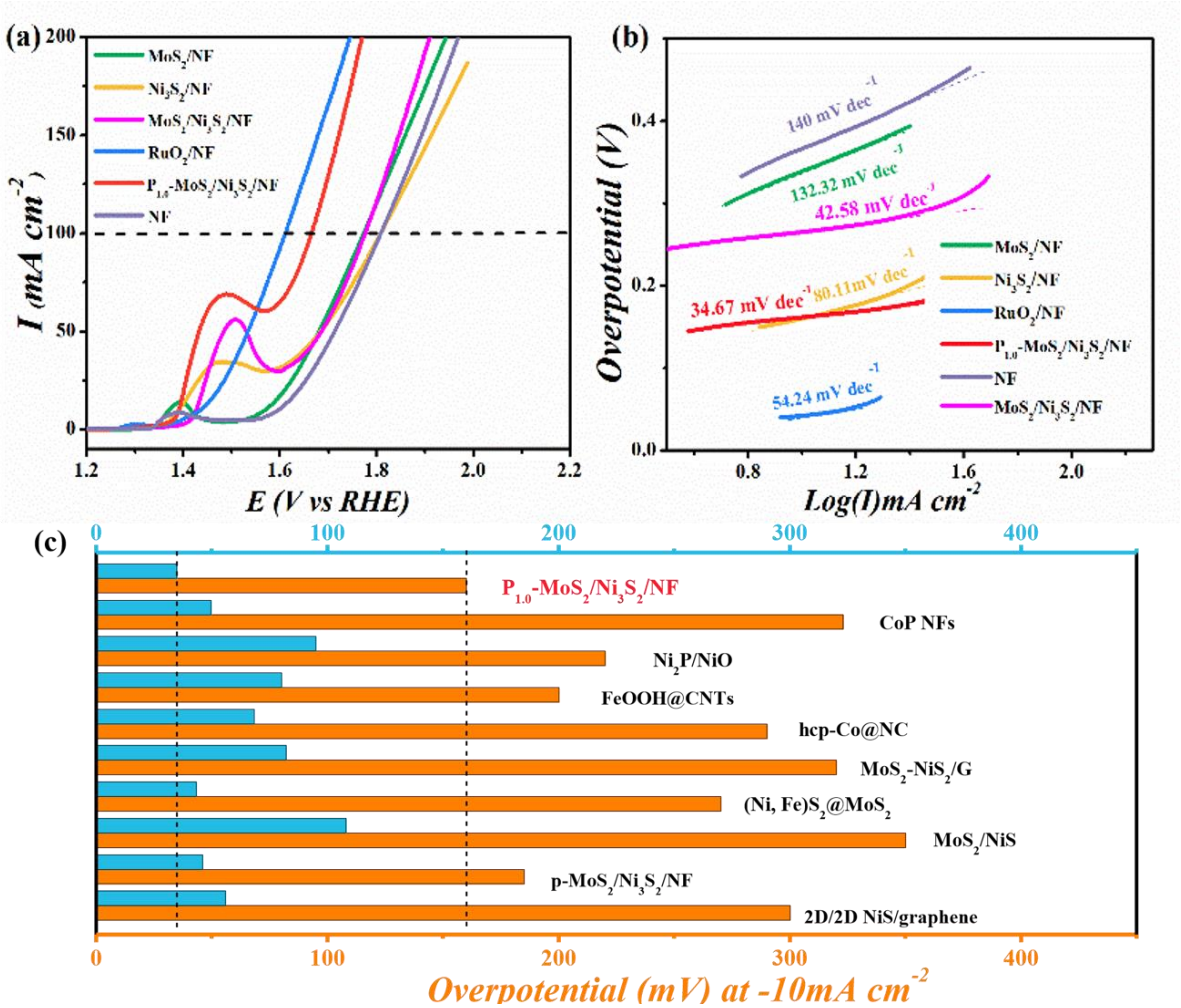

Figure 9. OER performance of MoS_2/NF, Ni_3S_2/NF, RuO_2/NF, MoS_2/Ni_3S_2/NF and $P_{1.0}$-MoS_2/Ni_3S_2/NF in 1M KOH solution: (**a**) OER polarization curves, (**b**) Tafel curves, (**c**) Comparison of the overpotential (at 10 mA cm^{-2}) and the Tafel slope values of recent reports on metal oxide or sulfide electrocatalysts,

Table 3. Comparison of overpotentials and Tafel slopes of $P_{1.0}$-MoS_2/Ni_3S_2/NF with reported bifunctional electrocatalysts for HER and OER in an alkaline medium.

	HER		OER		Ref.
	Overpotential/ mV at -10 mA cm^{-2}	Tafel slope / mV dec^{-1}	Overpotential/ mV at 10 mA cm^{-2}	Tafel slope / mV dec^{-1}	
$P_{1.0}$-MoS_2/Ni_3S_2/NF	53	40.95	160	34.67	This work
MoS_2/Ni_3S_2	110	83	175	68	[12]
2D/2D NiS/graphene	70	50.1	300	55.8	[48]
NiMoS	78	68	260	59	[49]
(Ni, Fe)S_2@MoS_2	130	101.22	270	43.21	[1]
MoS_2–Ni_3S_2 HNRs/NF	98	61	249	57	[23]
MoS_2/NiS_2	62	50.1	278	91.7	[50]
MoS_2/NiS	244	97	350	108	[51]
MoS_2-NiS_2/NGF	172	70	370	-	[52]
MoS_2-NiS_2/G	141	77	320	82	[53]
p-MoS_2/Ni_3S_2/NF	99	71	185	46	[33]
Ni_3S_2/MnS	116	41	228	88	[34]
hcp-Co@NC	90	90.7	290	68.2	[54]
CoIIFe-ONC	284 (-50 mA cm^{-2})	75.8	258	41.7	[55]
FeOOH@CNTs	56	61	200	80	[56]
Ni_2P/NiO	84	114.2	220	94.9	[57]
Ni/NiCoP NHs	90	95	260 (20 mA cm^{-2})	80	[58]
NF-Ni_3S_2/MnO_2	102	69	260	61	[59]
CoP NFs	136	56.2	323	49.6	[60]
($CoFeN_x$ HNAs/NF)	200	66.04	259 (50 mA cm^{-2})	57.6	[61]
NMoNi/SWCNT	130	128	225	54	[62]
p-MoS_2/Ni_3S_2/NF	99	71	185	46	[16]

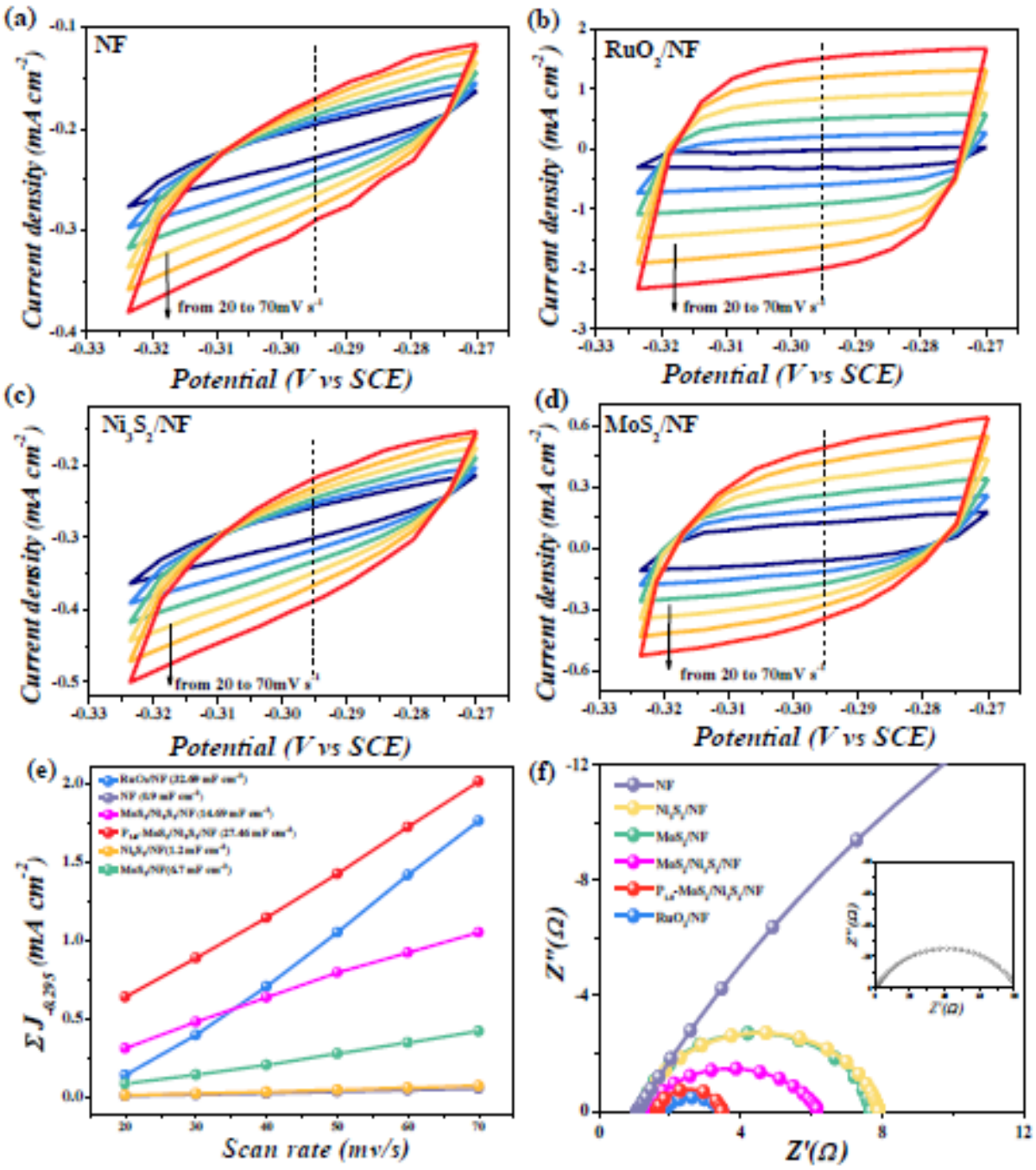

Figure 10 CV of (**a**) NF, (**b**) RuO_2/NF, (**c**) Ni_3S_2/NF and (**d**) MoS_2/NF at different scan rates (20 to 70 mV s^{-1}), (**e**) C_{dl} values determined by plotting the current density $J_{-0.295}$ variation at different scanning rates, and (**f**) Nyquist plots of NF, MoS_2/NF, Ni_3S_2/NF, RuO_2/NF, MoS_2/Ni_3S_2/NF and $P_{1.0}$-MoS_2/Ni_3S_2/NF in 1M KOH solution.

Excellent long-term stability of the $P_{1.0}$-MoS_2/Ni_3S_2/NF was further confirmed by a chronopotentiometry test. $P_{1.0}$-MoS_2/Ni_3S_2/NF exhibited a little change of operating

potential from 1.64V to1.67V for 28 h at a positive current of 80 mA cm^{-2} in 1M KOH solution (**Figure 11a**).

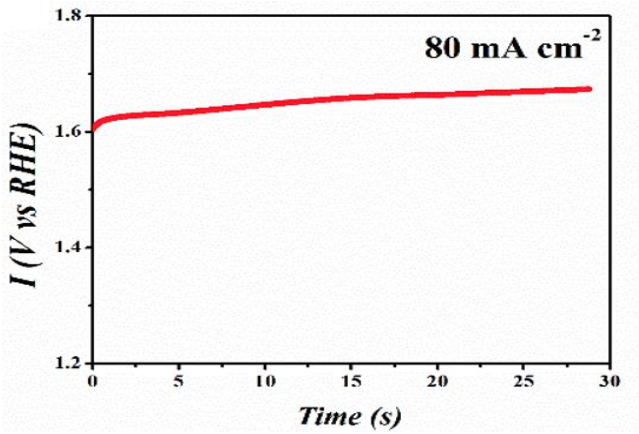

Figure 11 chronopotentiometry test of $P_{1.0}$-MoS_2/Ni_3S_2/NF in 1M KOH solution for 28 hours

SEM and XPS analyses of $P_{1.0}$-MoS_2/Ni_3S_2/NF sample after the 30 h OER test were performed to validate the electrochemical results. From the SEM image acquired after 30 h OER test (**Figure 12**), $P_{1.0}$-MoS_2/Ni_3S_2/NF retained the original nanostructured morphology.

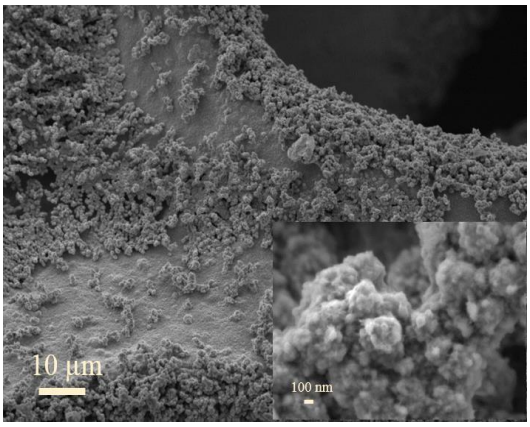

Figure 12. Low and high magnification (inset) SEM images of $P_{1.0}$-MoS_2/Ni_3S_2/NF after 30 h OER test.

Based on the intensity of the characteristic peaks in Figure 13a, the atomic

concentrations of Ni 2p, Mo 3d, S 2p, P 2p and O 1s were summarized in Table 4, from which it is clear that the atomic concentrations of Mo 3d and S 2p decreased from 7.15 and 28.21 at% to 4.13, and 15.96 at%, respectively, indicating the loss of Mo and S during the OER process, while the atomic concentration of O 1s increased from 18.02 to 26.48 at%.

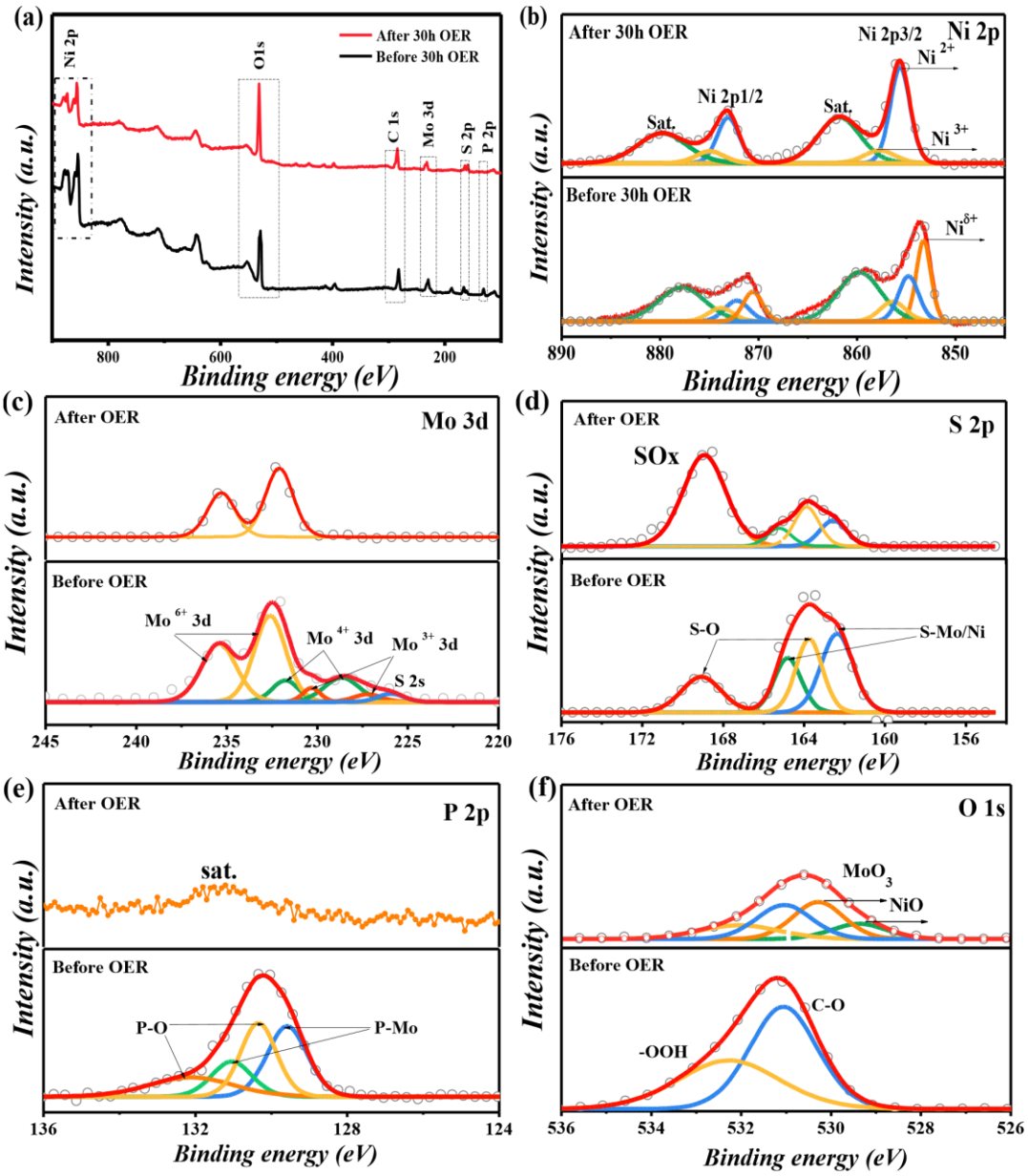

Figure 13. XPS analysis of $P_{1.0}$-MoS_2/Ni_3S_2/NF before and after 30 h OER test in 1M KOH: (a) Survey spectra and (b-f) high-resolution of Ni2p, S2p, P2p Mo3d, and O1s.

The characteristic peaks of $Ni^{\delta+}$ in Ni 2p (**Figure 13b)** at round 852.6 and 870.6 eV disappeared due to the oxidation of $Ni^{\delta+}$ during the OER test. [17] In addition, Mo (**Figure 13c**) was oxidized into a higher valence state (+6). In the meantime, S-O and P-O peaks merged in the S 2p (**Figure 13c**) and P 2p (**Figure 13d**) high-resolution XPS plots, respectively, suggesting the formation of oxides which could enhance OH^- adsorption and decrease the Gibbs free energy of intermediates.[18] The presence of NiO and MoO_3 in O 1s (**Figure 13f**) is consistent with the partial oxidation of Ni_3S_2 and MoS_2 during the OER test. Here, NiO.[63] could decrease the kinetic OER barrier and enhance the OER performance of $P_{1.0}$-MoS_2/Ni_3S_2/NF.

Table 4. Atomic percent (at%) of different elements obtained from XPS spectra of $P_{1.0}$-MoS_2/Ni_3S_2/NF before and after 30 h OER test.

Sample/name	Before (at.%)	After 30 h OER (at.%)
Ni	35.49	34.56
Mo	7.15	4.13 ↓
S	21.81	15.96
P	3.98	3.07 ↓
O	18.02	26.48 ↓
C	13.37	15.81 ↑

2.3.5 HER Performance of P- MoS_2/Ni_3S_2/NF

The behavior of $P_{1.0}$-MoS_2/Ni_3S_2/NF for HER activity was also assessed in alkaline conditions (1M KOH). The HER activities of P_x-MoS_2/Ni_3S_2/NF electrocatalysts with different P precursor amounts were also evaluated (**Figure 14a, b**). Similarly, $P_{1.0}$-MoS_2/Ni_3S_2/NF achieved the highest electrochemical performance among MoS_2/Ni_3S_2/NF and $P_x$$MoS_2$/$Ni_3S_2$/NF (x = 0.2, 0.4, 0.8 and 2 mM) samples.

From **Figure 14c**, a very low potential (0.255 V) was required to obtain 100 mA cm^{-2} compared to MoS_2/NF (0.429 V), Ni_3S_2/NF (0.453 V), and NF (0.490 V), being close to Pt (0.182 V). Meanwhile, the HER kinetics were evaluated by analyzing the Tafel plots (**Figure 14d**). The Tafel plot value of $P_{1.0}MoS_2/Ni_3S_2$/NF (40.95 mV dec^{-1}) is much lower than that recorded for MoS_2/NF (119.38 mV dec^{-1}), Ni_3S_2/NF (136.61 mV dec^{-1}), MoS_2/Ni_3S_2/NF (103.55 mV dec^{-1}), and NF (148.06 mV dec^{-1}). Although there is a small difference with Pt, the HER performance of $P_{1.0}$-MoS_2/Ni_3S_2/NF is so far one of the best among reported metal oxide and sulfide HER catalysts in alkaline solutions (**Figure 14e** and **Tables 3**). The process of HER in alkaline solution could be separated into Volmer water dissociation, Tafel, and Heyrovsky steps,[64] according to the Tafel slope value, as shown in **Table 5**.

Table 5. Mechanism of HER in alkaline solution

Step	Reaction	Tafel slope (mV dev^{-1})
Volmer step-water dissociation	$2H_2O + 2e^- \rightarrow 2H_{ads} + 2OH^-$	120
Tafel step	$2H_{ads} \rightarrow H_2$	40
Heyrovsky step	$H_2O + H_{ads} + e^- \rightarrow H_2 + OH^-$	30

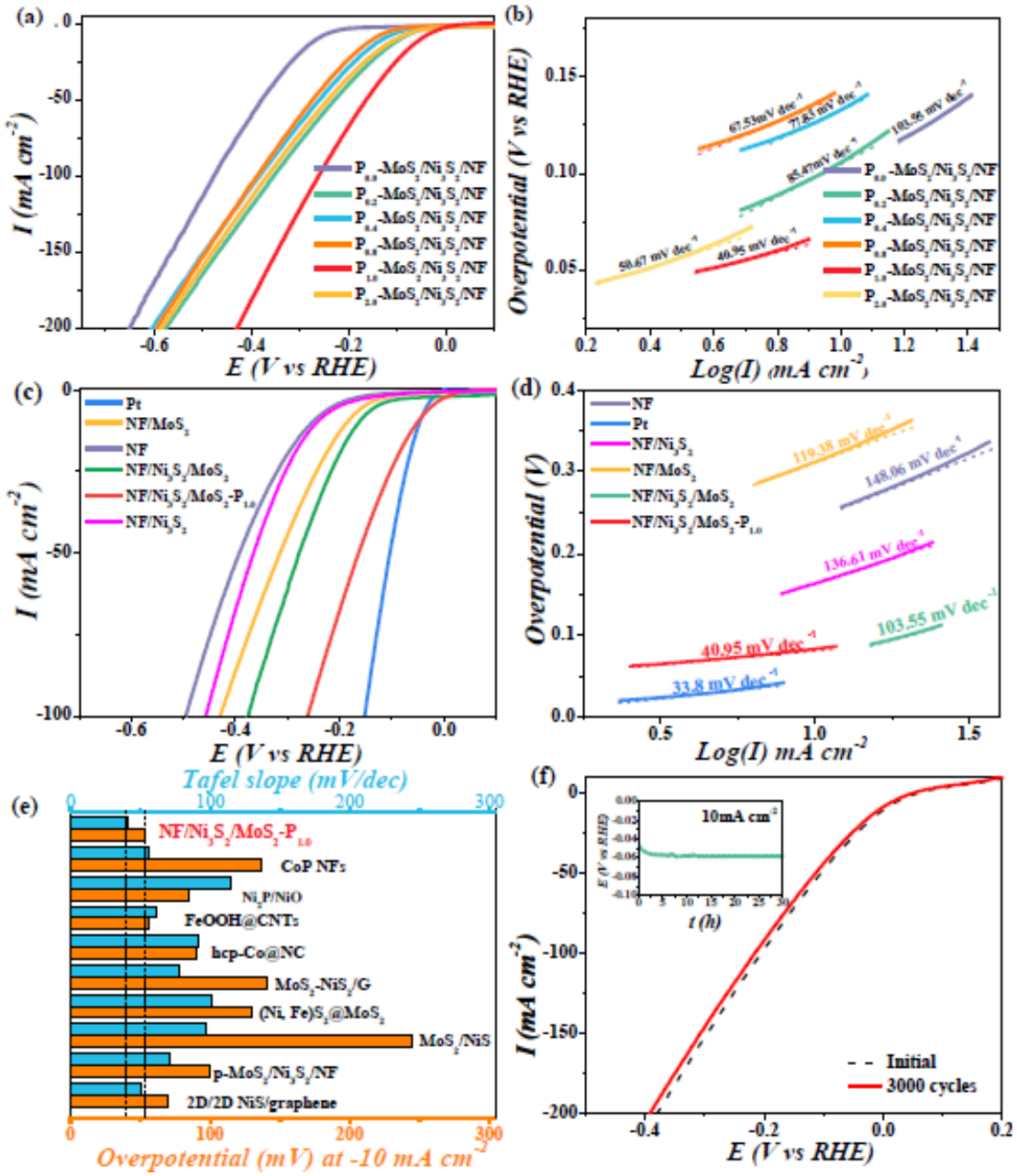

Figure 14. (**a**) CV curves, (**b**) Tafel plots of P_x-MoS_2/Ni_3S_2/NF (x=0, 0.2, 0.4, 0.8, 1.0 and 2.0 mM), (**c**) HER polarization plots, (**d**) Tafel curves of MoS_2/NF, Ni_3S_2/NF,MoS_2/Ni_3S_2/NF, Pt and $P_{1.0}$-MoS_2/Ni_3S_2/NF, (**e**) Comparison of overpotential (at 10 mA cm^{-2}) and Tafel slope values of recent reports on metal oxides or sulfides, and (**f**) LSV curves before and after 3000 CV cycles of $P_{1.0}$-MoS_2/Ni_3S_2/NF, inset is the chronopotentiometry test.

The decrease in the Tafel slope to 40.95 mV dec-1 indicates that the water dissociation process was enhanced due to the P dopant by tuning the surface interaction

between Ni_3S_2 and MoS_2. Besides, the H absorption energy on P atoms is lower than that of S atoms due to lower electronegativity, which helps H2 desorption from the catalyst surface.

2.3.4 Turnover Frequency (TOF) calculation

CV measurements (**Figure 8a-e** and **10a-d**) were used to estimate the number of active sites *n* of the investigated electrocatalysts using the equation (2) [23], as shown in **Table 6**. It is possible to convert the current densities, derived from the HER polarization curve (**Figure 14c**), into TOF values using equation (3). At an overpotential of -150 mV *vs.* RHE, the best performing electrocatalysts, namely $MoS_2/Ni_3S_2/NF_{.0}$-$MoS_2/Ni_3S_2/NF$ generated current densities of 7.7×10^{-3} and 44×10^{-3} A cm^{-2}, respectively. *Q* values of 3.04×10^{-3} and 5.76×10^{-3} C were determined respectively for $MoS_2/Ni_3S_2/NF$ and $P_{1.0}$-$MoS_2/Ni_3S_2/NF$. Introducing the values of *I* and *Q* in equation (3) gave TOF values of 2.53 and 7.64 s^{-1} for respectively $MoS_2/Ni_3S_2/NF$ and $MoS_2/Ni_3S_2/NF$ catalysts. The high TOF value of the $P_{1.0}MoS_2/Ni_3S_2/NF$ electrocatalyst (7.64 s^{-1}) adds another proof for its outstanding catalytic activity. This is also evident from its highest number of active sites (*n*, mol) deduced from **Eq 2.2**, **Table 6**.

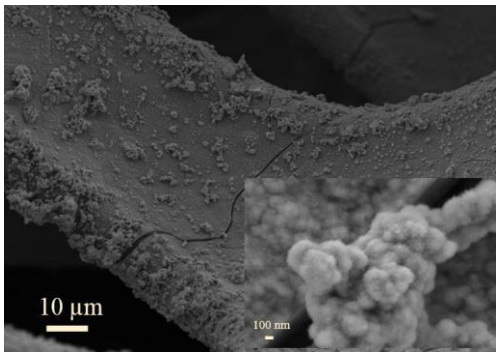

Figure 15. Low- and high-magnification (inset) SEM images of $P_{1.0}$-$MoS_2/Ni_3S_2/NF$ after 30 h HER test.

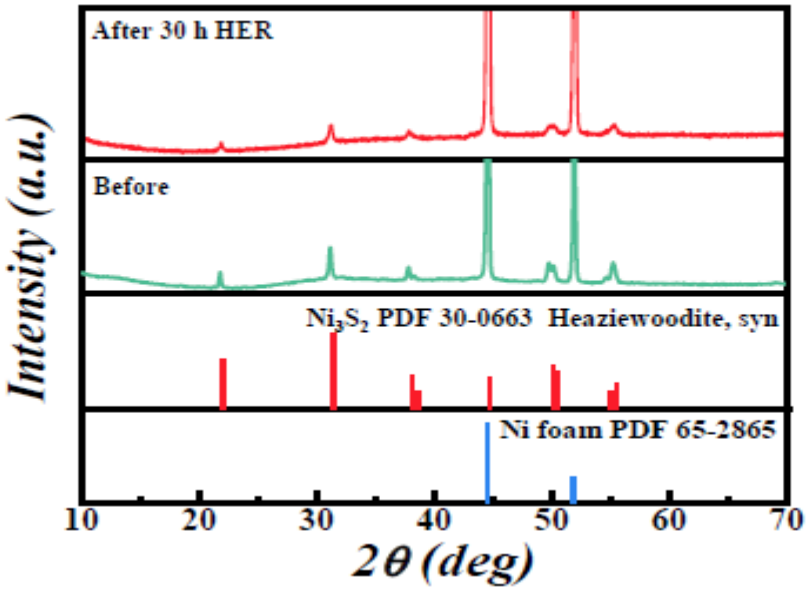

Figure 16. XRD patterns of $P_{1.0}$-MoS_2/Ni_3S_2/NF before and after 30 h HER.

2.3.5 Faradaic efficiency calculations

The Faradaic efficiency (ε %) of the best performing electrocatalyst, namely $P_{1.0}MoS_2$/Ni_3S_2/NF for the HER and OER was also calculated to further confirm its enhanced electrocatalytic activity. $P_{1.0}$-MoS_2/Ni_3S_2/NF recorded a large quantity of H_2 (28.5 μmol h^{-1}) and O_2 (9.9 μmol h^{-1}), as determined by GC, corresponding to ε values of 99.5% and 99.2%, respectively for the HER and OER. These values are very close to those measured for Pt/C (99.8%) and RuO_2 (99.6%), the state-of-the-art electrocatalysts for respectively the HER and OER.

Table 6. Double-layer capacitance (Cdl), electrochemical active surface area (EASA), net voltammetry charge (Q), and the number of active sites (n) estimated for the investigated electrocatalysts from CV measurements.

Material	Cell voltage /V at 10 mA cm^{-2}	Overpotential / mV at 10 mA cm^{-2}	Ref.
$P_{1.0}$-MoS_2/Ni_3S_2/NF	**1.42**	**190**	**This work**
MoS_2/Ni_3S_2	1.56	330	12
2D/2D NiS/graphene	1.55	320	6
NiMoS	1.53	300	49
(Ni, Fe)S_2@MoS_2	1.56	330	1
MoS_2–Ni_3S_2 HNRs/NF	1.5	270	23
MoS_2/NiS_2	1.59	-	50
MoS_2/NiS	1.64	-	51
MoS_2-NiS_2/NGF	1.64	-	52
MoS_2-NiS_2/G	1.58	-	53
p-MoS_2/Ni_3S_2/NF	1.50	-	33
Ni_3S_2/MnS	1.54	310	34
hcp-Co@NC	1.58	-	54
CoIIFe-ONC	1.71	-	55
FeOOH@CNTs	1.46	-	56
Ni_2P/NiO	1.52	-	57
Ni/NiCoP NHs	1.57	340	58
NF-Ni_3S_2/MnO_2	1.52	290	59
CoP NFs	1.65	420	60
($CoFeN_x$ HNAs/NF)	1.59	360	61
NMoNi/SWCNT	1.6 (20 mA cm^{-2})	-	62

2.3.6 Water splitting performance

Since it is of immense importance of developing a bi-functional water-splitting catalyst for commercial needs, $P_{1.0}$-MoS_2/Ni_3S_2/NF was tested for both HER and OER in a corrosion free medium in a two-electrode system. Meanwhile, the state-of-the-art

catalysts Pt plate || RuO_2/NF were tested for comparison. **Figure 17a** shows that the assembled $P_{1.0}MoS_2/Ni_3S_2$/NF || $P_{1.0}$-MoS_2/Ni_3S_2/NF couple could drive the cell at 10 mA cm^{-2} under a cell voltage of 1.433 V, as compared to Pt plate || RuO_2/NF system (1.429 V); this performance overpasses that of so-far reported metal oxides and sulfides (**Figure 17b** and **Table 6**). **Figure 17c** reveals that $P_{1.0}$-MoS_2/Ni_3S_2/NF || $P_{1.0}$-MoS_2/Ni_3S_2/NF system could deliver stable current densities of 20 and 40 mA cm^{-2} at cell voltages of respectively 1.50 and 1.65 V for 60 h, exhibiting high activity and excellent long-term stability.

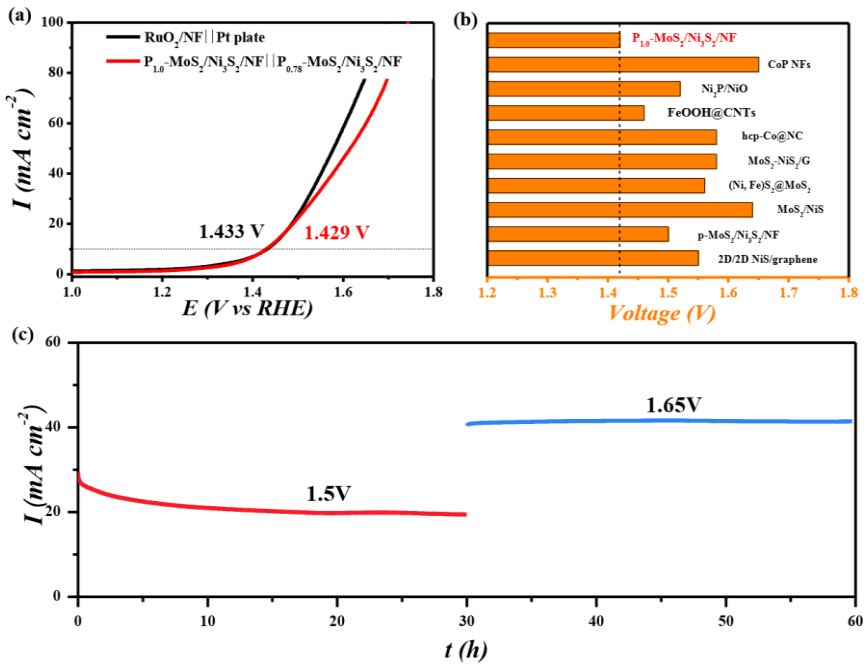

Figure 17. (**a**) Polarization curves of $P_{1.0}$-MoS_2/Ni_3S_2/NF || $P_{1.0}$-MoS_2/Ni_3S_2/NF and Pt plate || RuO_2/NF for overall water splitting. (**b**) Overpotential at 10 mA cm^{-2} of recent reports on metal oxides or sulfides bi-functional water-splitting catalysts. (**c**) Chronoamperometric measurements of overall water splitting in 1M KOH aqueous solution at an applied potential of 1.50 and 1.65 V for 60 h.

Table 7. Comparison of cell voltage and overpotential of $P_{1.0}$-MoS_2/Ni_3S_2/NF with reported bifunctional electrocatalysts for overall water splitting in an alkaline medium.

Material	Cell voltage /V at 10 mA cm^{-2}	Overpotential / mV at 10 mA cm^{-2}	Ref.
$P_{1.0}$-MoS_2/Ni_3S_2/NF	**1.42**	**190**	**This work**
MoS_2/Ni_3S_2	1.56	330	65
2D/2D NiS/graphene	1.55	320	48
NiMoS	1.53	300	49
(Ni, Fe)S_2@MoS_2	1.56	330	1
MoS_2–Ni_3S_2 HNRs/NF	1.5	270	23
MoS_2/NiS_2	1.59	-	50
MoS_2/NiS	1.64	-	51
MoS_2-NiS_2/NGF	1.64	-	52
MoS_2-NiS_2/G	1.58	-	53
p-MoS_2/Ni_3S_2/NF	1.50	-	33
Ni_3S_2/MnS	1.54	310	34
hcp-Co@NC	1.58	-	54
CoIIFe-ONC	1.71	-	55
FeOOH@CNTs	1.46	-	56
Ni_2P/NiO	1.52	-	57
Ni/NiCoP NHs	1.57	340	58
NF-Ni_3S_2/MnO_2	1.52	290	59
CoP NFs	1.65	420	60
($CoFeN_x$ HNAs/NF)	1.59	360	61
NMoNi/SWCNT	1.6 (20 mA cm^{-2})	-	62

2.3.7 Theoretical calculation analysis

For understanding the intrinsic catalytic activity of P_n-MoS_2/Ni_3S_2/NF (n represents the number of S atoms replaced by P), the Gibbs free energies of oxygen-containing intermediates (ΔG_{M^*}) and hydrogen (ΔG_{H^*}) were investigated by density

functional theory (DFT) calculations. During the OER procedure in an alkaline medium, four proton-transfer steps are involved with 3 different adsorption intermediates (OH*, O*, and OOH*), where the asterisk denotes the adsorption sites. According to the HR-TEM image, two-phase composite P_n-MoS_2 (001)/Ni_3S_2 (110) and P_n-MoS_2(001)/Ni_3S_2(001) represents essentially the interface between P_n-MoS_2 and Ni_3S_2, so two theoretical models of P_n-MoS_2/Ni_3S_2 were constructed to assess their synergistic optimization for Gibbs energy for water splitting performance. A series of models P_n-MoS_2 (001)/Ni_3S_2 (001) models (n =2, 4, 6, 8, 10, and 12) with different P-doped atoms based on the precursor used in the experimental synthesis process were constructed. For P_n-MoS_2 (001)/Ni_3S_2 (110) structures (n=1, 2, 3, 4, and 5), the number of P atoms is less than 6 because obvious distortion was found on this heterostructure beyond 6 P atoms. Herein, we calculated ΔG_{M^*}(M = OH, O, and OOH) on the surface of P_n-MoS_2(001)/Ni_3S_2(001) and P_n-MoS_2(001)/Ni_3S_2(110). The calculated theoretical structures are displayed in Figure 18a, b and **Figure 19a, b**. The free energy diagrams are summarized in **Figure 18c-e**, **Figure 19c**.

From the computation results, the heterostructure consisted of P_n-MoS_2 (001)/Ni_3S_2 (110) could not possess water splitting activity. According to our calculations, the intermediate *OOH on P_n-MoS_2 (001)/Ni_3S_2(110) is not stable, leading to *O and *OH formation (**Figure 18a**), and the free energy of the following step is at least 3 eV, which means that a significant quantity of energy is required. As for HER, molecular H_2O almost could not decompose on the interface of P_n-MoS_2 (001)/Ni_3S_2 (110) due to physical adsorption with a larger distance of 2.85Å than 1.85Å between molecular H_2O and active sites P_n-MoS_2 (001)/Ni_3S_2 (001), as shown in **Figure 18 d, e**. As water decomposition is a very important step for HER in alkaline solution, even though H adsorption energy of Pn-MoS_2 (001)/Ni_3S_2 (110) hetero-interface (0.023 eV)

is very close to zero compared with those of P_n-MoS_2(001)/Ni_3S_2 (110) (n=1, 2, 3, 4 and 5). While, for the P_n-MoS_2 (001)/Ni_3S_2 (001) interface, both ΔG(OH*) and ΔG(O*) are negative, indicating a strong interaction between OH, O, and catalysts. For all P_n-MoS_2/Ni_3S_2 catalysts, the formation of the OOH* species is the rate-determine step (RDS), with free energy changing from 1.81 to 0.87 eV.

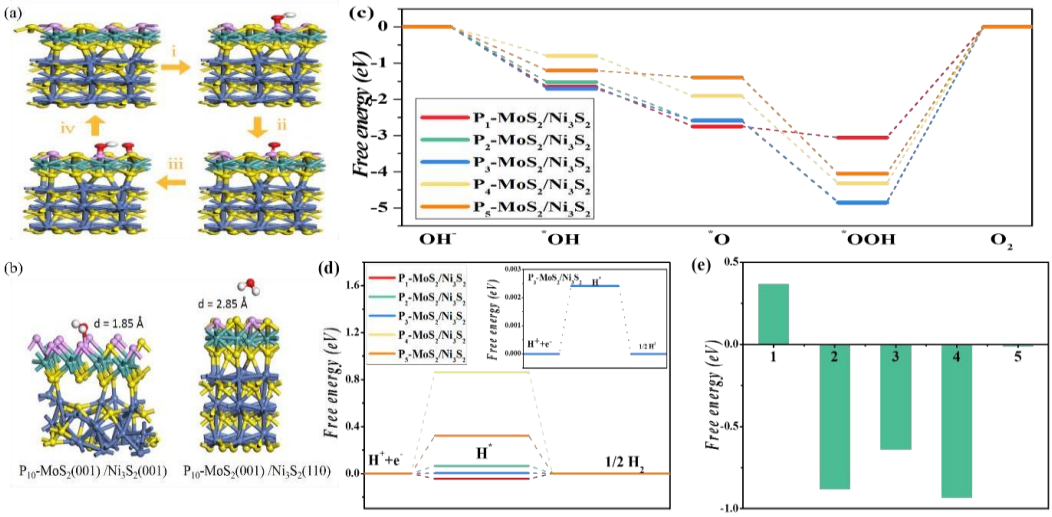

Figure 18 DFT calculation of P_{10}-MoS_2 (001)/Ni_3S_2 (110) heterostructure: (**a-b**) Optimized structure models for the adsorption of *OH, *O and *OOH intermediates under OER, and H* and H_2O under HER in an alkaline media. (**c, d**) Free energy diagrams for OER (U=1.23V) and HER (U=0V); (f) the trend of overpotential for HER and OER. (**e**) H_2O molecular adsorption energy.

After P doping, the free energy and overpotential of MoS_2/Ni_3S_2 increased first, then decreased and reached a minimum at P_{10}, then further increased (Figure 19d, f).The above results manifest that the P-doped MoS_2 (001)/Ni_3S_2 (001) hetero-interfaces could favorably optimize the adsorption energy of OER intermediates and minimize the reaction barrier. Thus, the P doped interface of the P_{10}-MoS_2 (001)/Ni_3S_2 (001) system is the main contributor for the catalytic activity by tuning the electron structure and increasing the active surface area.

In addition, the optimized H* adsorption structures of the catalysts and hydrogen adsorption energy (ΔG_{H^*}) which was determined to examine the catalytic performance for HER, are exhibited in **Figure 19b** and **Figure 19e.** The free energies for HER of P_n-MoS_2 (001)/Ni_3S_2 (001) (x=0, 1, 2, 4, 6, 8, 10 and 12) are calculated for comparison. The absolute values of ΔG_{H*} are decreased upon increasing the P dopant atom number, and reached a minimum at P_{10} with 0.32 eV in **Figure 19e, f**, indicating that the HER process is also kinetically favored on these catalysts. Furthermore, we also evaluated the water adsorption energy according to the optimized adsorption structures of molecular water in **Figure 19g**, which is crucial for water dissociation. From the above DFT calculation results, P doping could favorably modulate the adsorption free energy between H_2O molecule or HER/OER active intermediates and P_{10}-MoS_2/Ni_3S_2. The tuning of the interactions between P_{10}-MoS_2 and Ni_3S_2 could participate to the optimal ΔG_{M^*} for OER, along with favorable ΔG_{H^*} and ΔE_{H2O} provided by the heterointerface effects between P_n-MoS_2 and Ni_3S_2, which synergistically leads to enhanced electrochemical activity for overall water splitting, as confirmed by the experimental results.

Based on the above discussion, the improved electrocatalytic activity of the developed P_xMoS_2/Ni_3S_2/NF heterostructures could be attributed to: i) the specific heterostructure featuring a large surface area and the hierarchical architecture with a large inner cavity which could act as a container for intimate contact with the electrolyte and provide abundant active sites; ii) the P dopant in $MoS_{2-x}P_x$/Ni_3S_2 has optimized electronic structure configuration, as confirmed by XPS data, which could enhance electron transport; iii) the strong electron interaction of the heterogeneous interfaces in $MoS_{2-x}P_x$/Ni_3S_2 could generate abundant electroactive sites and optimize the adsorption free energies of HER/OER active intermediates, favoring water adsorption process, and

ultimately enhancing the whole reaction kinetics.

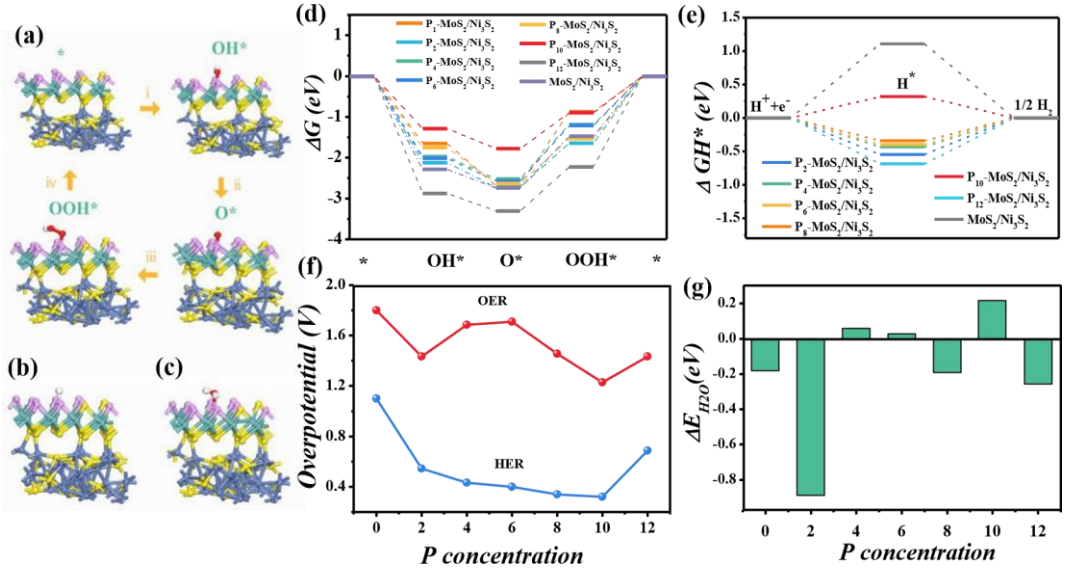

Figure 19. DFT calculation on theP_{10}-MoS_2 (001)/Ni_3S_2 (001) interface: (**a-c**) Optimized structure models for the adsorption of *OH, *O and *OOH intermediates under OER, and H* and H_2O under HER in an alkaline media. (**d, e**) Free energy diagrams for OER (U=1.23V) and HER (U=0V); (f) the trend of overpotential for HER and OER. (**g**) H_2O molecular adsorption energy.

2.3 Conclusion

In summary, we successfully constructed hierarchical $P_{1.0}$-MoS_2/Ni_3S_2/NF heterostructure by facile hydrothermal strategy. Extensive characterization and theoretical calculation results proved the formation of flower-like heterostructure featuring large surface area, optimized electronic configuration and chemisorption energy, abundant heterogeneous interfaces, and abundant electroactive sites. All these favorable features synergistically boosted the HER/OER activity and improved the stability of the electrode material in alkaline conditions. When the $P_{1.0}$-MoS_2/Ni_3S_2/NF electrode was used in a two-electrode alkaline electrolyze system, it could drive current densities of 20 and 40 mA cm^{-2} at ultralow cell voltages of respectively only 1.50 and 1.65 V with good stability for over 60 h. Taken together, the data collected in our work

may open new avenues for rational design of inexpensive and highly-active electrode materials for various electrochemical applications.

References

1. Liu, Y. *et al.* Interface engineering of (Ni, Fe)S_2@MoS_2 heterostructures for synergetic electrochemical water splitting. *Appl. Catal. B Environ.* **247**, 107–114 (2019).

2. Zhang, H., Maijenburg, A. W., Li, X., Schweizer, S. L. & Wehrspohn, R. B. Bifunctional heterostructured transition metal phosphides for efficient electrochemical water splitting. *Adv. Funct. Mater.* **30**, 2003261 (2020).

3. She, Z. W. *et al.* Combining theory and experiment in electrocatalysis: Insights into materials design. *Science.* **355**, 80 (2017).

4. Kou, T. *et al.* Theoretical and experimental insight into the effect of nitrogen doping on hydrogen evolution activity of Ni_3S_2 in alkaline medium. *Adv. Energy Mater.* **8**, 1703538 (2018).

5.Yang, M.-Q., Wang, J., Wu, H. & Ho, G. W. Noble metal-free nanocatalysts with vacancies for electrochemical water splitting. *Small* **14**, 1703323 (2018).

6. Zhang, D., Mou, H., Lu, F., Song, C. & Wang, D. A novel strategy for 2D/2D NiS/graphene heterostructures as efficient bifunctional electrocatalysts for overall water splitting. *Appl. Catal. B Environ.* **254**, 471–478 (2019).

7. Wan, K. *et al.* Hierarchical porous Ni_3S_4 with enriched high-valence Ni sites as a robust electrocatalyst for efficient oxygen evolution reaction. *Adv. Funct. Mater.* **29**, 1900315 (2019).

8. Kang, Z. *et al.* Engineering an earth-abundant element-based bifunctional electrocatalyst for highly efficient and durable overall water splitting. *Adv. Funct. Mater.* **29**, 1807031 (2019).

9. Wang, J. *et al.* Water dissociation kinetic-oriented design of nickel sulfides via tailored dual sites for efficient alkaline hydrogen evolution. *Adv. Funct. Mater.* **31**,

2008578 (2021).

10. Li, Y. *et al.* Facile dynamic synthesis of homodispersed Ni_3S_2 nanosheets as a high-efficient bifunctional electrocatalyst for water splitting. *ChemCatChem* **11**, 1320–1327 (2019).

11. Fei, B. *et al.* Ultrathinning nickel sulfide with modulated electron density for efficient water splitting. *Adv. Energy Mater.* **10**, 2001963 (2020).

12. Zhang, J. *et al.* Interface engineering of MoS_2/Ni_3S_2 heterostructures for highly enhanced electrochemical overall-water-splitting activity. *Angew. Chem* **128**, 6814–6819 (2016).

13. Shit, S. *et al.* Cobalt sulfide/nickel sulfide heterostructure directly grown on nickel foam: an efficient and durable electrocatalyst for overall water splitting application. *ACS Appl. Mater. Interfaces* **10**, 27712–27722 (2018).

14. Zhao, Y. *et al.* Hatted 1T/2H-phase MoS_2 on Ni_3S_2 nanorods for efficient overall water splitting in alkaline media. *Chem. - A Eur. J.* **26**, 2034–2040 (2020).

15. Cao, J., Zhou, J., Zhang, Y., Wang, Y. & Liu, X. Dominating role of aligned MoS_2/Ni_3S_2 nanoarrays supported on three-dimensional Ni foam with hydrophilic interface for highly enhanced hydrogen evolution reaction. *ACS Appl. Mater. Interfaces* **10**, 1752–1760 (2018).

16. Li, F., Zhang, D., Xu, R. C., Fu, W. F. & Lv, X. J. Superhydrophilic Heteroporous MoS_2/Ni_3S_2 for Highly Efficient Electrocatalytic Overall Water Splitting. *ACS Appl. Energy Mater.* **1**, 3929–3936 (2018).

17. Zhang, Y. *et al.* Tremella-like Ni_3S_2/MnS with ultrathin nanosheets and abundant oxygen vacancies directly used for high speed overall water splitting. *Appl. Catal. B Environ.* **257**, 117899 (2019).

18. Luo, X. *et al.* Interface engineering of hierarchical branched Mo-doped Ni_3S_2/Ni_xP_y

hollow heterostructure nanorods for efficient overall water splitting. *Adv. Energy Mater.* **10**, 1903891 (2020).

19. Qin, Y. *et al.* Nitrogen-doped $Ni_2P/Ni_{12}P_5/Ni_3S_2$ three-phase heterostructure arrays with ultrahigh areal capacitance for high-performance asymmetric supercapacitor. *Electrochim. Acta* **393**, 139059 (2021).

20. Lv, X.; Liu, G.; Liu, S.; Chen, W.; Cao, D.; Song, T.; Wang, N.; Zhu, Y. Three-dimensional flower-like Fe, C-doped-MoS_2/Ni_3S_2 heterostructures spheres for accelerating electrocatalytic oxygen and hydrogen evolution. *Crystals* **11**, 340 (2021).

21. Kong, Q. *et al.* Interface engineering of N-doped Ni_3S_2/CoS_2 heterostructures as efficient bifunctional catalysts for overall water splitting. *J. Electroanal. Chem.* **895**, 115516 (2021).

22. Liu, Y. R. *et al.* Ternary CoS_2/MoS_2/RGO electrocatalyst with CoMoS phase for efficient hydrogen evolution. *Appl. Surf. Sci.* **412**, 138–145 (2017).

23.Yang, Y. *et al.* MoS_2–Ni_3S_2 heteronanorods as efficient and stable bifunctional electrocatalysts for overall water splitting. *ACS Catal.* **7**, 2357–2366 (2017).

24. Jiao, S., Fu, X., Wang, S. & Zhao, Y. Perfecting electrocatalysts via imperfections: towards the large-scale deployment of water electrolysis technology. *Energy Environ. Sci.* **14**, 1722–1770 (2021).

25. Guo, P. *et al.* Initiating an efficient electrocatalyst for water splitting via valence configuration of cobalt-iron oxide. *Appl. Catal. B Environ.* **258**, 117968 (2019).

26. Beyene, B. B., Mane, S. B. & Hung, C. H. Highly efficient electrocatalytic hydrogen evolution from neutral aqueous solution by a water-soluble anionic cobalt(II) porphyrin. *Chem. Commun.* **51**, 15067–15070 (2015).

27. Jiao, Y., Zheng, Y., Davey, K. & Qiao, S. Z. Activity origin and catalyst design principles for electrocatalytic hydrogen evolution on heteroatom-doped graphene. *Nat.*

Energy **1**, 16130 (2016).

28. Kresse, G. & Joubert, D. From ultrasoft pseudopotentials to the projector augmented-wave method. *Phys. Rev. B* **59**, 1758 (1999).

29. Blöchl, P. E. Projector augmented-wave method. *Phys. Rev. B* **50**, 17953–17979 (1994).

30. Grimme, S., Antony, J., Ehrlich, S. & Krieg, H. A consistent and accurate ab initio parametrization of density functional dispersion correction (DFT-D) for the 94 elements H-Pu. *J. Chem. Phys.* **132**, 154104 (2010).

31. Nørskov, J. K. *et al.* Trends in the exchange current for hydrogen evolution. *J. Electrochem. Soc.* **152**, J23 (2005).

32. Yang, Y. *et al.* MoS_2–Ni_3S_2 Heteronanorods as Efficient and stable bifunctional electrocatalysts for overall water splitting. *ACS Catal.* **7**, 2357–2366 (2017).

33. Li, F., Zhang, D., Xu, R.-C., Fu, W.-F. & Lv, X.-J. Superhydrophilic heteroporous MoS_2/Ni_3S_2 for highly efficient electrocatalytic overall water splitting. *ACS Appl. Energy Mater.* **1**, 3929–3936 (2018).

34. Zhang, Y. *et al.* Tremella-like Ni_3S_2/MnS with ultrathin nanosheets and abundant oxygen vacancies directly used for high speed overall water splitting. *Appl. Catal. B Environ.* **257**, 117899 (2019).

35. Wang, D., Xie, Y. & Wu, Z. Amorphous phosphorus-doped MoS_2 catalyst for efficient hydrogen evolution reaction. *Nanotechnology* **30**, (2019).

36. Xu, Y. *et al.* Synergism of interface and electronic effects: bifunctional N-doped Ni_3S_2/N-doped MoS_2 hetero-nanowires for efficient electrocatalytic overall water splitting. *Chem. – A Eur. J.* **25**, 16074–16080 (2019).

37. Huang, X. *et al.* Activating basal planes and s-terminated edges of MoS_2 toward more efficient hydrogen evolution. *Adv. Funct. Mater.* **27**, 1604943 (2017).

38. Wang, C.-P. *et al.* Carbon layer coated Ni_3S_2/MoS_2 nanohybrids as efficient bifunctional electrocatalysts for overall water splitting. *ChemElectroChem* **6**, 5603–5609 (2019).

39. Zhu, T., Ding, J., Shao, Q., Qian, Y. & Huang, X. P,Se-codoped MoS_2 nanosheets as accelerated electrocatalysts for hydrogen evolution. *ChemCatChem* **11**, 689–692 (2019).

40. Pang, L. *et al.* CoO promoted the catalytic activity of nitrogen-doped MoS_2 supported on carbon fibers for overall water splitting. *ACS Appl. Mater. Interfaces* **11**, 31889–31898 (2019).

41. Peng, C. *et al.* Effect of surface charge distribution of phosphorus-doped MoS_2 on hydrogen evolution reaction. *ACS Appl. Energy Mater.* **4**, 4887–4896 (2021).

42. Cheng, C. *et al.* Facile preparation of nanosized MoP as cocatalyst coupled with g-C_3N_4 by surface bonding state for enhanced photocatalytic hydrogen production. *Appl. Catal. B Environ.* **265**, 118620 (2020).

43. Jiang, Y., Lu, Y., Lin, J., Wang, X. & Shen, Z. A Hierarchical MoP nanoflake array supported on ni foam: a bifunctional electrocatalyst for overall water splitting. *Small Methods* **2**, 1700369 (2018).

44. Wei, Y. *et al.* Controllable synthesis of P-doped MoS_2 nanopetals decorated N-doped hollow carbon spheres towards enhanced hydrogen evolution. *Electrochim. Acta* **297**, 553–563 (2019).

45. Bian, L. *et al.* Phosphorus-doped MoS_2 nanosheets supported on carbon cloths as efficient hydrogen-generation electrocatalysts. *ChemCatChem* **10**, 1571–1577 (2018).

46. Lv, X. *et al.* Three-dimensional flower-like Fe, C-doped-MoS_2/Ni_3S_2 heterostructures spheres for accelerating electrocatalytic oxygen and hydrogen evolution. *Cryst. 2021, Vol. 11, Page 340* **11**, 340 (2021).

47. Pu, Z., Amiinu, I. S., Liu, X., Wang, M. & Mu, S. Ultrastable nitrogen-doped carbon encapsulating molybdenum phosphide nanoparticles as highly efficient electrocatalyst for hydrogen generation. *Nanoscale* **8**, 17256–17261 (2016).

48. Zhang, D., Mou, H., Lu, F., Song, C. & Wang, D. A novel strategy for 2D/2D NiS/graphene heterostructures as efficient bifunctional electrocatalysts for overall water splitting. *Appl. Catal. B Environ.* **254**, 471–478 (2019).

49. Wang, C., Shao, X., Pan, J., Hu, J. & Xu, X. Redox bifunctional activities with optical gain of Ni_3S_2 nanosheets edged with MoS_2 for overall water splitting. *Appl. Catal. B Environ.* **268**, 118435 (2020).

50. Lin, J. *et al.* Defect-rich heterogeneous MoS_2/NiS_2 nanosheets electrocatalysts for efficient overall water splitting. *Adv. Sci.* **6**, 1900246 (2019).

51. Qin, Q., Chen, L., Wei, T. & Liu, X. MoS_2/NiS yolk–shell microsphere-based electrodes for overall water splitting and asymmetric supercapacitor. *Small* **15**, 1803639 (2019).

52. Kuang, P., He, M., Zou, H., Yu, J. & Fan, K. 0D/3D MoS_2-NiS_2/N-doped graphene foam composite for efficient overall water splitting. *Appl. Catal. B Environ.* **254**, 15–25 (2019).

53. Lonkar, S. P., Pillai, V. V. & Alhassan, S. M. Scalable solid-state synthesis of MoS_2–NiS_2/graphene nanohybrids as bifunctional electrocatalysts for enhanced overall water splitting. *Mater. Adv.* **1**, 794–803 (2020).

54. Li, N. *et al.* Phase-mediated robust interfacial electron-coupling over core-shell Co@carbon towards superior overall water splitting. *Appl. Catal. B Environ.* **266**, 118621 (2020).

55. Guo, P. *et al.* Initiating an efficient electrocatalyst for water splitting via valence configuration of cobalt-iron oxide. *Appl. Catal. B Environ.* **258**, 117968 (2019).

56. Li, H. *et al.* Biomimetic design of ultrathin edge-riched FeOOH@Carbon nanotubes as high-efficiency electrocatalysts for water splitting. *Appl. Catal. B Environ.* **255**, 117755 (2019).

57. Zhang, F. *et al.* A novel nickel-based honeycomb electrode with microtapered holes and abundant multivacancies for highly efficient overall water splitting. *Appl. Catal. B Environ.* **276**, 119141 (2020).

58. Lin, Y. *et al.* Construction of multi-dimensional core/shell Ni/NiCoP nano-heterojunction for efficient electrocatalytic water splitting. *Appl. Catal. B Environ.* **259**, 118039 (2019).

59. Xiong, Y., Xu, L., Jin, C. & Sun, Q. Interface-engineered atomically thin Ni_3S_2/MnO_2 heterogeneous nanoarrays for efficient overall water splitting in alkaline media. *Appl. Catal. B Environ.* **254**, 329–338 (2019).

60. Ji, L., Wang, J., Teng, X., Meyer, T. J. & Chen, Z. CoP Nanoframes as bifunctional electrocatalysts for efficient overall water splitting. *ACS Catal.* **10**, 412–419 (2019).

61. Li, D. *et al.* Holey cobalt–iron nitride nanosheet arrays as high-performance bifunctional electrocatalysts for overall water splitting. *ACS Appl. Mater. Interfaces* **12**, 29253–29263 (2020).

62. Majeed, A. *et al.* Monolayer carbon-encapsulated Mo-doped Ni nanoparticles anchored on single-wall carbon nanotube film for total water splitting. *Appl. Catal. B Environ.* **269**, 118823 (2020).

63. Zhang, J. *et al.* 3D coral-like Ni_3S_2 on Ni foam as a bifunctional electrocatalyst for overall water splitting. *ACS Appl. Mater. Interfaces* **10**, 31330–31339 (2018).

64. Feng, J.X., Wu, J.-Q., Tong, Y.-X. & Li, G.-R. Correction to "Efficient hydrogen evolution on cu nanodots-decorated Ni_3S_2 Nanotubes by optimizing atomic hydrogen adsorption and desorption". *J. Am. Chem. Soc.* **141**, 13697 (2019).

65. Zhang, J. *et al.* Interface engineering of MoS_2/Ni_3S_2 heterostructures for highly enhanced electrochemical overall-water-splitting activity. *Angew. Chemie Int. Ed.* **55**, 6702–6707 (2016).

Chapter 3

Dual-Functional N Dopants in MoS_2/rGO Heterostructure - toward Efficient and Durable Water Splitting

3.1 Introduction

Hydrogen has attracted huge attention as a candidate for a sustainable and green energy, owing to its high energy density and contamination-free features. Water electrolysis has been recognized as a highly promising way to realize the scalable hydrogen production, sparking a search for electrocatalysts featuring high activity and excellent stability for water splitting. [1–3]

Water splitting reaction comprises two half reactions, namely, hydrogen evolution reaction (HER) and oxygen evolution reaction (OER). Up to now, extensive research focused on developing HER catalysts that could operate in strongly acidic conditions and OER catalysts that could work in strongly alkaline conditions, due to thermodynamic barrier and potential application in proton-exchange membranes.[4] Transition metal sulfides, [5–7] phosphides, [8,9] and carbides [10,11] have proven comparable catalytic activity and stability with noble metal based catalysts for HER in strong acidic electrolytes. On the other hand, Ni, Fe, Co, Mn and Cu oxide- or hydroxide-based materials are effective catalysts for OER in alkaline aqueous solution. The general research trend in electrocatalysis field is the integration of the overall reaction into one single device, as it could decrease the overall cost by reducing the preparation process duration of the whole water splitting device.

For the last decade, MoS_2 was recognized as a promising HER candidate for noble metal-based catalysts in acid environment, because of its low adsorption energy of

intermediate H*. In contrast, pristine MoS_2 owns a poor performance (an overpotential larger than 200 mV at 10 mA cm^{-2}) in alkaline solution due to the instability and unsuitable orbital orientation, which reduces the adsorption and dissociation of water molecules. Thus, considerable efforts have been pursued with the aim to decreasing the kinetic energy barrier of water dissociation and facilitating the desorption of the OH^- formed on active sites, including dopant metal anions (Ni, Co and Fe). [12–15]

Unfortunately, it is difficult to insert large metal atoms into MoS_2 and, at the same time, metal dopants in MoS_2 basal plane could destroy the stable MoS_2 structures by promoting the formation of terrace sites or MoS_3 phase.[16] From above reasons, one possible way to address this limitation is through introduction of nonmetal atoms (N, P, C and O) into MoS_2 matrix because of their smaller size, especially N atoms, which could increase the number of exposed active sites and improve the conductivity. Qing et al. found that 2H-MoS_2/N-doped mesoporous graphene with interfacial Mo−pyridinic N coordination was able to improve the HER activity of S edges in MoS_2 over a large pH range.[17] The OER performance of two-dimensional (2D) transition-metal dichalcogenides (TMDs) have been investigated and the S edges were proved to be the active sites. [18,19] Based on this assumption, Mohanty et al. found that MoS_2 quantum dots required only 370 mV to deliver a current density of 10 mA cm^{-2}.[20] While the OER activity of the N-doped MoS_2 has not been reported so far.

Herein, we aim to construct a unique nitrogen-doped MoS_2/N-doped reduced graphene oxide (N-MoS_2/N-rGO) heterostructure by a one-step hydrothermal method and assess its electrochemical performance for water splitting. The N-MoS_2 nanoflowers, generated on the surface of N-rGO, contain plentiful of active catalytic sites for excellent electrochemical catalytic properties, while the internal N-rGO as conductive support guarantees rapid charge transfer and decrease the stacking of MoS_2

nanosheets. The impact of N dopant is not only enhancing the conductivity of MoS_2 and rGO to ensure excellent electronic transfer, but also increasing the d spacing between MoS_2 layers to increase the number of exposed active sites, and also optimize the electron distribution around S and Mo atoms enhancing the initial catalytic activity and reactivity of MoS_2.

3.2. Experimental section

3.2.1. Synthesis of N-doped MoS_2/N-doped rGO catalysts

N-doped MoS_2/N-doped RGO (N-MoS_2/N-rGO) catalyst was synthesized by a one-step hydrothermal method. [21] A GO solution was prepared by dispersing 50 mg of GO into 20 mL of pure water followed by magnetic stirring and sonication until formation of a uniform dispersion. In a second container, Mo, S, and N precursors' solution was prepared by adding thioacetamide (0.30 g), ammonium molybdate tetrahydrate (0.49 g) and dicyanamide (0.50 g) into 20 mL of water. Then, these two solutions were mixed and plced into a 50 mL Teflon autoclave and maintained at 180°C for 24 h. After that, the formed sample was washed with water and ethanol for several times before placing into the fridge for overnight, and the frozen sample was freeze-dried at -84°C for 72 h. In order to study the effects of N content on the activity and morphology of MoS_2/rGO, other samples were prepared by adjusting the dosage of dicyanamide to 0.25 and 0.75 g. The resulting N-MoS_2/N-rGO materials were labeled as N-MoS_2/N-rGO-1, N-MoS_2/N-rGO-2 and N-MoS_2/N-rGO-3, according to the initial dicyandiamide content (0.25, 0.50 and 0.75 g, respectively).

Pure MoS_2 was prepared under similar experimental conditions in absence of GO and dicyanamide. Thioacetamide (0.30 g) was disovled in 40 mL of Milli-Q water and ammonium molybdate tetrahydrate (0.49 g) was added under magnetic stirring at room

temperature. Then, the resulting solution was placed into a 50 mL autoclave and heated at 180 °C for 24 h. After that, the formed sample was washed with water and ethanol for several times before placing it into the fridge for overnight, and the frozen sample was freeze-dried at -84°C for 72 h.

N-MoS_2 were obtained by mixing Mo (0.49g ammonium molybdate tetrahydrate), S (0.3g thioacetamide), and N (0.5g dicyanamide) precursors in 20 mL aqueous solution prior to magnetic stirring and sonication. Then, the mixture was placed into 50 mL autoclave and maintained at180 °C for 24 h. After that, the formed sample was washed with water and ethanol for several times before freeze-drying at -84°C for 72 h.

N-rGO was also prepared through a similar way. 20 mL of GO (50 mg) aqueous solution was sonicated until formation of a uniform dispersion. 20 mL of dicyanamide (0.5 g) were stirred for 30 min. Then, both of these solutions were placed into a 50 mL autoclave and maintained at 180 °C for 24 h. After that, the formed sample was washed with water and ethanol for several times before freeze-drying at -84°C for 72 h.

MoS_2/rGO was obtained in absence of dicyanamide using the same experimental conditions. 20 mL of GO (50 mg) aqueous solution was sonicated until formation of a uniform dispersion. A mixture of 20 mL of thioacetamide (0.30 g) and ammonium molybdate tetrahydrate (0.49 g) aqueous solution was stirred for 30 min. Then, both solutions were placed into a 50 mL autoclave and heated at 180 °C for 24 h. After that, the formed sample was washed with water and ethanol for several times, stored in the fridge for overnight, and the frozen sample was freeze-dried at -84°C for 72 h.

3.2.2. Electrochemical measurements

The electrochemical tests, including cyclic voltammetry (CV) and electrochemical impedance spectroscopy (EIS), were performed on a ModuLab-MTS electrochemical test station (Solartron, France) using a standard three electrodes system with the

prepared catalyst acting as the working electrode, Ag/AgCl (0.197 V *vs.* RHE) as the reference electrode, and graphite as the counter electrode. All measurements were recorded in 30 mL of 0.5 M sulfuric acid (H_2SO_4) electrolyte. All catalyst samples were prepared by dispersing 4 mg of the synthesized materials under sonication in an ethanol solution (V_{water}: $V_{ethanol}$ = 4:1) of Nafion (80 µL) to produce a homogeneous ink. 5 µL of ink was dropped onto a glassy carbon electrode (GCE) before drying at room temperature. Linear sweep voltammetry (LSV) and cyclic voltammetry curves were acquired at a scanning rate of 2 mV s^{-1} and 100 mV s^{-1}, respectively. The potential of the working electrode (WE) was measured *versus* the Ag/AgCl reference electrode, and was converted to the reversible hydrogen electrode (RHE)'s scale employing the formula ($E_{RHE} = E_{Ag/AgCl}$ + 0.059 pH + +0.197).

The electrochemical impedance spectroscopy (EIS) tests were performed in a frequency range (100000 - 0.01 Hz) with an AC potential of 10 mV. All the results were simulated based on the equivalent circuit shown in **Figure 1**.

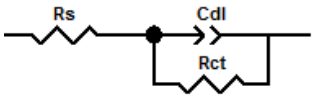

Figure 1. The equivalent circuit model for EIS.

Where R_s, C_{dl} and R_{ct} represent solution resistance, double layer capacity, and reaction resistance, respectively. Here, constant Phase Angle Element (CPE) is employed to replace double layer capacity due to the unperfected Nyquist plot caused by the unsmooth surface of the catalyst.

In order to calculate the capacitance (C_{dl}), cyclic voltammetry measurements were conducted in a narrow potential window (-0.1 to +0.1 V *vs.* Ag/AgCl) at various scanning rates (20 to 100 mV s^{-1}).

The cycling stability was assessed at a scanning rate of 100 mV s^{-1} for 3000 cycles. For the durability, chronopotentiometry was conducted at a geometric current density of 10 mA cm^{-2} for at least 14 h.

Faradaic efficiency: both HER and OER Faradaic efficiencies of the investigated catalysts were assessed by quantifying the quantity of the released gas through gas chromatography during the applied CA measurements (the catalyst is held at -1.0 V *vs.* RHE for 1 h in 0.5 M H_2SO_4 or 1.0 M KOH solutions at 25 ^oC). Measurements were conducted in a two-compartment bulk electrolysis cell with standard configuration. The cell consists of three electrodes: a working electrode, a counter electrode (a graphite rod, Sigma-Aldrich, 99.999%) and a reference electrode (either Ag/AgCl or Hg/HgO, NaOH (0.1 M); the former is used for the electrolysis in acidic medium, while the latter is employed for the electrolysis in alkaline medium). The measured quantity of the gas is then divided by the amount of the gas calculated from the charge passed through the WE during CA (assuming 100% Faradaic efficiency). Gas chromatography (GC) was performed with a pneumatically operated automatic gas sampling valve on an Agilent 7890A gas chromatograph to monitor the liberated gas. The electrolysis cell was linked to the GC setup by means of custom-made airtight glass-to-metal adapters and 1/8 in internal diameter copper tubing. The oven temperature was set at 45 °C, and Ar with a flow rate of roughly 3 mL min^{-1} was the carrier gas.

3.3. Results and discussion

3.3.1. Materials characterization

One-step hydrothermal method was employed for simultaneous N-doping and growth of MoS_2 nanoflowers on N-doped rGO nanosheets to produce N-MoS_2/N-rGO, as reported in our previous work[21], as schematically depicted in **Figure 1a**.

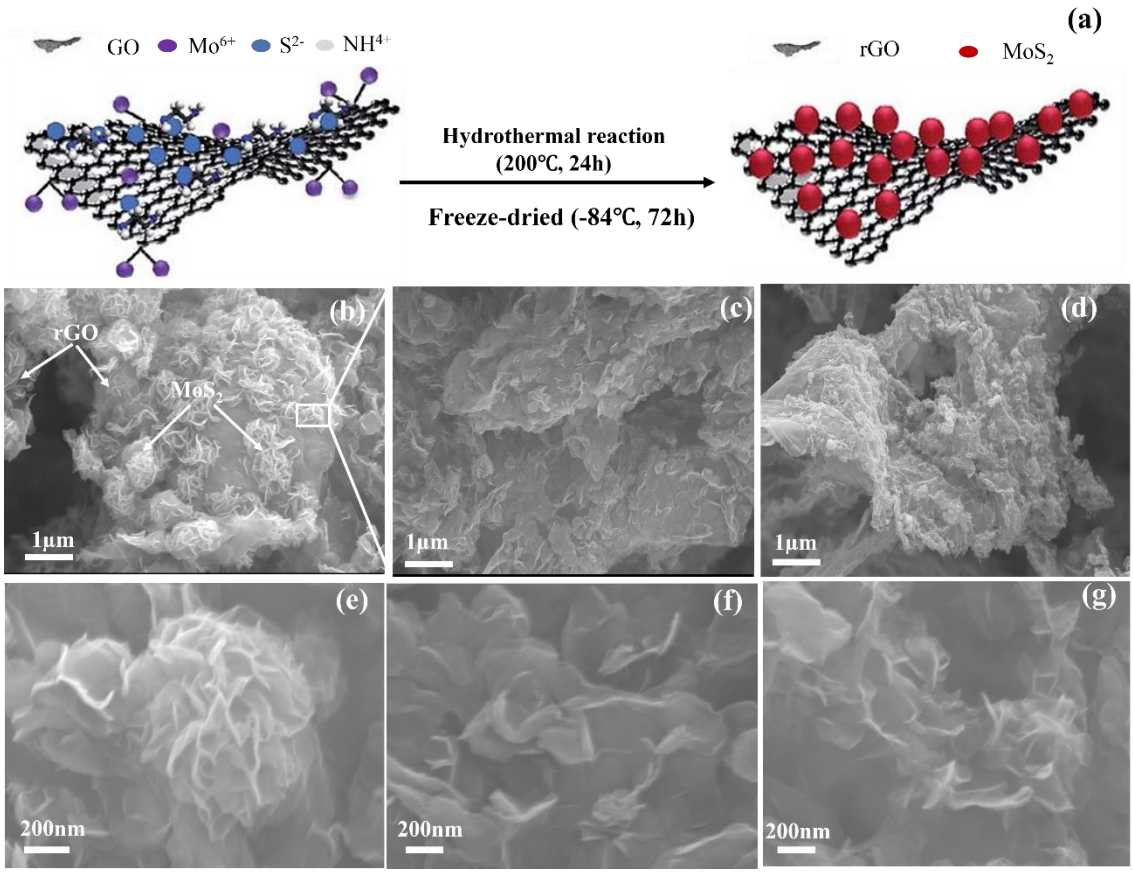

Figure 1. (**a**) Schematic illustration of the preparation of N-MoS_2/N-rGO. SEM images at different magnifications of (**b, e**) N-MoS_2/N-rGO-2, (**c, f**) N-MoS_2/N-rGO-1 and (**d, g**) N-MoS_2/N-rGO-3.

The morphology of N-MoS_2/N-rGO for three different dicyanamide (N precursor) dosages (0.25, 0.50 and 0.75 g) was characterized by scanning electron microscopy (SEM), **Figure 1b-g**. The SEM images of N-MoS_2/N-rGO-1 sample (prepared using 0.25 g of dicyanamide) in **Figure 1 c, f** reveals rGO sheets covered with MoS_2 nanosheets with a size of 300-500 nm. Here, rGO sheets play a role as a support material, which could increase conductivity and large surface area, and at the same time limiting MoS_2 nanosheets agglomeration, both of which restrict the catalytic efficiency of bulk MoS_2 as an electrocatalyst.[1] Upon increasing the dicyanamide precursor concentration (**Figure 1b** and **e**), MoS_2 nanoflowers composed of smaller size nanosheets (100 nm)

are clearly formed on rGO sheets. According to previous reports, this N-MoS_2/N-rGO-2 hierarchical structure MoS_2 nanosheets could not just expose more edge sites, but also improve the electrons transport ability to conductivity supports, enhancing the HER and OER activities. [22,23] Further increase of the dicyanamide content to 0.75 g led to the disappearance of the MoS_2 nanoflower structure, as seen in **Figure 1 d, g**.

As discussed in the next section, N-MoS_2/N-rGO-2 exhibited the best electrochemical activity. Therefore, this sample was characterized in more details.

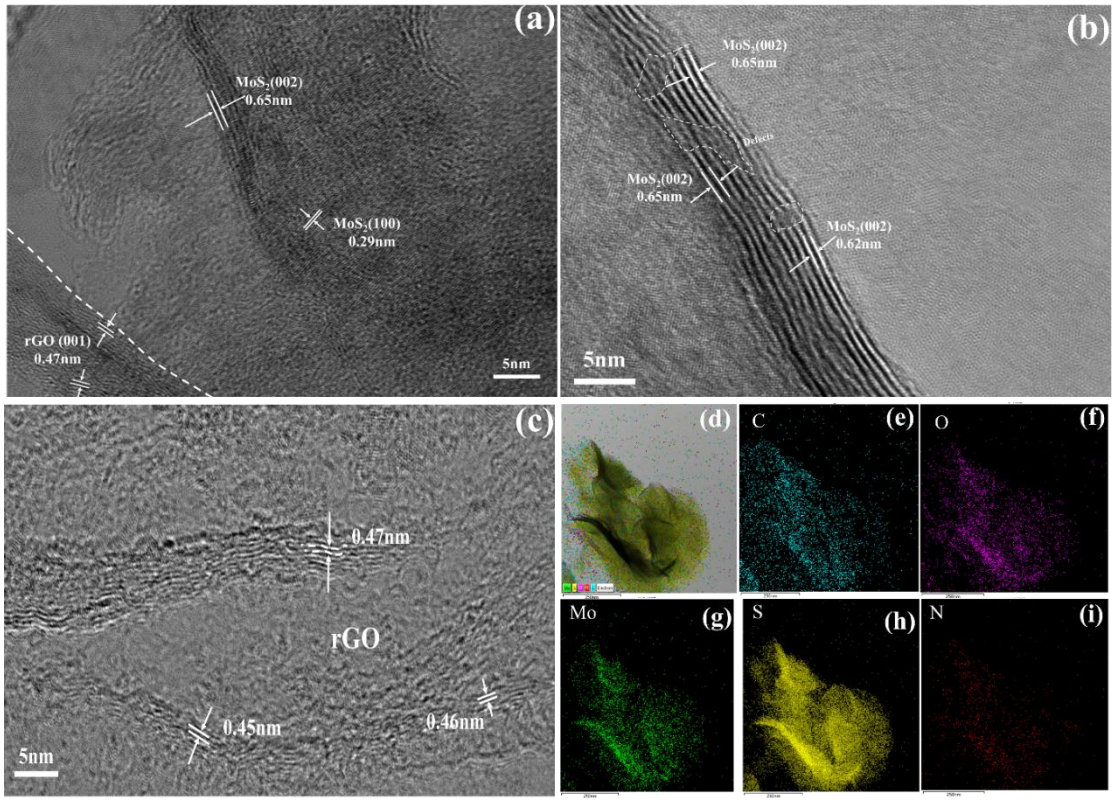

Figure 2. (a-c) High resolution TEM images and (d) STEM image and the corresponding element mapping of (e) C, (f) O, (g) Mo, (h) S, and (i) N of N-MoS2/N-rGO-2.

Additionally, two types of lattice or Moiré fringes were observed in the bright field TEM image of N-MoS_2/N-rGO-2 in **Figure 2a-c**, corresponding to MoS_2 with two fringes of 0.65 and 0.67 nm assigned to (002) crystal face and rGO with fringes of 0.35

and 0.37 nm.[24] Moreover, the energy dispersive X-ray spectroscopy (EDX) mapping in **Figure 2d-i** demonstrates that the N-MoS_2/N-rGO-2 comprises the expected C, N, S, Mo, and O elements. In addition, the N element (**Figure 1k)** was homogeneously distributed over the MoS_2 and rGO sheets, suggesting that N is successfully introduced into MoS_2/rGO by using dicyandiamide as N source.

As displayed in the XRD patterns (**Figure 3**), pure MoS_2 prepared by the same process in absence of GO and dicyanamide mainly shows peaks at around 14.1°, 33.1°, 36.3°, and 58.2° assigned respectively to the (002), (101), (102), and (110) diffraction planes (JCPDS no. 37-1492).

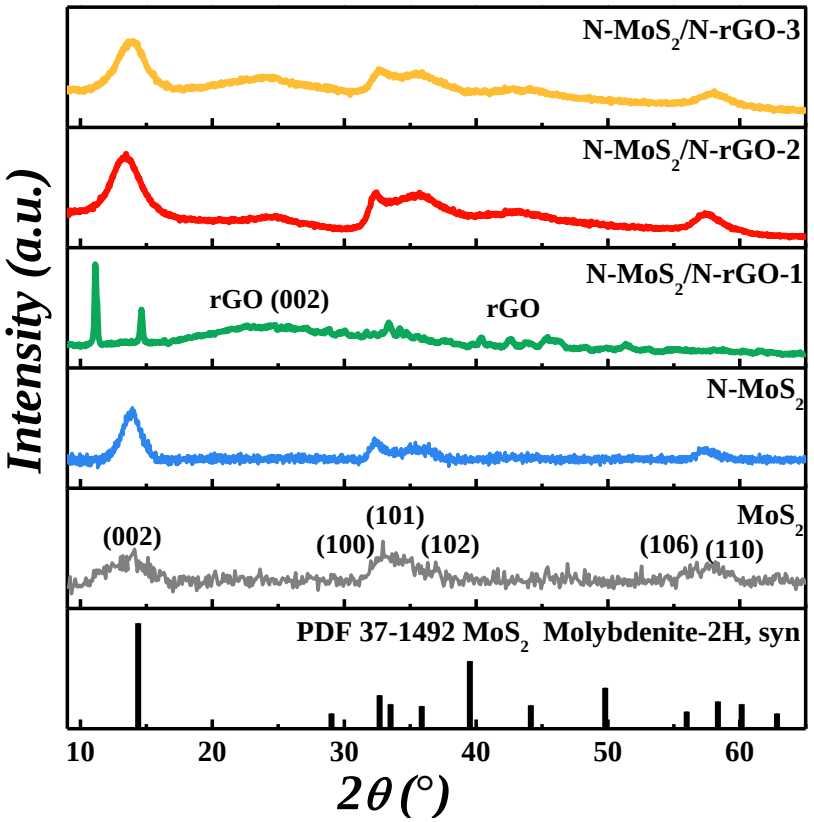

Figure 3. XRD patterns of MoS_2, N-MoS_2, and N-MoS_2/N-rGO-n (n=1, 2 and 3).

All peaks are broad and exhibit low intensity, most likely due to the poor crystallinity of the materials prepared under our experimental conditions. After nitrogen

doping of MoS_2, no new peak related to N-group phase exists, indicating that N atoms are effectively doped into the MoS_2. After mixing with GO during the hydrothermal process, the XRD pattern features, in addition of the above XRD peaks assigned to MoS_2, a broad peak at around 24.3° implying the random arrangement of (002) phase, and a peak at around 44.5° due to the (001) orientation caused by the disordered structure in rGO matrix. [25] In addition, the (002) diffraction peak of N-MoS_2/N-rGO-2 downshifted by 0.78° compared with the standard peaks of MoS_2 bulk powder; the average d value calculated according to Bragg's Law increases from 0.62 to 0.66 nm, which totally confirms the TEM results.

Raman spectroscopy was used to further characterize the structure of N-rGO, MoS_2, N-MoS_2, MoS_2/rGO and N-MoS_2/N-rGO-n (n= 1, 2 and 3), as shown in **Figure 4**. Two characteristic peaks of N-rGO located at ~1358 and 1592 cm^{-1}, associated respectively with the D band (related to edges and defects in the carbon network) and G band (in-plane vibrations of sp^2 carbon atoms in the network) are obvious (**Figure 4a**). The intensity ratio of the D-band to the G-band (I_D/I_G) is commonly used to reflect the lattice defects and degree of disorder in graphene. The I_D/I_G ratio increased from 0.74 for N-rGO to 0.96 for MoS_2/rGO, suggesting that more sp^2 domains were formed. A larger I_D/I_G ratio of 1.26 infers more structural edge defects present in N-MoS_2/rGO-2 after N-MoS_2 nanosheets grown on N-rGO.

From **Figure 4b and c**, the peaks at around 376.1 and 401.9 cm^{-1} are ascribed to the in-plane E^1_{2g} (the displacement of Mo and S atoms) and out-of-plane A_{1g} mode (symmetric displacements of S atoms along the c-axis) of the MoS_2. After N doping, there are no N-group appeared on the spectrum, and the A_{1g} mode displays a positive shift to 402.3 cm^{-1}, which also confirms that N substituted S in MoS_2 matrix. The A_{1g} exhibits a positive shift to 406.7cm^{-1} for N-MoS_2/N-rGO-2. Moreover, the intensity

ratio of A_{1g}/E^1_{2g} for N-MoS_2/N-rGO-2 (1.66) is higher than those of bulk MoS_2 (1.38), N-MoS_2 (1.62), MoS_2/rGO (1.42), N-MoS_2/N-rGO-1 (1.53) and N-MoS_2/N-rGO-3 (1.58), confirming that N-MoS_2/N-rGO-2 owns the high content of Mo-N bonds than N-MoS_2, and N-MoS_2/N-rGO-1, and N-MoS_2/N-rGO-3, which are the main active sites for HER and OER[16,24] According to the above analysis, edge-terminated N-MoS_2 sheets were formed on N-rGO through the one-pot hydrothermal method.

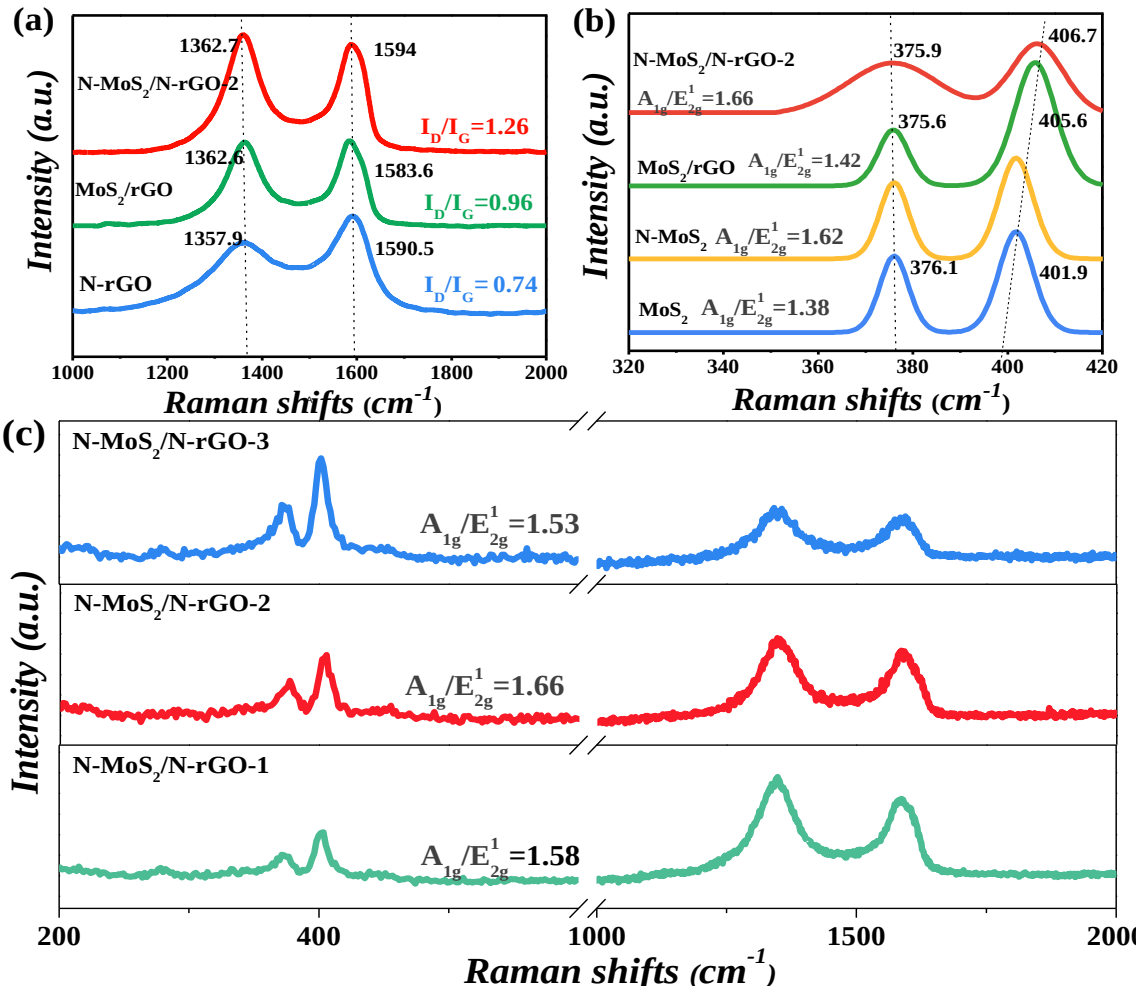

Figure 4. Raman spectra of: (**a**) N-rGO, MoS_2/rGO and N-MoS_2/N-rGO-2; (**b**) MoS_2, N-MoS_2, MoS_2/rGO, and N-MoS_2/N-rGO-2; (**c**) N-MoS_2/N-rGO-n (n=1, 2, and 3).

In order to deeper understand the chemical bonding between different chemical elements, XPS analysis of main elements, especially N composition in the three N-

MoS_2/N-rGO-1, 2 and 3 samples, was performed (**Figure 5**). There are 5 main characteristic peaks, including S_{2p} (161.8 eV), Mo_{3d} (228.8 eV), C_{1s} (284.8 eV), N_{1s} (394.8 eV) and O_{1s} (532.8 eV), confirming the results of EDX analysis. The O_{1s} signal originates most likely from residual oxygen-containing groups in rGO or the oxidation of the material during the hydrothermal process. In order to understand the effects of N concentration on the HER and OER performance of N-MoS_2/N-rGO, the N content was determined by calculating the intensity of the N_{1s} peaks in the XPS survey spectra (**Figure 5**), and the corresponding atomic concentrations of the different elements are summarized in **Table 1**.

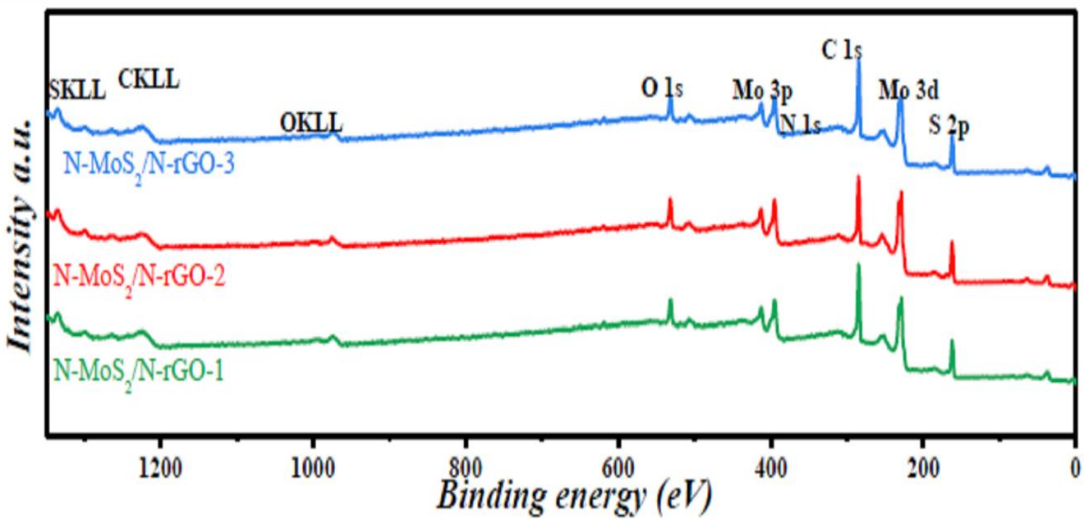

Figure 5. XPS survey spectra of N-MoS_2/N-rGO-1, N-MoS_2/N-rGO-2, and N-MoS_2/N-rGO-3

It is worth mentioning that N contents of 7.88, 9.06 and 14.12% were calculated for N-MoS_2/N-rGO-1, 2, and 3, respectively. There is a clear increasing trend of the N content with the increase of the initial dicyanamide (nitrogen precursor) concentration. At the same time, the atomic percentages of S and O atoms decrease, indicating that part of S atoms in MoS_2 were replaced by N and GO was reduced to a higher degree in

the presence of increased concentration of N precursor (dicyanamide). In this study, we found that N-MoS_2/N-rGO-2 (9.06 at% of N) has the best performance for HER and OER.

Table 1. Atomic percentage (at%) of different elements obtained from XPS spectra of N-MoS_2/N-rGO-1, N-MoS_2/N-rGO-2 and N-MoS_2/N-rGO-3.

	N-MoS_2/N-rGO-1	N-MoS_2/N-rGO-2	N-MoS_2/N-rGO-3
O (at%)	11.59	9.57 ↓	7.03 ↓
C (at%)	49.51	50.69	51.95
N (at%)	7.88	9.06 ↑	14.12 ↑
S (at%)	20.76	19.72 ↓	16.89 ↓
Mo (at%)	10.25	10.96	10.01

The C_{1s} high resolution plot of N-MoS_2/N-rGO-n (n=1, 2, 3) can be fitted with a strong peak due to C=C/C-C (sp^2/sp^3) at around 284.8 eV, C-N peak at ~ 285.5 eV which demonstrates that N was introduced into rGO, and a weaker peak assigned to C-O (286.3 eV), confirming the reduction of GO to rGO (**Figure 6a**). With the increase of N content, the C-N contribution increases from 16.88% for N-MoS_2/N-rGO-1, to 20.51% for N-MoS_2/N-rGO-2 and 23.85% for N-MoS_2/N-rGO-3, as shown in **Figure 6a**. This means that more N atoms were doped into rGO matrix with the increase of N precursors, which could improve the stability of the carbon material structure stability at high potential (at least 1.23 V) like OER process.[26]

The high resolution of the Mo3d of MoS_2 in Figure 6b can be deconvoluted into a small component ascribed to S2s (225.5 eV) and two characteristic peaks of Mo^{4+} 3d5/2 (228.4 eV) and Mo^{4+} 3d3/2 (231.9 eV), indicating the Mo^{4+} oxidation state of MoS_2. The other peaks at around 230.8 and 234.3eV are ascribed to Mo^{6+}, resulting from the

oxidation of the catalyst in air to form MoO_3. After N doping, the two-characteristic peaks of Mo^{4+} 3d3/2 and Mo^{4+} 3d5/2 showed a positive shift of +0.4 and +0.1 eV compared with those of pure MoS_2. In addition, a couple of Mo-N peaks appeared at around 1.6 and 1.2 eV higher than the bonding energy of Mo-S bond, which could confirm that N was doped into the MoS_2 matrix. After hybridization with N-rGO, the two-characteristic peaks of Mo^{4+} 3d3/2 and Mo^{4+} 3d5/2 have a further positive shift to 228.9 eV and 232.1eV, suggesting that the hybrid structure could enhance the interaction of electrons on the interface of N-MoS_2/N-rGO. This above charge transportation could optimize the adsorption energy of intermediates like H*, OH* and OOH*.[16,26] Furthermore, the content ratio of Mo-N/Mo-S bonds was determined by integrating the area of Mo3d characteristic peaks for Mo-S and Mo-N in Figure 6c and **Table 2**. The ratio of N-MoS_2/N-rGO-2 was the highest (0.8), as compared with N-MoS_2/N-rGO-1 (0.6) and N-MoS_2/N-rGO-3 (0.5), which could improve the stability, enhance the conductivity, and optimize the absorption and desorption of intermediate on the surface of MoS2 for HER and OER.[16,26]

The S_{2p} spectra of MoS_2 (**Figure 6d**) could be deconvoluted into two main peaks located at 161.4 and 163.2 eV assigned respectively to $S_{2p3/2}$ and $S_{2p1/2}$. After N-doping, these two characteristic peaks shifted by +0.2 and -0.2 eV, respectively. For N-MoS_2/N-rGO-2, the $S_{2p3/2}$ and $S_{2p1/2}$ move to 161.7 eV and 163.0 eV.

Figure 6e presents the high resolution XPS of the N_{1s}. For N-MoS_2, the two peaks at around 394.7 and 401.6 eV are assigned respectively to Mo_{3p} and N_{1s}. A shoulder peak at around 396.4 eV beside Mo_{3p} belong to Mo-N bonding, confirming N replacing S sites in MoS_2 matrix.[27] After hybridization with N-rGO, 3 kinds of C-N bonds were found at 397.9 399.8 and 401.9 eV, ascribed to pyridine-N, pyrrolic-N, and graphitic-N, respectively. From previous reports, pyrrolic N and pyridinic N possess excellent

activity and high stability, especially pyridinic N.[17]

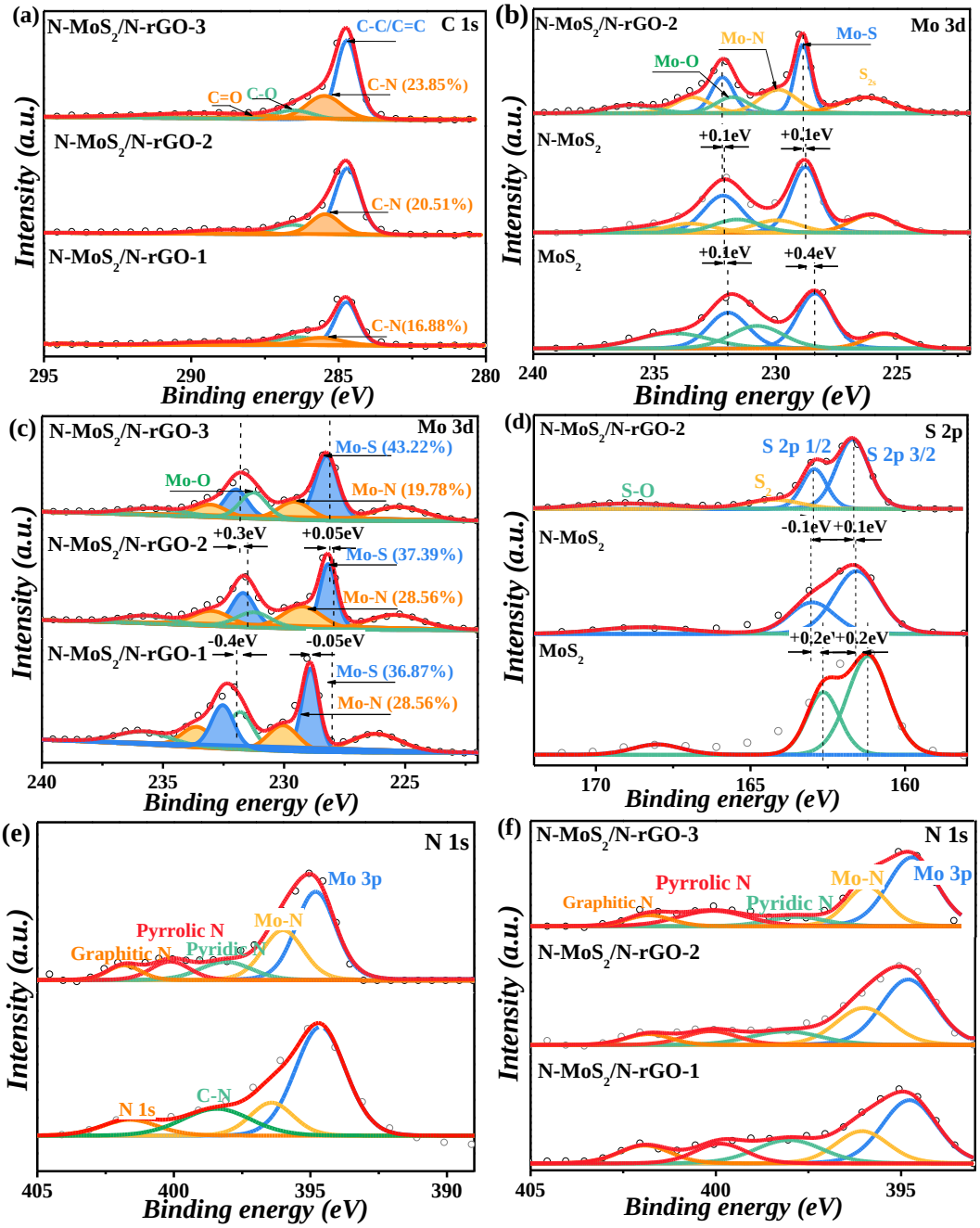

Figure 6. XPS analysis of MoS_2, N-MoS_2, and N-MoS_2/N-rGO-n (n=1, 2 and 3); high resolution of (**a**) C_{1s}, (**b, c**) Mo_{3d}, (**d**) S_{2p}, and (**e, f**) N_{1s}.

Moreover, the content of Mo_{3p}, Mo-N, pyridinic-N, pyrrolic-N, and graphitic-N (**Table 2**) were calculated from the high resolution XPS spectrum of N_{1s} in **Figure 6f**. Obviously, N-MoS_2/N-rGO-2 has the highest content (26.33%) for Mo-N compared

with those of N-MoS_2/N-rGO-1 (19.56%) and N-MoS_2/N-rGO-3 (22.94%), confirming the results of high ratio of Mo-N/Mo-S content in Mo_{3d}. The content of pyridine-N decreased from 18. 05% for N-MoS_2/N-rGO-1 to 12.23% for N-MoS_2/N-rGO-2 and 7.6% for N-MoS_2/N-rGO-3, while the content of pyrrolic-N in N-MoS_2/N-rGO-2 decreased to 9.39% from 10.66% in N-MoS_2/N-rGO-1.

From the above results, we can confirm that N atoms have been doped into rGO and substituted S sites on MoS_2, and a N-MoS_2/N-rGO-2 hybrid with larger electrochemical active surface area and more active sites could optimize the HER and OER performance of MoS_2.

Table 2. Mo-N, pyridinic-N, and pyrrolic N contents determined from the high-resolution of N 1s.

	N-MoS_2/N-rGO-1	N-MoS_2/N-rGO-2	N-MoS_2/N-rGO-3
Mo3p	39.97	45.69	47.77
Mo-N (%)	19.56	26.33 (Maximum)	22.94
Pyridinic N (%)	18.05	12.23 0.0117	7.60
Pyrrolic N (%)	10.66	9.39	14.07
Graphitic N (%)	11.76	6.36	6.81

3.3.2 OER performance of N-MoS_2/N-rGO

The OER performance of N-rGO, MoS_2, N-MoS_2, MoS_2/rGO, N-MoS_2+N-rGO (physical mixing) and N-MoS2/N-rGO-n (n1, 2, and 3) was assessed by Linear Sweep Voltammetry (LSV) measurements using graphite rod as a reference electrode and Ag/AgCl as a reference electrode in 1M KOH solution at a scanning rate of 5 mV s^{-1}. RuO_2 as one of the best OER catalysts was employed as a standard counterpart. **Figure 7a** clearly reveals that N-MoS_2/N-rGO-2 displays the lowest overpotential (0.38 V) to

achieve a current density of 50 mA cm^{-2}, only 0.07 V larger than that of RuO_2, far smaller than N-rGO (0.74 V), MoS_2 (0.75 V), N-MoS2 (0.67 V), MoS_2/rGO (0.6 V). N-MoS_2+N-rGO (0.57 V). Further, the influence of the N content in N-MoS_2/N-rGO was optimized by checking the OER performance of as-synthesized N-MoS_2/N-rGO-n (1, 2, and 3) samples, as shown in **Figure 7a**. The overpotential at a current density of 50 mA cm^{-2} of N-MoS_2/N-rGO-2 is also 0.13 and 0.11 V smaller than those of N-MoS_2/N-rGO-1 and N-MoS_2/N-rGO-3, respectively. The enhancement of N-MoS_2/N-rGO-2 is dependent on the synthesis effects of highest composition of N dopant tuning the electron structure around Mo and S edges, and the formation of Mo-N-C bond boosting the charge transfer between N-MoS_2 and N-rGO.

Meantime, the Tafel slopes of the above samples were obtained by linear fitting the polarized curves, according to the Tafel equation ($\eta = b \log j + a$, where j is the current density and b is the Tafel slope), **Figure 7b.** The N-MoS_2/N-rGO-2 acquired the smallest Tafel slope of 87.5 mV dec^{-1} compared with N-rGO (192 mV dec^{-1}), MoS_2 (151.4 mV dec^{-1}), N-MoS_2 (157.2 mV dec^{-1}), MoS_2/rGO (108.6 mV dec^{-1}), N-MoS_2+N-rGO (141.7 mV dec^{-1}), N-MoS_2/N-rGO-1 (107.9 mV dec^{-1}) and N-MoS_2/N-rGO-3 (103.6 mV dec^{-1}), although being still larger than that of RuO_2 (52.82 mV dec^{-1}). The smaller Tafel slope value of N-MoS_2/N-rGO-2 infers a faster electron transfer process of OER. The overpotential and Tafel slope of N-MoS_2/N-rGO are much lower compared to other MoS_2-based materials (**Figure 7c** and **Table 3**), indicating that controlled incorporation of nitrogen into MoS_2 has a beneficial effect on its electrochemical properties. This testifies that N-MoS_2/N-rGO-2 heterostructure could enhance the kinetics of water oxidation due to the synergic effects of N doping and Mo-pyridinic N-C charge transfer pathways.

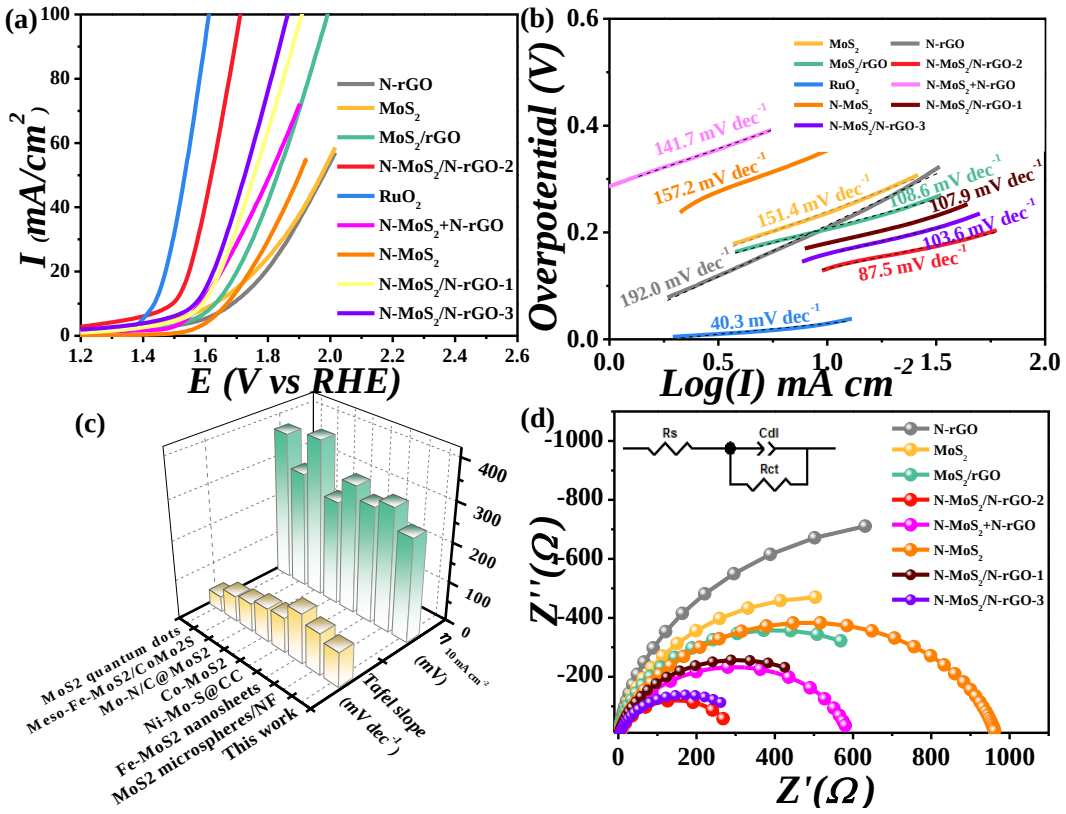

Figure 7. OER performance of N-rGO, MoS_2, N-MoS_2, MoS_2/rGO, N-MoS_2+N-rGO, N-MoS_2/N-rGO-2, and RuO_2 in 1M KOH solution: (**a**) OER polarization curves, (**b**) Tafel plots, (**c**) Comparison of the overpotential (at 10 mA cm^{-2}) and the Tafel slope values of recent reports on MoS_2-based electrocatalysts, (**d**) Nyquist plots.

Electrochemical impedance spectroscopy (EIS) was further performed to evaluate the kinetic of the developed catalysts. From **Figure 7d** and **Table 4,** N-MoS_2 has a smaller R_{ct} of 938.1 Ω compared with pure MoS_2 (1047 Ω), which could confirm that N dopant could improve the conductivity and decrease the charge transfer of OER on the surface of MoS_2. After hybridization of N-MoS_2 with N-rGO, it could be noticed that the R_{ct} of N-MoS_2/N-rGO-2 further decreases to 290 Ω compared to N-MoS_2, far smaller than those of N-rGO (1598 Ω), MoS_2/rGO (799.5 Ω), N-MoS_2/N-rGO-1 (604.9 Ω) and N-MoS_2/N-rGO-3 (337.8 Ω). And the R_{ct} value of physical mixture of N-MoS_2+N-rGO (545 Ω) is almost 1 times larger than that of N-MoS_2/N-rGO-2, reflecting

a faster charge transfer rate through Mo-pyridinic N-C bonding[17], resulting in a rapid reaction rate in OER kinetics.

Table 3. Comparison of overpotentials and Tafel slopes of N-MoS_2/N-rGO-2 with reported MoS_2-based electrocatalysts for OER in an alkaline medium.

	Overpotential (mV) @10 mA cm^{-2}	Tafel slope (mV dec^{-1})	Reference
N-MoS_2/N-rGO	260	87.5	This work
MoS_2 microspheres/NF	310	105	[28]
Fe-MoS_2 nanosheets	>290	126	[29]
Ni-Mo-S@CC	320	88	[30]
Co-MoS_2	260	85	[31]
Mo–N/C@MoS_2	390	72	[32]
Meso-Fe-MoS_2/$CoMo_2S$	290	65	[33]
MoS_2 quantum dots	370	39	[20]

Table 4. The fitting parameters of EIS for GC, rGO, MoS_2, MoS_2/rGO, and N-MoS2/N-rGO-n (n1, 2, 3) in 1M KOH solution.

	R_s/Ohm	C_{dl}/mF cm^{-2}	R_{ct}/Ohm
GC	1.69	0.065	2873
N-rGO	1.45	0.099	1598
MoS_2	1.87	0.073	1047
N-MoS_2	1.99	0.015	938.1
MoS_2/rGO	1.68	0.100	799.5
N-MoS_2+N-rGO	1.74	0.081	545
N-MoS_2/N-rGO-1	1.41	0.095	604.9
N-MoS_2/N-rGO-2	3.07	0.131	290
N-MoS_2/N-rGO-3	2.87	0.121	337.8

The cycling stability of the N-MoS_2/N-rGO-2 for the OER was tested by CV in 1M KOH solution. As shown in **Figure 8**, there is no significant difference between the initial cycle and that recorded after 3000 cycles, indicating excellent durability in the electrochemical process. In addition, the stability was also assessed through chronopotentiometry measurements (insert of **Figure 8**). The overpotential at 20 mA cm^{-2} of N-MoS_2/N-rGO-2 slightly increased by 20 mV over 15 h. The above stability results confirm that N-MoS_2/N-rGO-2 features an excellent stability in 1M KOH.

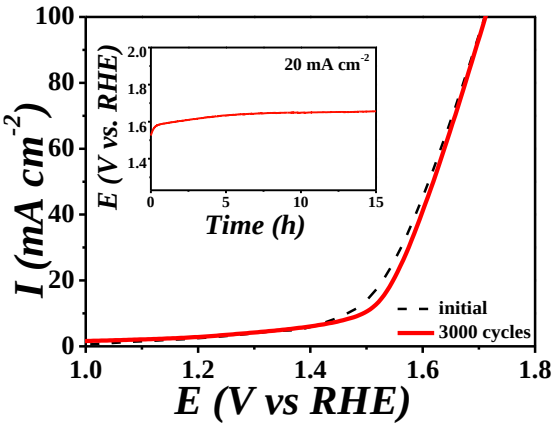

Figure 8 LSV curves before and after cycling stability study after 3000 cycles of N-MoS_2/N-rGO-2, the insert is the chronopotentiometry test in 1M KOH; scanning rate=100 mV s^{-1}.

To estimate the electrochemically active surface area (ECSA), the electrochemical double layer capacitance (C_{dl}) at the solid−liquid interface was calculated using CV) measurements in the potential range from -0.1 to +0.1 V (*vs.* Ag/AgCl) in 1 M KOH (**Figure 9 a-i**) at different scanning rates (20 to 100 mV dec^{-1}).

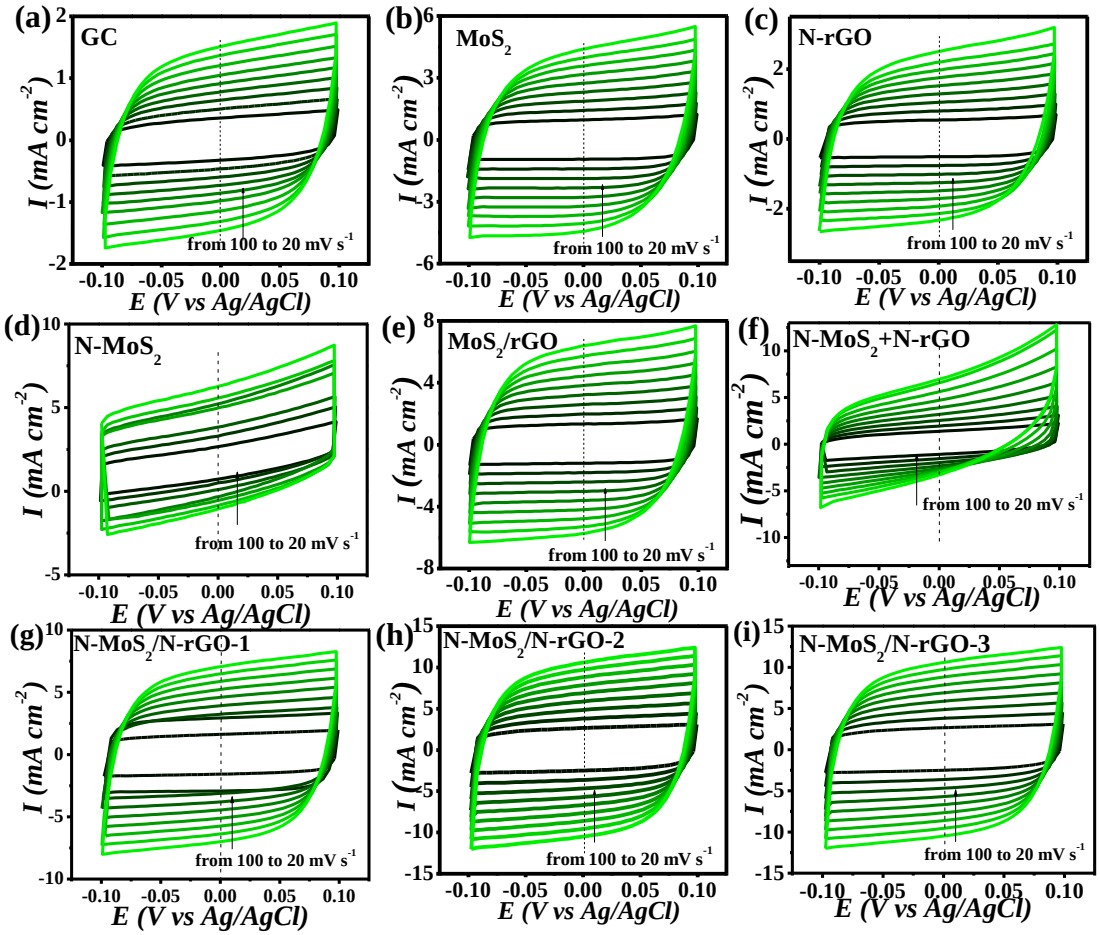

Figure 9. CVs recorded within a potential window from -0.1V to +0.1V (vs. Ag/AgCl) at different scan rates (20 to 100 mV s-1) of (a-i) GC, MoS_2,N-rGO, N-MoS_2, MoS_2/rGO, N-MoS_2+N-rGO, and N-MoS_2/N-rGO-x (x=1, 2, and 3), respectively in 1M KOH.

The GC has a smallest C_{dl} of 13.79 mF cm^{-2}. The C_{dl} value of N-MoS_2 (44.2 mF cm^{-2}) is similar to that of pure MoS_2 (42.96 mF cm^{-2}). While after formation of the N-MoS_2/N-rGO heterostructure, the C_{dl} of N-MoS2/N-rGO-n (n0,1,2 and 3) increases to 59.8 mF cm^{-2} (MoS_2/rGO), 64.1 mF cm^{-2} (N-MoS_2/N-rGO-1), 54.7 mF cm^{-2} (N-MoS_2/N-rGO-3), and reaching the highest value of 98.5 mF cm^{-2} (N-MoS2/N-rGO-2), as shown in **Figure 10**. Meanwhile, the C_{dl} of N-MoS_2+N-rGO (48.2 mF cm^{-2}) also increases slightly compared with single N-MoS_2 and N-rGO components. From ECSA analysis, the surface area of N-MoS_2/N-rGO-2 is 7.1 cm^2, which is higher than the

values recorded for N-MoS_2/N-rGO-1 (3.9 cm^2), N-MoS_2/N-rGO-3 (4.65 cm^2), N-MoS_2+N-rGO (3.5 cm^2), MoS_2/rGO (4.3 cm^2), N-MoS_2 (3.2 cm^2), MoS_2 (3.11 cm^2), and N-rGO (1.68 cm^2). Based on the comparison with the counter parts, the unique nanoflower morphology in N-MoS_2/N-rGO-2 achieves a higher surface area with much more active sites.

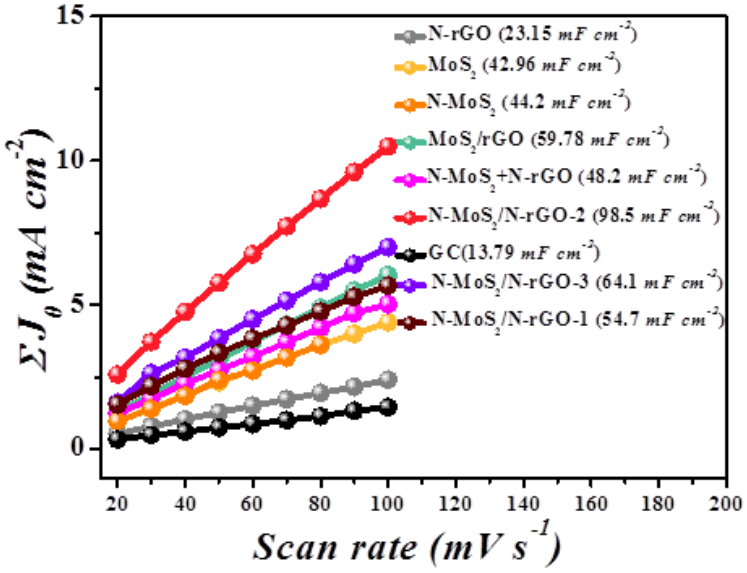

Figure 10. C_{dl} values determined by plotting the current density J_0 variation at different scanning rates.

3.3.3 HER performance of N-MoS_2/N-rGO

The performance of N-MoS_2/N-rGO-2 for HER was also assessed in alkaline condition (1M KOH) and acid solution (0.5M H_2SO_4). From **Figure 11a**, N-rGO dispkays the lowest activity for HER in alkaline solution. N-MoS_2 exhibits a smaller overpotential (0.821 V) to deliver 100 mA cm^{-2} compared with MoS_2 (0.668 V), meaning that N could improve the activity of MoS_2 by replacing S in MoS_2 matrix. After growing N-MoS_2 on N-rGO, a very low potential of 0.298 V was required to deliver 100 mA cm^{-2} in 1M KOH solution, even though there is still a gap with Pt (0.084

V). Furthermore, the effects of N composition on HER performance was also valued by recording the LSV curves of N-MoS_2/N-rGO (n=0, 1, and 3). N-MoS_2/N-rGO-2 still possesses the smallest overpotential than those of MoS_2/N-rGO (0.539 V), N-MoS_2/N-rGO-1 (0.415V), and N-MoS_2/N-rGO-3 (0.381V).

Apart from alkaline solution, N-MoS_2/N-rGO-2 also recorded the best performance in acid solution with a lower overpotential of 0.114 V to achieve 100 mA cm^{-2}, slightly higher than that of Pt (0.078V), far lower than those of pure MoS_2 (0.571 V), N-MoS_2 (0.513 V), N-rGO (> 0.80 V), MoS_2/rGO (0.465 V), N-MoS_2+N-rGO (0.478 V), N-MoS_2/N-rGO-1 (0.18 V) and N-MoS_2/N-rGO-3 (0.202 V), as shown in **Figure 11d**. Although the performance in alkaline is better than MoS_2 and N-MoS_2, the overpotential is still lower than that in acid solution. Meanwhile, the Tafel slope values of N-MoS_2/N-rGO-2 were 46.47 and 39.05 mV dec^{-1} in alkaline and acid solutions, respectively, which outperform those of N-MoS_2 and N-rGO. The process of HER could be separated into Volmer (Tafel slope of ~ 120 mV dec^{-1}), Tafel (Tafel slope of ~ 40 mV dec^{-1}), and Heyrovsky (Tafel slope of about 30 mV dec^{-1}) steps. The decreased Tafel slope of N-MoS_2/N-rGO-2 indicates that the HER pathway is governed by the Volmer−Heyrovsky mechanism in both acid and alkaline solutions. At the same time, the Volmer water dissociation process was enhanced due to the N-Mo and pyridinic N-C charge transfer pathway, which could optimize the adsorption and desorption energy of intermediates H*and OH*.[17]

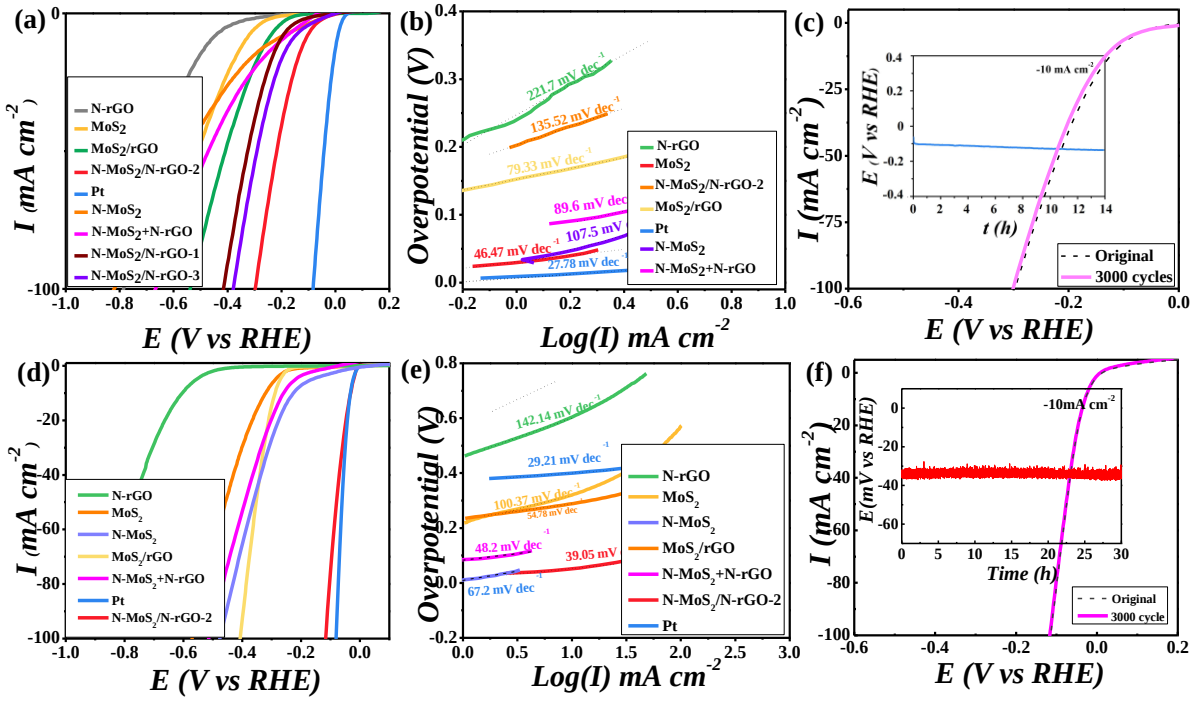

Figure 11. The HER performance: (a, c) polarization curves, (b, d) Tafel plots of Pt sheet, N-MoS_2/NrGO-2, MoS2/rGO, MoS2 and rGO, (e) LSV curves of N-MoS_2/N-rGO-2 before and after 3000 cycles, inserts are thes time-current curves of N-MoS_2/N-rGO-2 at -10 mA cm^{-2} in 1M KOH and 0.5M H_2SO_4, respectively

In addition, N-MoS_2/N-rGO-2 also showed excellent long-term stability in both alkaline and acid solutions, as shown in **Figure 11c, f**. Obviously, the current density of N-MoS_2/N-rGO-2 electrode dropped slightly after 3000 cycles and a remarkable stability at -10 mA cm^{-2} with an overpotential decrease of 36% after 14 h in the alkaline solution. Besides, N-MoS_2/N-rGO-2 could deliver -10 mA cm^{-2} with an overpotential of 35 mV for 30 h, proving its good stability in 0.5M H_2SO_4 solution. Moreover, the CV curve after 3000 cycles coincides with the original one. These above results infer that N-MoS_2/N-rGO-2 could maintain the HER activity and stability in 1M KOH and 0.5M H_2SO_4 solutions. Compared with MoS_2-based materials reported in the scientific

literature for HER in both alkaline and acid solutions (**Figure 12a, b, Table 5** and **6**), N-MoS_2/N-rGO-2 exhibited a better performance, especially in acid solution.

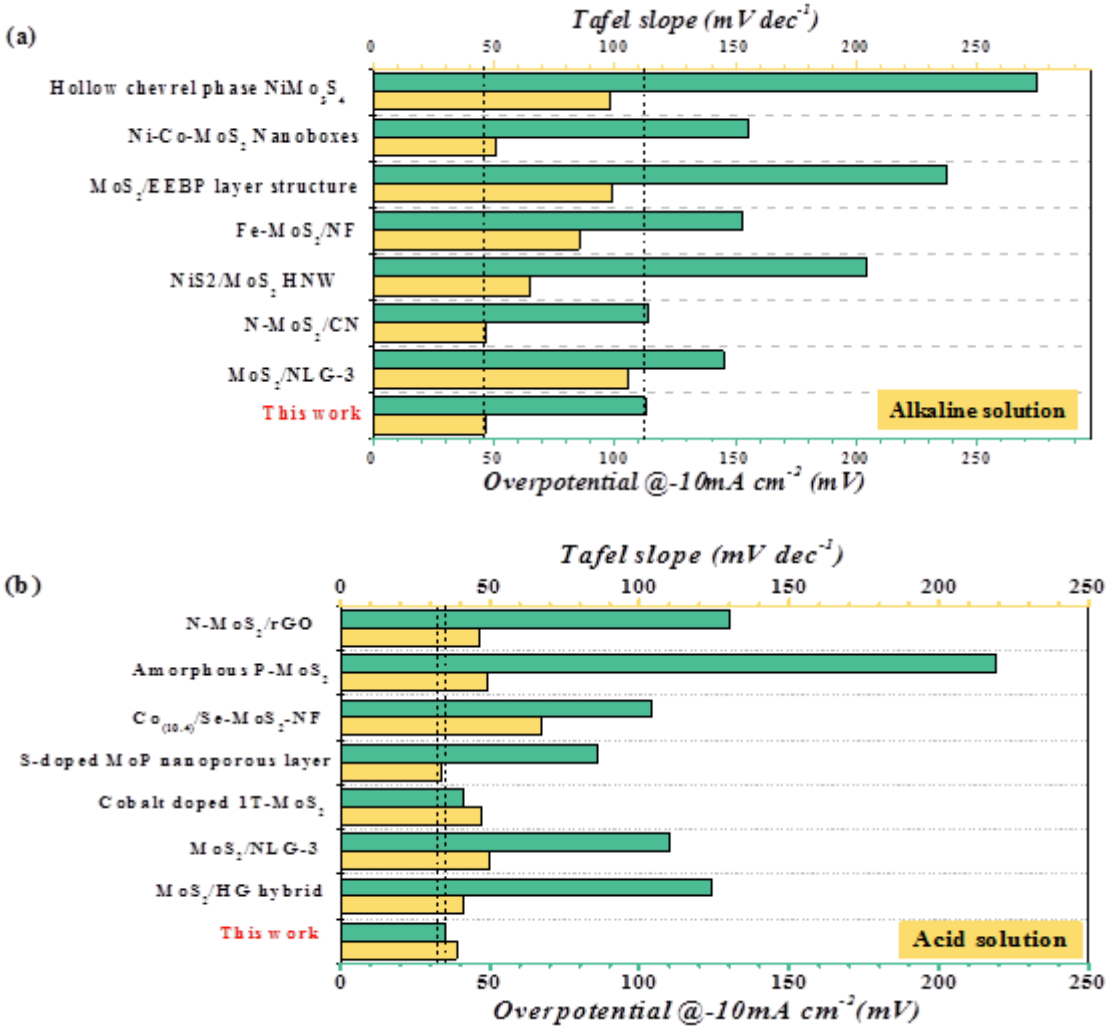

Figure 12 (a, b) Comparison of the overpotential at 10 mA cm^{-2} and the Tafel slope values of recent reports on MoS_2-based electrocatalysts.

Table 5. Comparison of overpotentials and Tafel slopes of N-MoS_2/N-rGO-2 with reported MoS_2-based electrocatalysts for HER in an alkaline medium.

	Overpotential (mV) @10 mA cm^{-2}	**Tafel slope** (mV dec^{-1})	**Reference**
N-MoS_2/N-rGO	**112.8**	**46.4**	**This work**
MoS_2	>220 mV	-	[34]
MoS_2/NLG-3	145	105.8	[17]
N-MoS_2/CN	114	46.8	[35]
1T, 2H-MoS_2	320@20mA cm^{-2}	65	[36]
NiS_2/MoS_2 HNW	204	65	[37]
Fe-MoS_2 /NF	153	85.6	[38]
MoS_2/EEBP layer structure	237	99	[39]
Ni-Co-MoS_2 Nanoboxes	155	51	[40]
Amorphous $CoMoS_x$ Gel	210 @ 5 mA cm^{-2}	-	[41]
Hollow Chevrel Phase $NiMo_3S_4$	275	98	[42]

Similar with the EIS in alkaline solution, the EIS in 0.5M H_2SO_4 solution are shown in **Figure 13** and the simulated results are summarized in the **Table 7**. N-MoS_2/N-rGO-2 possesses a smaller charge transfer resistance of (128.4 Ω) compared to MoS_2 (1248 Ω), N-MoS_2 (1098 Ω), N-rGO (1648 Ω), MoS_2/rGO (1069 Ω), and N-MoS_2+N-rGO (1119 Ω) in 0.5M acid solution, which also confirms that the Mo-pyridinic N-C bonds improved the charge transfer step.

Table 6. Comparison of overpotentials and Tafel slopes of N-MoS_2/N-rGO-2 with reported MoS_2-based electrocatalysts for HER in an acid medium.

	Overpotential (mV) @10 mA cm^{-2}	**Tafel slope** (mV dec^{-1})	**Reference**
N-MoS_2/N-rGO	**35.1**	**39.05**	**This work**
MoS_2/HG hybrid	124	41	[24]
MoS_2/NLG-3	110	50.1	[17]
Cobalt doped 1T-MoS_2	41	47	[43]
S-doped MoP nanoporous layer	86	34	[3]
Co(10.4)/Se-MoS_2-NF	104	67	[44]
Amorphous P-MoS_2	219	49	[45]
MoP/S	86	-	[46]
N-MoS_2/rGO	130	46.5	[47]
$Mo_{0.5}W_{0.5}S_2$	138	55	[48]
PDAC/MoS_2-C	195	82	[49]

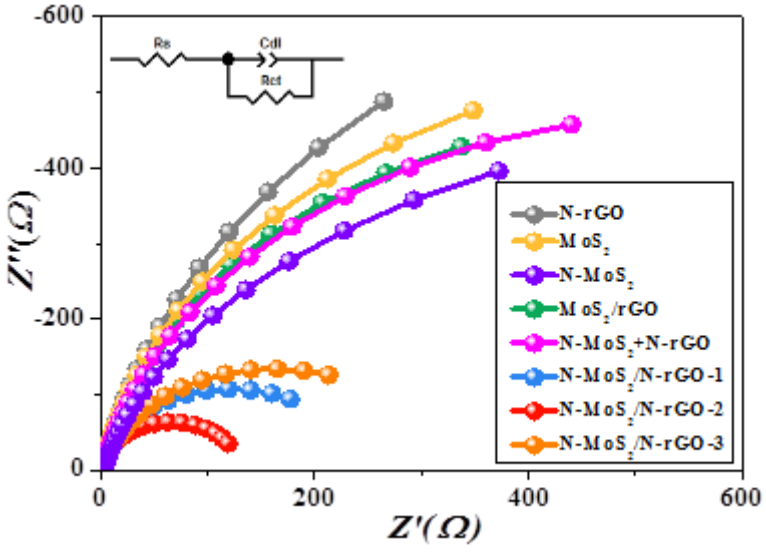

Figure 13. Nyquist plots of N-MoS_2/N-rGO-n (n=1, 2, and 3) in 0.5 M H_2SO_4 solution.

Table 7. The fitting parameters of EIS for N- rGO, MoS_2, N-MoS_2, MoS_2/rGO, N-MoS_2+N-GOr, and N-MoS2/N-rGO-n (n=1, 2, 3) in 0.5M H_2SO_4 solution.

	R_s/Ohm	C_{dl}/mF cm^{-2}	R_{ct}/Ohm
N-rGO	1.56	0.15	1648
MoS_2	1.81	0.14	1248
N-MoS_2	1.99	0.01	1098
MoS_2/rGO	1.99	0.15	1069
N-MoS_2+N-rGO	1.74	0.08	1119
N-MoS_2/N-rGO-1	1.641	0.27	0.93007
N-MoS_2/N-rGO-2	**1.67**	**0.37**	**128.4**
N-MoS_2/N-rGO-3	1.88	0.19	320

To estimate the electrochemically active surface area (ECSA) in acid solution, the electrochemical double layer capacitance (C_{dl}) at the solid-liquid interface was calculated by CV measurements in the -0.1 to +0.1V (*vs.* Ag/AgCl) potential range in 0.5M H_2SO_4 solution (**Figure 14 a-f**).

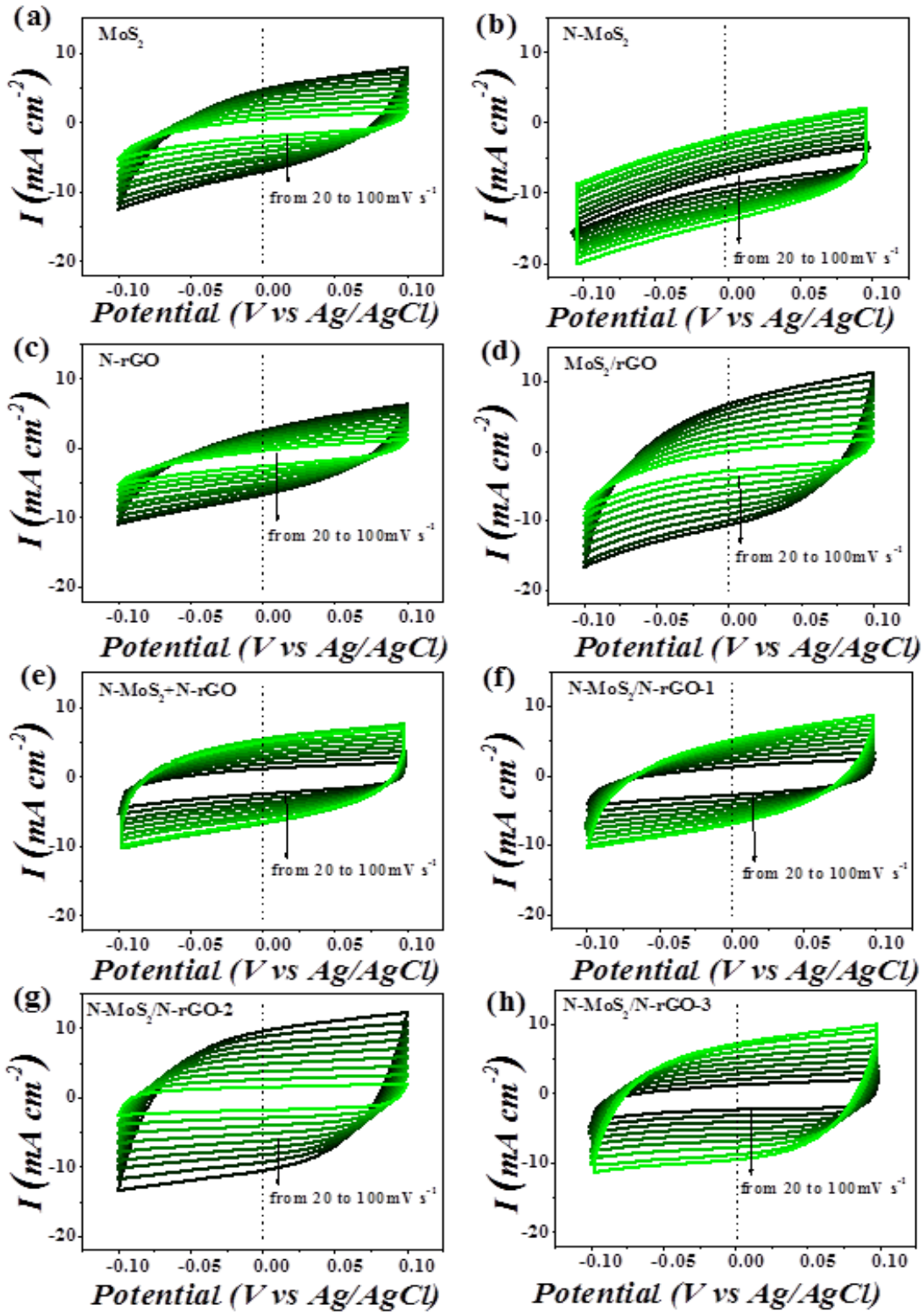

Figure 14. CVs curves within a potential window from -0.1V to +0.1V (*vs. Ag/AgCl*) at different scan rates (20 to 100 mV s^{-1}) of (**a-h**) MoS_2, N-MoS_2, N-rGO, MoS_2/rGO, N-MoS_2+N-rGO and N-MoS2/N-rGO-n (n=1, 2, and 3), respectively, in 0.5M H_2SO_4.

The N-MoS_2/N-rGO-2 exhibits the largest C_{dl} of 111 mF cm^{-2}, compared to N-MoS_2+N-rGO (67.1 mF cm^{-2}), MoS_2/rGO (72 mF cm^{-2}), N-MoS_2 (62.2 mF cm^{-2}), MoS_2 (59 mF cm^{-2}) and N-rGO (45 mF cm^{-2}), as shown in **Figure 14**. In the ECSA analysis, the surface area of N-MoS_2/N-rGO-2 is 7.1 cm^2, which is higher than the value for N-MoS_2+N-rGO (6.1cm^2), MoS_2/rGO (6 cm^2), N-MoS_2 (5.7cm^2), MoS_2 (4.9 cm^2), and N-rGO (3.75 cm^2). Based on comparison with the counter parts, the unique nanoflower morphology in N-MoS_2/N-rGO-2 achieves a higher surface area with much more active sites.

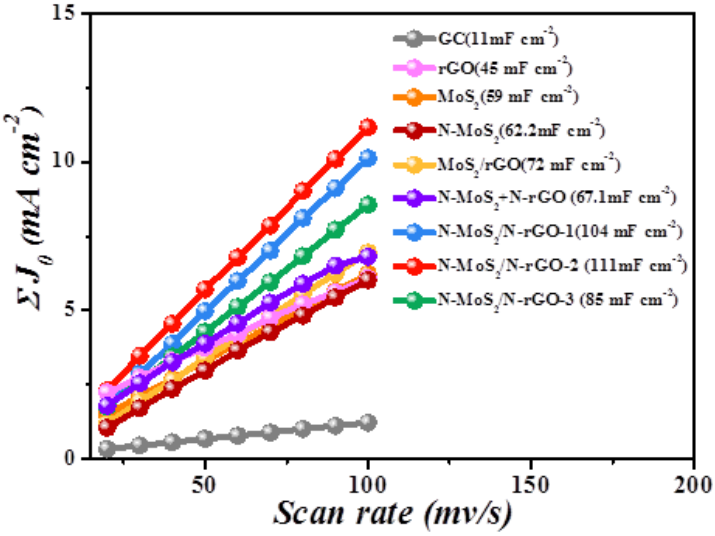

Figure 15. C_{dl} determined by plotting the current density J_0 variation *versus* the scan rate of MoS_2, N-MoS_2, N-rGO, MoS_2/rGO, N-MoS_2+N-rGO and N-MoS2/N-rGO-n (n=1, 2, and 3) in 0.5M H_2SO_4 with a scan rate from 20 mv s^{-1} to 100 mv s^{-1}.

3.3.4 Turnover Frequency (TOF) Calculation

The active sites of MoS_2, N-MoS_2, N-rGO, and MoS_2/rGO, and N-MoS_2/N-rGO-2 were calculated according to the cyclic voltammetry test in **Figure 13(a-d, g)** using the **Eq. 3.1**.

$$n = \frac{Q}{2F} \tag{3.1}$$

Where n is the stoichiometric number of electrons transferred in the HER process, Q is the net voltammetry charge transfer which was calculated by subtracting charges resulting from the bare

glassy carbon electrode. F is the Faraday constant (96485 C mol^{-1}). And the TOF were also calculated by using the **Eq. 3.2:**

$$\mathrm{TOF} = \frac{|\mathrm{I}|}{2\mathrm{nF}} = \frac{|\mathrm{I}|}{\mathrm{Q}} \tag{3.2}$$

Where I is the current density (mA cm^{-2}) at a specific overpotential (here the I was chosen at an overpotential of 200 mV). The values of Q and TOF and Faradaic efficiency of MoS_2, N-MoS_2, N-rGO, and MoS_2/rGO, and N-MoS_2/N-rGO-2 in both acid and alkaline solution are summarized in **Table 8**. N-MoS_2/N-rGO-2 exhibits the higher TOF values of 7.843 s^{-1} (0.987 s^{-1}) in both acid (alkaline) solution than 0.034 s^{-1} (0.033 s^{-1}), 0.006 s^{-1} (0.014 s^{-1}), 0.325 s^{-1} (0.676 s^{-1}) and 0.016 s^{-1} (0.159 s^{-1}) of MoS_2, N-rGO, N-MoS_2, and MoS_2/rGO, respectively, which also indicates that the N-MoS_2/N-rGO-2 has outstanding catalytic activity. Besides, from the number of active sites calculated according the **Eq.1**, N-MoS_2/N-rGO-2 displays the highest value of 1.61E^{-07} (2.16E^{-07}) in acid solution (in alkaline solution), compared with MoS_2: 1.23E^{-07} (8.64E^{-08}), N-MoS_2: 1.19E^{-07} (6.43E^{-08}), N-rGO: 7.48E^{-08} (3.51E^{-07}), and MoS_2/rGO: 1.42E^{-07} (1.17E^{-07}) in acid (alkaline) solution, which also adds an evidence for its highest activity.

3.3.5 Faradaic efficiency measurements

Both HER and OER Faradaic efficiencies of the investigated catalysts were assessed by quantifying the quantity of the released gas through gas chromatography during the applied CA measurements (the catalyst is held at -1.0 V *vs.* RHE for 1 h in 0.5M H_2SO_4 or 1.0M KOH solutions at 25 ºC). The Faradaic efficiency values (ε) for both the HER and OER [50] were calculated according to the formula shown below **Eq. 3.3**:

$$\varepsilon(\%) = \frac{\mathrm{V_m}}{\mathrm{V_c}} \times 100\% \tag{3.3}$$

Where V_m is the measured value of gas, V_c the theoretical (calculated) value of H_2 ($V_{calc.}$), obtained from the charge passed (assuming 100% Faradaic efficiency) through the WE during the CPE, using the relation **Eq. 3.4**:

$$V_c = \frac{Q(CPE)}{nF} \quad (3.4)$$

Where *F* is the Faraday's constant (*F* = 96485 C), and *Q*(CPE) is the charge passed through the *WE* during the CPE. The factor (*n*) is the number of electrons transferred during the HER (*n* = 2 due to H^+ reduction, $2H^+ + 2e^- = H_2$) and OER (*n* = 4 due to the oxidation of OH^-, $4OH^- = 2H_2O + O_2 + 4e^-$).

So the Faradaic efficiency (ε(%)) could be caculated by **Eq. 3.5**:

$$\varepsilon(\%) = \frac{nFV_m}{Q(CPE)} \times 100\% \quad (3.5)$$

Table 8. Net voltemetry charge transfer (Q), current density at an overpotential of 200 mV, turnover frequence (TOF) and the number of active sites (n) for the studied catalysts.

	0.5M H_2SO_4				1M KOH			
	Q ($C\ cm^{-2}$)	I@200mV ($mA\ cm^{-2}$)	TOF (s^{-1})	n	Q ($C\ cm^{-2}$)	I @200mV ($mA\ cm^{-2}$)	TOF (s^{-1})	n
MoS_2	0.024	-0.82	0.034	1.23E-07	0.017	-0.55	0.033	8.64E-08
N-rGO	0.014	-0.09	0.006	7.48E-08	0.068	-0.94	0.014	3.51E-07
N-MoS_2	0.023	-7.43	0.325	1.19E-07	0.012	-8.39	0.676	6.43E-08
MoS_2/rGO	0.027	-0.45	0.016	1.42E-07	0.023	-3.60	0.159	1.17E-07
N-MoS_2/N-rGO-2	**0.031**	**-244.22**	**7.843**	1.61E-07	**0.042**	**-41.19**	**0.987**	2.16E-07

The obtained results of theoretical and measured amounts of H_2 evolved in both acid and alkaline solution and O_2 evolved in alkaline solution for the investigated electrocatalysts during 1 h of CGE are collected in **Figure 16** and **Tables 9-11**.

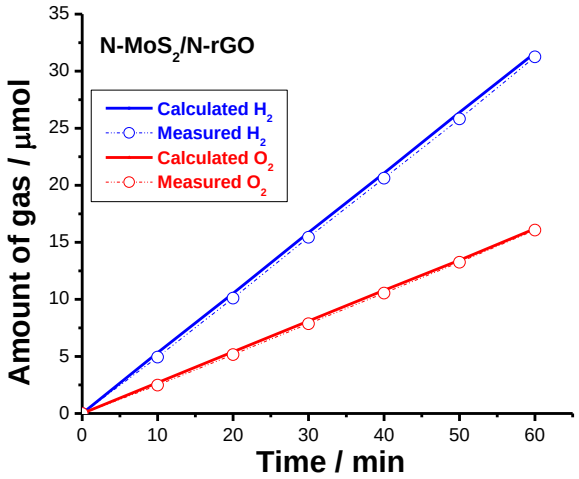

Figure 16. Faradaic efficiency measurements for both HER and OER by N-MoS_2/N-rGO-2 catalysts in 1 M KOH. The electrode was held at -1.0 V *vs.* RHE (for the HER) and +1.0 V *vs.* RHE (for the OER) for 1 h in 1.0 M KOH solutions at 25 °C. The amount of the gas liberated expected from the amount of charge passed assuming 100% Faradaic efficiency is shown as a solid line. The amount of the released gas detected by the GC is shown as hollow spheres.

Table 9. Mean value (standard deviation) of V_{H2} (measured and calculated) obtained after 1 h of a controlled potential electrolysis (CPE)*, together with the Faradaic Efficiency values, *FE* (%), for the studied catalysts.

Catalyst	V_m (H_2 / µmol h^{-1})	Q(CPE) (C)	$V_{calc.}$ H_2 / µmol h^{-1}	FE (%)
N-rGO	11.88(0.15)	3.048926	15.8(0.2)	75.2(0.8)
MoS_2	16.45(0.2)	3.743618	19.4(0.24)	84.8(0.87)
N-MoS_2	23.35(0.3)	4.940032	25.6(0.3)	91.2(0.93)
MoS_2/rGO	27.50(0.32)	5.538239	28.7(0.33)	95.7(1.05)
N-MoS_2/rGO	30.70(0.34)	5.943476	30.8(0.35)	99.6(1.1)
Pt/C	31.79(0.2)	6.136446	31.8(0.2)	99.9(0.9)

* CPE: the catalyst is held at -1.0 V vs. RHE for 1 h in 0.5 M H_2SO_4 solution at 25 °C.

From the **Tables 9-11**, it is very clear that N-MoS_2/N-rGO-2 features the best performance for both HER and OER due to the largest volumes of H_2 of 9.54 µmol h^{-1} (30.70 µmol h^{-1} in acid solution) and O_2 (29.26 µmol h^{-1}). And it also displays the highest ε(%) values of 99.8% (98.8% in acid

solution) for HER and 99.2% for OER in alkaline solution, which are comparable those measured for their corresponding state-of-the-art electrocatalysts, namely, Pt/C (99.9%) and RuO_2 (99.8%).

Table 10. Mean value (standard deviation) of V_{H2} (measured and calculated) obtained after 1 h of a controlled potential electrolysis (CPE)*, together with the Faradaic Efficiency values, *FE* (%), for the studied catalysts.

Catalyst	V_m (H_2 / μmol h^{-1})	Q(CPE) (C)	$V_{calc.}$ H_2 / μmol h^{-1}	FE (%)
N-rGO	10.98(0.2)	2.88	14.9(0.17)	73.7(0.9)
MoS_2	15.31(0.22)	3.59	18.6(0.21)	82.3(0.92)
N-MoS_2	22.77(0.28)	4.79	24.8(0.27)	91.8(1.1)
MoS_2/rGO	26.76(0.35)	5.44	28.2(0.3)	94.9(1.08)
N-MoS_2/rGO	29.54(0.42)	5.77	29.9(0.4)	98.8(1.2)
Pt/C	31.44(0.22)	6.10	31.6(0.2)	99.5(1.02)

* CPE: the catalyst is held at -1.0 V vs. RHE for 1 h in 1.0 M KOH solution at 25 °C.

3.3.6 Water splitting performance

Since it is of immense importance of developing a bi-functional water-splitting catalyst for commercial needs, N-MoS_2/N-rGO-2 was tested for both HER and OER in 1M KOH aqueous solution in a two-electrode system. **Figure 17** shows that the assembled N-MoS_2/N-rGO-2 || NMoS_2/N-rGO-2 system could deliver stable current densities of 10, 20, 30 and 50 mA cm^{-2} at cell voltages of respectively 1.48, 1.63, 1.71, and 1.83 V for 28 h. This performance overpasses that of so-far reported with reported MoS_2-based and rGO-based materials (**Table 12**), indicating high activity and excellent long-term stability .

Table 11. Mean value (standard deviation) of VO2 (measured and calculated) obtained after 1 h of a controlled potential electrolysis (CPE)*, together with the Faradaic Efficiency values, FE (%), for the studied catalysts.

Catalyst	V_m (O_2 / μmol h^{-1})	Q(CPE) (C)	$V_{calc.}$ (O_2 / μmol h^{-1})	FE (%)
N-rGO	10.32(0.17)	5.60	14.5(0.2)	71.2(1.1)
MoS_2	15.43(0.21)	7.37	19.1(0.26)	80.8(1.2)
N-MoS_2	21.07(0.26)	9.15	23.7(0.35)	88.9(1.1)
MoS_2/rGO	25.97(0.36)	10.73	27.8(0.4)	93.4(1.3)
N-MoS_2/rGO	29.26(0.42)	11.39	29.5(0.44)	99.2(1.5)
RuO_2	31.34(0.21)	12.12	31.4(0.2)	99.8(1.05)

* CPE: the catalyst is held at -1.0 V vs. RHE for 1 h in 1.0 M KOH solution at 25 °C.

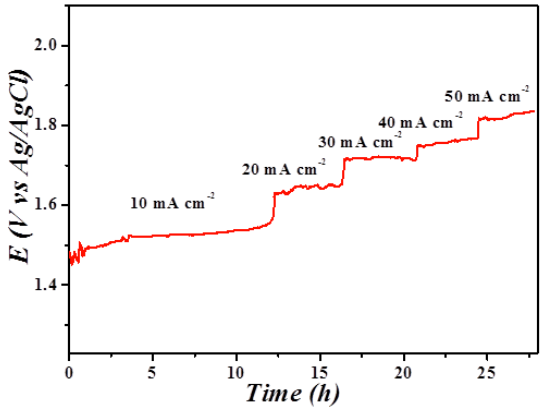

Figure 17 Chronoamperometric measurements of overall water splitting in 1M KOH aqueous solution at an applied current density of 10, 20, 30 and 50 mA cm^{-2}.

Table 12. Comparisons of cell potential for N-MoS_2/N-rGO_2 with reported MoS_2-based and rGO-based materials for overall water splitting.

Catalysis	Cell potential (mV) @10 mA cm^{-2}	Reference
N-MoS_2/N-rGO	1.48	This work
MoS_2-NiS_2/NGF	1.64	[51]
CoSx@Cu_2MoS_4-MoS_2/NSG	1.60	[52]
MoS_2–CoS_2@PCMT	1.59	[53]
porous C–N-MoS_2/CC-700	1.58	[54]
Co_9S_8@MoS_2/N-doped hollow carbon	1.56	[55]
$NiCo_2S_4$/N, S co-doped reduced graphene oxide	1.58	[56]
Co−SCN/RGO	1.63	[57]
NCS@N-rGO/NF	1.63	[58]
$CoNi_2S_4$–CNFs	1.55	[59]
$NiSe_2$/$FeSe_2$/rGO	1.57	[60]

3.4. Conclusion

In summary, we successfully constructed hierarchical N-MoS_2/N-rGO heterostructure by a facile hydrothermal strategy. Extensive characterization results proved the formation of flower-like heterostructure featuring large surface area, and optimized electronic configuration, abundant heterogeneous interfaces, and abundant electroactive sites. All these favorable features synergistically boosted the OER activity in alkaline solution and HER in both base and acid solutions, and improved the stability of the electrode material in alkaline conditions. When the N-MoS_2/N-rGO-2 electrode was used in a two-electrode alkaline electrolyzer system, it could drive current densities of 10, 20, 30 and 50 mA cm^{-2} at ultralow cell voltages of respectively only 1.48, 1.57, 1.65, and 1.74V with good stability for over 28 h. Taken together, the data collected in our work may open new avenues for rational design of inexpensive and highly-active electrode materials for various electrochemical processes.

3.5 References

1. Jaramillo, T. F. *et al.* Identification of active edge sites for electrochemical H_2 evolution from MoS_2 nanocatalysts. *Science (80-.).* **317**, 100–102 (2007).

2.Staszak-Jirkovský, J. *et al.* Design of active and stable Co-Mo-S_x chalcogels as pH-universal catalysts for the hydrogen evolution reaction. *Nat. Mater.* **15**, 197–203 (2016).

3.Liang, K. *et al.* S-Doped MoP nanoporous layer toward high-efficiency hydrogen evolution in ph-universal electrolyte. *ACS Catal.* **9**, 651–659 (2019).

4.Wang, H. *et al.* Electronic modulation of non-van der waals 2d electrocatalysts for efficient energy conversion. *Adv. Mater.* **33**, 1–25 (2021).

5.Zhang, J. *et al.* 3D Coral-like Ni_3S_2 on Ni foam as a bifunctional electrocatalyst for overall water splitting. *ACS Appl. Mater. Interfaces* **10**, 31330–31339 (2018).

6.Zhang, D., Mou, H., Lu, F., Song, C. & Wang, D. A novel strategy for 2D/2D NiS/graphene heterostructures as efficient bifunctional electrocatalysts for overall water splitting. *Appl. Catal. B Environ.* **254**, 471–478 (2019).

7.Liu, Y. *et al.* Interface engineering of (Ni, Fe)S_2@MoS_2 heterostructures for synergetic electrochemical water splitting. *Appl. Catal. B Environ.* **247**, 107–114 (2019).

8.King, L. A. *et al.* A non-precious metal hydrogen catalyst in a commercial polymer electrolyte membrane electrolyser. *Nat. Nanotechnol.* **14**, 1071–1074 (2019).

9.Yang, F., Chen, Y., Cheng, G., Chen, S. & Luo, W. Ultrathin nitrogen-doped carbon coated with CoP for efficient hydrogen evolution. *ACS Catal.* **7**, 3824–3831 (2017).

10.Liu, C. *et al.* Integration of Ni doping and a Mo_2C/MoC heterojunction for hydrogen evolution in acidic and alkaline conditions. *ACS Appl. Mater. Interfaces* **13**, 22646–22654 (2021).

11.Zhang, X. *et al.* High-Performance MoC Electrocatalyst for Hydrogen Evolution Reaction Enabled by Surface Sulfur Substitution. *ACS Appl. Mater. Interfaces* **13**, 40705–40712 (2021).

12.Zhang, J. *et al.* Engineering water dissociation sites in MoS_2 nanosheets for accelerated electrocatalytic hydrogen production. *Energy Environ. Sci.* **9**, 2789–2793 (2016).

13.Ma, F. *et al.* One-step synthesis of Co-doped 1T-MoS_2 nanosheets with efficient and stable HER activity in alkaline solutions. *Mater. Chem. Phys.* **244**, 122642 (2020).

14.Ma, X. *et al.* Ultrathin Co(Ni)-doped MoS_2 nanosheets as catalytic promoters enabling efficient solar hydrogen production. *Nano Res.* **9**, 2284–2293 (2016).

15.Shi, Y. *et al.* Energy level engineering of MoS_2 by transition-metal doping for accelerating hydrogen evolution reaction. *J. Am. Chem. Soc.* **139**, 15479–15485 (2017).

16.Xiao, W. *et al.* Dual-Functional N dopants in edges and basal plane of MoS_2 nanosheets toward efficient and durable hydrogen evolution. *Adv. Energy Mater.* **7**, 1–10 (2017).

17.Qin, J. *et al.* Activating edge-Mo of 2H-MoS_2 via coordination with pyridinic N-C for pH-universal hydrogen evolution electrocatalysis. *ACS Catal.* **11**, 4486–4497 (2021).

18.Wu, J. *et al.* Exfoliated 2D transition metal disulfides for enhanced electrocatalysis of oxygen evolution reaction in acidic medium. *Adv. Mater. Interfaces* **3**, 1–6 (2016).

19.Karmodak, N. & Andreussi, O. Oxygen evolution on MoS_2 edges: activation through surface oxidation. *J. Phys. Chem. C* **125**, 10397–10405 (2021).

20.Mohanty, B. *et al.* MoS_2 Quantum Dots as Efficient Catalyst Materials for the Oxygen Evolution Reaction. *ACS Catal.* **8**, 1683–1689 (2018).

21.Li, M. *et al.* Flower-like Nitrogen-co-doped MoS_2@RGO Composites with

Excellent Stability for Supercapacitors. *ChemElectroChem* **8**, 2903–2911 (2021).

22.Hernandez Ruiz, K. *et al.* Effect of microstructure on HER catalytic properties of MoS_2 vertically standing nanosheets. *J. Alloys Compd.* **747**, 100–108 (2018).

23.She, Z. W. *et al.* Combining theory and experiment in electrocatalysis: Insights into materials design. *Science (80).* **355**, (2017).

24.Han, X. *et al.* Hydrogen evolution reaction on hybrid catalysts of vertical MoS_2 nanosheets and hydrogenated graphene. *ACS Catal.* **8**, 1828–1836 (2018).

25.Hidayah, N. M. S. *et al.* Comparison on graphite, graphene oxide and reduced graphene oxide: Synthesis and characterization. *AIP Conf. Proc.* **1892**, (2017).

26.Li, X., Wang, C., Xue, H., Pang, H. & Xu, Q. Electrocatalysts optimized with nitrogen coordination for high-performance oxygen evolution reaction. *Coord. Chem. Rev.* **422**, 213468 (2020).

27.Wang, H. *et al.* Structural and electronic optimization of MoS_2 edges for hydrogen evolution. *J. Am. Chem. Soc.* **141**, 18578–18584 (2019).

28.Yan, K. & Yiran, L. Direct growth of MoS_2 microspheres on Ni foam as a hybrid nanocomposite efficient for oxygen evolution reaction. *Small* **12**, 2975–2981 (2016).

29.Tang, B. *et al.* Simultaneous edge and electronic control of MoS_2 nanosheets through Fe doping for an efficient oxygen evolution reaction. *Nanoscale* **10**, 20113–20119 (2018).

30.Wang, Y. *et al.* Controlled synthesis of Ni-doped MoS_2 hybrid electrode for synergistically enhanced water-splitting process. *Chem. - A Eur. J.* **26**, 4097–4103 (2020).

31.Xiong, Q. *et al.* Cobalt covalent doping in MoS_2 to Induce Bifunctionality of Overall Water Splitting. *Adv. Mater.* **30**, 1801450 (2018).

32.Amiinu, I. S. *et al.* Multifunctional Mo–N/C@MoS_2 electrocatalysts for HER, OER,

ORR, and Zn–air batteries. *Adv. Funct. Mater.* **27**, 1702300 (2017).

33.Guo, Y. *et al.* Mesoporous iron-doped MoS_2/$CoMo_2S_4$ heterostructures through organic-metal cooperative interactions on spherical micelles for electrochemical water splitting. *ACS Nano* **14**, 4141–4152 (2020).

34.Zhang, J. *et al.* Engineering water dissociation sites in MoS_2 nanosheets for accelerated electrocatalytic hydrogen production †. *Energy Environ. Sci* **9**, 2789 (2016).

35.Sa, Y. J. *et al.* Heterogeneous Co-N/C electrocatalysts with controlled cobalt site densities for the hydrogen evolution reaction: structure-activity correlations and kinetic insights. *ACS Catal.* **9**, 83–97 (2019).

36.Wang, S. *et al.* Ultrastable in-plane 1T–2H MoS_2 heterostructures for enhanced hydrogen evolution reaction. *Adv. Energy Mater.* **8**, (2018).

37.Kuang, P., Tong, T., Fan, K. & Yu, J. In situ fabrication of Ni-Mo bimetal sulfide hybrid as an efficient electrocatalyst for hydrogen evolution over a wide pH range. *ACS Catal.* **7**, 6179–6187 (2017).

38.Xue, J. Y. *et al.* In situ generation of bifunctional Fe-doped MoS_2 nanocanopies for efficient electrocatalytic water splitting. *Inorg. Chem.* **58**, 11202–11209 (2019).

39.Liang, T., Liu, Y., Cheng, Y., Ma, F. & Dai, Z. Scalable synthesis of a mos_2/black phosphorus heterostructure for pH-universal hydrogen evolution catalysis. *ChemCatChem* **12**, 2840–2848 (2020).

40.Yu, X. Y. *et al.* Formation of Ni–Co–MoS_2 nanoboxes with enhanced electrocatalytic activity for hydrogen evolution. *Adv. Mater.* **28**, 9006–9011 (2016).

41.Staszak-Jirkovský, J. *et al.* Design of active and stable Co–Mo–Sx chalcogels as pH-universal catalysts for the hydrogen evolution reaction. *Nat. Mater. 2015 152* **15**, 197–203 (2015).

42.Jiang, J., Gao, M., Sheng, W. & Yan, Y. Hollow chevrel-phase $NiMo_3S_4$ for

hydrogen evolution in alkaline electrolytes. *Angew. Chemie* **128**, 15466–15471 (2016).

43.Qiao, W. *et al.* Construction of Active orbital via single-atom cobalt anchoring on the surface of 1T-MoS_2 basal plane toward efficient hydrogen evolution. *ACS Appl. Energy Mater.* **3**, 2315–2322 (2020).

44.Zheng, Z. *et al.* Boosting hydrogen evolution on MoS_2 via co-confining selenium in surface and cobalt in inner layer. *Nat. Commun.* **11**, (2020).

45.Wang, D., Xie, Y. & Wu, Z. Amorphous phosphorus-doped MoS_2 catalyst for efficient hydrogen evolution reaction. *Nanotechnology* **30**, 205401 (2019).

46.Kibsgaard, J. & Jaramillo, T. F. Molybdenum phosphosulfide: an active, acid-stable, earth-abundant catalyst for the hydrogen evolution reaction. *Angew. Chemie* **126**, 14661–14665 (2014).

47.Geng, S. *et al.* Two-dimensional confined synthesis of metastable 1t-phase mos_2 nanosheets for the hydrogen evolution reaction. *ACS Appl. Nano Mater.* **5**, 1377–1384 (2022).

48.Wang, H. *et al.* Optimizing MoS_2 Edges by Alloying Isovalent W for Robust Hydrogen Evolution Activity. *ACS Catal.* **8**, 9529–9536 (2018).

49.Sangeetha, D. N., Santosh, M. S. & Selvakumar, M. Flower-like carbon doped MoS_2/Activated carbon composite electrode for superior performance of supercapacitors and hydrogen evolution reactions. *J. Alloys Compd.* **831**, 154745 (2020).

50.Beyene, B. B., Mane, S. B. & Hung, C.-H. Highly efficient electrocatalytic hydrogen evolution from neutral aqueous solution by a water-soluble anionic cobalt(II) porphyrin. *Chem. Commun.* **51**, 15067–15070 (2015).

51.Kuang, P., He, M., Zou, H., Yu, J. & Fan, K. 0D/3D MoS_2-NiS_2/N-doped graphene foam composite for efficient overall water splitting. *Appl. Catal. B Environ.* **254**, 15–

25 (2019).

52.Nguyen, D. C. *et al.* Rational Design of Core@shell Structured CoS_x@Cu_2MoS_4 Hybridized MoS_2/N,S-Codoped Graphene as Advanced Electrocatalyst for Water Splitting and Zn-Air Battery. *Adv. Energy Mater.* **10**, 1–14 (2020).

53.Yang, J., Chai, C., Jiang, C., Liu, L. & Xi, J. MoS_2–CoS_2 heteronanosheet arrays coated on porous carbon microtube textile for overall water splitting. *J. Power Sources* **514**, 230580 (2021).

54.Chen, W. *et al.* Partial sulfur vacancies created by carbon-nitrogen deposition of MoS_2 for high-performance overall electrocatalytic water splitting. *Nanoscale* **13**, 14506–14517 (2021).

55.Kim, M. *et al.* Kirkendall effect induced bifunctional hybrid electrocatalyst (Co_9S_8@MoS_2/N-doped hollow carbon) for high performance overall water splitting. *J. Power Sources* **493**, 229688 (2021).

56.Li, H. *et al.* $NiCo_2S_4$ microspheres grown on N, S co-doped reduced graphene oxide as an efficient bifunctional electrocatalyst for overall water splitting in alkaline and neutral pH. *Nano Res.* **15**, 950–958 (2022).

57.Jo, W. K., Moru, S. & Tonda, S. Cobalt-coordinated sulfur-doped graphitic carbon nitride on reduced graphene oxide: an efficient metal-(n,s)-c-class bifunctional electrocatalyst for overall water splitting in alkaline media. *ACS Sustain. Chem. Eng.* **7**, 15373–15384 (2019).

58.Lee, H. S., Pan, J., Gund, G. S. & Park, H. S. Vertically aligned $NiCo_2S_4$ nanosheets deposited on n-doped graphene for bifunctional and durable electrode of overall water splitting. *Adv. Mater. Interfaces* **7**, 1–8 (2020).

59.Ranjith, K. S. *et al.* Ultrathin rGO-wrapped free-standing bimetallic $CoNi_2S_4$-carbon nanofibers: an efficient and robust bifunctional electrocatalyst for water splitting.

Nanotechnology **31**, (2020).

60. Ahmad, M., Xi, B., Gu, Y., Zhang, H. & Xiong, S. $NiSe_2/FeSe_2$ heterostructured nanoparticles supported on rGO for efficient water electrolysis. *Inorg. Chem. Front.* **9**, 448–457 (2022).

Chapter 4

Exfoliation of Ti_3AlC_2 in $NaBF_4$/HCl Aqueous Solution for Effective Hydrogen Evolution Reaction in Acidic Medium

4.1 Introduction

Molecular hydrogen (H_2) represents an essential and non-exhaustible energy carrier due to its sustainability, high energy density and zero emission. H_2 production is mainly achieved through water splitting under photocatalytic, electrocatalytic or photoelectrochemical driven processes. Even though, these processes own all the attributes for green H_2 generation, they require semiconductor- or metal-based catalysts to drive the water splitting efficiently. For instance, electrochemical water splitting i.e. hydrogen evolution reaction (HER) catalyzed by noble metals such as Pt/C is one of the most effective processes for H_2 generation, owing to fast reaction kinetics (small Tafel slope) and low overpotential. Despite these advantages, the use of noble metal catalysts for industrial applications is hindered by the high cost and low abundance of these metals.

The last decades have seen a steady increase of reports on the design of transition metal-based electrocatalysts with a performance that could reach or even outperform that of Pt/C for HER and particularly in alkaline media. Despite these outstanding features, the long-term stability of transition metal catalysts was pointed out in many scientific literature reports. In addition, most of these catalysts have been processed in form of nanomaterials to expose a high density of active sites (high surface area) and thus improve their performance. Although this approach satisfies the requirement for

high performance, nanomaterials commonly face aggregation, which is responsible of decline of the density of active sites and hence the catalytic activity. To address this hurdle, the nano-catalysts are supported on various carbon-based materials such as carbon nanotubes and graphene. Even though, graphene and its derivatives (graphene oxide and reduced graphene oxide) have been essentially applied as supports in electrocatalysis, their intrinsic catalytic activity is relatively limited for HER.

Following the discovery of graphene, a 2D material with many beneficial features, the last decades have witnessed tremendous and continuous efforts in the development of 2D materials to fulfill the many challenging issues the world is facing in various critical research and technological fields, including energy, environment and biomedicine. Among these, transition metal carbides and nitrides (MXenes) have experienced a rapid development, owing to their fascinating properties, such as good mechanical strength, high electrical conductivity, and enhanced surface area, recognized as beneficial attributes for potential applications in electrocatalysis.[1,2]

Up to now, MXenes are mainly synthesized through etching with hydrofluoric acid (HF) [3] or reaction-generated HF [4] at room temperature. However, this method could limit the synthesis of various MXenes due to the instability of Al-containing MAX-phase precursors in fluoride-based aqueous solutions, reduce material performance with inert F-termination, and cause environment problem by F-containing solution. Therefore, the development of F-containing salt or even no F-containing etching solution is intensively sought after to extend further MXenes' applications, in which monofluoride (LiF, NaF, KF and NH_4F)[4–6] is mostly mixed with concentrated hydrochloric acid (HCl) and difluorides (($NaHF_2$, KHF_2, $NH4HF_2$)[7–9] . Nevertheless, direct contact with fluoride was inevitable during the etching reaction in those methods.

Herein, we synthesized $Ti_xC_yT_x$ via a hydrothermal method using a mixture of sodium tetrafluoroborate ($NaBF_4$) and hydrochloric acid (HCl), and assessing the effects of hydrothermal duration, temperature, concentration of HCl and $NaBF_4$ on the etching process, to find the optimized etching condition. Besides, the resulted $Ti_xC_yT_x$ samples showed a promising performance for the hydrogen evolution in 0.5M H_2SO_4 solution. Our strategy provides a promising pathway for the facile and sustainable production of MXenes-based materials.

4.2 Experimental section

4.2.1 Synthesis of MXenes

Ti_3C_2 powder was prepared by etching 200 mg of Ti_3AlC_2 (MAX phase) powder in different concentrations of $NaBF_4$ (0, 0.1M, 0.2M and 0.3M, named as S-F0, S-F1, S-F2 and S-F3, respectively) + HCl (0, 4M, 8M and 10M, named as S-H0, S-H4, S-H8 and S-H10, respectively) at different temperatures (100, 120, 140, 160 and 180°C, named as S-100, S-120, S-140, S-160, and S-180, respectively) for variable durations (8, 12, 24 and 36 h, named as S-8, S-12, S-12, S-24, and S-36, respectively). The variables and corresponded name are summarized in **Table 1**.

Table 1 Variables of the synthesis of MXenes.

Temperature		Duration		Concentration of $NaBF_4$		Concentration of HCl	
Value (°C)	Name	Value (h)	Name	Value (M)	Name	Value (M)	Name
100	S-100	8	S-8	0	S-F0	0	S-H0
120	S-120	12	S-12	0.1	S-F1	4	S-H4
140	S-140	24	S-240.	0.2	S-F2	8	S-H8
160	S-160	36	S-36	0.3	S-F3	12	S-H12
180	S-180						

CPE*: Temperature is set as a variable, others are fixed at 0.2M, 8M and 12h assigned for the concentration of $NaBF_4$ and HCl and duration. Duration is set as a as a variable, others are fixed

at 0.2M, 8M, and 160°C assigned for the concentration of $NaBF_4$ and HCl and temperature. The concentration of $NaBF_4$ is set as a variable, others are fixed at 8M, 12h and 160 °C assigned for the concentration of HCl, duration and temperature. The concentration of HCl is set as a variable, others are fixed at 0.2M, 12h and 160 °C assigned for the concentration of $NaBF_4$, duration and temperature.

As a counterpart, 200 mg of Ti_3C_2 power was also etched in 30 mL of HF under magnetic stirring at room temperature for 48 h. All resulted mixed solutions were centrifuged and sonicated in ethanol and pure water until the pH of the supernatant reached about 6. Then all samples were placed in a refrigerator for 24 h before being freezing-dried at -84°C for 48 h.

4.2.2 Electrochemical experiments

All electrochemical experiments were tested in a conventional three electrode system with Saturated Calomel Electrode (SCE) and graphite rod as reference and counter electrodes, respectively. For the working electrode preparation, 4 mg of the samples were dispersed into 1 mL of ethanol/water solution (1:2) along with 10 μL Nafion as catalyst binder and sonicate the solution for 10 min. From the resulting catalyst ink, 10 μL was drop-casted onto glassy carbon electrode (GCE, d=3 mm) and kept for overnight drying and directly utilized as a working electrode. Linear Sweep Voltammetry (LSV) curves were recorded in a potential range from 0.2 to -1.0 V (*vs.* RHE) at a scan rate of 5 mV s^{-1} in 0.5 M H_2SO_4.

Electrochemical Impedance spectroscopy (EIS) analysis was performed at a frequency range of 100 KHz to 0.01 Hz with an amplitude of 10 mV.

Stability test of the catalyst was performed under the same potential window over 3000 LSV cycles at a scan rate of 100 mV s^{-1}. Further, chronopotentiometry was measured by varying the current density (20, 40, 60, 80 and 100 mA cm^{-2}) for

approximately 6 h each respectively.

4.3 Results and discussion

The aim of the present study was to investigate sodium tetrafluoroborate ($NaBF_4$) as a fluoride source for etching "Al" in Ti_3AlC_2 MAX phase on the electrochemical activity of the generated Ti_3C_2 MXenes sheets. The influence of different operating parameters such as $NaBF_4$ concentration, temperature, time and addition of HCl was systematically assessed to achieve the most effective catalyst for electrochemical hydrogen evolution in acidic medium (**Figure 1**).

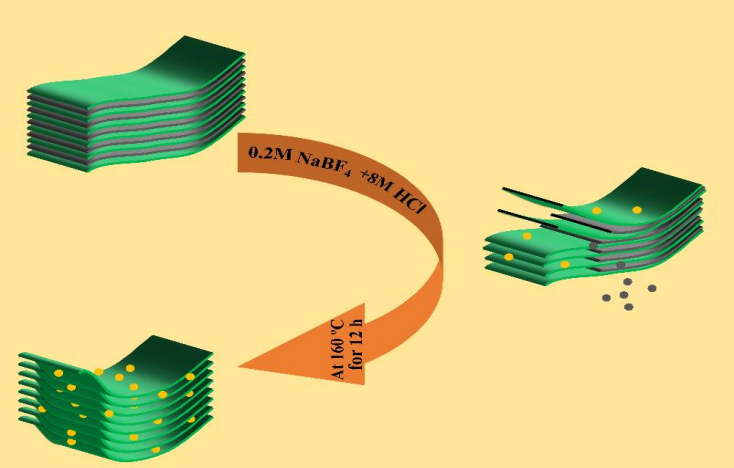

Figure 1. Scheme of the etching process of Ti_3AlC_2, the yellow ball represents the chemical group adsorbed on Ti_3C_2 layers, such as O, OH, F or Cl; the gray ball corresponds to Al element.

The crystal structure of the $Ti_xC_yT_x$ MXenes, prepared by Ti_3AlC_2 etching in 0.2M $NaBF_4$/8M HCl at 160 °C for 12 h, was assessed using X-ray diffraction (XRD) analysis and compared to that of Ti_xC_y MXenes, produced using the common etching method in HF-based aqueous solution, and that of Ti_3AlC_2 MAX phase precursor. **Figure 2** clearly reveals the alteration of the crystal structure of the initial Ti_3AlC_2 MAX phase precursor after chemical etching in both HF and $NaBF_4$/HCl aqueous solutions. The XRD plot of Ti_3AlC_2 comprises very sharp peaks at 2θ of 9.5°, 19.1°, 33.9°, 38.7°, 41.7°, 48.3°,

52.3°, 56.3°, 60.1°, 65.4°, 70.3°, 73.8° and 75.5° ascribed respectively to the (002), (004), (011), (014), (015), (00 10), (018), (019), (110), (01 11), (01 12), (118) and (025) diffraction planes.[15] After etching in 0.2M $NaBF_4$/8M HCl at 160 °C for 12 h, the absence of the main characteristic peaks of the MAX phase at 9.5° and 38.7° and the appearance of several broad features at 6.5°, 7.3°, 34.5°, 35.9°, 38.9°, 40.1°, 40.4°, 41.8°, 60.4°, 60.5°, 60.7°, and 74.6° clearly indicate the successful MXenes formation. The peaks at 7.3°, 34.5°, 41.°8 and 60.7° are ascribed to the (002), (103), (105) and (110) diffractions planes, respectively, in good agreement with our recent study. [16] The broadening effect was attributed in many reports to cation and water intercalations during the Al dissolution in the etchant solution. [15] Of note, some additional peaks due to TiC are also present in the diffractogram. This contrasts with the diffraction pattern of Ti_3AlC_2 MAX phase etched in HF at room temperature. 7.2, 14.3, 28.8, 34.2, 35.9, 37.0, 40.7, 41.7, 44.9, 60.9, and 65.5°. Again, most of the sharp diffraction peaks of the Ti_3AlC_2 were absent after etching and new broader features appeared. Taken together, the XRD data provided strong evidence of Al etching in $NaBF_4$/HCl solution.

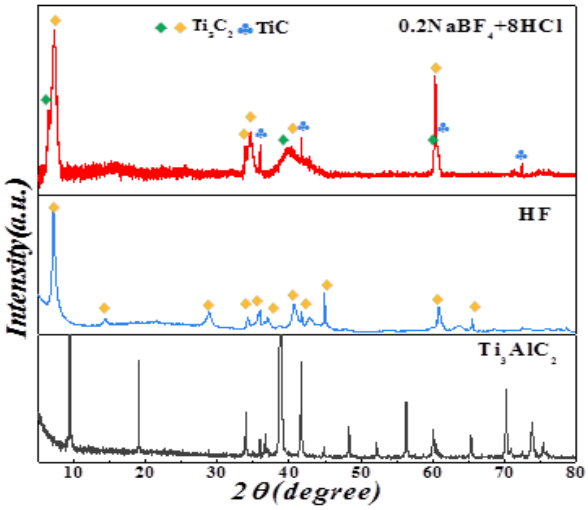

Figure 2. XRD patterns of pristine Ti_3AlC_2 before and after etching in HF for 48h or 0.2M $NaBF_4$/8M HCl at 160 ºC for 12h.

Furthermore, Raman spectroscopy, a valuable tool commonly used to study the structural features of 2D materials, was used to follow the changes after MAX etching in HF and $NaBF_4$/HCl aqueous solutions (**Figure 3**). The Raman spectrum of the initial Ti_3AlC_2 MAX phase comprises several sharp peaks at 143, 240, 442, 606 cm^{-1} and a broader shoulder at 699 cm^{-1}. The first 3 peaks are ascribed to different Ti-Al vibration modes, while the last bands are assigned to Ti-C vibrations. After etching in 0.3M $NaBF_4$/8M HCl at 160 °C for 12 h or the commonly used HF aqueous solutions at room temperature (24 h), the vibrations bands due to Ti-Al vanished while those originating from Ti-C vibrations remained unaltered even though they became broader. The results clearly infer that Ti-Al bonds were removed in both etching solutions, in good agreement with previously-reported data.

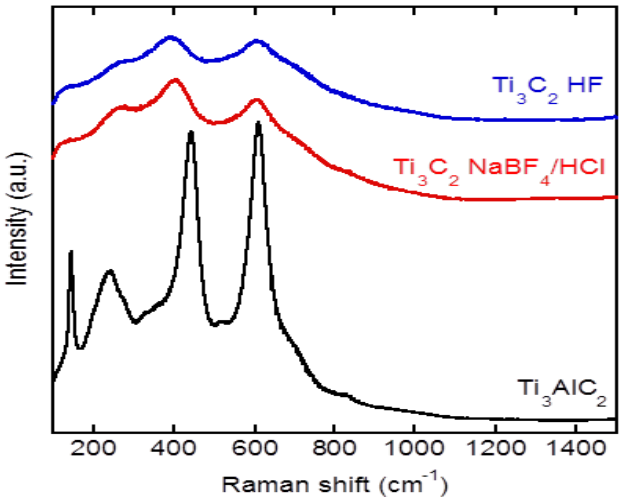

Figure 3. Raman spectra of Ti_3AlC_2 before and after etching in etching in HF for 48h or 0.3M $NaBF_4$/8M HCl at 160 ºC for 12h.

X-ray photoelectron spectroscopy (XPS) was used to track the chemical and electronic state changes of the Ti_3AlC_2 MAX phase upon etching in HF and $NaBF_4$/HCl aqueous solutions. The XPS survey spectrum of the Ti_3AlC_2 MAX precursor comprises the characteristic peaks ascribed to Al 2p, C 1s, Ti 2p and O 1s with atomic

concentration distribution of 14.51, 31.73, 14.28, and 39.48 at. %, respectively (**Table 2**). The presence of oxygen component most likely originates from partial oxidation of the material and eventual surface contamination during material storage and handling (**Figure 4a**). Chemical etching in the commonly-used HF aqueous solution at room temperature led to the disappearance of the peaks due to Al 2s and Al 2p accompanied with an increase of F content (20.68 at. %) and a significant decrease of the O 1s from 39.48 to 30.62 at.%. It has been acknowledged that O and F could bind to the MXenes surface.[15] Meanwhile the concentrations of C 1s and Ti 2p remained almost unaltered. The situation is totally different for the Ti_3AlC_2 MAX precursor etched in $NaBF_4$/HCl where a substantial increase of the C (31.76 to 46.06 at. %) ant Ti (14.28 to 21.63 at. %) contents were obvious, while the O content decreased significantly (39.48 to 23.45 at. %). It is of note that the Al component was absent in the XPS survey profile of Ti_3AlC_2 etched in 0.2M $NaBF_4$/8M HCl at 160 °C for 12 h. The data clearly indicate the effective etching of the MAX phase in $NaBF_4$/HCl at high temperature. The presence of F (4.08 at. %) and Cl (4.78 at. %) suggests their potential contribution in the surface termination of the MXenes sheets.

Table 2. Atom percent of Ti_3AlC_2 before and after etching in HF at room temperature for 48 h and 0.2M $NaBF_4$/8M HCl at 160°C for 12h

Name	**Atomic %**		
	MAX	**HF for 48h**	**0.2MNaBF4/8HCl at 160°C for 12h**
Al 2p	14.51	-	-
Cl 2p	-	-	4.78
C 1s	31.73	33.37	46.06
Ti 2p	14.28	15.33	21.63
O 1s	39.48	30.62	23.45
F 1s	-	20.68	4.08

From Ti 2p high resolution in **Figure 4b**, the main Ti $2p_{3/2}$ peaks of Ti-C for Ti_3AlC_2, are located at around 454.8, 455.1, and 455.3 eV. After etching with HF or 0.2M $NaBF_4$/8M HCl at 160 ºC for 12h, the Ti $2p_{3/2}$ peaks at around 455.1, 456,4, and 457.4 eV are ascribed to Ti-C-T_O, Ti-C-$T_{F/O}$ and Ti-C-T_F in $Ti_3C_2T_x$ and $Ti_xC_yT_x$, which is caused by the adsorption of F and O on Ti atoms. Besides, the Ti 2p3/2 peak at around of 458.8 eV mainly raised from TiO_2 due to the oxidation of Ti upon exposure to ambient air.

The C 1s high-resolution spectrum of Ti_3AlC_2 can be curve-fitted with 3 components at around 281.5, 284.9, 286.0, and 287.4 eV ascribed respectively to C-Ti, C-C, C-O and C=O bonds (**Figure 4c**).[16,17] After etching in HF or 0.2M $NaBF_4$/8MHCl aqueous solutions, similar XPS spectra and fittings were recorded, suggesting that the carbon chemical environment was not affected during the Ti_3AlC_2 MAX etching. The Al 2p high-resolution plot in **Figure 4d** also confirms the selective etching of Al elements from Ti_3AlC_2 phase in both $NaBF_4$/HCl and HF etching conditions.

The O 1s spectrum of Ti_3AlC_2 in **Figure 4e** comprises TiO_2 (530.0 eV), OH-TiO_2 (531eV), and Al_2O_3 (532.2 eV) components. Apart from TiO_2 peaks, the peak of O_x/OH-termination on $Ti_3C_2T_x$ and $Ti_xC_yT_x$ appeared around at 531.63 and 531.90 eV. From **Figure 4f**, F-Ti, F-Al, and Al $(OF)_x$ signals are observed at around 684.8, 686.6, and 687.9 in $Ti_3C_2T_x$ and $Ti_xC_yT_x$. However, the content of Al $(OF)_x$ and F-Al decrease significantly upon etching in 0.2M $NaBF_4$/8M HCl at 160°C for 12 h, confirming this condition could almost completely remove the Al-containing residues. The binding energies of all elements are summarized in **Table 3.**

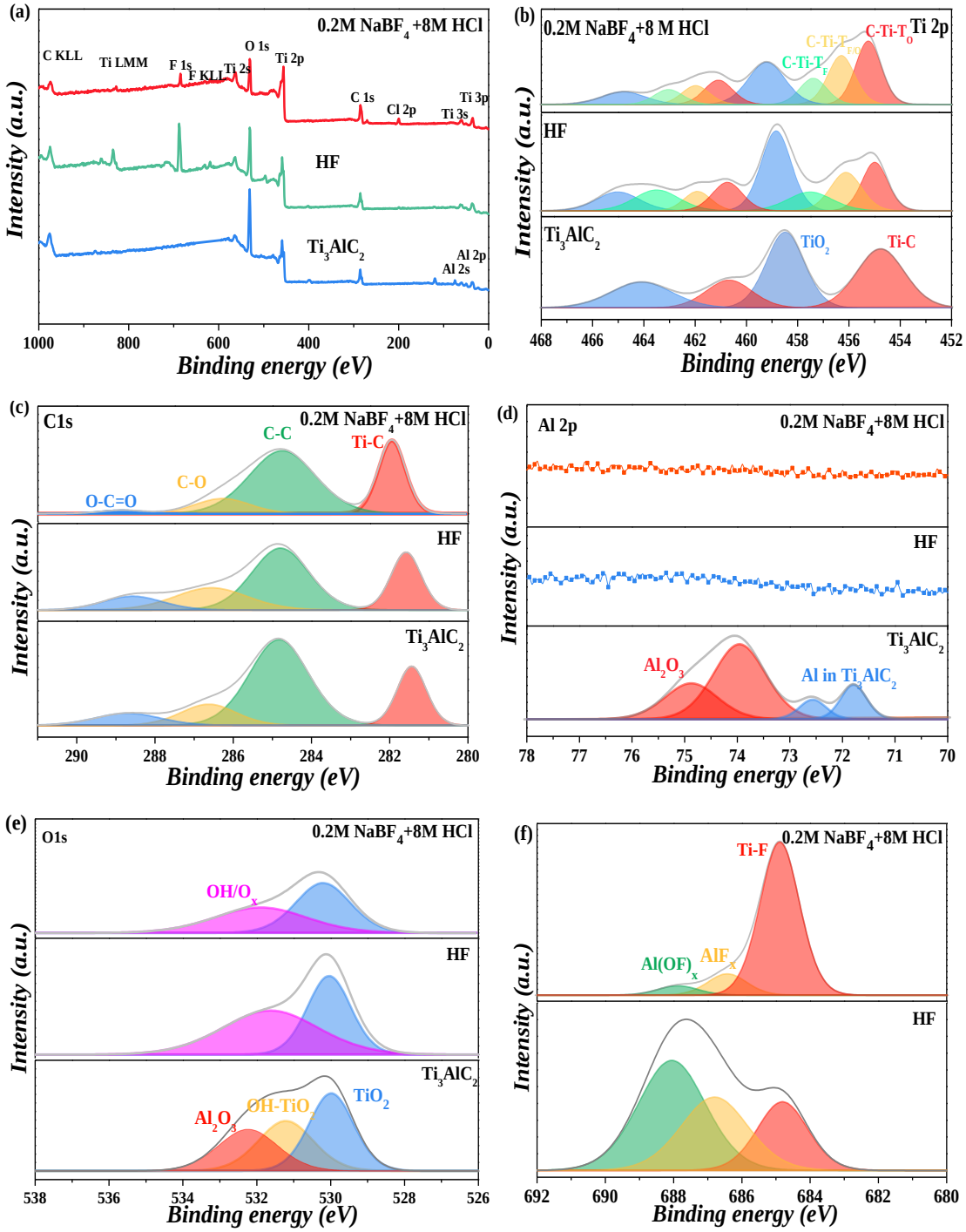

Figure 4. XPS spectra of Ti_3AlC_2 precursor before and after etching in HF or 0.2M $NaBF_4$/ 8M HCl at 160°C for 12h: (**a**) survey spectra, and high-resolution component peak fits of (**b**) Ti 2p, (**c**) C 1s, (**d**) Al 2p, and (**e**) O 1s, (**f**) F 1s regions.

Table 3 summarizes the fitted high-resolution XPS peaks of Ti_3AlC_2 before and after etching with HF at room temperature for 48 h or 0.2M $NaBF_4$/8M HCl at 160°C for 12h.

Region	Binding energy (eV)			Assignment
	MAX	HF	0.2M $NaBF_4$+8M HCl at 160°C for 12h	
Ti 2p3/2 (2p1/2)	454.8 (460.8)	455.0 (460.7)	455.2 (461.1)	C–Ti–O
		456.10 (461.9)	456.3 (462.0)	C–Ti–O/F
		457.5 (463.5)	457.4 (463.0)	C–Ti–F
	458.5 (464.1)	458.8 (465.1)	459.21 (464.8)	TiO_2
C 1s	281.5	281.6	281.9	C–Ti–(O/OH/F)
	284.9	284.8	284.7	C–C
	287.4	286.9	286.8	CH_x/C–O
F 1s	-	684.8	684.9	C–Ti–F
	-	686.8	686.5	AlF_x
	-	688.05	687.9	$Al(OF)_x$
O 1s	529.9	530.05	530.2	TiO_2
	531.7	531.6	531.9	C–Ti–O_x and/or OR
	532.2			Al_2O_3

The morphology of the Ti_3AlC_2, $Ti_xC_yT_x$, $Ti_3C_2T_x$ are observed by SEM, as shown in **Figure 5**. The Ti_3AlC_2 MAX phase consists of large crystals with layered morphology (**Figure 5a-c**). The flake-shape folded structure shown in **Figure 5d-i** demonstrates the successful synthesis of MXenes. In addition, the distance between the layers of $Ti_xC_yT_x$ is larger than that of $Ti_3C_2T_x$. EDS analysis of these three samples in **Figure 6a-c** adds another proof that Al element have been selectively removed from

the MAX phase.

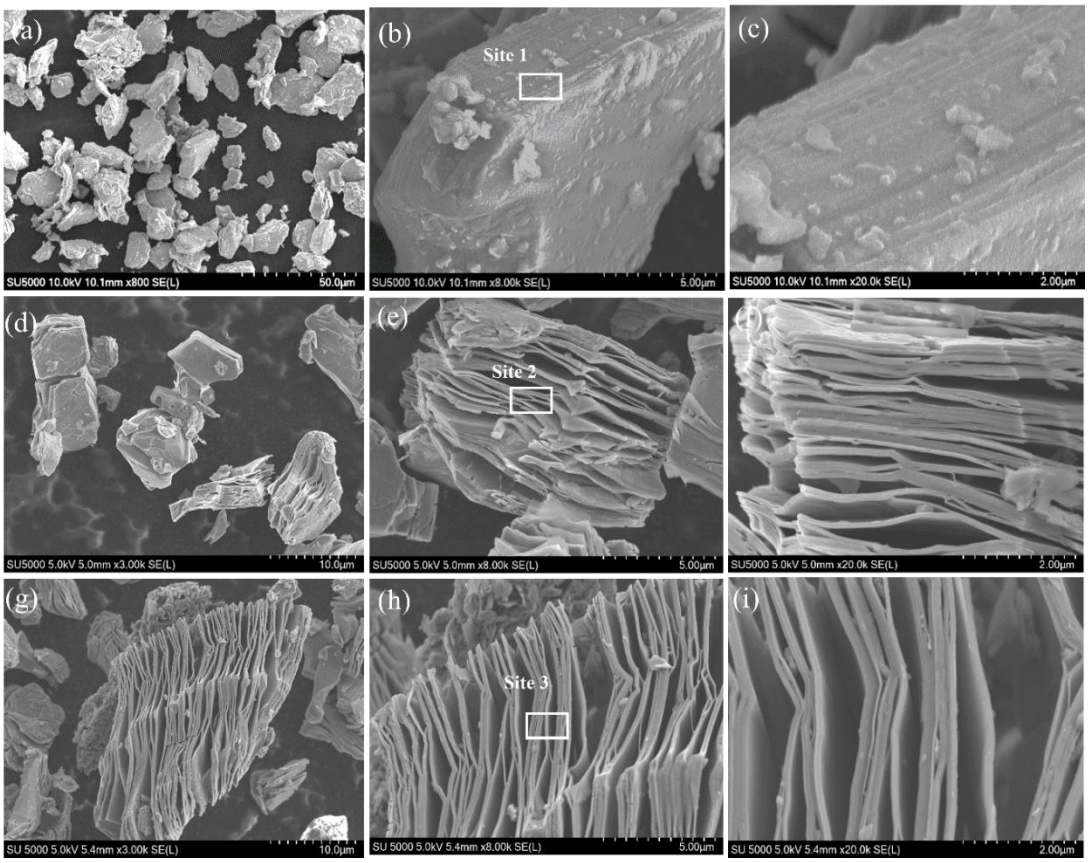

Figure 5. SEM analysis of Ti_3C_2 obtained by chemical etching of Ti_3AlC_2 in 0.2M $NaBF_4$/8M HCl at 160 °C for 12 h (**a, d**, **g**), HF at room temperature for 48 h (**b, e, h**) and water at 160 °C for 12 h (**c, f, i**).

In order to understand the influence of the temperature, duration, concentrations of $NaBF_4$ and HCl on Ti_3AlC_2 etching, XRD patterns of resulted Ti_xC_yTx samples synthesized at different etching conditions are displayed in **Figure 7**. Herein, the control variable was employed to study the above-mentioned factors. The duration and concentrations of HCl and $NaBF_4$ are set as 12h, 8M and 0.2M, separately, when the temperature was chosen as a variable. From **Figure 7a**, the sharp diffraction peak at 2θ of 38.73º, assigned to (103) facet of Ti_3AlC_2, disappeared when the hydrothermal process was performed at a temperature of 120℃.

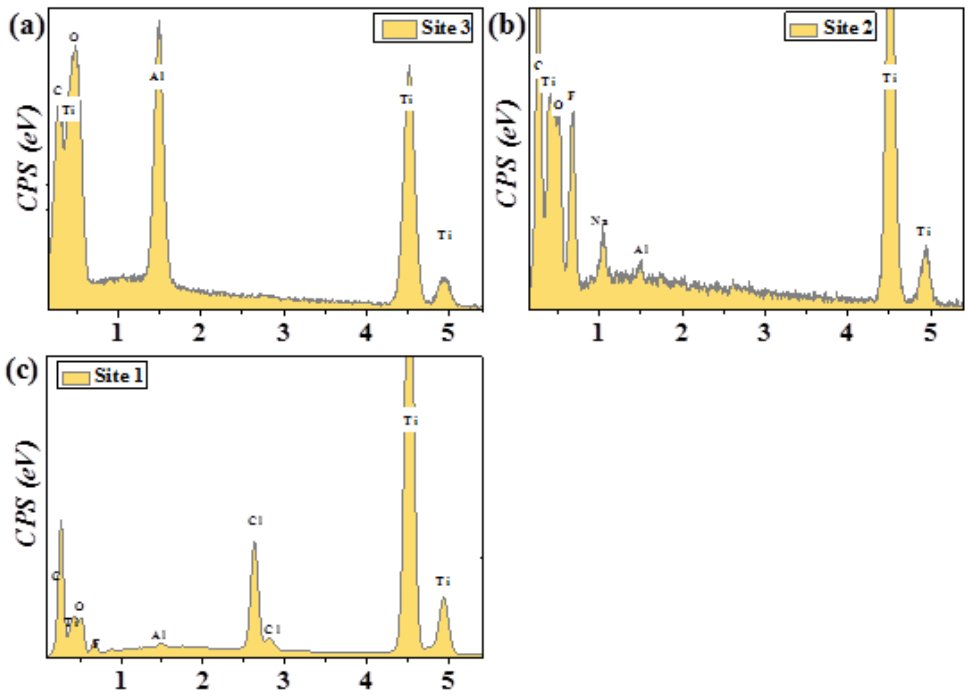

Figure 6. Energy dispersive spectra (EDS) of (**a**) site 1 in **Figure 5d**, (**b**) site 2 in **Figure 5e**, and (**c**) site 3 in **Figure 5f**.

Upon varying the temperature, it is clear only Ti_3C_2 and TiC peaks are observed when the temperature was increased to 140 and 160 ºC, while the crystal peaks of TiO_2 at 25.06°, 47.90°, 53.83° and 62.53º assigned respectively to the (101), (200), (105) and (213) plans were found when the temperature increase to 180° C. The diffraction peaks at 35.9° and 41.7° might be attributed to the TiC impurity, probably originating from the synthesis process of Ti_3AlC_2. The SEM and EDS were employed to test the morphology and composition of samples synthesized at 100 and 180 ºC in **Figure 8a, b**. Although the layered structure was kept, there was no obvious flake-shape structure in the sample etched at 100°C (**Figure 8a**). It is clear that the flake-shaped structure appeared in the sample etched at 180°C is similar to that of the sample etched at 160°C in **Figure 5g-i**, while small amount of TiO_2 was detected on the surface of $Ti_xC_yT_x$ flakes. From above analysis, we found that the temperature of 120, 140 or 160°C is suitable for the hydrothermal etching process of MAX phase.

Figure 7b displays the XRD of studied MXenes samples etched with 0.2 M $NaBF_4$/8M HCl, at 160°C for 8, 12, 24 and 36 h. The peak of the (002) facet of Ti_3C_2 is shifted to low angle (**Figure 7b**) with the increase of the hydrothermal reaction time, suggesting that the longer reaction time, the more complete the etching was. And it is clear that there are still some Ti_3AlC_2 diffraction peaks at 2θ of 16.69° and 35.9º for a hydrothermal duration of 8 h, while these peaks disappeared when the hydrothermal duration was prolonged to 12 h. Meanwhile, the intensity of the peak at 6.5°, assigned to the (002) facet of Ti_3C_2, increases when the hydrothermal duration was 24 h, suggesting better crystallization of $Ti_xC_yT_x$. However, the characteristic peaks of TiO_2 were observed at around of 25.21°, 47.89°, 53.82°, 54.87° and 62.43º due respectively to the (101), (200), (105), (211) and (213) diffraction planes which was caused by the oxidation of $Ti_xC_yT_x$. The morphology of S-8 and S-36 are shown in the **Figure 8c, d**. Obviously, the etching process was not complete due to the closed-stacked layered structure, which is confirmed by the small signal of Al element found in the selected areas of sites 3 and 4 in **Figure 8 c, d**. The SEM morphology of S-36 is flake-shaped structure with plenty of small pieces of TiO_2. The small signal of Al element in **Figure 9c** further confirms the etching process was not complete. The EDS results in **Figure 9d** indicates that the small pieces exhibit higher oxygen content, which could confirm the oxidation of Ti_3C_2 during the hydrothermal process. The Al element could be completely removed from MAX phase when the hydrothermal duration is 12 and 24 h.

The effect of the concentration of HCl on the etching process of Ti_3AlC_2 were assessed by XRD measurements. And other factors such as the concentration of $NaBF_4$ (0.2M), temperature (160°C) and duration (12 h) were fixed. From **Figure 7c**, the strong intensity of Ti_3AlC_2 characteristic peaks at 2θ around of 9.0°, 19.5° and 38.5º proved that the Al was not completely removed from Ti_3AlC_2 matrix without HCl. When the concentration of HCl increased to 8M, all above diffraction peaks for Ti_3AlC_2 disappeared and only the diffraction

peaks for Ti_3C_2 and TiC were observed. In addition, the peak of (002) facets of Ti_3C_2 shifted to low angle (**Figure 7c**) with the increase of the concentration of HCl, demonstrating complete etching of Al. The difference of diffraction peaks of S-H8 and S-H10 is negligible. The closely stacked layer morphology in **Figure 8e** and the strong intensity EDS peak of Al in **Figure 9e** indicate that the HCl is important for this etching process. The morphology of S-H10 in **Figure 8f** looks similar with that of $Ti_xC_yT_x$ in **Figure 5g-i**, and EDS analysis of S-H10 confirmed that Al was removed totally from Ti_3AlC_2 MAX phase. Thus, the $Ti_xC_yT_x$ could be synthesized when the concentration of HCl is higher than 4M as other variables are fixed.

In order to understand the influence of the concentration of $NaBF_4$ on the MAX etching process, XRD measurements of the resulting MXenes samples obtained by using 0, 0.1, 0.2 and 0.3M $NaBF_4$ and 8M HCl at 160°C for 12 h were performed. A small characteristic peak for Ti_3AlC_2 was still observed for S-F1, while this peak disappeared when the concentration of $NaBF_4$ increased to 0.2M. At the meantime, increasing the concentration of $NaBF_4$ to 0.3M revealed stronger (002) peak of Ti_3C_2 along with a shift to lower diffraction position, which means that Al was completely etched from Ti_3AlC_2 MAX phase and well-crystallized Ti_3C_2 was obtained using 0.3M $NaBF_4$ + 8M HCl at 160°C for 12 h. The sample without $NaBF_4$ in **Figure 8g** maintained the morphology of Ti_3AlC_2 MAX phase in **Figure 5a-c**, which means this etching process could not be conducted without fluoride. The strong EDS signal of Al element in **Figure 9g** further confirmed this result. The appearance of flaked structure in **Figure 8i** and the disappearance of EDS peaks of Al element in **Figure 9i** represent a strong evidence of the complete etching with 0.3M $NaBF_4$ and 8M HCl at 160°C for 12 h. The optimized concentration of $NaBF_4$ is larger than 0.2M when the concentration of HCl, the duration and temperature were set as 8M, 12h and 160ºC.

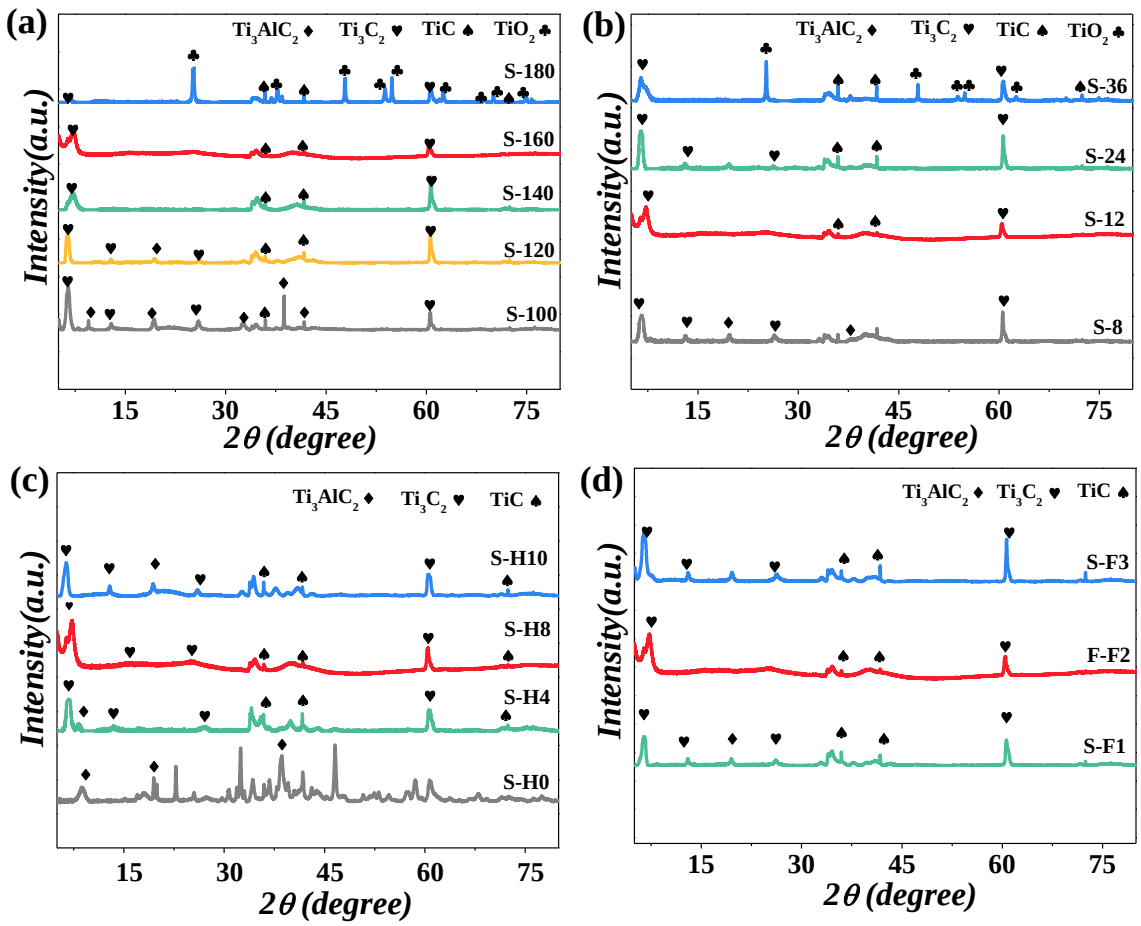

Figure 7. XRD patterns of Ti_3AlC_2 etched in (**a**) 0.2M $NaBF_4$+8M HCl solution at 100, 120 ,140, 160 and 180 °C for 12 h, (**b**) 0.2M $NaBF_4$+8M HCl solution at 160 °C for 8, 12, 24, and 36 h, (**c**) 0.2M $NaBF_4$ without and with 4, 8 and 10M HCl solution at 160 °C for 12 h, (**d**) 0, 0.1 0.2 and 0.3M $NaBF_4$+8M HCl solution at 160 °C for 12 h.

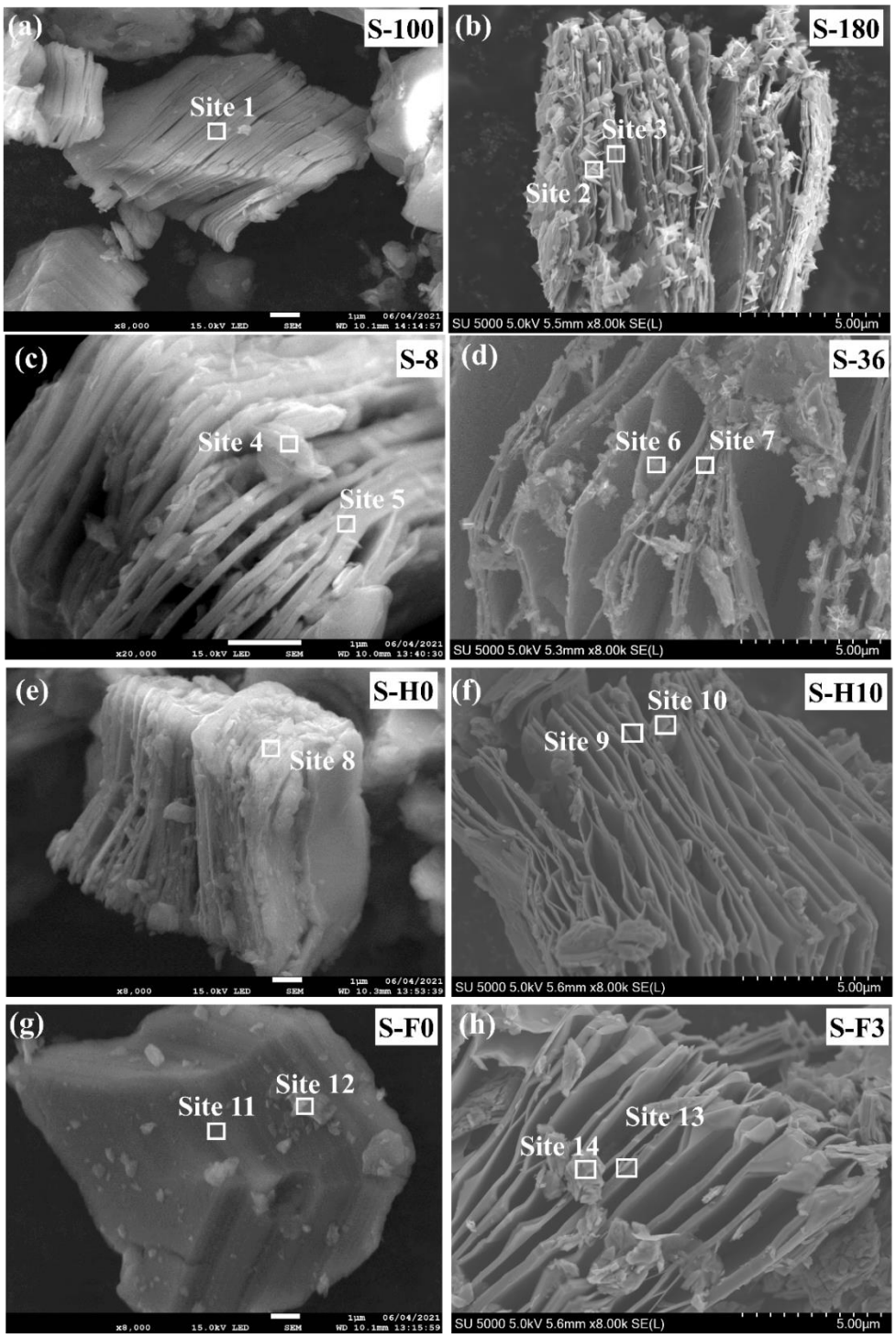

Figure 8. SEM micrographs of Ti_3AlC_2 etched in 0.2M $NaBF_4$ + 8M HCl solution at 160 °C for (**a**) 8 h and (**b**) 36 h, 0.2M $NaBF_4$ + 8M HCl solution at (**c**) 100 °C and (**d**) 180 °C for 12 h, 0.2M $NaBF_4$ without (**e**) and with 10M (**f**) HCl solution at 160 °C for 12 h, 8M HCl without (**g**) and 0.3M $NaBF_4$ (**h**) at 160°C for 12 h.

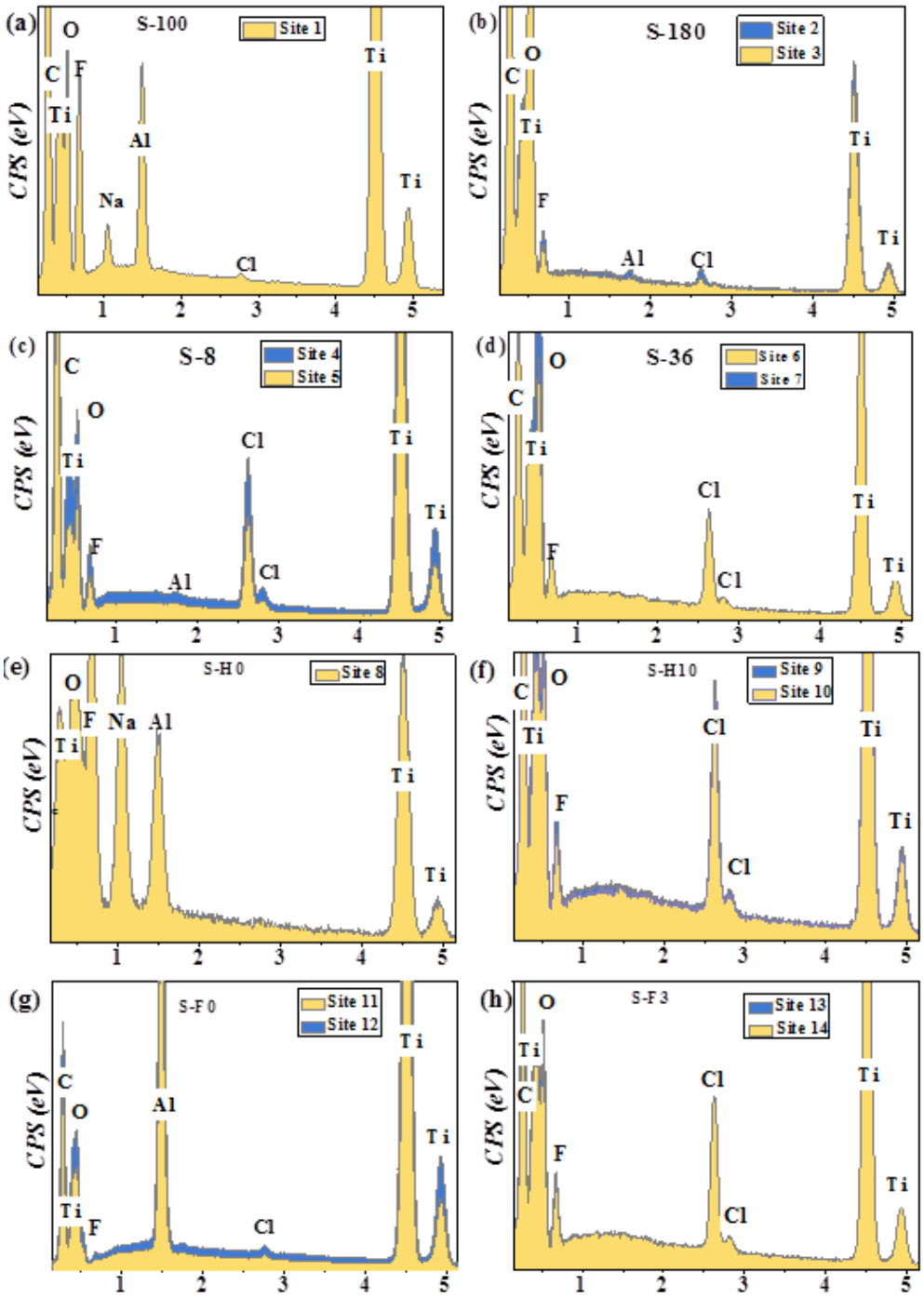

Figure 9. EDS analysis: (**a**) Sites 1 and 2 in **Figure 8a**; (**b**) Sites 3 and 4 in **Figure 8b**; (**c**) Site 5 in **Figure 8c**; (**d**) Sites 6 and 7 in **Figure 8d**; (**e**) Site 8 in **Figure 8e**; (**f**) Sites 9 and 10 in **Figure 8f**; (g) Sites 11 and 12 in **Figure 8g**; (h) Sites 13 and 14 in **Figure 8h**.

4.3.3 HER performance of MXenes

The influence of the different etching parameters on the electrochemical performance of the $Ti_xC_yT_x$ MXenes was studied by linear sweep voltammetry (LSV) in 0.5 M H_2SO_4 solution. **Figure 10a, b** presents the LSV plots and Tafel slopes of Ti_xC_y produced by etching of Ti_3AlC_2 in 0.2M $NaBF_4$ /8M HCl at various temperatures (100, 120, 140, 160, and 180 °C) for 12 h. The relation between overpotential at 10 mA cm^{-2} from **Figure 10a** and Tafel slope from **Figure 10b** are plotted in **Figure 11**. It could be seen that the overpotential at 10 mA cm^{-2} decreased from 306.8 to as low as 154.9 mV at 160ºC and then increased to 190.3 mV at 180ºC.

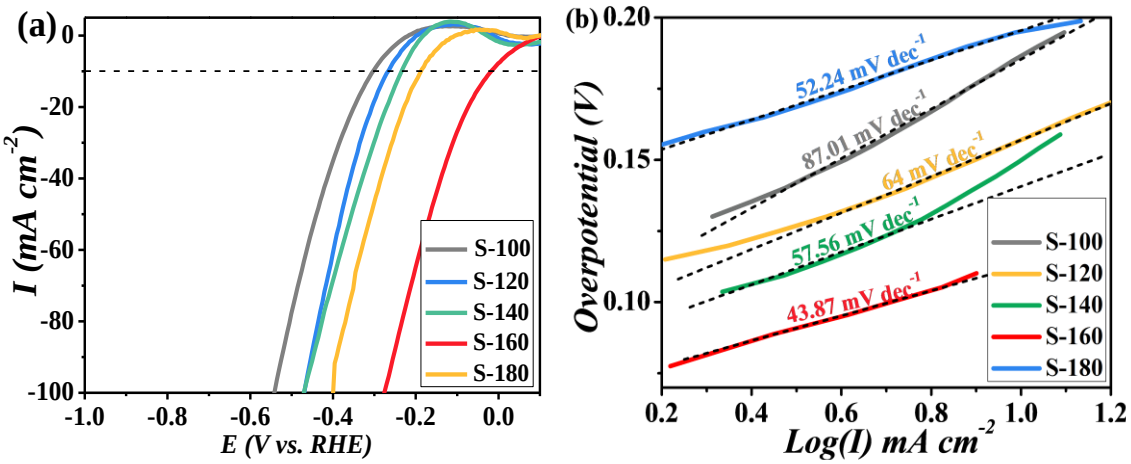

Figure 10. HER performance of $Ti_xC_yT_x$ prepared by Ti_3AlC_2 etching in 0.2M $NaBF_4$/8M HCl at 100, 120, 140, 160, and 180 °C for 12 h: (**a**) LSV curves and (**b**) Tafel slopes.

The relation between the hydrothermal temperature and Tafel slope showed similar tendency, and the lowest Tafel slope was recorded at 160 ºC. The lowest overpotential to drive 10 mA cm^{-2} and Tafel slope inferred that 160 °C was the optimal temperature for HER in 0.5M H_2SO_4 aqueous solution under these operating conditions. The sample obtained at 160 °C recorded the lowest overpotential of 25.6 mV at 10 mA

cm^{-2}, which is comparable to the value recorded for Pt/C (26.8 mV) under otherwise identical experimental conditions. Similarly, the Tafel slope (43.87 mV dec^{-1}) acquired by this sample is approaching that of Pt/C (31.25 mV dec^{-1}), a golden standard electrocatalyst for HER in acidic media.

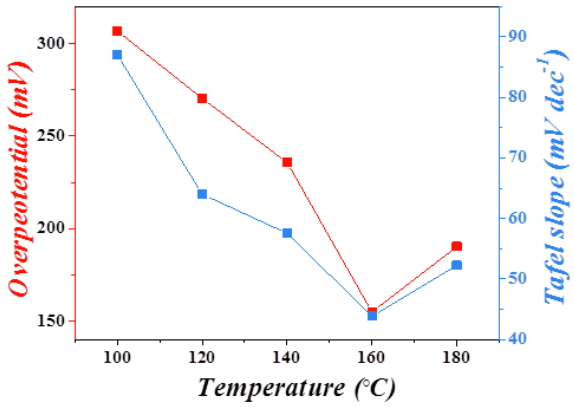

Figure 11. Overpotential at -10mA cm^{-2} and Tafel slope of $Ti_xC_yT_x$ as a function with etching temperature.

The influence of the etching time on Ti_3AlC_2 in 0.2M $NaBF_4$/8M HCl at 160 °C was further evaluated for the HER in 0.1 M H_2SO_4 aqueous solution. **Figure 12a,b** presents the LSV plots and Tafel slopes of Ti_xC_y produced by etching of Ti_3AlC_2 in 0.2M $NaBF_4$ /8M HCl at 160°C for 8, 12, 24, and 36 h. The relation between overpotential at 10 mA cm^{-2} from **Figure 10a** and Tafel slopes from **Figure 10b** are plotted in **Figure 13**. The obtained data clearly evidenced that increasing the etching time beyond 12 h had a detrimental effect on the electrocatalytic performance of the Ti_xC_y catalyst for HER.

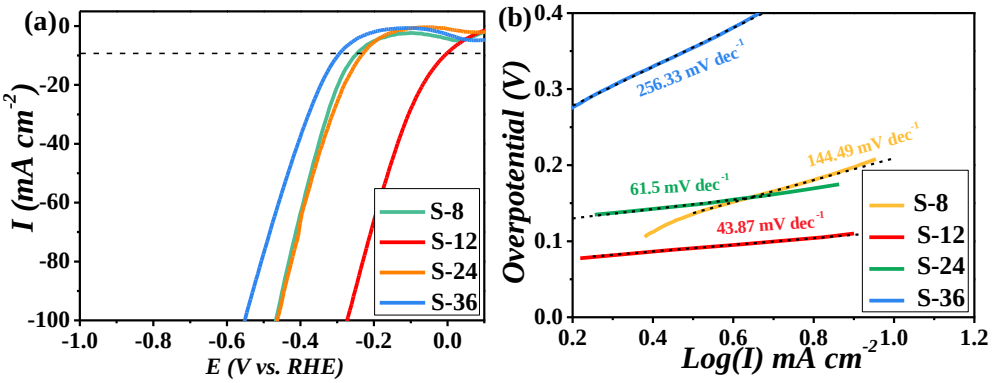

Figure 12. HER performance of $Ti_xC_yT_x$ prepared by Ti_3AlC_2 etching in 0.2M $NaBF_4$/8M HCl at 100, 120, 140, 160, and 180 °C for 12 h: (**a**) LSV curves and (**b**) Tafel slopes.

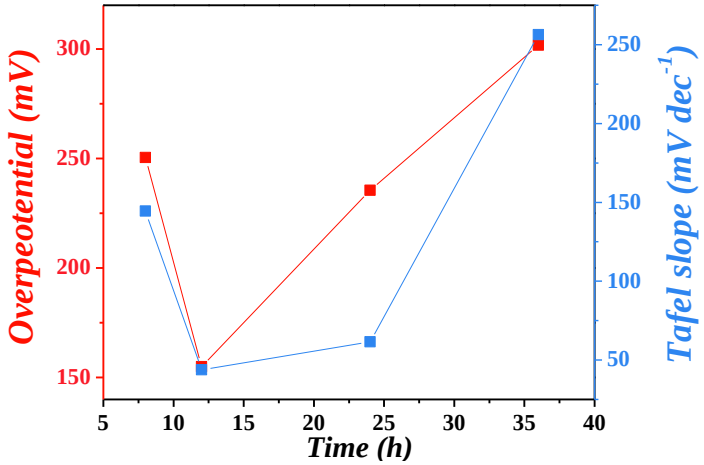

Figure 13. Overpotential at -10 mA cm^{-2} and Tafel slope values of $Ti_xC_yT_x$ as a function of etching duration.

Similarly, the impact of $NaBF_4$ concentration on the Ti_3AlC_2 etching in 8M HCl/$NaBF_4$ at 160 °C for 12 h was studied to determine the optimum etching conditions. **Figure 14a, b** depicts the LSV plots and Tafel slopes of Ti_xC_y produced by etching of Ti_3AlC_2 in 0, 0.1, 0.2 and 0.3M $NaBF_4$ and 8M HCl at 160°C for 12h. The relation between overpotential at 10 mA cm^{-2} from **Figure 14a** and Tafel slope from **Figure 14b** are plotted in **Figure 15**. It was found that increasing $NaBF_4$ concentration beyond 0.2 M was not beneficial for the electrocatalytic performance of the Ti_xC_y MXenes

sheets (**Figure 15**). Of note, a $NaBF_4$ concentration of 0.3M gave an overpotential value of 250.6 mV at 10 mA cm^{-2} which is slightly higher than that recorded in absence of $NaBF_4$ (225.01 mV). The result clearly highlights the key role of an appropriate $NaBF_4$ concentration to achieve the best performance of the Ti_xC_y MXenes under our experimental conditions.

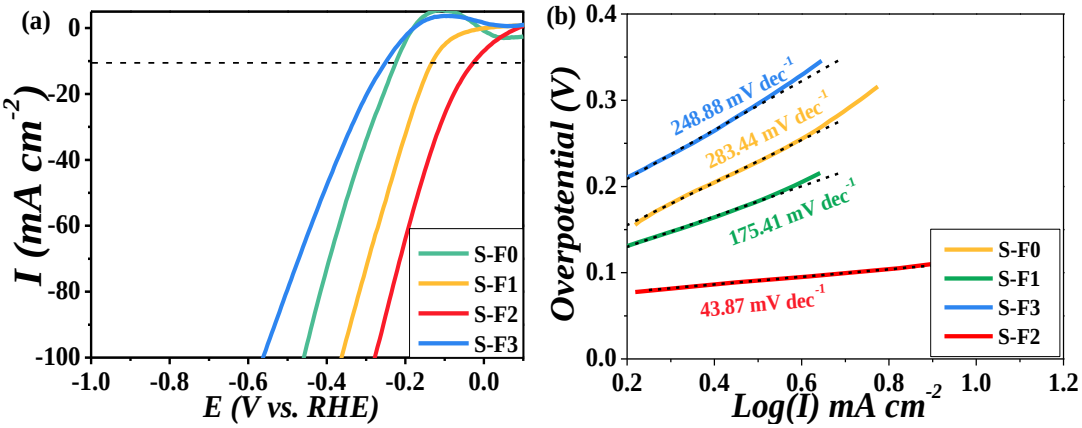

Figure 14. HER performance of $Ti_xC_yT_x$ prepared by Ti_3AlC_2 etching in 0, 0.1, 0.2, and 0.3M $NaBF_4$ and 8M HCl at 160 °C for 12 h: (**a**) LSV curves and (**b**) Tafel slope.

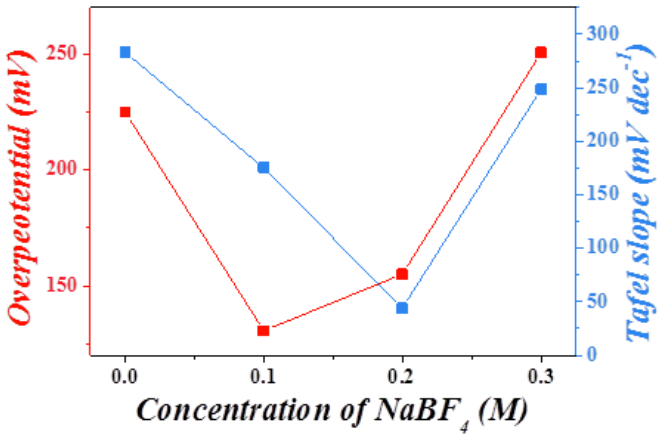

Figure 15. Overpotential at -10 mA cm^{-2} and Tafel slope of $Ti_xC_yT_x$ as a function of $NaBF_4$ concentration.

Finally, **Figure 16a, b** displays the LSV plots and Tafel slopes of Ti_xC_y produced by etching of Ti_3AlC_2 in varying concentrations of HCl (0-12 M) + 0.2M $NaBF_4$ at

160 °C for 12 h. The relation between overpotential at 10 mA cm^{-2} from **Figure 16a** and Tafel slope from **Figure 16b** are plotted in **Figure 17**. The overpotential decreased from 270.3 mV at 0M HCl to 154.9 mV at a concentration of 8M, and then to 150.6 mV at 10M. Similarly, the Tafel slope decreased to 43.87 mV dec^{-1} at the concentration of 8M, while it increased to 106.76 mV dec^{-1} at 10M. It is clear that the optimum HER performance was attained for 8M.

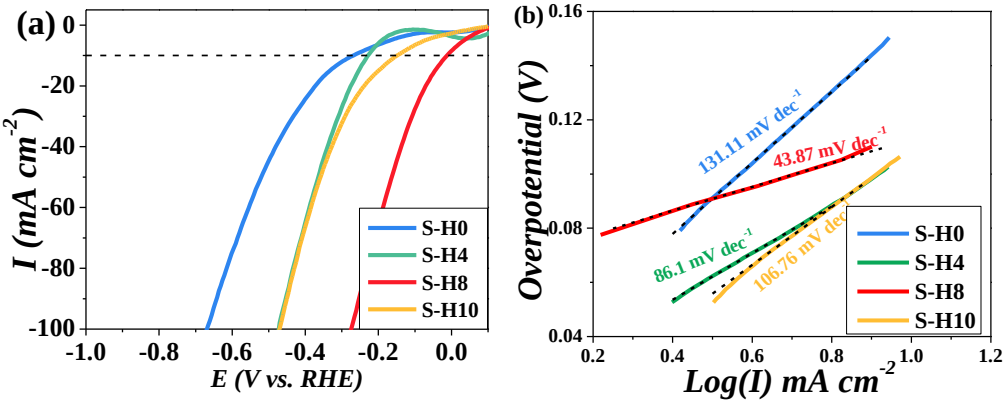

Figure 16. HER performance of $Ti_xC_yT_x$ prepared by Ti_3AlC_2 etching in 0.2M $NaBF_4$ + 0, 4, 8 or 10M HCl at 160 °C for 12 h: (**a**) LSV curves and (**b**) Tafel slopes.

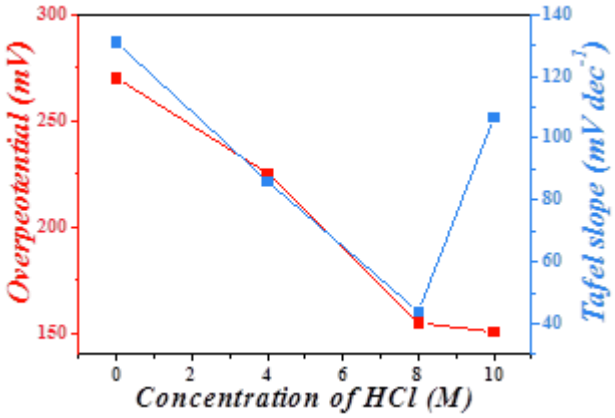

Figure 17. Overpotential at -10 mA cm^{-2} and Tafel slope of $Ti_xC_yT_x$ as a function of the concentration of HCl.

Electrochemical impedance spectroscopy (EIS) results have been recognized as a

good way to elucidate the mechanism behind the HER behavior. The EIS measurements were conducted to understand the effects of synthesis conditions on the HER performance. The resistance was fit using an equivalent circuit model including solution resistance (R_s), constant phase element (CPE), and charge transfer resistance (R_{ct}). The Nyquist plots of all studied samples are shown in **Figure 18**. Obviously, the R_{ct} decreased with the increase of temperature, duration and the concentration of $NaBF_4$ and HCl and reached a lowest value of 121.4 Ω at 160°C, 12h, 0.2M and 8M, respectively. Thus, the lowest charge transfer resistance of samples synthesized with 0.2M $NaBF_4$/8M HCl at 160 ºC for 12h indicated good HER catalytic activity.

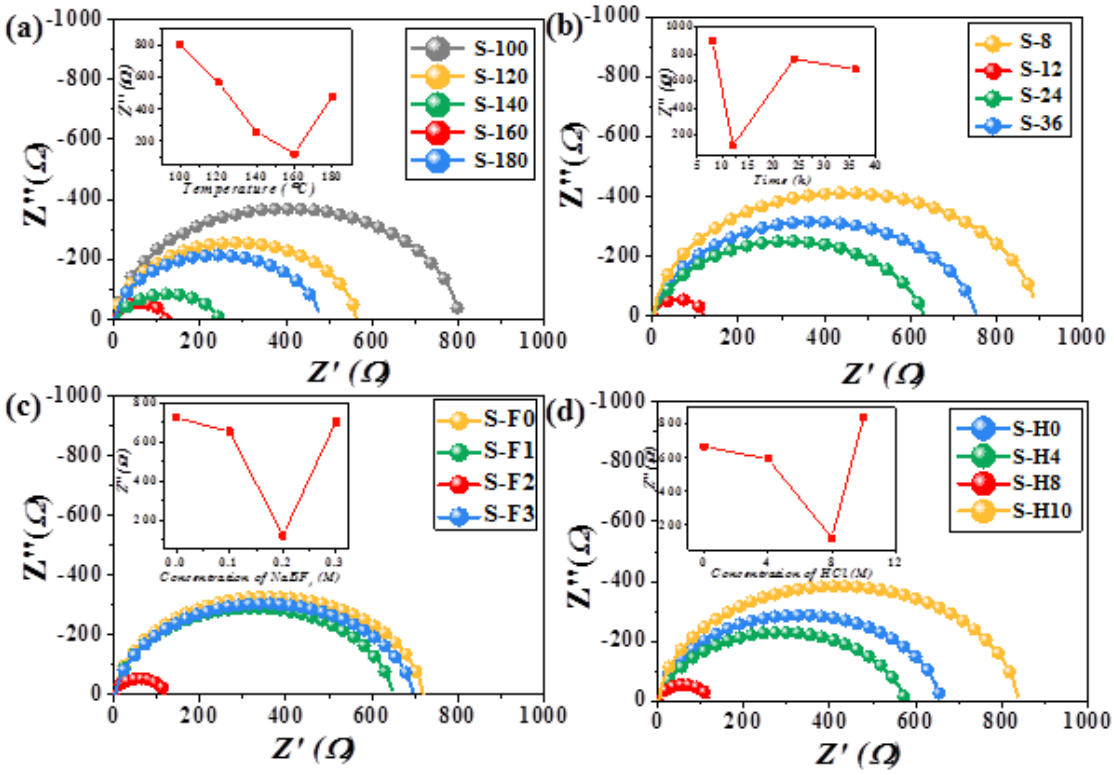

Figure 18. Nyquist plots of Ti_xC_y prepared by Ti_3AlC_2 etching in (**a**) 0.2M $NaBF_4$+8M HCl at 100, 120, 140, 160 or 180 °C for 12h, (**b**) 0.2M $NaBF_4$+8M HCl at 160 °C for 8, 12, 24, or 36 h, (**c**) 8M HCl+$NaBF_4$ (0, 0.1, 0.2, 0.3M) at 160 °C for 12 h, and (**d**) 0.2M $NaBF_4$+HCl (0, 4, 8, 10M) at 160 °C for 12 h.

The electrochemical surface area (ECSA) values of all samples prepared under

different conditions were estimated by the cyclic voltammetry (CV) method at various potential scan rates (20 - 70 mV s^{-1}) from -0.1 to 0.1 V *vs.* SCE in 0.5M H_2SO_4 solution. The potential range of -0.1 to 0.1 V range is the non-faradic area, where no electrochemical reaction occurs. The CV curves of studied samples are displayed in **Figures 19a-e**, **20a-c**, **21a-c** and **22a-c**. The current density at 0 V *vs.* SCE from above CV curves are plotted as a function of the potential scan rate in **Figures 19f**, **20d**, **21d**, and **22d**.

Similarly, the ECSA values of samples prepared under variable etching conditions were plotted as a function of temperature (**Figure 19g**), duration (**Figure 20e**), concentration of $NaBF_4$ (**Figure 21e**) and HCl (**Figure 22e**).

From **Figure 19f, g**, the double layer capacitance (C_{dl}) increased from 22.4 μF cm^{-2} at 100 ºC 89 μF cm^{-2} at 160 ºC, and then decreased to 72 μF cm^{-2} at 180ºC. A similar tendency was observed with increase of hydrothermal temperature. And the MXenes samples had the largest ECSA of 2.25 cm^2 when the hydrothermal temperature was set at 160 ºC compared with other counter samples. The hydrothermal duration has a significant role on the value of ECSA. Although the amount of Al could be removed completely from Ti_3AlC_2 MAX phase with the increase of the hydrothermal duration, the ECSA decreased rapidly to 0.8 cm^2 for an etching time of 36h after an optimal value of 2.5 cm^2 for 12h (Figure **20e**). the concentration of $NaBF_4$ had less effect on the values of ECSA, which ranged between 1.5 and 2.25 cm^2, and the maximal value of 2.25 cm^2 was determined for 0.2M in **Figure 21e.** Form the **Figure 22e,** 8M HCl was most suitable for the etching process in terms of large ECSA (2.25 cm^2). However, the higher concentration (10M) of HCl was not beneficial. From above analysis, we could find that $Ti_xC_yT_x$ synthesized in 0.2M $NaBF_4$ and 10M HCl at 160 °C for 12h achieved the

best HER performance due to the smallest charge transfer and largest ECSA values.

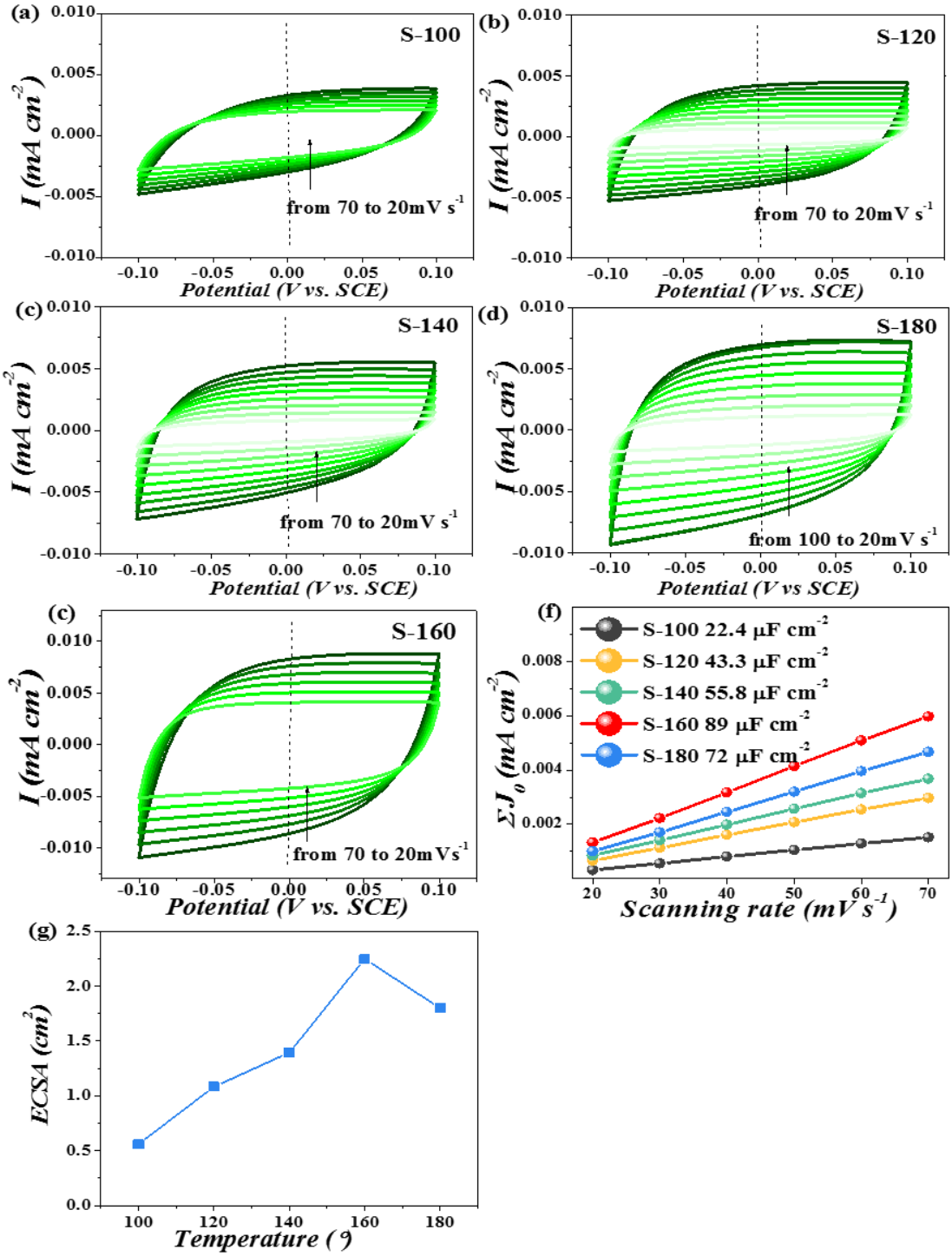

Figure 19. CVs at various scanning rates (20 to 70 mV s^{-1}) in 0.5M H_2SO_4 of Ti_xC_y after etching in 0.2M $NaBF_4$+8M HCl for 12h at (**a**) 100°C, (**b**) 120°C, (**c**) 140°C and (**d**) 180 °C. (e) 160°C; (**f**) current density at 0V as a function of scan rate (20 to 70mV s^{-1}), (**g**) ECSA as a function of hydrothermal temperature.

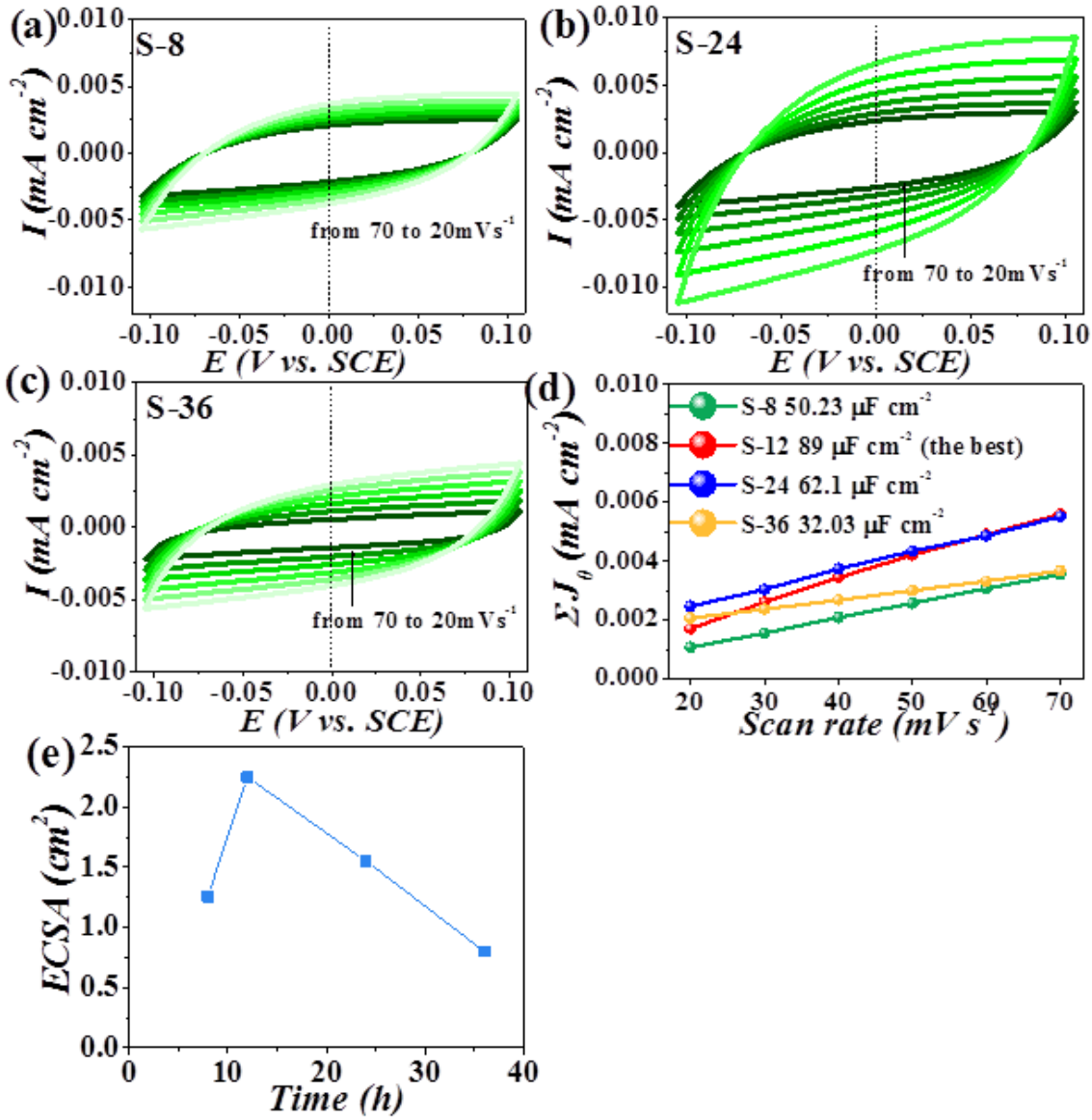

Figure 20. CVs at various scanning rates (20 to 70 mV s^{-1}) in 0.5M H_2SO_4 of $Ti_xC_yT_x$ after etching with 0.2M $NaBF_4$+8M HCl at 160°C for (**a**) 8h, (**b**) 24h, and (**c**) 36h for 12h, (**f**) current density at 0V as a function of scan rate (20 to 70mV s^{-1}), (**g**) ECSA as a function of hydrothermal duration.

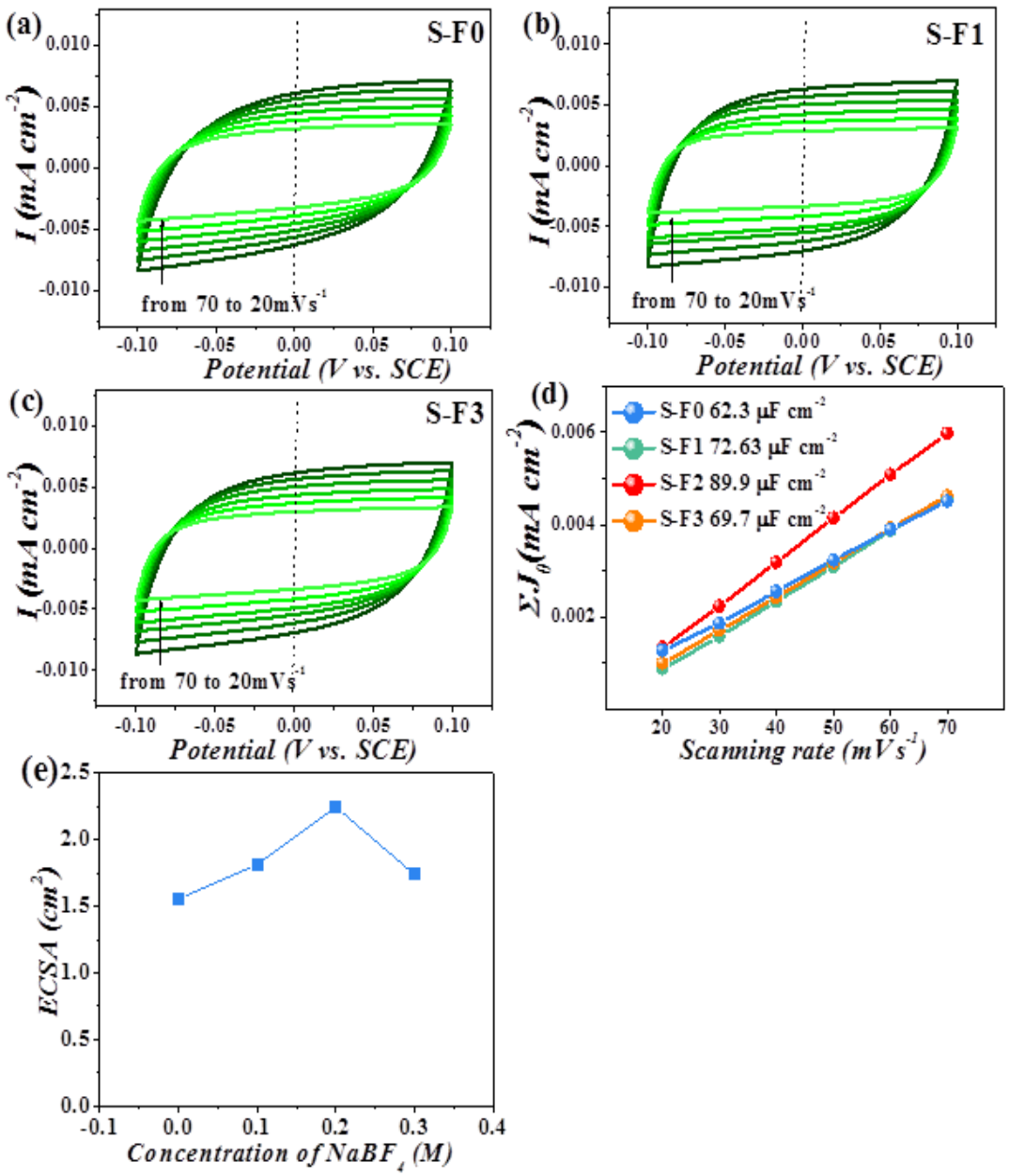

Figure 21. CVs at various scanning rates (20 to 70 mV s^{-1}) of Ti_xC_y after etching in 8M HCl+(**a**) 0M, (**b**) 0.1M, (**c**) 0.2M and (**d**) 0.3M $NaBF_4$ at 160°C for 12 h. (**f**) current density at 0V as a function of scan rate (20 to 70 mV s^{-1}), (**g**) ECSA as a function of the concentration of $NaBF_4$..

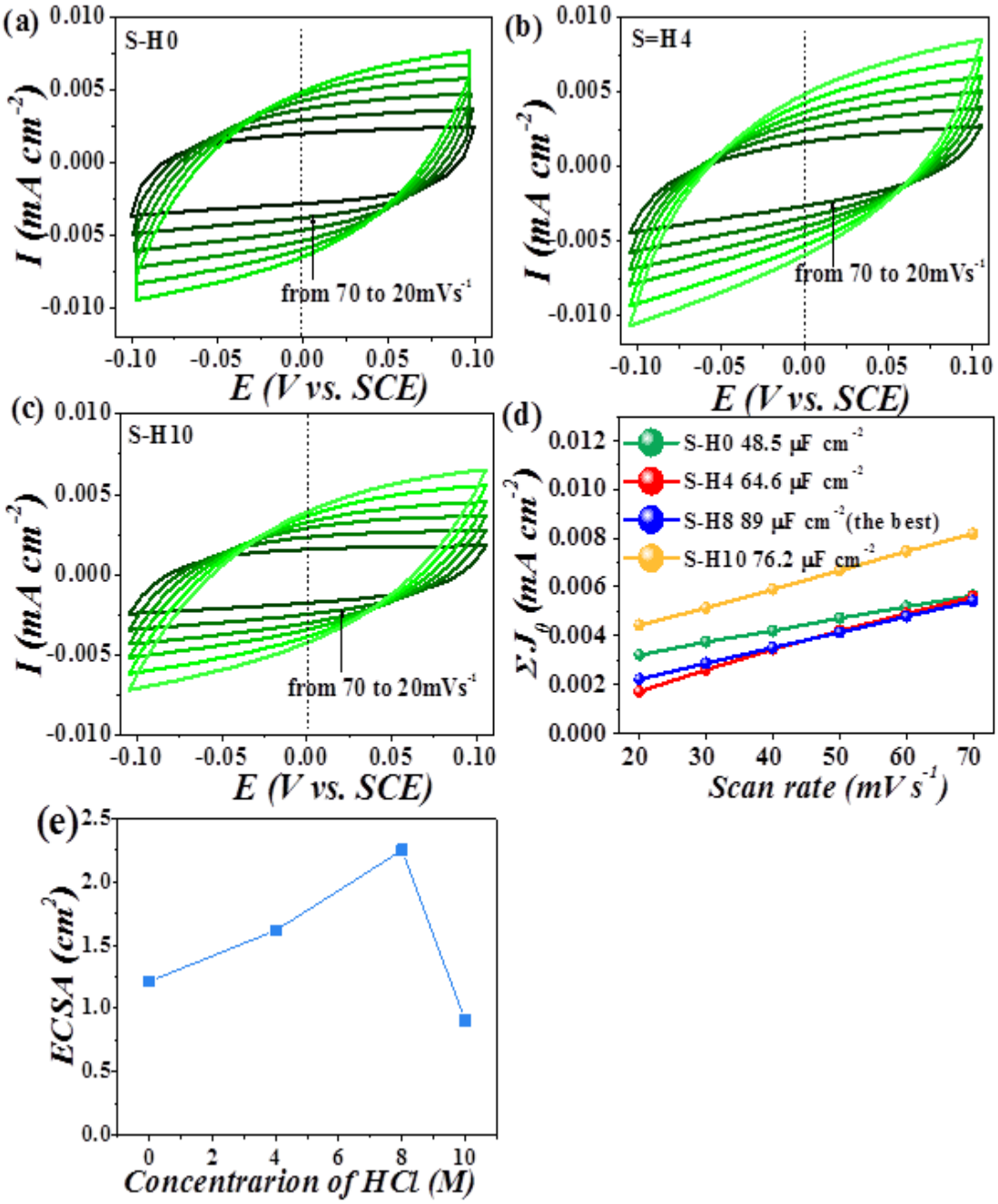

Figure 22. CVs at various scanning rates (20 to 70 mV s^{-1}) of Ti_xC_y after etching in 0.2M $NaBF_4$+(**a**) 0M, (**b**) 4M and (**c**) 10M HCl at 160°C for 12 h. (**d**) current density at 0V as a function of scan rate (20 to 70mV s^{-1}), (**e**) ECSA as a function of the concentration of HCl.

Finally, we compared the HER performance of $Ti_xC_yT_x$ synthesized in 0.2M $NaBF_4$+8M HCl at 160℃for 12h with that of $Ti_3C_2T_x$ prepared by using HF at room

temperature for 48h. The $Ti_xC_yT_x$ sample featured the best performance with a lowest overpotential of 157.2 mV (*vs.* RHE) to deliver 10 mA cm^{-2}, compared with the sample etched with HF (246.1 mV), although still have a gap with Pt (26.8 mV), **Figure 23a, b**. To gain more insight into the activity, the Tafel slopes of the MXenes samples were determined, as shown in **Figure 23b** $Ti_xC_yT_x$ exhibited a Tafel slope of 43.87 mv dec^{-1} which is much smaller than that of the sample etched with HF (97.37mV dec^{-1}), and close to that of Pt (31.25 mV dec^{-1}), which is so far one of the best among reported MXenes-based HER catalysts in acid solutions (**Table 4**). Theoretically, three principle steps are involved in the hydrogen evolution reaction, referred to as the Volmer (1), the Heyrovsky (2), and the Tafel (3) steps.

$$\text{Volmer: } H^+ + e^- \rightarrow H_{ads} \quad (1)$$

$$\text{Heyrovsky: } H^+ + e^- + H_{ads} \rightarrow H_2 \quad (2)$$

$$\text{Tafel: } H_{ads} + H_{ads} \rightarrow H_2 \quad (3)$$

Experimentally-measured Tafel slope has often been used as a parameter to identify the mechanism and rate-determining step of HER. The Tafel slope 40-50 mV dec^{-1} measured of Ti_3C_2Tx in this work matched with the Volmer-Heyrovsky-step mechanism for the HER process (39 mV dec^{-1}), thus the rate-determining step could be the Heyrovsky step. While for Ti_3C_2 etched with HF, the Tafel is closer to 120 mV dec^{-1}, the rate-determining step could be the Volmer step.

The impedance could release kinetic conditions of an electrochemical reaction by the active resistance. From **Figure 23c**, $Ti_3C_2T_x$ has a smaller R_{ct} of 566.2Ω than the sample etching with HF (664.0 Ω), indicating a fast charge transport kinetics, which is responsible for the excellent HER activity.

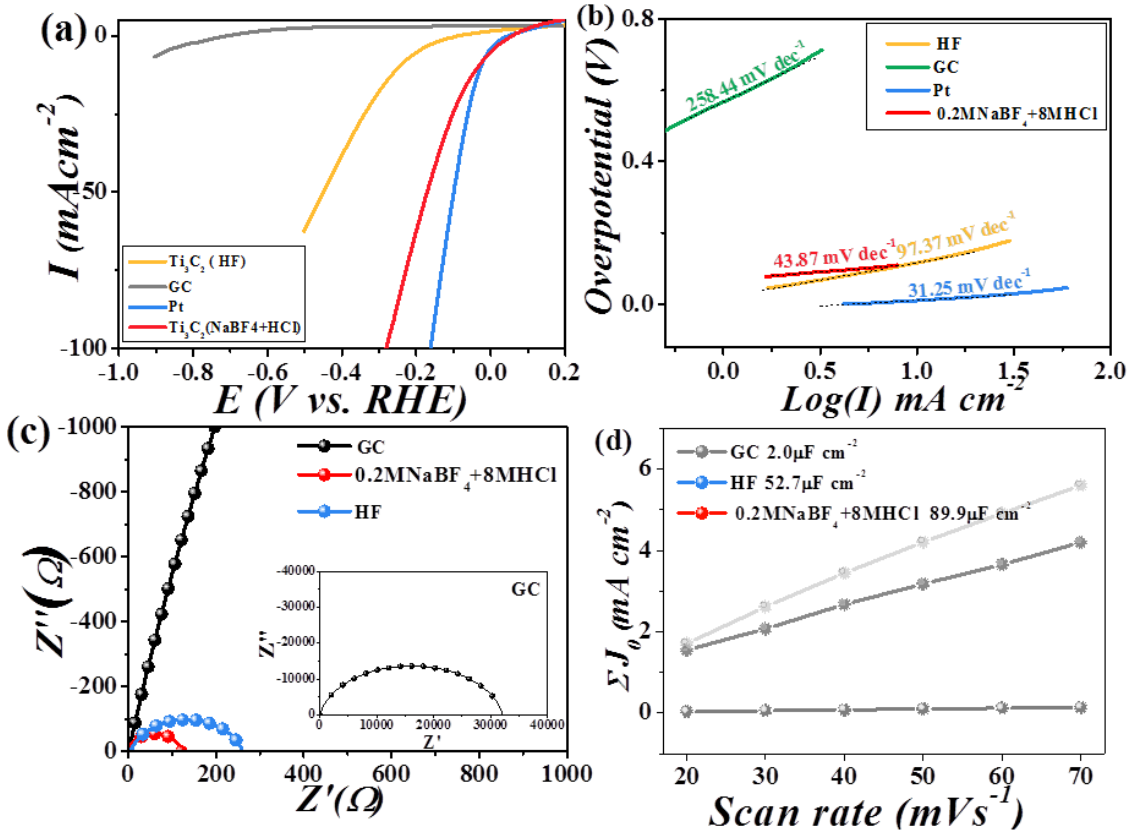

Figure 23. HER performance of MXenes prepared by etching of Ti_3AlC_2 MAX in (**a**) 0.2M $NaBF_4$/8M HCl at 160 °C for 12 h and (**b**) HF for 48 h at room temperature along with that of bare glassy carbon electrode and Pt plate in 0.5M H_2SO_4 solution.

In addition, the electrochemical active surface area (ECSA) was assessed based on the double layer capacitance (C_{dl}) *vs.* scan rate (from 20 to 70 mV s^{-1}) plot in **Figure 23d**. Compared with Ti_3C_2 sample etched with HF (52.7 mF) and GC (2 mF), $Ti_3C_2T_x$ displayed a larger C_{dl} of 89.8 mF， suggesting that the larger ECSA could further enhance the activity of $Ti_3C_2T_x$ for HER process.

The number of active sites (n) of studied samples were calculated based on the **Eq. 4.1**

$$n = \frac{Q}{2F} \tag{4.1}$$

Where *n* is the stoichiometric number of electrons transferred in the HER process, Q is the net voltammetry charge transfer which was calculated by subtracting charges resulting from the bare glassy carbon electrode.

Correspondingly, $Ti_3C_2T_x$ etched with $NaBF_4$+HCl showed the largest number of active sites of $1.96E^{-04}$, compared with Ti_3C_2 etched with HF. This could add another evidence to the best performance of $Ti_xC_yT_x$ etched with $NaBF_4$+HCl.

Table 4. Comparison of the overpotential and Tafel slope values of the Ti_xC_y prepared by chemical etching of Ti_3AlC_2 in 0.2M $NaBF_4$+8M HCl at 160 °C for 12 h and previously-reported MXenes-based electrocatalysts.

Electrode material	Overpotential (mV) at -10 mA cm^{-2}	Tafel slope ($mV\ dec^{-1}$)	Electrolyte	Ref.
$Ti_xC_yT_x$	157.2	43.87	0.5M H_2SO_4	This work
N-Ti_2CT_x	215	67	0.5M H_2SO_4	[18]
$Nb_4C_3T_x$	263	142.7	0.5M H_2SO_4	[19]
P-Mo_2C/Ti_3C_2	172	56.2	0.5M H_2SO_4	[21]
Phosphorus-doped Mo_2CT_x	186	-	0.5M H_2SO_4	[22]
Ti_3C_2 NFs	169	97	0.5M H_2SO_4	[25]
$Ti_3C_2O_x$	190	60.7	0.5M H_2SO_4	[26]
P_3–V_2CT_x	163	74	0.5M H_2SO_4	[27]
Nitrogen-doped $Ti_3C_2T_x$	198	92	0.5M H_2SO_4	[28]
N-doped MXenes	162	69	0.5M H_2SO_4	[31]
$Ti_{0.2}Al_{1.8}C_4O_5$ nanowires	248	121	0.5M H_2SO_4	[33]
$TiVCT_x/MoS_2$-CNT	180	79	0.5M H_2SO_4	[35]
P-Mo_2C/Ti_3C_2@NC	177	57.3	0.5M H_2SO_4	[36]
Ti_3C_2/MoS_x	165	41	0.5M H_2SO_4	[37]
$MoSe_2$/MXenes	180	91	0.5M H_2SO_4	[38]
$MoTe_2/Ti_3C_2T_x$	293	65	0.5M H_2SO_4	[40]

Stability is a major concern for an industrial-oriented application. To confirm the HER stability, cyclic voltammetry of $Ti_xC_yT_y$ was recorded for 3000 cycles in a potential range from -0.6 to 0.2V (*vs.* RHE) in 0.5M H_2SO_4 at 100 mV s^{-1}. Before and after 3000 cycles, CV plots of $Ti_xC_yT_y$ showed no remarkable difference. Moreover, it also could maintain a stable current density of 20, 40, 60, 80, and 100 mA cm^{-2} at an overpotential of respectively 160, 217, 251, 269, and 315 V for 28 h, as shown in **Figure 24b**.

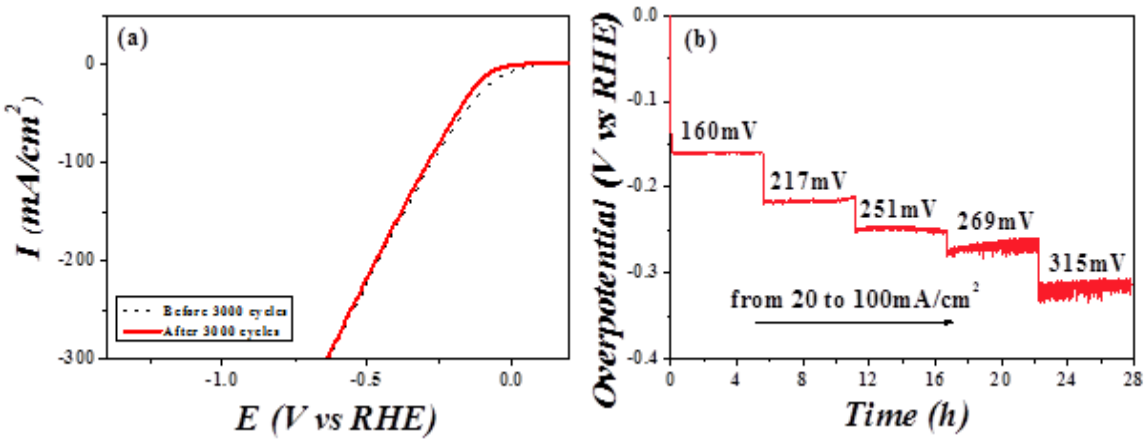

Figure 24. (**a**) CV curves before and after 3000 CV cycles, and (**b**) chronopotentiometry test of Ti_3C_4/TiC prepared by Ti_3AlC_2 etching in 0.2M $NaBF_4$/8M HCl at 160 °C for 12 h.

4.4 Conclusion

In conclusion, we have developed a low-F-containing etching strategy toward 2D MXenes $Ti_3C_2T_x$ (T=O, OH). The selective removal of the Al layer from Ti_3AlC_2 in 0.2M $NaBF_4$+ 8M HCl solution at 160 ℃ could lead to oxygen-rich MXenes sheets. Thanks to the hydrothermal etching process, 2D MXenes sheets with abundant oxygen surface groups exhibited high excellent catalytic activity for hydrogen evolution in 0.5M H_2SO_4 solution, with a low overpotential of 157.2 mV (*vs.* RHE) to drive a current

density of 10mA cm^{-2} and a Tafel slope of 43.87 mv dec^{-1}, and could also maintain a stable current density of 20, 40, 60, 80, and 100 mA cm^{-2} at an overpotential of respectively 160, 217, 251, 269, and 315 V for 28 h. Our strategy provides a promising pathway for the facile and sustainable production of highly-stable MXenes materials.

4.5 References

1. Liu, H. J. & Dong, B. Recent advances and prospects of MXenes-based materials for electrocatalysis and energy storage. *Mater. Today Phys.* **20**, 100469 (2021).

2. Kang, Z. *et al.* Recent progress of MXenes and MXenes-based nanomaterials for the electrocatalytic hydrogen evolution reaction. *J. Mater. Chem. A* **9**, 6089–6108 (2021).

3. Naguib, M., Mochalin, V. N., Barsoum, M. W. & Gogotsi, Y. 25th anniversary article: MXenes: a new family of two-dimensional materials. *Adv. Mater.* **26**, 992–1005 (2014).

4. Ghidiu, M., Lukatskaya, M. R., Zhao, M. Q., Gogotsi, Y. & Barsoum, M. W. Conductive two-dimensional titanium carbide 'clay' with high volumetric capacitance. *Nature* **516**, 78–81 (2015).

5. Liu, F. *et al.* Preparation of Ti_3C_2 and Ti_2C MXenes by fluoride salts etching and methane adsorptive properties. *Appl. Surf. Sci.* **416**, 781–789 (2017).

6. Zhang, T. *et al.* Synthesis of two-dimensional $Ti_3C_2T_x$ MXenes using HCl+LiF etchant: enhanced exfoliation and delamination. *J. Alloys Compd.* **695**, 818–826 (2017).

7. Wu, X. *et al.* Engineering multifunctional collaborative catalytic interface enabling efficient hydrogen evolution in all pH range and seawater. *Adv. Energy Mater.* **9**, 1901333 (2019).

8. Feng, A. *et al.* Fabrication and thermal stability of NH_4HF_2-etched Ti_3C_2 MXenes. *Ceram. Int.* **43**, 6322–6328 (2017).

9. Feng, A. *et al.* Two-dimensional MXenes Ti_3C_2 produced by exfoliation of Ti_3AlC_2. *Mater. Des.* **114**, 161–166 (2017).

10. Wei, Y., Zhang, P., Soomro, R. A., Zhu, Q. & Xu, B. Advances in the synthesis of 2D MXenes. *Adv. Mater.* **33**, 1–30 (2021).

11. Xuan, J. *et al.* Organic-base-driven intercalation and delamination for the

production of functionalized titanium aarbide nanosheets with superior photothermal therapeutic performance. *Angew. Chem. Int. Ed.* **128**, 14789–14794 (2016).

12. Zou, G. *et al.* Hydrogenated core–shell MAX@$K_2Ti_8O_{17}$ pseudocapacitance with ultrafast sodium storage and long-term cycling. *Adv. Energy Mater.* **7**, 1700700 (2017).

13. Li, L., Li, G., Tan, L., Zhang, Y. & Wu, B. Highly efficiently delaminated single-layered MXenes nanosheets with large lateral size. *Langmuir* **33**, 9000–9006 (2017).

14. Li, T. *et al.* Fluorine-free synthesis of high-purity Ti_3C_2Tx (T=OH, O) via alkali treatment. *Angew. Chem. Int. Ed.* **57**, 6115–6119 (2018).

15. Shekhirev, M., Shuck, C. E., Sarycheva, A. & Gogotsi, Y. Characterization of MXenes at every step, from their precursors to single flakes and assembled films. *Prog. Mater. Sci.* **120**, 100757 (2021).

16. Ghosh, M., Szunerits, S., Cao, N., Kurungot, S. & Boukherroub, R. Single-step synthesis of exfoliated $Ti_3C_2T_x$ MXenes through $NaBF_4$/HCl etching as electrode material for asymmetric supercapacitor. *ChemistrySelect* **7**, 1–8 (2022).

17. Halim, J. *et al.* X-ray photoelectron spectroscopy of select multi-layered transition metal carbides (MXenes). *Appl. Surf. Sci.* **362**, 406–417 (2016).

18. Yoon, Y. *et al.* Enhanced electrocatalytic activity by chemical nitridation of two-dimensional titanium carbide MXenes for hydrogen evolution. *J. Mater. Chem. A* **6**, 20869–20877 (2018).

19. Tan, Y. *et al.* $Nb_4C_3T_x$ (MXenes) as a new stable catalyst for the hydrogen evolution reaction. *Int. J. Hydrogen Energy* **46**, 1955–1966 (2021).

20. Zang, X. *et al.* Self-assembly of large-area 2d polycrystalline transition metal carbides for hydrogen electrocatalysis. *Adv. Mater.* **30**, 1–8 (2018).

21. Tang, Y. *et al.* Phosphorus-doped molybdenum carbide/MXenes hybrid architectures for upgraded hydrogen evolution reaction performance over a wide pH

range. *Chem. Eng. J.* **423**, 130183 (2021).

22. Qu, G. *et al.* Phosphorized MXenes-phase molybdenum carbide as an earth-abundant hydrogen evolution electrocatalyst. *ACS Appl. Energy Mater.* **1**, 7206–7212 (2018).

23. Cui, B. *et al.* Solution-plasma-assisted bimetallic oxide alloy nanoparticles of Pt and Pd embedded within two-dimensional $Ti_3C_2T_x$ nanosheets as highly active electrocatalysts for overall water splitting. *ACS Appl. Mater. Interfaces* **10**, 23858–23873 (2018).

24. Zhang, J. *et al.* Single platinum atoms immobilized on an MXenes as an efficient catalyst for the hydrogen evolution reaction. *Nat. Catal. 2018 112* **1**, 985–992 (2018).

25.Yuan, W. *et al.* MXenes Nanofibers as highly active catalysts for hydrogen evolution reaction. *ACS Sustain. Chem. Eng.* **6**, 8976–8982 (2018).

26. Jiang, Y. *et al.* Oxygen-functionalized ultrathin $Ti_3C_2T_x$ MXenes for enhanced electrocatalytic hydrogen evolution. *ChemSusChem* **12**, 1368–1373 (2019).

27. Yoon, Y. *et al.* Precious-metal-free electrocatalysts for activation of hydrogen evolution with nonmetallic electron donor: chemical composition controllable phosphorous doped vanadium carbide MXenes. *Adv. Funct. Mater.* **29**, 1–12 (2019).

28. Le, T. A. *et al.* Synergistic effects of nitrogen doping on MXenes for enhancement of hydrogen evolution reaction. *ACS Sustain. Chem. Eng.* **7**, 16879–16888 (2019).

29. Zhang, X. *et al.* Platinum nanoparticle-deposited $Ti_3C_2T_x$ MXenes for hydrogen evolution reaction. *Ind. Eng. Chem. Res.* **59**, 1822–1828 (2020).

30. Li, Z. *et al.* In situ formed Pt_3Ti nanoparticles on a two-dimensional transition metal carbide (MXenes) used as efficient catalysts for hydrogen evolution reactions. *Nano Lett.* **19**, 5102–5108 (2019).

31. Han, M. *et al.* Efficient tuning the electronic structure of N-doped Ti-based MXenes

to enhance hydrogen evolution reaction. *J. Colloid Interface Sci.* **582**, 1099–1106 (2021).

32. Liu, H. *et al.* Single-atom Ru anchored in nitrogen-doped MXenes (Ti_3C_2T: X) as an efficient catalyst for the hydrogen evolution reaction at all pH values. *J. Mater. Chem. A* **8**, 24710–24717 (2020).

33. Saha, J. & Subramaniam, C. Thermochemically nanostructured off-stoichiometric $Ti_{0.2}Al_{1.8}C_4O_5$ nanowires as robust electrocatalysts for hydrogen evolution from corrosive acidic electrolyte. *Catal. Today* **370**, 26–35 (2021).

34. Wu, X., Wang, Z., Yu, M., Xiu, L. & Qiu, J. Stabilizing the MXenes by carbon nanoplating for developing hierarchical nanohybrids with efficient lithium storage and hydrogen evolution capability. *Adv. Mater.* **29**, 1–8 (2017).

35. Lin, Y. *et al.* Self-Supporting electrocatalyst film based on self-assembly of heterogeneous bottlebrush and polyoxometalate for efficient hydrogen evolution reaction. *Macromol. Rapid Commun.* **2100915**, 1–7 (2022).

36. Tang, Y., Yang, C., Sheng, M., Yin, X. & Que, W. Synergistically coupling phosphorus-doped molybdenum carbide with MXenes as a highly efficient and stable electrocatalyst for hydrogen evolution reaction. *ACS Sustain. Chem. Eng.* **8**, 12990–12998 (2020).

37. Li, S. *et al.* One-step synthesis of modified Ti_3C_2 MXenes-supported amorphous molybdenum sulfide electrocatalysts by a facile gamma radiation strategy for efficient hydrogen evolution reaction. *ACS Appl. Energy Mater.* **3**, 10882–10891 (2020).

38. Huang, J. J. *et al.* A facile method to produce $MoSe_2$/MXenes hybrid nanoflowers with enhanced electrocatalytic activity for hydrogen evolution. *J. Electroanal. Chem.* **856**, 113727 (2020).

39. Tan, Y. *et al.* Carbon-coated $MoSe_2/Mo_2CT_x$ (MXenes) heterostructure for efficient

hydrogen evolution. *Mater. Sci. Eng. B Solid-State Mater. Adv. Technol.* **271**, (2021).

40. Liu, Z. *et al.* Boosted hydrogen evolution reaction based on synergistic effect of RuO_2@MoS_2 hybrid electrocatalyst. *Appl. Surf. Sci.* **538**, 148019 (2021).

41. Hu, L. *et al.* Experimental and theoretical investigation on MoS_2/MXenes heterostructure as an efficient electrocatalyst for hydrogen evolution in both acidic and alkaline media. *New J. Chem.* **44**, 7902–7911 (2020).

42. Li, X. *et al.* Edge-oriented, high-percentage 1T′-phase MoS_2 nanosheets stabilize Ti_3C_2 MXenes for efficient electrocatalytic hydrogen evolution. *Appl. Catal. B Environ.* **284**, 119708 (2021).

43. Li, M. *et al.* Hierarchical few-layer fluorine-free $Ti_3C_2T_X$ (T = O, OH)/MoS_2 hybrid for efficient electrocatalytic hydrogen evolution. *J. Mater. Chem. A* **9**, 922–927 (2021).

44. Wang, H. *et al.* Confined growth of pyridinic N-Mo_2C sites on MXenes for hydrogen evolution. *J. Mater. Chem. A* **8**, 7109–7116 (2020).

45. Ren, J. *et al.* 2D organ-like molybdenum carbide (MXenes) coupled with MoS_2 nanoflowers enhances the catalytic activity in the hydrogen evolution reaction. *CrystEngComm* **22**, 1395–1403 (2020).

46. Yan, Y. *et al.* Interfacial optimization of PtNi octahedrons@Ti_3C_2 MXenes with enhanced alkaline hydrogen evolution activity and stability. *Appl. Catal. B Environ.* **291**, 120100 (2021).

Chapter 5

Conclusion and Perspective

With the increase of global energy consumption rapidly around the world at the time of fossil fuels depleting, major concern has been raised over the substantial and green energy future. Development renewable and green pathways to produce fuels and chemicals plays an important role to meet carbon zero neutral goal. Hydrogen have been considered as a promising energy as a high energy density energy carrier and carbon-free during oxidation. One possible is to directly or indirectly use sunlight to produce hydrogen by splitting water.

Water splitting process whereby dissociating water molecular using electricity into hydrogen and oxygen is catalyzed most effectively by Pt-based and Ru/Ir-based materials respectively. However, the high cost and scarcity of these noble metal-based materials have hindered the large completely commercialized of electrochemical water splitting. It is therefore of importance to develop efficient catalysts for hydrogen evolution based on the materials with cheap and abundant.

Larger efforts have been made to find alternatives to noble-metal based catalysts in the last several decades. Although a series of noble-metal free materials have been found to promising alternatives to noble-metal based materials, it still has a gap to replace Pt-group metals in industry application.

In present thesis, we have designed and developed high-efficiency, high-stability, and cost-effective electrocatalysts using a facile and environmentally friendly process. Firstly, we developed an ultrathin hierarchical P-doped MoS_2/Ni_3S_2 heterostructure on nickel foam (NF) by one step hydrothermal method in Chapter Two. We tried to use P dopants to modified the electron structure of MoS_2/Ni_3S_2 heterostructure to enhance the

performance for both HER and OER in alkaline solution. In second part, Nitrogen-doped MoS_2/N-doped reduced graphene oxide (N-MoS_2/N-rGO) heterostructure were synthesized by hydrothermal methods in Chapter three. Here, we try to optimize the insert activity and conductivity of MoS2 by doping N and employing N-rGO as a conductive support at one time. And in the last project, we try to explore the performance of MXenes for HER in acid solution. All of these materials were characterized by a variety of different techniques, such as SEM, TEM, XRD, XPS, and Raman, and the catalytic performance were tested by electrochemical technique including LSV, CV, EIS, and chronopotentiometry.

From above experiment and analysis, it is easy to find that the interface structure e.g. growth MoS_2 on Ni_3S_2 or supports materials highly dispersed MoS_2 nanosheet on rGO could enhance the electrocatalysis performance by increase the surface area and expose more active sites of MoS_2, and also could decrease the charge transfer resistance and optimize the kinetic of electrochemical reaction.

And the N and P dopant could increase the intrinsic activity of MoS_2, by change the electron structure of Mo and S, which could make the adsorption free energy of intermediates including H and O-containing group closer zero. Furthermore, the N and P dopants could change the morphology of MoS_2/Ni_3S_2 and MoS_2/rGO to a nanoflower structure which could expose more active site for HER and OER.

In the coming days, we will try to insight into these heterostructure catalysis, and find main active sites and explain the mechanism.

For P doped MoS_2/Ni_3S_2/NF, the XPS will be employed to characterize the atom percentage of all elements, especially P, for all P doped samples. And then using the TEM to reconfirm the interface structure of P-MoS_2/Ni_3S_2/NF and reconfirm the DFT module and try to calculate the adsorption free energy of H and O containing

intermediates on Mo and S beside P dopant.

For N-MoS_2/N-rGO, DFT calculate the active sites for OER, because MoS_2 is inert for OER, and if possible, find a way to confirm the Mo-N-C charger transfer tunnel.

For MXenes, further study the effects of etching condition on HER. and then try to grow MoS_2 on MXenes and check the HER and OER performance.

Finally yielding a formation to understand optimizing mechanism of dopant atoms on catalysts for both HER and OER, which could rational guidance toward the development of improved catalysts.

Appendix

Experiment part

6.1 Characterization technologies

6.1.1 Scanning Electron Microscopy (SEM)

SEM images were obtained using an electron microscope SU5000 (Hitachi) equipped with an EDX/EBSD AZtec coupled system from Oxford Instruments (60 mm^2 SDD detector and EBSD Symmetry camera).

6.1.2 X-Ray Diffraction (XRD)

XRD patterns were collected on a high flux Rigaku Smartlab rotated anode, working with a copper Kα radiation (1.5418 Å) at an applied voltage of 45 kV and an anode current of 200 mA in the 2θ range of 5-90°. The beam was made parallel through a multilayer mirror and reflection geometry was used.

6.1.3 Transmission Electron Microscopy (TEM)

TEM analysis was performed on a TECNAI-G2 working at 200 kV with a resolution of 1.9 Å, equipped with an EDS spectrometer. The TEM samples were prepared by depositing ~20 μL of scratched particles solution onto carbon 200 mesh grid and drying at room temperature.

6.1.4 X-ray Photoelectron Spectroscopy (XPS)

XPS measurements were carried out with an ESCALAB 220 XL spectrometer from Vacuum Generators featuring a monochromatic Al Kα X-ray source (1486.6 eV) and a spherical energy analyzer operated in the CAE (constant analyzer energy) mode

(CAE=100 eV for survey spectra and CAE=40 eV for high-resolution spectra), using the electromagnetic lens mode. No flood gun source was needed due to the conducting character of the substrates. The angle between the incident X-rays and the analyzer is 58°. The detection angle of the photoelectrons is 30°. The binding energy was calibrated using the C_{1s} photoelectron peak at 284.8 eV as the reference.

6.1.5 Raman spectroscopy

Raman spectroscopy measurements were acquired using a visible LabRam HR spectrometer (Horiba Jobin Yvon, France). The Raman backscattering was excited with 473 nm wavelength. The beam was focused on the sample surface through an optical objective (100, 0.9 NA) with a lateral resolution (XY) of less than 1 mm. The spectral resolution was better than 2 cm^{-1}.

Publications

- Haye E., **Miao Y.**, et al. Enhancing Cycling Stability and Specific Capacitance of Vanadium Nitride Electrodes by Tuning Electrolyte Composition. *Journal of The Electrochemical Society*, 2022. https://doi.org/10.1149/1945-7111/ac7353.
- Pang L., **Miao Y**., et al. "Enhanced Electrocatalytic Activity of PtRu/nitrogen and Sulphur Co-doped Crumbled Graphene in Acid and Alkaline Media ". *Journal of Colloid and Interface Science*, 2021, 590: 154-163. https://doi.org/10.1016/j.jcis.2021.01.049